FACULTY OF ENGINEERING
AND ARCHITECTURE

UV Photonic Integrated Circuits for Label-Free Structured Illumination Microscopy and Quantitative Phase Imaging

Chupao Lin

Doctoral dissertation submitted to obtain the academic degree of
Doctor of Photonics Engineering

Supervisors
Prof. Nicolas Le Thomas, PhD - Prof. Roel Baets, PhD
Department of Information Technology
Faculty of Engineering and Architecture, Ghent University

March 2023

GHENT
UNIVERSITY

ISBN 978-94-6355-695-8
NUR 950
Wettelijk depot: D/2023/10.500/27

Members of the Examination Board

Chair

Prof. Em. Daniël De Zutter, PhD, Ghent University

Other members entitled to vote

Christian Haffner, PhD, imec
Prof. Kristiaan Neyts, PhD, Ghent University
Prof. Joyce Poon, PhD, Max Planck Institute for Microstructure Physics, Germany
Prof. Dries Van Thourhout, PhD, Ghent University

Supervisors

Prof. Nicolas Le Thomas, PhD, Ghent University
Prof. Roel Baets, PhD, Ghent University

Dankwoord

As I began to write the acknowledgment, it suddenly hit me that this would be the last moment of my Ph.D. program. Over the past 4.5 years, my time in the Photonic Research Group at UGent has been filled with unforgettable memories.

First and foremost, I would like to express my gratitude to my promoter, Prof. Nicolas Le Thomas. Your unwavering support during my difficult times has been invaluable. I have not only learned how to conduct scientific research, but also how to do it rigorously. This is a treasure that I will always cherish. My heartfelt thanks also go to my co-promoter, Prof. Roel Baets, for supporting this project.

I would like to acknowledge and thank my collaborators, Prof. Jolien, Prof. Christophe, and Juan from the Cocoon group for their contributions. Your world-class ALD thin films have been essential to the success of my project. I would also like to thank Prof. Nico for providing beautiful biological cell samples.

My sincere appreciation goes to Steven, Muneeb, and Liesbet for their support in the cleanroom. I am grateful to the administrative staff, Ilse Meersman, Ilse Van Royen, and Mike for helping me with the paperwork. I would also like to express my gratitude to Kristien for resolving any PC issues.

I am grateful to my colleagues in office 150.032, Ali, Alexandros, Clemens, Jasper, Paul, Emadreza, Irfan, Mattias, Manuel, and Meryem for making our office a joyful place. Your companionship has been a source of comfort and inspiration.

Lastly, I would like to thank my Chinese colleagues, Haolan, Xiaomin, Xiaoning, Yufei, Yuting, Hong, Xiangfeng, Zuyang, Yang, Zhongtao, Chao, Biwei, Shiyu, Yanlu, Xin, Chenming, Yize, Shengbiao, Ying, Yujie, Dongbo, and Chonghuai, for their companionship. I am especially grateful to Jing for sharing his senior experience and practical skills.

最后，我想感谢我的父母和姐姐。没有你们无条件的支持，我在学术这条路上将寸步难行。我要特别感谢我的妻子欧阳玥玲。我是如此幸运能够在这千里之外的他乡与你相遇，相识，相知，相爱，一起组建属于我们自己的家庭。是你的支持让我能够卸下浮躁，专心从事自己想做的工作。

Gent, March 2023
Chupao Lin

Table of Contents

List of Figures

List of Tables

List of Acronyms

A

ALD	Atomic layer Deposition
AlO_x	Aluminum Oxide
AWG	Arrayed Waveguide Grating
AlN	Aluminum Nitride
AFM	Atomic Force Microscopy

B

BOX	Buried Oxide

C

CCD	Charge-Coupled Device
CMOS	Complementary metal oxide semiconductor
CLSM	Confocal Laser Scanning Microscopy

D

DC	Directional Coupler
DI	Deionized
DMD	Digital Mirrored Devices
DIC	Differential Interference Contrast

E

EIC	Electronic Integrated Circuits
EUV	Extreme Ultra-Violet
EME	EigenMode Expansion

F

FDTD	Finite Difference Time Domain
FoV	Field-of-View
FWHM	Full Width at Half Maximum

G

GLIM	Gradient Light Interference Microscopy
GC	Grating out-Coupler

H

H_2O	Water
HfO_x	Hafnium Oxide

I

ICP	Inductively Coupled Plasma
IPA	Isopropyl Alcohol

K

KK	Kramers-Kronig relations

L

LN	Lithium Niobate
LED	Light Emitting Diodes
LPCVD	Low Pressure Chemical Vapor Deposition

M

MF	Mixed Frequency
MTF	Modulation Transfer Function
MMI	Multimode Interference

N

NA	Numerical Aperture

O

OTF	Optical Transfer Function

P

PALM	Photoactivated Localization Microscopy
PECVD	Plasma-Enhanced Chemical Vapor Deposition
PIC	Photonic Integrated Circuit
PAINT	Points Accumulation for Imaging in Nanoscale Topography
PCB	Printed Circuit Board
PTF	Phase Transfer Function

Q

QPM	Quantitative Phase Microscopy
QPI	Quantitative Phase Imaging

R

RIE	Reactive-Ion Etching

S

SRM	super-resolution microscopy
SIM	Structured Illumination Microscopy
SSIM	Saturated Structured Illumination Microscopy
STED	Stimulated Emission Depletion Microscopy
STORM	Stochastic Optical Reconstruction Microscopy
SEM	Scanning Electron Microscope
Si	Silicon
SiN_x	Silicon Nitride
SiO_2	Silicon Dioxide
SLIM	Spatial Light Interference Microscopy
SNR	Signal-to-Noise-Ratio
SLM	Spatial Light Modulators
SM	Signle Mode

T

TE	Transverse Electric
TIE	Transport of Intensity Equation
TMA	trimethylaluminum

U

UV	Ultraviolet
UHP	Upper-Half-Plane

W

wDPM	white-light Diffraction Phase Microscopy
WF	Wide Field

Nederlandse samenvatting –Summary in Dutch–

1 Inleiding

Fotonische geïntegreerde schakelingen (PIC) hebben de ontwikkeling van veel gebieden mogelijk gemaakt, waaronder telecommunicatie [1–3], kwantuminformatie [4, 5] en bio-sensing [6, 7]. De huidige mature technologieplatform van fotonische geïntegreerde schakelingen werken bÿ zichtbare of infrarode golflengten. Het is echter erg interessant om kortere golflengten in het ultraviolette (UV) bereik te onderzoeken, met het oog op één sterkere interactie tussen licht en materie. één verscheidenheid aan moleculen vertoont autofluorescentie met UV-lichtexcitatie, zoals het collagéén, elastine, flavine-adenine-dinucleotide en nicotinamide-adenine-dinucleotide (NADH) in biologische cellen. Deze intrinsieke fluorescentie is niet alléén interessant voor detectie van UV/Visible spectroscopie, maar ook voor labelvrije beeldvorming. De optische resolutie van conventionele microscopie wordt beperkt door diffractie, gegeven door $\frac{\lambda}{2NA}$, waarbij NA de numerieke apertuur van microscoopobjectieven is. Superresolutie gestructureerde verlichtingsmicroscopie (SIM) werd voorgesteld om de diffractielimiet te omzeilen en één hogere optische resolutie te bereiken, wat één van de wijdverspreide superresolutiemicroscopietechnieken is. De huidige gestructureerde verlichtingsmicroscoop kan echter alléén werken bij zichtbare golflengten vanwege één gebrek aan efficiënte manieren om UV-straling met één laag verlies te manipuleren. Bovendien is het SIM-systeem omvangrijk, gecompliceerd en duur, wat de belangrijkste redenen zijn waarom deze geavanceerde microscopie niet zo algeméén wordt gebruikt als conventionele microscopie. In deze context is er behoefte aan de ontwikkeling van één apparaat dat werkt als één add-on-module, niet alléén om conventionele microscopen te upgraden naar microscopen met gestructureerde verlichting, maar ook om de werkgolflengte uit te breiden naar het UV-bereik. Onze uitgangshypothese was de volgende: UV-compatibele PIC's die UV-licht met weinig verlies kunnen manipuleren, zullen naar verwachting één compacte oplossing mogelijk maken.

Momenteel maken superresolutiemicroscopietechnieken gebruik van de fluorescentie van fluoroforen om de diffractielimiet te doorbreken. Bijgevolg worden deze technieken ook beperkt door het fotobleken van fluoroforen, wat de beeldvorming met één lange acquisitietijd belemmert. Als alternatief vertrouwt kwantitatieve fasebeeldvorming (QPI) op de elastische verstrooiing van het object, die stabiel is in de tijd en géén last heeft van stroomuitval gedurende één lange acquisitietijd. Deze techniek registreert niet alléén de amplitude maar ook de fase-informatie van het afgebeelde object. Momenteel is de configuratie van QPI meestal omvangrijk vanwege de behoefte aan één op interferometrie gebaseerde opstelling. Om één hoge robuustheid te bereiken bÿ meting van de faze, moet het optische systeem mechanisch extreem stabiyel zijn om elke fasefluctuatie van de referentie- en objectbundel te voorkomen. Als alternatief is de recent gerapporteerde op intensiteit gebaseerde kwantitatieve fasebeeldvorming op basis van Kramers-Kronig (KK)-relaties veelbelovend voor het bieden van één oplossing voor één robuuste bepaling van de fase van het verstrooide veld [8]. Deze benadering vereist één zeer nauwkeurige regeling van de hoek van de verlichtingsbundels. Van PIC's wordt verwacht dat ze op één compacte en kosteneffectieve manier aan deze eis voldoen, door flexibele routeringscircuits en rooster-uitkoppelingen op één enkele chip te integreren om bundels onder één specifieke hoek te buigen.

Het proefschrift omvat de ontwikkeling van één UV-PIC-platform met lage verliezen, UV-PIC-gebaseerde labelvrije super-opgeloste gestructureerde verlichtingsmicroscopie en UV-PIC-gebaseerde kwantitatieve fasebeeldvorming. Momenteel is er géén volwassen PIC-platform dat compatibel is met UV-golflengten. De eerste stap van dit project was de ontwikkeling van laag verlies monomodale geïntegreerde golfgeleiders, door op zoek te gaan naar de juiste materialen om de golfgeleider te fabriceren. Vervolgens stelde ik één op UV-PIC gebaseerde SIM-techniek voor. Voordat ik gestructureerde belichtingsmicroscopie implementeerde met behulp van één UV-PIC, ontwierp, fabriceerde en karakteriseerde ik de on-chip optische componenten die nodig zijn voor het genereren van gestructureerde verlichting. Ten slotte heb ik de op UV-PIC KK-relaties gebaseerde QPI-techniek voorgesteld en gevalideerd, door de bepaling van de fase van het veld verstrooid door zuivere fase objecten op één robuuste manier.

2 Resultaten

2.1 Ontwikkeling van één UV-compatibel geïntegreerd fotonisch platform met behulp van ALD-aluminalagen

Er zijn twee belangrijke problemen bij het ontwikkelen van lage verliezen monomodale geïntegreerde golfgeleiders, namelijk materiaalabsorptieverlies en verstrooiingsverlies. Het UV-licht gedefinieerd in het bereik van 200 nm $< \lambda <$ 400 nm heeft energie in één bereik van 3.1 eV $\sim$ 6.2 eV, wat inhoudt dat de bandgap van het materiaal minimaal 6.2 eV moet zijn om directe absorptie van UV-licht te voorkomen. De veelgebruikte materialen zoals silicium en siliciumnitride vertonen één hoge absorptie bij UV-golflengten vanwege hun lage bandgap. Daarom heb ik eerst het thermische oxide SiO_2 met brede bandgap geselecteerd als de onderste bekleding en de HfO_x en AlO_x gebruikt als de kernlaag van de golfgeleider. De atomaire laagafzettingstechniek (ALD) werd gekozen om de HfO_x- en AlO_x-lagen te laten groeien vanwege de eigenschappen van hoge precisiecontrole van de laagdikte en hoge uniformiteit. Na het simuleren van de golfgeleidergeometrie om monomodale propagatie te realiseren, heb ik het droogetsproces van HfO$_x$ en AlO$_x$ geoptimaliseerd om gladde zijwanden te verkrijgen. Vergeleken met het op fluor gebaseerde gasetsen in één reactieve ionenetser (RIE), is aangetoond dat het op chloor gebaseerde gasetsen in ICP-RIE resulteert in hogere etssnelheden en gladdere zijwanden. Met ons huidige proces absorbeert de ALD-HfO$_x$-laag sterk het UV-licht bij één werkgolflengte van 360 nm, terwijl de ALD-AlO$_x$ naar verwachting één van de kandidaten zou zijn om lage verliezen monomodale golfgeleiders te bereiken die werken bÿ UV-golflengten. Figuur 1 toont de resultaten van de geoptimaliseerde AlO$_x$ golfgeleiders. Het verstrooide licht van één 1.1 μm brede spiraalvormige AlO$_x$ golfgeleider wordt getoond in Fig. 1(a). Het golfgeleiderverlies werd gemeten door het verval van de intensiteit van het verstrooide licht langs de voortplantingsrichting analyseren, zie Fig. 1(b). Door de breedte van de golfgeleider te variëren, verkreeg ik de relatie tussen het voortplantingsverlies en de breedte van de golfgeleider, zie Fig. 1(c). Één monomodale golfgeleider met laag verlies van 3 dB/cm wordt bereikt bij één werkgolflengte λ= 360 nm, met één golfgeleiderbreedte van 800 nm en één hoogte van 120 nm.

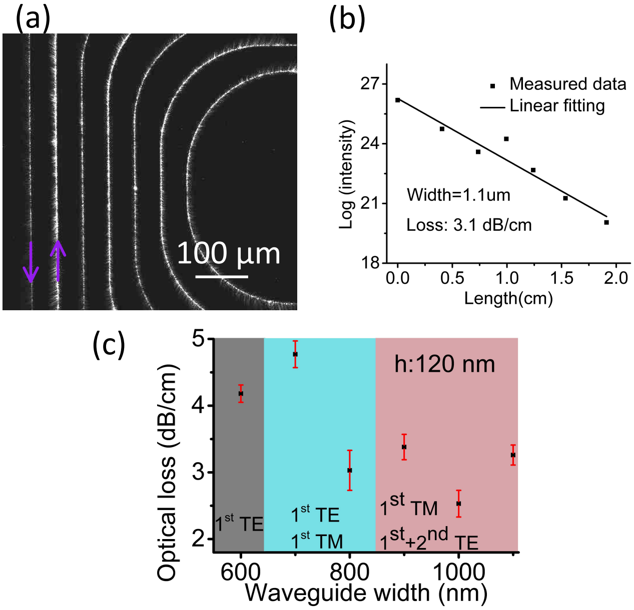

Figuur 1: (a) Afbeelding van het verstrooide licht van één deel van één spiraalvormige golfgeleider bÿ één excitatiegolflengte van 360 nm. De breedte van de golfgeleider is 1.1 μm. *(b) Lineaire fit van de logaritme van de intensiteit van het verstrooid licht van devoortplantingslengte. (c) Relatie tussen het voortplantingsverlies en de breedte van de golfgeleider.*

2.2 UV-PICs voor labelvrije super-opgeloste gestructureerde verlichtingsmicroscopie

De configuratie van de gestructureerde verlichtingsmicroscopie bestaat uit twee hoofdonderdelen, één standaardmicroscoop en één module om de gestructureerde verlichting te genereren en te regelen. Hier stel ik één op een UV-PIC gebaseerde add-on-module voor om de gestructureerde verlichtingspatronen te genereren en te regelen. De gefabriceerde UV-PIC die drie individuele circuits bevat wordt getoond in Fig. 2. Elk circuit bevat monomodale routeringsgolfgeleiders, één 1x2 MMI-straalsplitser, twee roosteruitkoppelingen en één on-chip thermische faseverschuiver. De gestructureerde verlichtingspatronen worden gegenereerd over drie verschillende oriëntaties, geroteerd over 120 ^{o}, waarvan de fase wordt aangepast door de on-chip thermische faseverschuiver. Het schema van de UV-PIC-basis SIM-configuratie wordt geïllustreerd in Fig. 2(b). Het UV-licht wordt gekoppeld van één monomodale vezel naar on-chip fotonische circuits, en wordt dan gesplitst en afgebogen naar de vrije ruimte om interferentiefzanjepatronen te genereren. Het fluorescerende monster boven de chip op het beeldvlak wordt geëxciteerd door de gestructureerde verlichting en zendt zichtbare fluorescentie-emissie uit, die wordt opgevangen door het microscoopobjectief. De verkregen beelden worden verwerkt met één algoritme ontwikkeld voor de reconstructie van één super-opgelost beeld. In deze benadering werkt de UV-PIC als één add-on-module voor standaardmicroscopen zonder het optische beeldvormingssysteem aan te passen en super-opgeloste beeldvorming te bereiken. Figuren 2(c) en (d) tonen de optische beelden van NADH-moleculen in gistcellen verkregen door respectievelijk één conventionele wide-field (WF) microscoop en de voorgestelde UV-PIC-gebaseerde SIM. Met één verzamelende numerieke apertuur van 1.32 en één excitatie numerieke apertuur van 0.5 werd één resolutieverbetering van $1.5\times$ bereikt. Fijnere details kunnen duidelijk worden opgelost met de SIM-techniek, zoals dubbele membranen die niet kunnen worden onderscheiden door conventionele WF-microscopie. Het laatste resultaat bevestigt dat de op UV-PIC gebaseerde SIM-techniek in staat is tot labelvrije super-opgeloste beeldvorming met biologische cellen.

2.3 UV-PICs voor kwantitatieve fasebeeldvorming

Vergeleken met conventionele op interferometrie gebaseerde QPI, biedt de op KK-relaties gebaseerde QPI-benadering één robuustere faseherwinning, aangezien de fase wordt opgehaald uit intensiteitsbeelden, die ongevoelig is voor faseverstoring in het optische systeem. De vereiste van de perfecte match tussen de excitatie numerieke apertuur NA$_{ex}$ met de verzamelende NA$_{col}$ van één is de sleutel voor het implementeren van deze aanpak. Hier stel ik UV-PIC's voor voor de implementatie van de op KK-relaties gebaseerde QPI, waarbij de UV-PIC's zijn ontworpen om schuine verlichtingen te genereren met één zeer nauwkeurige regeling van de hoeken. één reeks rooster-uitkoppelingen is ontworpen met verschillende vulfactoren en roosterafstanden op één enkele chip om NA $_{ex}$ te variëren en NA $_{col}$ te

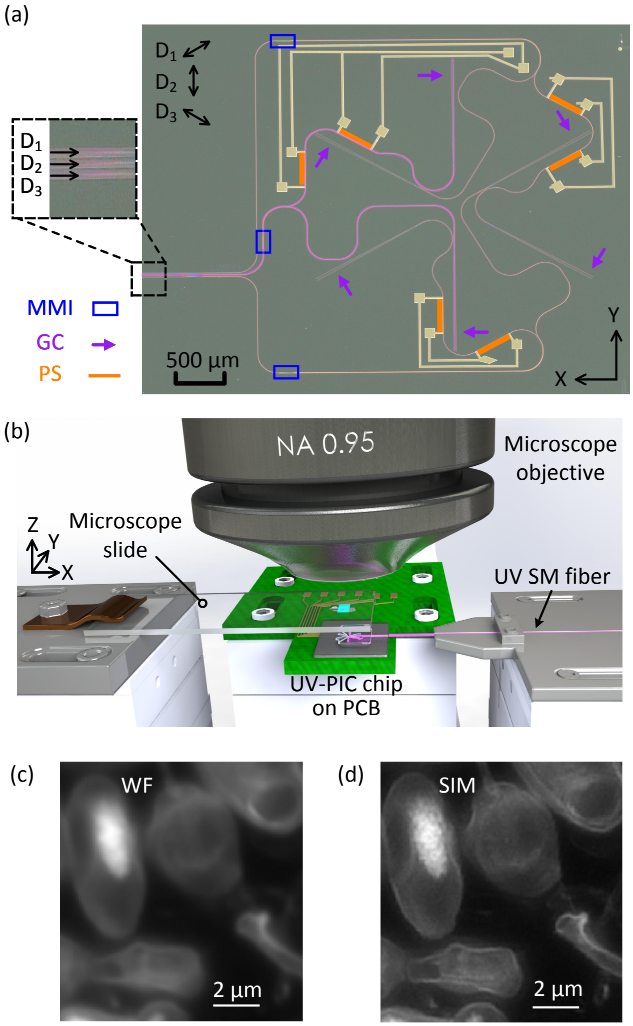

Figuur 2: (a) Optische afbeeldingen van de gefabriceerde UV-PIC voor 2D SIM. (b) Schema van de op de UV-PIC gebaseerde far-field SIM-opstelling inclusief één conventionele microscoop boven het microscoopobjectief. (c) Standaard wide-field en (d) gereconstrueerde SIM-afbeeldingen van NADH-moleculen in gistcellen.

matchen. één optisch beeld van de gefabriceerde UV-PIC wordt getoond in Fig. 3(a), die uit vier individuele circuits bestaat. Elk circuit bevat één monomodale golfgeleider, één adiabatische versmalling en één roosteruitkoppeling. Nadat het UV-licht is gekoppeld van één monomodale vezel naar het on-chip circuit, buigt de roosteruitkoppeling van het circuit het geleide licht af naar de vrije ruimte en verlicht het object onder het microscoopobjectief onder één bepaalde hoek. De oriëntatie van schuine verlichtingen werd geschakeld door de optische vezel zijdelings te verplaatsen om selectief het optische circuit en de rooster te activeren. Door de oriëntatie van schuine verlichting over 360 graden te draaien in één stap van 90 graden, werden vier onbewerkte beelden verkregen en nabewerkt om de fasekaart op te terughalen uit het intensiteitsbeeld. Ten slotte werden alle frequentiebanden aan elkaar gelinkt in het Fourier-domein en gedeconvolueerd om het 2D-fasebeeld met hoge resolutie te vormen. Met kennis van de brekingsindex van het object wordt de hoogtekaart verkregen uit de opgehaalde fasekaart. Figuur 3(b) toont de opgehaalde hoogtekaart van één vierkante pilaar structuur bovenop één dekglaasje. Het profiel langs de stippellijn is uitgezet in Fig. 3(c). Het is te zien dat de vierkante pilaar hoogte van 43 nm goed werd geëxtraheerd. Bovendien werd de fasegevoeligheid van de op de UV-PIC gebaseerde QPI gemeten door één blanco dekglaasje af te beelden, zie Fig. 3(d). Doon de histogramgrafiek in Fig. 3(e) te analyseren, bleek de hoogteresolutie zo laag te zijn, met name 1.3 nm. Dit resultaat toont aan dat de prestaties van de op UV-PIC gebaseerde QPI momenteel vergelijkbaar zijn met die van omvangrijke optica, terwijl de kosten en afmetingen van de configuratie drastisch afnemen.

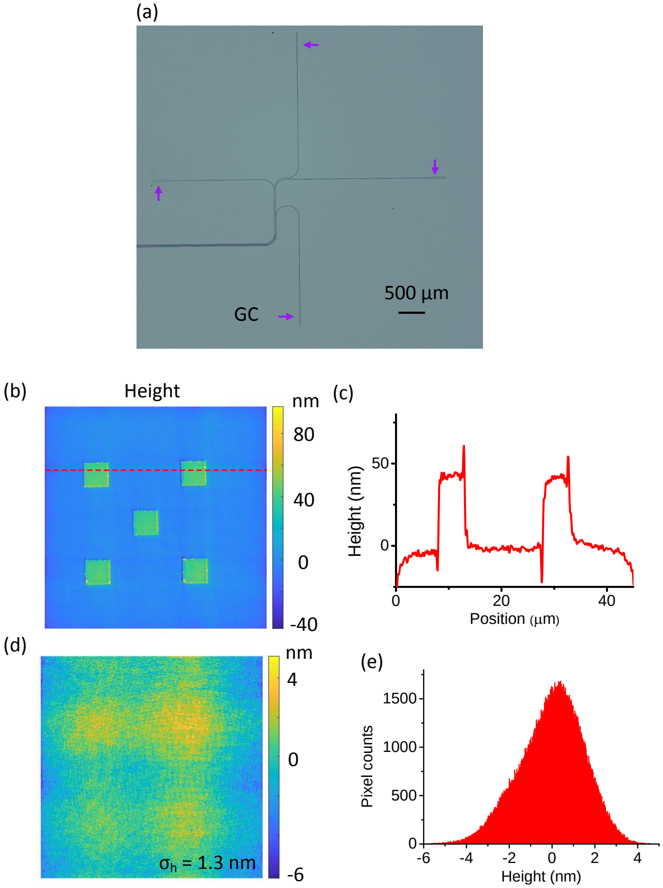

Figuur 3: (a) Optische afbeeldingen van de gefabriceerde fotonische circuits voor KK-QPI. (b) Opgehaalde hoogtekaart van één vierkante pilaar object met zuivere fase. (c) Dwarsdoorsnede langs de stippellijn in (b). (d) Faseruis van de op UV-PIC gebaseerde QPI door één leeg object af te beelden. Fasegevoeligheid σ_h*= 1,3 nm. (d) Histogramplot van (d).*

References

[1] Jing Zhang, Grigorij Muliuk, Joan Juvert, Sulakshna Kumari, Jeroen Goyvaerts, Bahawal Haq, Camiel Op de Beeck, Bart Kuyken, Geert Morthier, Dries Van Thourhout, Roel Baets, Guy Lepage, Peter Verheyen, Joris Van Campenhout, Agnieszka Gocalinska, James O'Callaghan, Emanuele Pelucchi, Kevin Thomas, Brian Corbett, António José Trindade, and Gunther Roelkens. *III-V-on-Si photonic integrated circuits realized using micro-transfer-printing*. APL Photonics, 4(11), 2019.

[2] Gunther Roelkens, Amin Abassi, Paolo Cardile, Utsav Dave, Andreas de Groote, Yannick de Koninck, Sören Dhoore, Xin Fu, Alban Gassenq, Nannicha Hattasan, Qiangsheng Huang, Sulakshna Kumari, Shahram Keyvaninia, Bart Kuyken, Lianyan Li, Pauline Mechet, Muhammad Muneeb, Dorian Sanchez, Haifeng Shao, Thijs Spuesens, Ananth Subramanian, Sarah Uvin, Martijn Tassaert, Kasper van Gasse, Jochem Verbist, Ruijun Wang, Zhechao Wang, Jing Zhang, Joris van Campenhout, Xin Yin, Johan Bauwelinck, Geert Morthier, Roel Baets, and Dries van Thourhout. *III-V-on-Silicon Photonic Devices for Optical Communication and Sensing*. Photonics, 2(3):969–1004, 2015.

[3] W. Bogaerts, D. Perez, J. Capmany, D. A. B. Miller, J. Poon, D. Englund, F. Morichetti, and A. Melloni. *Programmable photonic circuits*. Nature, 586(7828):207–216, 2020.

[4] Jianwei Wang, Fabio Sciarrino, Anthony Laing, and Mark G. Thompson. *Integrated photonic quantum technologies*. Nature Photonics, 14(5):273–284, 2019.

[5] Galan Moody, Volker J. Sorger, Daniel J. Blumenthal, Paul W. Juodawlkis, William Loh, Cheryl Sorace-Agaskar, Alex E. Jones, Krishna C. Balram, Jonathan C. F. Matthews, Anthony Laing, Marcelo Davanco, Lin Chang, John E. Bowers, Niels Quack, Christophe Galland, Igor Aharonovich, Martin A. Wolff, Carsten Schuck, Neil Sinclair, Marko Lončar, Tin Komljenovic, David Weld, Shayan Mookherjea, Sonia Buckley, Marina Radulaski, Stephan Reitzenstein, Benjamin Pingault, Bartholomeus Machielse, Debsuvra Mukhopadhyay, Alexey Akimov, Aleksei Zheltikov, Girish S. Agarwal, Kartik Srinivasan, Juanjuan Lu, Hong X. Tang, Wentao Jiang, Timothy P. McKenna, Amir H. Safavi-Naeini, Stephan Steinhauer, Ali W. Elshaari, Val Zwiller, Paul S. Davids, Nicholas Martinez, Michael Gehl, John Chiaverini, Karan K. Mehta, Jacquiline Romero, Navin B. Lingaraju, Andrew M. Weiner, Daniel Peace, Robert Cernansky, Mirko Lobino, Eleni Diamanti, Luis Trigo Vidarte, and Ryan M. Camacho. *2022 Roadmap on integrated quantum photonics*. Journal of Physics: Photonics, 4(1), 2022.

[6] X. Jia, J. Roels, R. Baets, and G. Roelkens. *A Miniaturised, Fully Integrated NDIR CO(2) Sensor On-Chip*. Sensors (Basel), 21(16), 2021.

[7] A. Dhakal, A. Raza, F. Peyskens, A. Z. Subramanian, S. Clemmen, N. Le Thomas, and R. Baets. *Efficiency of evanescent excitation and collection of spontaneous Raman scattering near high index contrast channel waveguides.* Opt Express, 23(21):27391–404, 2015.

[8] YoonSeok Baek and YongKeun Park. *Intensity-based holographic imaging via space-domain Kramers–Kronig relations.* Nature Photonics, 15(5):354–360, 2021.

English summary

1 Introduction

Photonic integrated circuits (PIC) have facilitated the development of a lot of fields including telecommunication [1–3], quantum information [4, 5], and biosensing [6, 7]. The current mature platforms of photonic integrated circuits operate at visible or infrared wavelengths. However, it is very interesting to explore shorter wavelengths in the ultra-violet (UV) range, in view of higher light-matter interaction. A variety of molecules exhibit autofluorescence with UV light excitation, such as the collagen, elastin, flavin adenine dinucleotide, and nicotinamide adenine dinucleotide (NADH) in biological cells. This intrinsic fluorescence is not only interesting for UV/Visible spectroscopy sensing but also for label-free imaging. The optical resolution of conventional microscopy is limited by diffraction, given by $\frac{\lambda}{2NA}$, where NA is the numerical aperture of microscope objectives. Super-resolution structured illumination microscopy (SIM) was proposed to bypass the diffraction limit and achieve a higher optical resolution, which is one of the widespread super-resolution microscopy techniques. However, the present structured illumination microscope can only work at visible wavelengths due to a lack of efficient ways to manipulate UV beams with a low loss. Besides, the SIM system is bulky, complicated, and expensive, which are the main reasons why this advanced microscopy is not used as widely as conventional microscopy. In this context, there is a need to develop a device that works as an add-on module not only to upgrade conventional microscopes to structured illumination microscopes but also to extend the working wavelength into the UV range. Our starting hypothesis was the following: UV-compatible PICs capable of manipulating UV light with low loss are expected to be a compact solution.

Currently, super-resolution microscopy techniques are making use of the fluorescence of fluorophores to break through the diffraction limit. As a consequence, these techniques are also limited by the photobleaching of fluorophores, which hinders the imaging with a long acquisition time. Alternatively, quantitative phase imaging (QPI) relies on the elastic scattering of the object, which is stable over time and does not suffer from the power drop for a long acquisition time. This technique records not only the amplitude but also the phase information of the imaged object. Currently, the configuration of QPI is mostly bulky due to the need for an interferometry-based setup. To reach high robustness of phase retrieval, the optical system must be extremely mechanically stable to avoid any phase fluctuation of the reference and object beam. Alternatively, the recently reported intensity-based quantitative phase imaging based on Kramers-Kronig (KK) relations is promising for providing a solution for a robust determination of the phase of the scattered field [8]. This approach requires a high accuracy control of the angle of the illumination beams. PICs are expected to meet this requirement in a compact and cost-effective way, by integrating flexible routing circuits and grating out-couplers on a single chip to diffract beams at a specific angle.

The thesis includes the topics of the development of a low-loss UV-PIC platform, UV-PIC-based label-free super-resolved structured illumination microscopy, and UV-PIC-based quantitative phase imaging. Currently, there is no mature PIC platform compatible with UV wavelengths. The first step of this project was the development of low-loss single-mode integrated waveguides, by starting to look for the proper materials to process the waveguide. Next, I proposed a UV-PIC-based SIM technique. Prior to implementing structured illumination microscopy using UV-PIC, I designed, fabricated, and characterized the on-chip optical components necessary for the generation of structured illuminations. Finally, I proposed and validated the UV-PIC KK-relations-based QPI technique, by achieving the determination of the phase of the field scattered by pure-phase objects in a robust way.

2 Results

2.1 Development of a UV-compatible integrated photonic platform using ALD-alumina layers

There are two main difficulties to develop low-loss single-mode integrated waveguides, namely material absorption loss and scattering loss. The UV light defined in the range 200 nm $<\ \lambda\ <$ 400 nm has energy in a range of 3.1 eV $\sim$ 6.2 eV, which implies that the bandgap of the material should be at least 6.2 eV in order to avoid direct absorption of UV light. The commonly used materials such as silicon and silicon nitride show high absorption at UV wavelengths due to their low bandgap. Therefore, I first selected the wide-bandgap thermal oxide SiO_2 as the bottom cladding and used the HfO_x and AlO_x as the core layer of the waveguide. The atomic layer deposition technique (ALD) was chosen to grow the HfO_x and AlO_x layers in view of its properties of high precision control of the layer thickness and high uniformity. After simulating waveguide geometry to realize single-mode propagation, I optimized the dry etching process of HfO_x and AlO_x to achieve smooth side walls. Compared with the fluorine-based gas etching in reactive ion etcher (RIE), the chlorine-based gas etching in ICP-RIE is demonstrated to result in higher etching rates and smoother side walls. With our current process, the ALD-HfO_x layer absorbs strongly the UV light at a working wavelength of 360 nm, while the ALD-AlO_x was expected to be one of the candidates to achieve low-loss single-mode waveguides operating at UV wavelengths. Figure 1 shows the results of the optimized AlO_x waveguides. The light scattered from a 1.1 μm-wide spiral AlO_x waveguide is shown in Fig. 1(a). The waveguide loss was measured by analyzing the intensity decay of the scattered light along the propagation length, see Fig. 1(b). Varying the waveguide width, I obtained the relationship between the propagation loss and the waveguide width, see Fig. 1(c). A single-mode low-loss waveguide of 3 dB/cm is achieved at a working wavelength λ= 360 nm, with a waveguide width of 800 nm and a height of 120 nm.

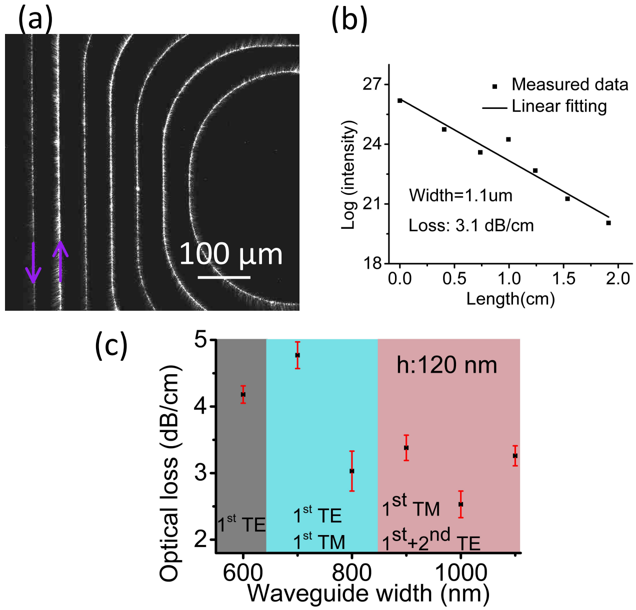

Figure 1: (a) Image of the scattered light from a part of a spiral waveguide with the excitation wavelength of 360 nm. The waveguide width is 1.1 µm. (b) Linear fitting of the logarithm of the intensity of scattered light and propagation length. (c) Relationship between the propagation loss and waveguide width.

2.2 UV-PIC for label-free super-resolved structured illumination microscopy

The configuration of the structured illumination microscopy consists of two main parts, a standard microscope and a module to generate and control the structured illumination. Here, I propose a UV-PIC-based add-on module to generate and control the structured illumination patterns. A fabricated UV-PIC is shown in Fig. 2, which includes three individual circuits. Each circuit includes single-mode routing waveguides, a 1x2 MMI beam splitter, two grating out-couplers, and an on-chip thermal phase shifter. The structured illumination patterns are generated over three different orientations rotated by 120 ^{o}, the phase of which is adjusted by the on-chip thermal phase shifter. The schematic of the UV-PIC-base SIM setup is illustrated in Fig. 2(b). The UV light is coupled from a single-mode

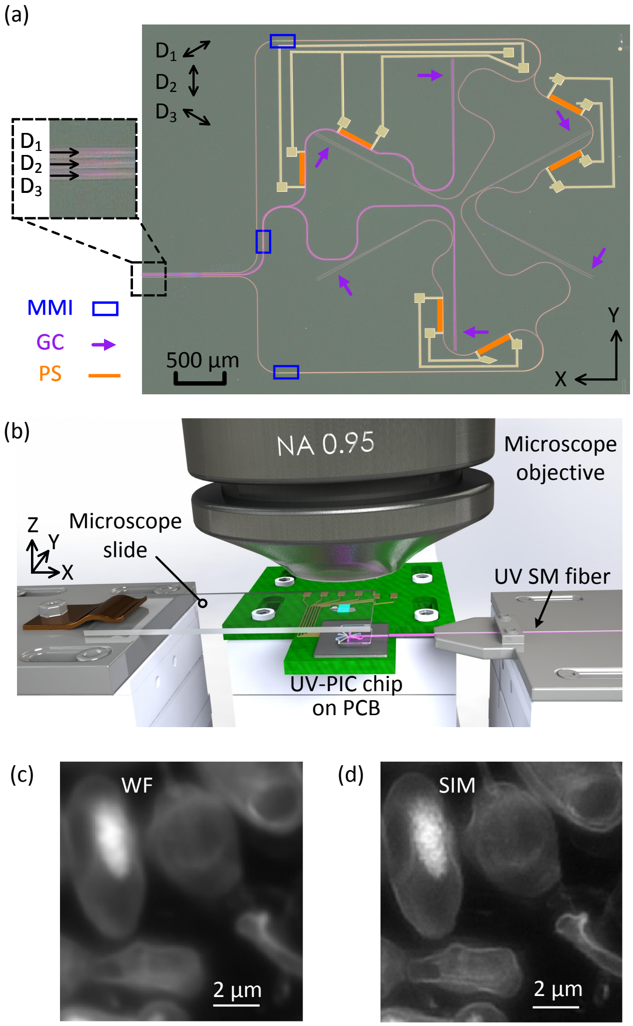

Figure 2: (a) Optical images of the fabricated UV-PIC for 2D SIM. (b) Schematic of the UV-PIC-based far-field SIM set-up including a conventional microscope above the microscope objective. (c) Standard wide-field and (d) reconstructed SIM images of NADH molecules in yeast cells.

fiber to on-chip photonic circuits and is then split and diffracted into free space in order to generate interference fringe patterns. The fluorescent sample above the chip at the imaging plane is excited by the structured illumination and emits visible fluorescence emission, which is collected by the microscope objective. The acquired images are processed with an algorithm developed for the reconstruction of a super-resolved image. In this approach, the UV-PIC is working as an add-on module to standard microscopes without modifying the optical imaging system and achieving super-resolved imaging. Figures 2(c) and (d) show the optical images of NADH molecules inside yeast cells acquired by a conventional wide-field (WF) microscope and the proposed UV-PIC-based SIM, respectively. With a collecting numerical aperture of 1.32 and an excitation numerical aperture of 0.5, a $1.5\times$ resolution enhancement was achieved. More fine features can be clearly resolved with the SIM technique, such as dual membranes which can not be distinguished by conventional WF microscopy. The last result validates that the UV-PIC-based SIM technique is capable of label-free super-resolved imaging with biological cells.

2.3 UV-PICs for quantitative phase imaging

Compared with conventional interferometry-based QPI, the KK-relations-based QPI approach offers more robust phase retrieval since the phase is retrieved from intensity images, which is insensitive to phase perturbation in the optical system. The requirement of the perfect match between the excitation numerical aperture NA_{ex} with the collection one NA_{col} is the key for implementing this approach. Here, I propose UV-PICs for the implementation of the KK-relations-based QPI, where the UV-PICs are designed to deliver oblique illuminations with a high-accuracy control of the angles. An array of grating out-couplers are designed with different filling factors and grating pitches on a single chip to vary NA_{ex} and match NA_{col}. An optical image of the fabricated UV-PIC is shown in Fig. 3(a), which consists of four individual circuits. Each circuit includes a single-mode waveguide, an adiabatic taper, and a grating out-coupler. After the UV light is coupled from a single-mode fiber to the on-chip circuit, the grating out-coupler of the circuit diffracts the guided light to free space and illuminate the object below the microscope objective at a given angle. The orientation of oblique illuminations was switched by laterally translating the optical fiber to selectively activate the optical circuit and the grating out-coupler. By rotating the orientation of oblique illumination by 360 degrees at a step of 90 degrees, four raw images were acquired and post-processed to retrieve the phase map from the intensity image. Finally, all the frequency bands were stitched in the Fourier domain and deconvoluted to form the high-resolution 2D phase image. With the knowledge of the refractive index of the object, the height map is obtained from the retrieved phase map. Figure 3(b) shows the retrieved height map of a square pillar structure on top of a coverslip. The profile along the dashed line is plotted in Fig. 3(c). It can be seen that the square pillar height of 43 nm was well recovered. Furthermore, the phase sensitivity of the UV-PIC-based QPI was measured by imaging a blank coverslip, see

Fig. 3(d). The height sensitivity turned out to be as low as 1.3 nm by analyzing the histogram plot in Fig. 3(e). This result demonstrates that the performance of the UV-PIC-based QPI is currently comparable with that of bulky optics, while the cost and dimension of the configuration decrease dramatically.

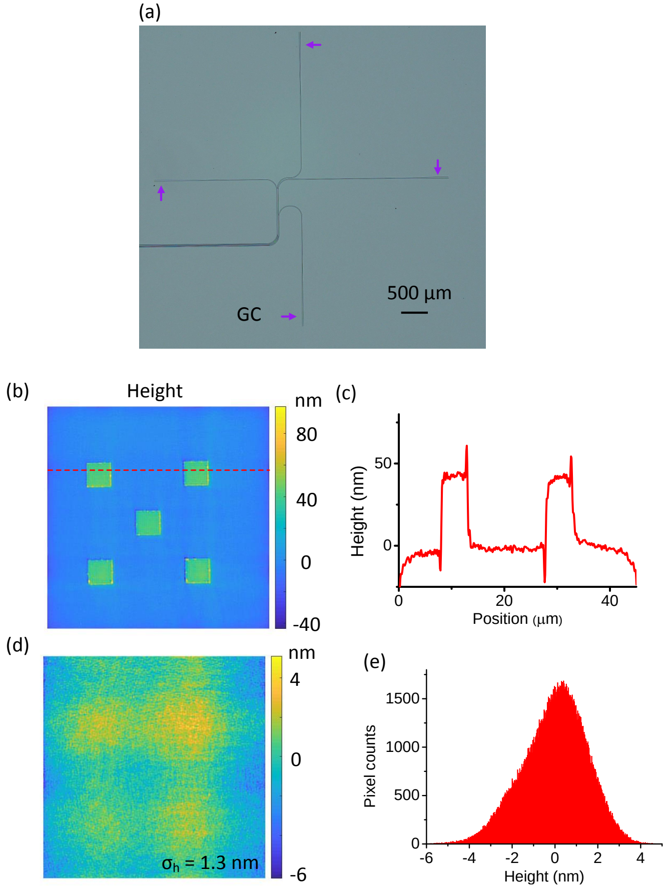

Figure 3: (a) Optical images of the fabricated photonic circuits for KK-QPI. (b) Retrieved height map of a pure phase square pillar object. (c) Cross-section along the dashed line in (b). (d) Phase noise of the UV-PIC-based QPI by imaging a blank object. Phase sensitivity σ_h *= 1.3 nm. (d) Histogram plot of (d).*

References

[1] Jing Zhang, Grigorij Muliuk, Joan Juvert, Sulakshna Kumari, Jeroen Goyvaerts, Bahawal Haq, Camiel Op de Beeck, Bart Kuyken, Geert Morthier, Dries Van Thourhout, Roel Baets, Guy Lepage, Peter Verheyen, Joris Van Campenhout, Agnieszka Gocalinska, James O'Callaghan, Emanuele Pelucchi, Kevin Thomas, Brian Corbett, António José Trindade, and Gunther Roelkens. *III-V-on-Si photonic integrated circuits realized using micro-transfer-printing*. APL Photonics, 4(11), 2019.

[2] Gunther Roelkens, Amin Abassi, Paolo Cardile, Utsav Dave, Andreas de Groote, Yannick de Koninck, Sören Dhoore, Xin Fu, Alban Gassenq, Nannicha Hattasan, Qiangsheng Huang, Sulakshna Kumari, Shahram Keyvaninia, Bart Kuyken, Lianyan Li, Pauline Mechet, Muhammad Muneeb, Dorian Sanchez, Haifeng Shao, Thijs Spuesens, Ananth Subramanian, Sarah Uvin, Martijn Tassaert, Kasper van Gasse, Jochem Verbist, Ruijun Wang, Zhechao Wang, Jing Zhang, Joris van Campenhout, Xin Yin, Johan Bauwelinck, Geert Morthier, Roel Baets, and Dries van Thourhout. *III-V-on-Silicon Photonic Devices for Optical Communication and Sensing*. Photonics, 2(3):969–1004, 2015.

[3] W. Bogaerts, D. Perez, J. Capmany, D. A. B. Miller, J. Poon, D. Englund, F. Morichetti, and A. Melloni. *Programmable photonic circuits*. Nature, 586(7828):207–216, 2020.

[4] Jianwei Wang, Fabio Sciarrino, Anthony Laing, and Mark G. Thompson. *Integrated photonic quantum technologies*. Nature Photonics, 14(5):273–284, 2019.

[5] Galan Moody, Volker J. Sorger, Daniel J. Blumenthal, Paul W. Juodawlkis, William Loh, Cheryl Sorace-Agaskar, Alex E. Jones, Krishna C. Balram, Jonathan C. F. Matthews, Anthony Laing, Marcelo Davanco, Lin Chang, John E. Bowers, Niels Quack, Christophe Galland, Igor Aharonovich, Martin A. Wolff, Carsten Schuck, Neil Sinclair, Marko Lončar, Tin Komljenovic, David Weld, Shayan Mookherjea, Sonia Buckley, Marina Radulaski, Stephan Reitzenstein, Benjamin Pingault, Bartholomeus Machielse, Debsuvra Mukhopadhyay, Alexey Akimov, Aleksei Zheltikov, Girish S. Agarwal, Kartik Srinivasan, Juanjuan Lu, Hong X. Tang, Wentao Jiang, Timothy P. McKenna, Amir H. Safavi-Naeini, Stephan Steinhauer, Ali W. Elshaari, Val Zwiller, Paul S. Davids, Nicholas Martinez, Michael Gehl, John Chiaverini, Karan K. Mehta, Jacquiline Romero, Navin B. Lingaraju, Andrew M. Weiner, Daniel Peace, Robert Cernansky, Mirko Lobino, Eleni Diamanti, Luis Trigo Vidarte, and Ryan M. Camacho. *2022 Roadmap on integrated quantum photonics*. Journal of Physics: Photonics, 4(1), 2022.

[6] X. Jia, J. Roels, R. Baets, and G. Roelkens. *A Miniaturised, Fully Integrated NDIR CO(2) Sensor On-Chip*. Sensors (Basel), 21(16), 2021.

[7] A. Dhakal, A. Raza, F. Peyskens, A. Z. Subramanian, S. Clemmen, N. Le Thomas, and R. Baets. *Efficiency of evanescent excitation and collection of spontaneous Raman scattering near high index contrast channel waveguides*. Opt Express, 23(21):27391–404, 2015.

[8] YoonSeok Baek and YongKeun Park. *Intensity-based holographic imaging via space-domain Kramers–Kronig relations*. Nature Photonics, 15(5):354–360, 2021.

1

Introduction

This chapter first introduces state-of-the-art advanced microscopy technologies including super-resolution microscopy (SRM) and quantitative phase imaging (QPI). Compared with conventional optical microscopy, the former exhibits higher optical resolutions and breakthroughs the diffraction limit, while the latter is capable of unveiling the optical path length of the imaged object. These advanced microscopy techniques require complex beam manipulation leading to bulky and expensive configurations, which is one of the main reasons why advanced microscopy techniques are not as widely used as conventional microscopy. There is a need to develop advanced microscopy in a low-cost and compact way and tackle these issues. Photonic integrated circuits, capable of integrating complex optical circuits in a compact size and compatible with massive production, are expected to be one of the solutions. In the second part of this chapter, I will introduce and compare different platforms of photonic integrated circuits. Besides, I will introduce state-of-the-art PIC-based advanced microscopy techniques. Finally, I will point out the research objectives and outline of this thesis.

1.1 Microscopy techniques

In this section, we will briefly introduce the development of optical microscopy and the current advanced microscopy techniques including fluorescence-based super-resolution microscopy techniques and coherent light based quantitative phase imaging. The typical super-resolution microscopy techniques discussed here include stimulated emission depletion microscopy (STED), photoactivated localization microscopy (PALM)/stochastic optical reconstruction microscopy (STORM), and structured illumination microscopy (SIM). The next is the QPM techniques including phase shifting, off-axis digital holographic microscopy, and the more recent intensity-based techniques. In the final subsection, we will discuss the photonic integrated circuits (PIC) and their application for miniaturized modules enabling conventional microscopes to become advanced microscopes.

1.1.1 Conventional optical microscopy

Microscopy is a technique to observe objects which can not be observed by the naked eye. The microscope techniques can be divided into three categories according to their working wavelengths: optical, electron and x-ray microscopy. Among them, optical microscopy is the easiest one to be reached, which generally works at visible wavelength, so at the early stage, sunlight can even be the source of illumination. The earliest record of using microscopy techniques can be traced back to the 13th century when people used only a single magnifying glass to enlarge the object [1]. In the 17th century, a more advanced compound microscope made of two lenses was reported [2], which is similar to the present microscope. In recent decades, the optical microscope has been rapidly developed not only in terms of the design and fabrication of optical components but also in terms of their functionality. The present conventional microscope includes a charge-coupled device (CCD)/complementary metal–oxide–semiconductor (CMOS) camera, a system of achromatic lenses, and an argon lamp or lasers. In conventional wide-field microscopy, the illumination interacts with the object in ways of light scattering, absorption, diffraction, and reflection. The objective collects the scattered or transmitted light to be recorded by a digital camera to form images. The microscopy technique only reveals the morphology of the objects and the optical resolution is limited to $\sim$200 nm in the visible range due to diffraction. Therefore, there is a need to develop advanced microscopy techniques to reveal more information and achieve a higher optical resolution. The development of camera sensors allows us to post-process the acquired images, which is one of the key components used in advanced microscopy techniques. Besides, the elaborated achromatic lenses and laser sources facilitate multi-color fluorescence imaging which allows to study specifically multiple structures in biological cells at the same time.

1.1.2 Super resolution microscopy

Although optical microscopy is able to inspect the morphology and monitor the movement of biological cells, many of the fine features are not resolvable due to the diffraction limit. In this part, we will introduce three typical super-resolution microscopy techniques, namely PALM/STORM, STED, and SIM respectively.

These techniques are all developed by taking advantage of the properties of fluorescence probes. PALM/STORM techniques make use of the photoswitching of fluorescent probes to localize the molecular position. STED takes advantage of the stimulated depletion of the excited fluorescent probes to restrict the area of the fluorescence emission. SIM technique is based on the spatial frequency mixing between a structured illumination and the fluorescence emission.

1.1.2.1 Single-molecule localization microscopy (PALM/STORM)

The PALM and STORM are using the same concept to localize the fluorescent probe. Therefore, they are categorized in the same technique 'localization microscopy'.

Due to the diffraction in conventional microscopy, a small point will be broadened after imaging by optical microscopy, which means two adjacent small objects become one blurred spot when the spacing between the objects is smaller than the microscopy resolution. In this context, localization microscopy is developed to bypass the spatial resolution limit by scarifying the temporal resolution. The concepts of PALM and STORM are demonstrated in the same period in 2006 by Betzig and Zhuang, respectively [3, 4]. The schematic of the localization microscopy is shown in Fig. 1.1. The technique behind is to control the fluorescence probes to emit one after another, which enables localizing every single fluorophore one by one even if it is broadened in the image. After acquiring and localizing hundreds even thousands of raw frames, a high-resolution image is reconstructed. In this way, the technique can achieve very high spatial resolution of $\sim$ 10nm [5]. The key of localization microscopy is the photo-switching fluorophores whose status of the fluorescence emission can be switched repeatably between "on" and "off". PALM uses a photoactivatable fluorescent protein to demonstrate its concept and similarly STORM was demonstrated by using a pair of synthetic dyes which also exhibits photo-switching properties. As a consequence, localization microscopy requires special fluorescence probes to stain the sample, which is however incompatible with standard protocols of fluorescence imaging.

1.1.2.2 Stimulated emission depletion (STED) microscopy

In the 1950s, Minsky originally proposed the basic concept of confocal laser scanning microscopy (CLSM) to overcome the axial resolution limit of traditional wide-field microscopy. With a pinhole in the imaging plane of the collection path, the light coming from an out-of-focus plane is eliminated and only the fluorescence close to the focal plane is collected. However, CLSM still obeys the diffraction limit and its lateral resolution is roughly the same as wide-field microscopy. STED is a kind of scanning microscopy to bypass the diffraction limit. It was first developed by S. Hell and J. Wichmann in 1994 [6] and was experimentally demon-

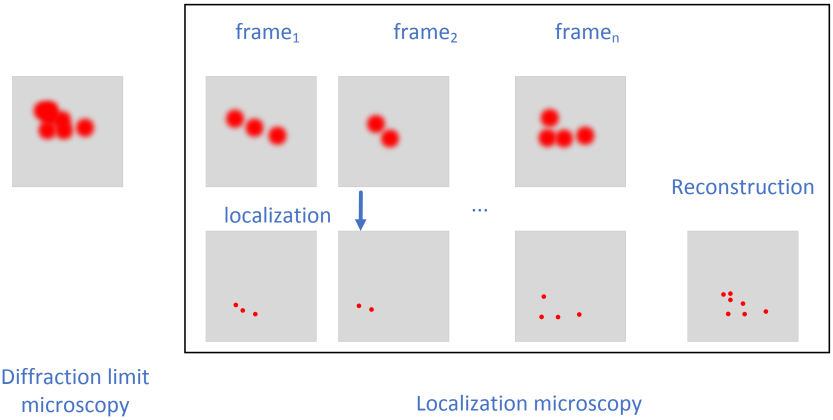

Figure 1.1: Schematic of localization microscopy.

strated in 1999 [7]. In addition to a single excitation beam used in conventional scanning microscopy, a STED setup employs an extra depletion laser beam in a donut shape to reshape the fluorescence, see Fig. 1.2(a). Since the lateral resolution of laser scanning microscopy is determined by the size of the focused beam, a smaller focal spot gives a better spatial resolution. The mechanism of reducing the focal size involved in SETD microscopy is shown in Fig.1.2(b). For conventional scanning microscopy, fluorophores are excited by the laser beam (green) and the molecular in a state S_0 jump to an excited state of a high energy level S_1. After initial vibrational relaxation, the molecular return to the ground state S_0 and emit fluorescence via spontaneous emission (yellow). In the STED system, the depletion beam initiates the stimulation emission which leads to a different electron transition (red) and an emission of a different wavelength. As the efficiency of the stimulation scales with the incident photons of the depletion laser, a high enough power is able to deplete the state S_1. In this way, the fluorescence of fluorophores located inside the donuts-shape depletion beam will not contribute to the final image and the fluorescence spot size is suppressed. The high lateral resolution of STED varies from 30 to 80 nm depending on the incident power [8]. However, the requirement of high laser power leads to high phototoxicity on biological samples.

1.1.2.3 Super-resolved structured illumination microscopy (SIM)

SIM is one of the most universally used super-resolution microscopy techniques since it is compatible with the standard protocol of sample preparation for fluorescence imaging. As the inventor of the SIM technique, Mats G. L. Gustafsson said:

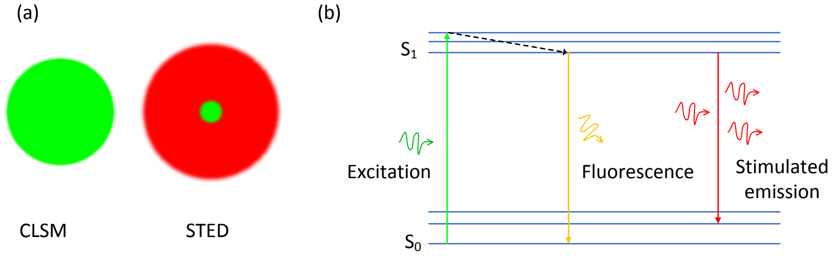

Figure 1.2: (a) Schematic of beam shape for confocal microscopy and STED. (b) Diagram of energy state involved in STED.

"I like to think in frequency space, rather than in real pace. [9]"

The SIM technique is closely involved with the frequency domain and the principle behind is spatial frequency mixing. In 1996, Gustafsson and Frohn demonstrated that using the structured sinusoidal illumination enables the standard microscope to record the frequency beyond the transmission bandwidth and bypass the diffraction limit [10, 11]. The microscopy system is regarded as a low-pass spatial filter that collects only the low spatial frequency falling inside the bandwidth. To achieve higher optical spatial resolution, the straightforward way is to design objectives of high numerical apertures (NA) and collect higher frequencies. Instead of making efforts on the design of the objective, SIM takes advantage of spatial frequency mixing to downconvert the high frequencies of samples and then allows microscopes to record the frequencies beyond the bandwidth. The schematic of the working principle of the typical two-dimensional (2D) SIM technique is shown in Fig. 1.3. Instead of using a uniform pattern for illumination to excite the samples, SIM uses structured illumination which is generated by a two-beam interference at the sample plane, see Fig. 1.3(a). With uniform illumination, standard wide-field microscopy can not see the frequency beyond its bandwidth. For instance, the modulation of periodical grating structures is not visible, see Fig. 1.3(c). With structured illumination, we can record the Moir$\acute{e}$ patterns which are generated by the frequency mixing between the fluorophore distribution of the object and the structured illumination. The generated Moir$\acute{e}$ patterns contain the down-converted high-frequency signals. To disentangle the mixed information, three phases (0, $2/3\pi$, $4/3\pi$) of structured illuminations for each orientation (0, 120^o, 240^o) are required, which means nine raw frames in total will be needed to reconstruct a single super-resolved image. The analytical formalism involved in 2D SIM will be discussed in chapter 2. Limited by the spatial frequency of the structured illumination, the typical linear SIM can only enhance the lateral resolution by a factor of $\sim$2. Considering the saturation property of the fluorescence, higher harmonic waves will be generated if the incident power is high enough. In 2005, Gustafsson demonstrated that the saturated SIM (SSIM) achieved a resolution of 50 nm and theoretically the resolution is only limited by the noise [12]. The constraint of SSIM is high phototoxicity on biological cells similar to the STED technique. Besides, SIM is also capable of 3D super-resolution imaging. The illumination in 2D SIM is only modulated in the lateral plane, while it is also modulated in the axial direction in 3D-SIM achieved by a three-beam interference. The extra cost is a lower time bandwidth because more raw frames are needed for the reconstruction. Fifteen raw frames in total are required to reconstruct a single super-resolved image in 3D SIM [13].

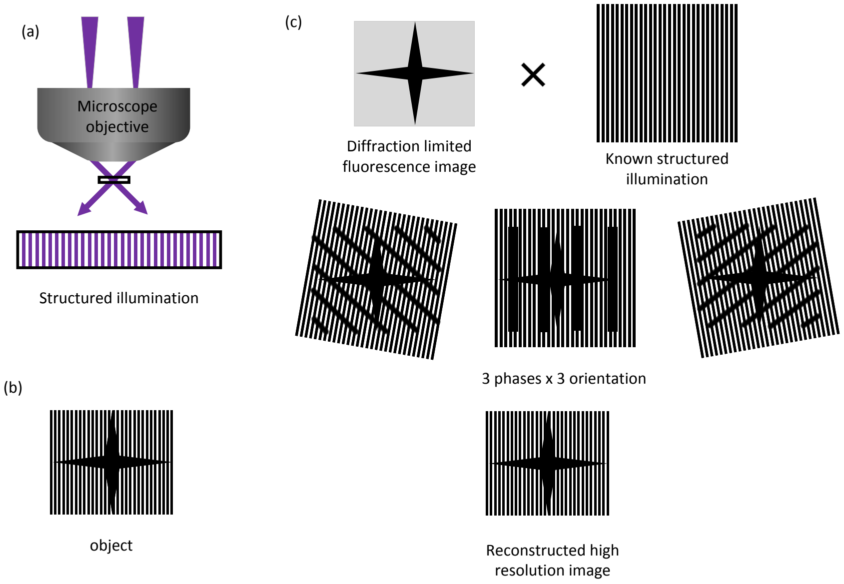

Figure 1.3: (a)Structured illumination generated by two-beam interference. (b) Ground truth of the object to be imaged. (c)Working principle of the typical 2D structured illumination microscopy.

1.1.3 Quantitative phase imaging

Fluorescence-based microscopy shows its advantages in terms of imaging specific structures in biological cells, but the requirements of labeling limit its capability for long-term live-cell imaging due to the toxicity of staining and quenching issues. Quantitative phase imaging has emerged as a kind of label-free imaging technique able to quantitatively retrieve the phase of the object. The phase images indicate not only the profile of the objects but also the information on refractive index and thickness. QPI techniques are generally developed to record the phase of the light field by interfering with the 'object wave' passing through the sample and the 'reference wave' without being disturbed. This section starts with the introduction of QPI techniques which are divided into two main categories, namely phase-shifting QPI and off-axis QPI respectively. Then, we introduce the space-domain Kramers-Kronig (KK) relations based QPI, a special case off-axis QPI that is investigated in this thesis.

1.1.3.1 Phase shifting quantitative phase imaging

The typical schematic of the phase shifting QPI is shown in Fig.1.4. A beam is divided into two beams via the first beam splitter (BS_1). One of the beams, namely the object wave, passes through the imaged object, which is collected by a microscope objective. Another beam, namely the reference wave, does not pass through any object and its waveform remains intact. Finally, the object wave and reference wave are combined at the second beam splitter, which generates the holography at the camera sensor. The recorded intensity can be written as:

$$I(x,y) = I_o + I_r(x,y) + 2\sqrt{I_o I_r(x,y)} cos[\omega\tau + \phi(x,y)] \tag{1.1}$$

where I_o and $I_r(x,y)$ are the intensities of the object wave and reference wave, respectively, ω is the angular frequency of the optical field, τ is the time delay and $\phi(x,y)$ is the phase difference between the two waves. The $\phi(x,y)$ can be retrieved according to four intensity images recorded at $\omega\tau$= 0, $\pi/2$, π, $3\pi/2$ [14]:

$$\phi(x,y) = tan^{-1}(\frac{I_{3\pi/2}(x,y) - I_{\pi/2}(x,y)}{I_0(x,y) - I_\pi(x,y)}) \tag{1.2}$$

Because of the requirement of a series of raw frames, the time-domain throughput of this technique is limited.

1.1.3.2 Off-axis quantitative phase imaging

The off-axis QPI is proposed to maximize the time-domain throughput, which can recover the phase image using only one frame. The schematic of the off-axis QPI is similar to that of the phase-shifting QPI except for the second beam-splitter, see Fig. 1.5. The beam splitter is placed in the optical path with an angle with respect to the propagation direction of the object wave. The intensity recorded at the camera is then given by:

$$I(x,y) = I_o + I_r(x,y) + 2\sqrt{I_o I_r(x,y)} cos[k_{off}x + \phi(x,y)] \tag{1.3}$$

The k_{off} is the spatial frequency of the reference beam determined by the off-axis angle θ, $k_{off} = \frac{2\pi}{\lambda} sin(\theta)$, λ is the working wavelength. From the equation we can see that the cross-term can be disentangled with the intensity of the object wave

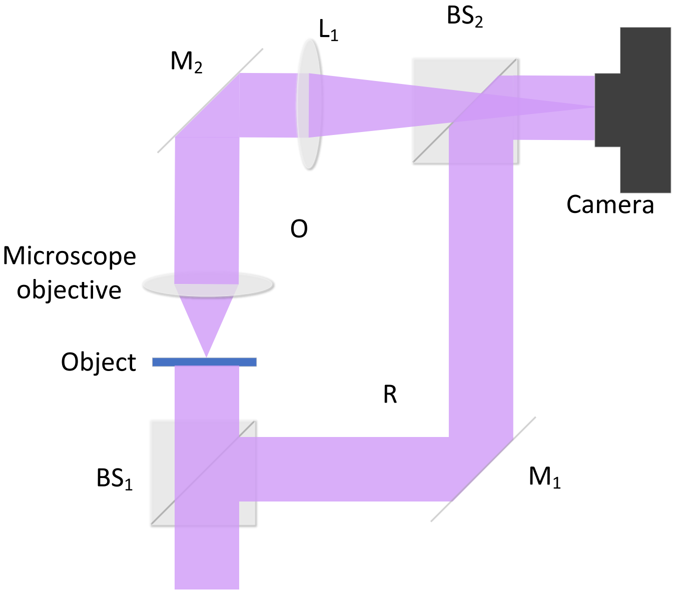

Figure 1.4: Configuration schematic of phase shifting QPI

at $k_{off} > k_{ape}$, where k_{ape} is the maximum bandwidth of the imaging system. As a result, the phase image $\phi(x, y)$ in the cross-term can be retrieved by side-band filtering in the frequency domain and followed by an inverse Fourier transform.

The advantage of the off-axis QPI is the capability of high-speed imaging. However, the cost is the lower space bandwidth since only a small side-band contributes to the final phase image.

1.1.3.3 Intensity-based quantitative phase imaging

QPI techniques generally require interferometry to record the phase information of the object wave and the reference wave and then retrieve the phase image of the object wave. As a consequence, the performance of such an interferometry setup relies on the stability of the phase. However, it is always difficult to protect the phase stability of the setup from many issues in practice, such as the mechanical vibration of the optical components and thermal fluctuation. In this context, it is especially interesting to develop an intensity-based QPI technique to minimize the influence introduced by phase instability. One of the approaches is using the transport of intensity equation (TIE) which was firstly proposed by Teague in 1983 [15]. TIE shows that the axial gradient of the intensity is correlated with the transverse Laplacian of the phase. It is relatively easy to implement this technique

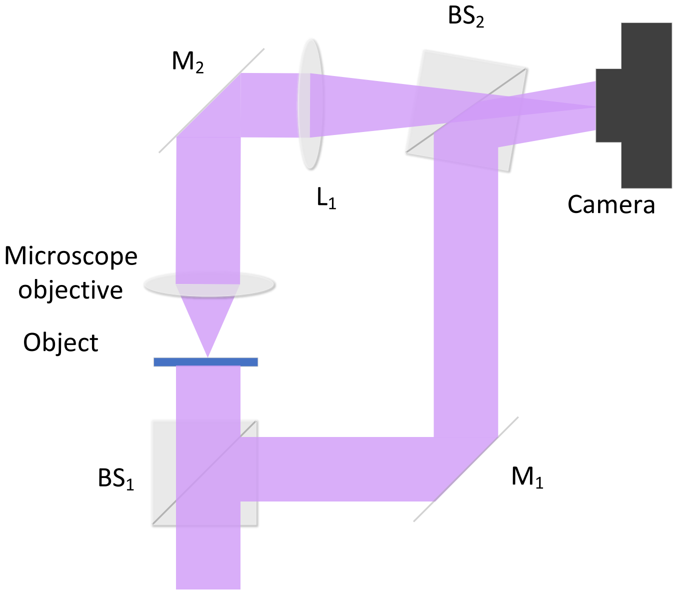

Figure 1.5: Configuration schematic of off-axis QPI

which requires only two intensity images with one in focus and another slightly out of focus. However, it suffers from poor reliability in the low spatial frequency because only the second-order derivative of the phase is measured and the phase retrieval is under certain assumptions [16]. Another approach is using the space-domain KK relations. This phase retrieval approach is first applied in electron microscopy by Misell in 1974 [17, 18]. A plane wave illumination illuminates the object in a normal way and the scatted light is collected by the objective. Instead of using a normal circular aperture, the aperture is reshaped to collect only the upper-half-plane (UHP) signal and vanish the frequencies in another half-plane in the k-space. Meanwhile, the unscattered illumination light is also collected to ensure the function analyticity of the collected field in UHP. The robustness of this approach is much better compared with TIE since the phase image is directly retrieved from the measured raw frames without any assumptions. The difficulties to implement this method are the precise control of the aperture. More recently, the space-domain KK-relations is applied in optical microscopy to increase the space throughput of off-axis QPI [19]. Besides, it has also been applied for intensity-based holographic imaging using oblique illumination to vanish the negative signals in the frequency domain [20, 21]. The formulation of the space-domain KK relations will be discussed in the chapter2 and the experimental implementation will be discussed in the chapter5.

1.1.4 The needs of add-on modules for advanced microscopy

Advanced microscopy including fluorescence-based super-resolution microscopy and quantitative phase microscopy achieves tremendous improvement compared with conventional microscopy. However, their sophisticated optical system inevitably increases the size and the cost of the microscope, which hampers their widespread use. One of the frequently asked questions in the super-resolution microscopy field [22] is: *"Can research-grade super-resolution (SIM) microscopes be built cost-efficiently?"* To tackle these issues, many efforts have been made to reduce the cost of the used devices in SIM, such as using low-cost light emitting diodes (LED), digital mirrored devices (DMD) and fibers [23–25]. However, the system is still bulky and the cost can be further reduced.

For the QPI techniques, it is even more difficult to scale down the microscope due to the need for interferometry. Some designs focused on simplifying and decreasing the size of the setup using later sheering QPI techniques, but the imaged objects have to be sparse [26, 27]. Alternatively, QPI techniques using add-on modules have been reported to boost the performance of differential interference contrast (DIC) microscopes, phase contrast microscopes and standard microscopes [28, 29], namely gradient light interference microscopy (GLIM), spatial light interference microscopy (SLIM) and white-light diffraction phase microscopy (wDPM) respectively. Cooperating with the commercial microscope, these techniques are able to achieve high space bandwidth similar to the standard phase shifting QPI. However, the add-on module is still bulky and complicated. More recently, inspired by the concept of DIC, Kwon proposed metasurface-based QPI which decreases dramatically the dimension of the QPI microscope [30]. Without using standard microscope objectives to collect light, it is difficult to design the aberration-free metasurfaces of high numerical aperture (NA) and therefore this QPI suffers from low resolution.

1.2 Photonic integrated circuits

In traditional bulky optical systems, light is routed and manipulated by a lot of lenses and mirrors. Consequently, the size of the optical system scales up dramatically with the degree of complexity. More importantly, the bulky system is prone to environmental perturbations such as thermal fluctuations, vibrations and humidity variations. In this context, the concept of integrated optics was proposed by Miller in 1969 [31]. Inspired by the well-developed electronic integrated circuits (EIC), the purpose of integrated optics is to integrate a large scale of optical components interconnected by low-loss routing waveguides in a single chip, also named *photonic integrated circuits* (PIC) nowadays. PIC is able to offer robust, compact and low-cost solutions for implementing complex optical functions that are hardly achievable at the same level of performance as standard bulk optics. In particular, bulk optics cannot compete with the large-scale manufacturing capabilities offered by the well-developed CMOS facilities [32–34]. PICs have already sparked a tremendous number of applications of paramount importance in telecommunications [35], healthcare [36], biological research [37, 38], quantum information and computation [39, 40], metrology [41, 42]. Ideally, the concept of integrated optics is proposed to integrate multiple different materials but very quickly series of technical problems emerged. At present, there are different platforms developed to target different specific problems.

1.2.1 Silicon photonics

Among other PIC platforms, the most technologically mature one is the silicon-on-insulator (SOI). The crystalline silicon (Si) exhibits high transparency at the communication wavelength of 1550 nm, which is highly used in the process of EIC. However, it was still very difficult to achieve a low-loss single-mode waveguide in the early stage because of the high side-wall scattering loss and high index contrast of $\sim$3.5. In 2004, Dumon *et. al* [43] reports a silicon waveguide with a loss of 2.4 dB/cm for a waveguide width of 500 nm, while the value climes up to 7.0 dB/cm as the waveguide width decrease to 450 nm. Today's fabrication of silicon platforms is much more mature, after improving the technique of dry etching recipe and photolithography. The propagation loss is reduced to $<$1 dB/cm for a strip waveguide with a dimension of 450 nm x 220 nm using a 300 mm CMOS platform [44]. With such a low loss, the silicon platform is excellent for passive optical components, such as connecting waveguides, multimode interferometer (MMI) beam splitters, arrayed waveguide gratings (AWG) and grating couplers. However, limited by its narrow bandgap of 1.1 eV, the silicon PIC is engineered mainly for the communication wavelength band and is unsuitable for ultra-violet (UV)/visible platforms due to their strong material absorption.

1.2.2 UV/Vis photonic integration platform

In the field of biology and quantum information, the UV/visible wavelengths are more interesting than the infrared wavelengths due to stronger light-matter interaction at shorter wavelengths. For instance, visible light from 400 nm to 700 nm is usually used to excite fluorescent probes for multi-color fluorescence imaging. Besides, the shorter UV wavelengths of 369 nm and 313 nm are generally required to excite the Yb^+ and Be^+ ions for quantum computing, respectively. To avoid material absorption of visible light, the material should have an energy bandgap as least wider than 3.1 eV.

SiN as a CMOS-compatible material has been widely investigated in the telecommunication wavelength. Benefiting from its lower refractive index of $\sim$2, the

SiN platform achieves ultra-low waveguide loss of 0.01 dB/cm [45, 46]. Besides, SiN has a low thermo-optic coefficient of 2.5 x 10^{-5} K^{-1} [47] and suffers fewer thermal fluctuations from the environment. Except for the infrared wavelengths, it is also an ideal platform for visible wavelengths in view of its wide bandgap of $\sim$5 eV [48–50]. Recently, the 200 mm SiN platform using the layer grown by the lower pressure chemical vapor deposition (LPCVD) is able to provide single-mode waveguides with a loss of $\sim$7 dB/cm, 2.5dB/cm and 1 dB/cm at a blue, green and red light, respectively [51]. This SiN platform has been used for beam shaping at visible wavelength and shows advantages over bulky optics in light-sheet fluorescence brain imaging [52] and beam-steering in brain tissues [53]. However, the SiN platform may not be the ideal option to operate at blue/violet wavelengths because the loss is increased considerably to $\sim$7 dB/cm.

Lithium niobate (LN) has large electro-optic and acousto-optic coefficients, which have been widely used for high-speed optical modulators at 1550 nm [54–56]. It is also a good platform for the visible wavelength in view of its moderate bandgap of 3.78 eV [57], demonstrating a low loss of 0.06dB/cm at λ= 647 nm [58]. However, LN is not a COMS-compatible material so the integration with other materials is a difficult technical issue that still needs to be solved.

Aluminum nitride (AlN) also offers the important capability of electro-optic modulation and second-order nonlinearity [59, 60]. Although the waveguide loss is still as high as 8 dB/cm at a UV wavelength of 390 nm [38], the property of strong nonlinearity compensates for this shortage and makes the AlN becoming a promising candidate for the UV-PIC platform. Currently, the single-crystal AlN is grown on the sapphire wafer which limits its size to 4/6 inches.

Aluminum oxide (Al_2O_3) is currently the best candidate for the UV-PIC platform because of its relatively low but sufficient refractive index of $\sim$1.7 and high uniformity of layer deposition via atomic layer deposition (ALD). The ALD-AlO_x layer has demonstrated a low material absorption loss of 4 dB/cm at a wavelength as short as 250 nm [61]. Furthermore, the integrated waveguide using the ALD-AlO$_x$ layer has recently been elaborated to realize a low loss of 3 dB/cm at 371 nm, with single-mode propagation [49, 62]. In this thesis, we elaborated the ALD-AlO_x platform a step further and realized a similar loss of 3 dB/cm but at a shorter wavelength of 360 nm and with a higher index contrast.

The present different platforms at visible/UV wavelengths are compared in table 1.1.

1.2.3 Photonic integrated circuits for advanced microscopy

Photonic integrated circuits allowing flexible on-chip beam manipulation are thriving for the on-chip super-resolution microscopy [63–66]. By using the evanescent field of integrated waveguides as the illumination beam, the photonic chip-enabled

Table 1.1: Reported waveguide loss of PIC platforms at UV/visible wavelengths

Platform	bandgap	waveguide loss	wavelengths	second-order nonlinearity
SiN	5 eV	5 dB/cm	430 nm	no
LN	3.8 eV	0.06 dB/cm	674 nm	yes
AlN	6.2 eV	8 dB/cm 3.5 dB/cm	390 nm 455nm	yes
AlO$_x$	5.1 $\sim$ 7.6 eV	3 dB/cm	371 nm	no

single molecular localization microscopy was first demonstrated by Diekmann in 2017, achieving a spatial resolution of 140 nm over a large field-of-view (FoV) of 0.5 x 0.5 mm using an objective of NA 0.45 [67]. Depending on the need, using a high NA 1.2 objective can increase the resolution up to 50 nm but the FoV is correspondingly decreased. In 2019, Archetti proposed the waveguide-based points accumulation for imaging in nanoscale topography (PAINT) and push the resolution down to 20 nm [68]. Except for the SMLM, PIC has also shown its advantages over bulky SIM by demonstrating a resolution enhancement factor of 2.3 which is higher than the general value of 2 [69]. Besides, making use of the total internal reflection illumination and high-index contrast, the PIC can also be applied for dark-field high-contrast scattering imaging [70].

At present, PIC-based microscopy is mainly based on evanescent illumination. The clear advantage is high signal-to-noise-ratio (SNR) because only the matter close to the waveguide surface interacts with the excitation beam, but consequently the imaged object needs to be attached to the photonic chip and can not be moved. This makes the sample preparation more complicated than the standard protocol, because the photonic chip needs to be involved during the sample preparation. More importantly, TIRF-based microscopy is not compatible with quantitative phase imaging, which further limits its capability of phase imaging. In this thesis, to tackle these issues, I proposed and implemented the UV-PIC-based label-free far-field SIM and QPI techniques, respectively.

1.3 Research objectives

Before starting this work, our hypothesis was that it is possible to develop a low-loss single-mode integrated waveguide at UV wavelength and such a platform will be applied for PIC-based advanced microscopy. My main objectives in this work were the following:

- The development of low-loss single-mode integrated waveguides for realizing the UV-PIC platform. This includes the design of the waveguide structures in simulation, the exploration of potential low-absorption materials, and the optimization of etching techniques.

- The design, fabrication, and characterization of optical components embedded in UV photonic circuits. This includes the design and optimization of adiabatic tapers, 1x2 MMI beam splitters, 2x2 beam splitters, grating out-couplers, and thermal phase shifters.
- The fabrication and characterization of UV photonic circuits and implementation of UV-PIC based SIM technique. This includes the layout design of photonic circuits, characterization of the generated far-field structured illumination and fluorescence imaging using the structured illumination.
- The development of reconstruction algorithm for structured illumination microscopy. This includes the implementation of the SIM technique in simulation, super-resolved image reconstruction using the experimental fluorescence images and validation of the concept of UV-PIC-based autofluorescence SIM technique with biological cells.
- The fabrication and characterization of photonic circuits and implementation of PIC-based QPI technique. This includes the layout design of photonic circuits, characterization of the generated far-field angled illumination and measurement of bright-field images using the generated oblique illumination.
- The development of reconstruction algorithm for space-domain KK-relations-based QPI. This includes the implementation of the KK-relations-based QPI technique in simulation, complex field reconstruction from experimental intensity images and validation of the concept of the PIC-based QPI technique.

The important achievements of this thesis are the development of a low-loss UV-compatible PIC platform, the demonstration of the UV-PIC-based SIM technique which upgrades a conventional visible microscope to a UV-compatible super-resolved autofluorescence SIM microscope in a low-cost and compact way, and the demonstration of the PIC-based QPI technique which provides the solution of a compact and robust quantitative phase imaging technique and paves the way for a chip-based multimodal advanced microscopy.

1.4 Thesis outline

This dissertation has already started with the introduction of the typical super-resolution microscopy techniques, quantitative phase imaging and current PIC platforms for visible and UV wavelengths. Besides, this chapter also points out the research objectives.

Chapter 2 gives the working principle and theoretical formalization involved in the super-resolved SIM technique and the space-domain KK-relations-based QPI technique.

Chapter 3 discusses the fabrication, and characterization of the PIC platform operating at UV wavelengths. ALD-AlO$_x$ and ALD-HfO$_x$ waveguides are investigated and in the following chapters the ALD-AlO$_x$ layer is selected for the fabrication of the photonic circuits.

Chapter 4 firstly discusses the design and fabrication of the UV-PIC for the generation of switchable structured illumination. Next, we describe the SIM reconstruction algorithm, the validation of the UV-PIC-based SIM technique and the characterization of the resolution enhancement of the proposed technique with a homemade spoke resolution target. Finally, we apply the UV-PIC-based SIM to image yeast cells and demonstrate the super-resolved autofluorescence SIM technique.

Chapter 5 firstly discusses the design and fabrication of the UV-PIC for the generation of switchable oblique illumination. Next, we describe the phase-retrieval reconstruction algorithm for space-domain KK-relations-based QPI and the validation of the PIC-based KK-QPI in the experiment. Finally, we discuss the characterization of the proposed technique in terms of phase precision, phase sensitivity and spatial resolution, respectively.

Chapter 6 summarizes all the results in this thesis and gives the prospect of this research work.

1.5 Publications

This dissertation has led to the following list of publications in conferences and international peer-reviewed journals.

1.5.1 Publications in international journals

1. **C. Lin**, J. SD Penaranda, J. Dendooven, C. Detavernier, D. Schaubroeck, N. Boon, R. Baets, N. Le Thomas, ”UV photonic integrated circuits for autofluorescence structured illumination microscopy”, **Nature Communications**, 12(1), 4360(2022).

2. **C. Lin**, D. Schaubroeck, R. Baets, N. Boon, N. Le Thomas, ”UV Photonic-Integrated-Circuits-Based Structured Illumination Microscopy With a Field of View Larger than 100 μm^2”, **IEEE Journal on Selected Topics in Quantum Electronics**, 29(4), 1-9(2023).

1.5.2 Publications in international conferences

1. **C. Lin**, J. SD Penaranda, J. Dendooven, C. Detavernier, D. Schaubroeck, N. Boon, R. Baets, N. Le Thomas, ”UV-compatible photonic integrated circuits for label-free structured illumination microscopy”, Frontier in Optics (**FiO**), FW6E.3(2022)

2. **C. Lin**, J. SD Penaranda, J. Dendooven, C. Detavernier, R. Baets, N. Le Thomas, ”Photonic integrated alumina waveguide gratings for far-field structured illumination at UV wavelengths”, Conference on Lasers and Electro-Optics (**CLEO**), STu1A.6(2021)

3. N. Le Thomas, Z. Liu, **C. Lin**, H. Zhao, R. Baets, ”Raman on-chip: Current status and future tracks”, Proc. SPIE, Integrated Optics: Devices, Materials, and Technology XXV, 11689, p.1168908(2021)

4. **C. Lin**, D. Schaubroeck, G. Roelkens, R. Baets, N. Le Thomas, ”Low-loss single-mode waveguides operating at UV/violet wavelengths and fabricated with contact optical lithography”, European Conference on Integrated Optics (**ECIO**), p.3 (2020)

5. **C. Lin**, R. Baets, G. Roelkens, N. Le Thomas, ”Design of slot waveguide for ultra-violet light based on atomic layer deposition”, European Conference on Integrated Optics (**ECIO**), p.W.Po1.5 (2019)

References

[1] T. C. Kriss and V. M. Kriss. *History of the operating microscope: from magnifying glass to microneurosurgery.* Neurosurgery, 42(4):899–907; discussion 907–8, 1998.

[2] William Rosenthal. *Spectacles and Other Vision Aids: A History and Guide to Collecting.* Norman Publishing, 1996.

[3] E. Betzig, G. H. Patterson, R. Sougrat, O. W. Lindwasser, S. Olenych, J. S. Bonifacino, M. W. Davidson, J. Lippincott-Schwartz, and H. F. Hess. *Imaging intracellular fluorescent proteins at nanometer resolution.* Science, 313(5793):1642–5, 2006.

[4] M. J. Rust, M. Bates, and X. Zhuang. *Sub-diffraction-limit imaging by stochastic optical reconstruction microscopy (STORM).* Nat Methods, 3(10):793–5, 2006.

[5] L. Mockl and W. E. Moerner. *Super-resolution Microscopy with Single Molecules in Biology and Beyond-Essentials, Current Trends, and Future Challenges.* J Am Chem Soc, 142(42):17828–17844, 2020.

[6] S. W. Hell and J. Wichmann. *Breaking the diffraction resolution limit by stimulated emission: stimulated-emission-depletion fluorescence microscopy.* Opt Lett, 19(11):780–2, 1994.

[7] T. A. Klar and S. W. Hell. *Subdiffraction resolution in far-field fluorescence microscopy.* Opt Lett, 24(14):954–6, 1999.

[8] T. Muller, C. Schumann, and A. Kraegeloh. *STED microscopy and its applications: new insights into cellular processes on the nanoscale.* Chemphyschem, 13(8):1986–2000, 2012.

[9] Barry R. Masters. *Structured Illumination Microscopy.* Superresolution Optical Microscopy: The Quest for Enhanced Resolution and Contrast. Springer International Publishing, 2020.

[10] M. G. Gustafsson. *Surpassing the lateral resolution limit by a factor of two using structured illumination microscopy.* J Microsc, 198(Pt 2):82–7, 2000.

[11] J. T. Frohn, H. F. Knapp, and A. Stemmer. *True optical resolution beyond the Rayleigh limit achieved by standing wave illumination.* Proc Natl Acad Sci U S A, 97(13):7232–6, 2000.

[12] M. G. Gustafsson. *Nonlinear structured-illumination microscopy: wide-field fluorescence imaging with theoretically unlimited resolution.* Proc Natl Acad Sci U S A, 102(37):13081–6, 2005.

[13] M. G. Gustafsson, L. Shao, P. M. Carlton, C. J. Wang, I. N. Golubovskaya, W. Z. Cande, D. A. Agard, and J. W. Sedat. *Three-dimensional resolution doubling in wide-field fluorescence microscopy by structured illumination*. Biophys J, 94(12):4957–70, 2008.

[14] Creath Katherine. *V phase-measurement interferometry techniques*. Progress in optics, 26:349–393, 1988.

[15] Michael Reed Teague. *Deterministic phase retrieval: a Green's function solution*. Journal of the Optical Society of America, 73(11), 1983.

[16] D. Paganin and K. A. Nugent. *Noninterferometric Phase Imaging with Partially Coherent Light*. Physical Review Letters, 80(12):2586–2589, 1998.

[17] D. L. Misell and A. H. Greenaway. *An application of the Hilbert transform in electron microscopy: I. Bright-field microscopy*. Journal of Physics D: Applied Physics, 7(6):832–855, 1974.

[18] D. L. Misell and A. H. Greenaway. *An application of the Hilbert transform in electron microscopy: II. Non-iterative solution in bright-field microscopy and the dark-field problem*. Journal of Physics D: Applied Physics, 7(12):1660–1669, 1974.

[19] YoonSeok Baek, KyeoReh Lee, Seungwoo Shin, and YongKeun Park. *Kramers–Kronig holographic imaging for high-space-bandwidth product*. Optica, 6(1), 2019.

[20] YoonSeok Baek and YongKeun Park. *Intensity-based holographic imaging via space-domain Kramers–Kronig relations*. Nature Photonics, 15(5):354–360, 2021.

[21] C. Lee, Y. Baek, H. Hugonnet, and Y. Park. *Single-shot wide-field topography measurement using spectrally multiplexed reflection intensity holography via space-domain Kramers-Kronig relations*. Opt Lett, 47(5):1025–1028, 2022.

[22] K. Prakash, B. Diederich, S. Reichelt, R. Heintzmann, and L. Schermelleh. *Super-resolution structured illumination microscopy: past, present and future*. Philos Trans A Math Phys Eng Sci, 379(2199):20200143, 2021.

[23] D. Dan, M. Lei, B. Yao, W. Wang, M. Winterhalder, A. Zumbusch, Y. Qi, L. Xia, S. Yan, Y. Yang, P. Gao, T. Ye, and W. Zhao. *DMD-based LED-illumination super-resolution and optical sectioning microscopy*. Sci Rep, 3:1116, 2013.

[24] Alice Sandmeyer, Mario Lachetta, Hauke Sandmeyer, Wolfgang Hübner, Thomas Huser, and Marcel Müller. *Cost-Effective Live Cell Structured Illumination Microscopy with Video-Rate Imaging*. ACS Photonics, 8(6):1639–1648, 2021.

[25] J. Pospisil, G. Wiebusch, K. Fliegel, M. Klima, and T. Huser. *Highly compact and cost-effective 2-beam super-resolution structured illumination microscope based on all-fiber optic components*. Opt Express, 29(8):11833–11844, 2021.

[26] V. Chhaniwal, A. S. Singh, R. A. Leitgeb, B. Javidi, and A. Anand. *Quantitative phase-contrast imaging with compact digital holographic microscope employing Lloyd's mirror*. Opt Lett, 37(24):5127–9, 2012.

[27] Y. Baek, K. Lee, J. Yoon, K. Kim, and Y. Park. *White-light quantitative phase imaging unit*. Opt Express, 24(9):9308–15, 2016.

[28] T. H. Nguyen, M. E. Kandel, M. Rubessa, M. B. Wheeler, and G. Popescu. *Gradient light interference microscopy for 3D imaging of unlabeled specimens*. Nat Commun, 8(1):210, 2017.

[29] Z. Wang, L. Millet, M. Mir, H. Ding, S. Unarunotai, J. Rogers, M. U. Gillette, and G. Popescu. *Spatial light interference microscopy (SLIM)*. Opt Express, 19(2):1016–26, 2011.

[30] Hyounghan Kwon, Ehsan Arbabi, Seyedeh Mahsa Kamali, Mohammad-Sadegh Faraji-Dana, and Andrei Faraon. *Single-shot quantitative phase gradient microscopy using a system of multifunctional metasurfaces*. Nature Photonics, 14(2):109–114, 2019.

[31] Stewart E. Miller. *Integrated Optics: An Introduction*. Bell System Technical Journal, 48(7):2059–2069, 1969.

[32] Bahram Jalali and Sasan Fathpour. *Silicon Photonics*. Journal of Lightwave Technology, 24(12):4600–4615, 2006.

[33] David J. Moss, Roberto Morandotti, Alexander L. Gaeta, and Michal Lipson. *New CMOS-compatible platforms based on silicon nitride and Hydex for nonlinear optics*. Nature Photonics, 7(8):597–607, 2013.

[34] W. Bogaerts, D. Perez, J. Capmany, D. A. B. Miller, J. Poon, D. Englund, F. Morichetti, and A. Melloni. *Programmable photonic circuits*. Nature, 586(7828):207–216, 2020.

[35] Christopher R. Doerr. *Silicon photonic integration in telecommunications*. Frontiers in Physics, 3, 2015.

[36] Ana Belén González and Jose Pozo. *The Biophotonics Revolution in Healthcare*. Optik and Photonik, 12(3):16–17, 2017.

[37] Ananth Z. Subramanian, Eva Ryckeboer, Ashim Dhakal, Frédéric Peyskens, Aditya Malik, Bart Kuyken, Haolan Zhao, Shibnath Pathak, Alfonso Ruocco, Andreas De Groote, Pieter Wuytens, Daan Martens, Francois Leo, Weiqiang Xie, Utsav Deepak Dave, Muhammad Muneeb, Pol Van Dorpe, Joris Van Campenhout, Wim Bogaerts, Peter Bienstman, Nicolas Le Thomas, Dries Van Thourhout, Zeger Hens, Gunther Roelkens, and Roel Baets. *Silicon and silicon nitride photonic circuits for spectroscopic sensing on-a-chip [Invited]*. Photonics Research, 3(5):B47–B58, 2015.

[38] L. Liu, D. Shan, X. Zhou, H. Shi, B. Song, F. Falke, A. Leinse, and R. Heideman. *TriPleX waveguide-based fluorescence biosensor for multichannel environmental contaminants detection*. Biosens Bioelectron, 106:117–121, 2018.

[39] R. J. Niffenegger, J. Stuart, C. Sorace-Agaskar, D. Kharas, S. Bramhavar, C. D. Bruzewicz, W. Loh, R. T. Maxson, R. McConnell, D. Reens, G. N. West, J. M. Sage, and J. Chiaverini. *Integrated multi-wavelength control of an ion qubit*. Nature, 586(7830):538–542, 2020.

[40] Zak David Romaszko, Seokjun Hong, Martin Siegele, Reuben Kahan Puddy, Foni Raphaël Lebrun-Gallagher, Sebastian Weidt, and Winfried Karl Hensinger. *Engineering of microfabricated ion traps and integration of advanced on-chip features*. Nature Reviews Physics, 2(6):285–299, 2020.

[41] C. Weimann, M. Lauermann, F. Hoeller, W. Freude, and C. Koos. *Silicon photonic integrated circuit for fast and precise dual-comb distance metrology*. Opt Express, 25(24):30091–30104, 2017.

[42] Edoardo Vicentini, Zhenhai Wang, Kasper Van Gasse, Theodor W. Hänsch, and Nathalie Picqué. *Dual-comb hyperspectral digital holography*. Nature Photonics, 15(12):890–894, 2021.

[43] P. Dumon, W. Bogaerts, V. Wiaux, J. Wouters, S. Beckx, J. Van Campenhout, D. Taillaert, B. Luyssaert, P. Bienstman, D. Van Thourhout, and R. Baets. *Low-Loss SOI Photonic Wires and Ring Resonators Fabricated With Deep UV Lithography*. IEEE Photonics Technology Letters, 16(5):1328–1330, 2004.

[44] Gustaf Winroth Patrick Ong Guy Lepage Celine Cailler Arnaud Rigny Konstantin K. Bourdelle Wim Bogaerts Dries Van Thourhout Joris Van Campenhout Shankar Kumar Selvaraja, Peter De Heyn and Philippe Absil. *Highly uniform and low-loss passive silicon photonics devices using a 300mm*

CMOS platform. Optical Fiber Communication Conference, page Th2A.33, 2014.

[45] Matthew W. Puckett, Kaikai Liu, Nitesh Chauhan, Qiancheng Zhao, Naijun Jin, Haotian Cheng, Jianfeng Wu, Ryan O. Behunin, Peter T. Rakich, Karl D. Nelson, and Daniel J. Blumenthal. *422 Million intrinsic quality factor planar integrated all-waveguide resonator with sub-MHz linewidth*. Nature Communications, 12(1), 2021.

[46] Junqiu Liu, Guanhao Huang, Rui Ning Wang, Jijun He, Arslan S. Raja, Tianyi Liu, Nils J. Engelsen, and Tobias J. Kippenberg. *High-yield, wafer-scale fabrication of ultralow-loss, dispersion-engineered silicon nitride photonic circuits*. Nature Communications, 12(1), 2021.

[47] A. Arbabi and L. L. Goddard. *Measurements of the refractive indices and thermo-optic coefficients of Si3N4 and SiO(x) using microring resonances*. Opt Lett, 38(19):3878–81, 2013.

[48] A. Z. Subramanian, P. Neutens, A. Dhakal, R. Jansen, T. Claes, X. Rottenberg, F. Peyskens, S. Selvaraja, P. Helin, B. DuBois, K. Leyssens, S. Severi, P. Deshpande, R. Baets, and P. Van Dorpe. *Low-Loss Singlemode PECVD Silicon Nitride Photonic Wire Waveguides for 532–900 nm Wavelength Window Fabricated Within a CMOS Pilot Line*. IEEE Photonics Journal, 5(6):2202809–2202809, 2013.

[49] Cheryl Sorace-Agaskar, Dave Kharas, Siva Yegnanarayanan, Ryan T. Maxson, Gavin N. West, William Loh, Suraj Bramhavar, Rajeev J. Ram, John Chiaverini, Jeremy Sage, and Paul Juodawlkis. *Versatile Silicon Nitride and Alumina Integrated Photonic Platforms for the Ultraviolet to Short-Wave Infrared*. IEEE Journal of Selected Topics in Quantum Electronics, 25(5):1–15, 2019.

[50] Theodore J. Morin, Lin Chang, Warren Jin, Chenlei Li, Joel Guo, Hyundai Park, Minh A. Tran, Tin Komljenovic, and John E. Bowers. *CMOS-foundry-based blue and violet photonics*. Optica, 8(5), 2021.

[51] W. D. Sacher, X. Luo, Y. Yang, F. D. Chen, T. Lordello, J. C. C. Mak, X. Liu, T. Hu, T. Xue, P. Guo-Qiang Lo, M. L. Roukes, and J. K. S. Poon. *Visible-light silicon nitride waveguide devices and implantable neurophotonic probes on thinned 200 mm silicon wafers*. Opt Express, 27(26):37400–37418, 2019.

[52] W. D. Sacher, F. D. Chen, H. Moradi-Chameh, X. Luo, A. Fomenko, P. T. Shah, T. Lordello, X. Liu, I. F. Almog, J. N. Straguzzi, T. M. Fowler, Y. Jung, T. Hu, J. Jeong, A. M. Lozano, P. G. Lo, T. A. Valiante, L. C. Moreaux,

J. K. S. Poon, and M. L. Roukes. *Implantable photonic neural probes for light-sheet fluorescence brain imaging*. Neurophotonics, 8(2):025003, 2021.

[53] W. D. Sacher, F. D. Chen, H. Moradi-Chameh, X. Liu, I. Felts Almog, T. Lordello, M. Chang, A. Naderian, T. M. Fowler, E. Segev, T. Xue, S. Mahallati, T. A. Valiante, L. C. Moreaux, J. K. S. Poon, and M. L. Roukes. *Optical phased array neural probes for beam-steering in brain tissue*. Opt Lett, 47(5):1073–1076, 2022.

[54] Mian Zhang, Cheng Wang, Xi Chen, Maxime Bertrand, Amirhassan Shams-Ansari, Sethumadhavan Chandrasekhar, Peter Winzer, and Marko Lončar. *Ultra-High Bandwidth Integrated Lithium Niobate Modulators with Record-Low* $V\pi$. In Optical Fiber Communications Conference and Exposition (OFC), pages 1–3.

[55] C. Wang, M. Zhang, X. Chen, M. Bertrand, A. Shams-Ansari, S. Chandrasekhar, P. Winzer, and M. Loncar. *Integrated lithium niobate electro-optic modulators operating at CMOS-compatible voltages*. Nature, 562(7725):101–104, 2018.

[56] Mengyue Xu, Yuntao Zhu, Fabio Pittalà, Jin Tang, Mingbo He, Wing Chau Ng, Jingyi Wang, Ziliang Ruan, Xuefeng Tang, Maxim Kuschnerov, Liu Liu, Siyuan Yu, Bofang Zheng, and Xinlun Cai. *Dual-polarization thin-film lithium niobate in-phase quadrature modulators for terabit-per-second transmission*. Optica, 9(1), 2022.

[57] Ajay Dhar and Abhai Mansingh. *Optical properties of reduced lithium niobate single crystals*. Journal of Applied Physics, 68(11):5804–5809, 1990.

[58] Julián H. Sierra, Ricardo C. Rangel, Ricardo E. Samad, Nilson Dias Vieira, Marco I. Alayo, and Daniel O. Carvalho. *Low-loss pedestal Ta2O5 nonlinear optical waveguides*. Optics Express, 27(26), 2019.

[59] X. Liu, A. W. Bruch, J. Lu, Z. Gong, J. B. Surya, L. Zhang, J. Wang, J. Yan, and H. X. Tang. *Beyond 100 THz-spanning ultraviolet frequency combs in a non-centrosymmetric crystalline waveguide*. Nat Commun, 10(1):2971, 2019.

[60] W. H. P. Pernice, C. Xiong, C. Schuck, and H. X. Tang. *Second harmonic generation in phase matched aluminum nitride waveguides and micro-ring resonators*. Applied Physics Letters, 100(22), 2012.

[61] M. M. Aslan, N. A. Webster, C. L. Byard, M. B. Pereira, C. M. Hayes, R. S. Wiederkehr, and S. B. Mendes. *Low-Loss Optical Waveguides for the Near Ultra-Violet and Visible Spectral Regions with Al(2)O(3) Thin Films from Atomic Layer Deposition*. Thin Solid Films, 518(17):4935–4940, 2010.

[62] Gavin N. West, William Loh, Dave Kharas, Cheryl Sorace-Agaskar, Karan K. Mehta, Jeremy Sage, John Chiaverini, and Rajeev J. Ram. *Low-loss integrated photonics for the blue and ultraviolet regime*. APL Photonics, 4(2):026101–7, 2019.

[63] O. I. Helle, D. A. Coucheron, J. C. Tinguely, C. I. Oie, and B. S. Ahluwalia. *Nanoscopy on-a-chip: super-resolution imaging on the millimeter scale*. Opt Express, 27(5):6700–6710, 2019.

[64] J. C. Tinguely, A. M. Steyer, C. I. Oie, O. I. Helle, F. T. Dullo, R. Olsen, P. McCourt, Y. Schwab, and B. S. Ahluwalia. *Photonic-chip assisted correlative light and electron microscopy*. Commun Biol, 3(1):739, 2020.

[65] A. Butola, D. A. Coucheron, K. Szafranska, A. Ahmad, H. Mao, J. C. Tinguely, P. McCourt, P. Senthilkumaran, D. S. Mehta, K. Agarwal, and B. S. Ahluwalia. *Multimodal on-chip nanoscopy and quantitative phase imaging reveals the nanoscale morphology of liver sinusoidal endothelial cells*. Proc Natl Acad Sci U S A, 118(47), 2021.

[66] L. E. Villegas-Hernandez, V. Dubey, M. Nystad, J. C. Tinguely, D. A. Coucheron, F. T. Dullo, A. Priyadarshi, S. Acuna, A. Ahmad, J. M. Mateos, G. Barmettler, U. Ziegler, A. B. Birgisdottir, A. K. Hovd, K. A. Fenton, G. Acharya, K. Agarwal, and B. S. Ahluwalia. *Chip-based multimodal super-resolution microscopy for histological investigations of cryopreserved tissue sections*. Light Sci Appl, 11(1):43, 2022.

[67] Robin Diekmann, Øystein I. Helle, Cristina I. Øie, Peter McCourt, Thomas R. Huser, Mark Schüttpelz, and Balpreet S. Ahluwalia. *Chip-based wide field-of-view nanoscopy*. Nature Photonics, 11(5):322–328, 2017.

[68] A. Archetti, E. Glushkov, C. Sieben, A. Stroganov, A. Radenovic, and S. Manley. *Waveguide-PAINT offers an open platform for large field-of-view super-resolution imaging*. Nat Commun, 10(1):1267, 2019.

[69] Øystein Ivar Helle, Firehun Tsige Dullo, Marcel Lahrberg, Jean-Claude Tinguely, Olav Gaute Hellesø, and Balpreet Singh Ahluwalia. *Structured illumination microscopy using a photonic chip*. Nature Photonics, 14(7):431–438, 2020.

[70] Nikhil Jayakumar, Firehun T. Dullo, Vishesh Dubey, Azeem Ahmad, Florian Ströhl, Jennifer Cauzzo, Eduarda Mazagao Guerreiro, Omri Snir, Natasa Skalko-Basnet, Krishna Agarwal, and Balpreet Singh Ahluwalia. *Multi-moded high-index contrast optical waveguide for super-contrast high-resolution label-free microscopy*. Nanophotonics, 11(15):3421–3436, 2022.

2

Fundamentals of SIM and KK-QPI

This chapter is devoted to introducing the theory of diffraction-limited conventional microscopy, super-resolved structured illumination microscopy and quantitative phase microscopy. Although the theory of the image formation in conventional optical microscopy is well-known, it is important to introduce the theory here in particular to stress the difference between the coherent and incoherent imaging. In this thesis, I will propose and demonstrate the concepts of the UV-PIC-based super-resolved SIM technique and the UV-PIC-based QPI technique, based on the knowledge of incohernet and coherent imaging respectively. The theory of imaging through a bandwidth-limited microscope is well-established and nowadays well-described by using the K-space. After discussing the concept of the Abbe resolution limit by using a simple grating object and a normal coherent illumination, the spatial resolution of incohernet imaging is introduced and compared in the K-space. Furthermore, the working principle of super-resolved structured illumination microscopy, which bypasses the diffraction limit, is presented based on the incoherent imaging system. In the end of this chapter, I will present the theory of the non-interferometry quantitative phase imaging based on Kramers-Kronig relations through K-space, which is based on the theory of coherent light imaging system .

2.1 Image formation theory of conventional optical microscopy

The purpose of optical microscopy is to reveal the details of an object with a size as small as possible. To quantify the smallest size resolvable with a microscope, Abbe proposed the ′resolution limit′ concept in 1873 [1]. The resolution limit was derived based on diffraction and interference, see the schematic in Fig. 2.1.

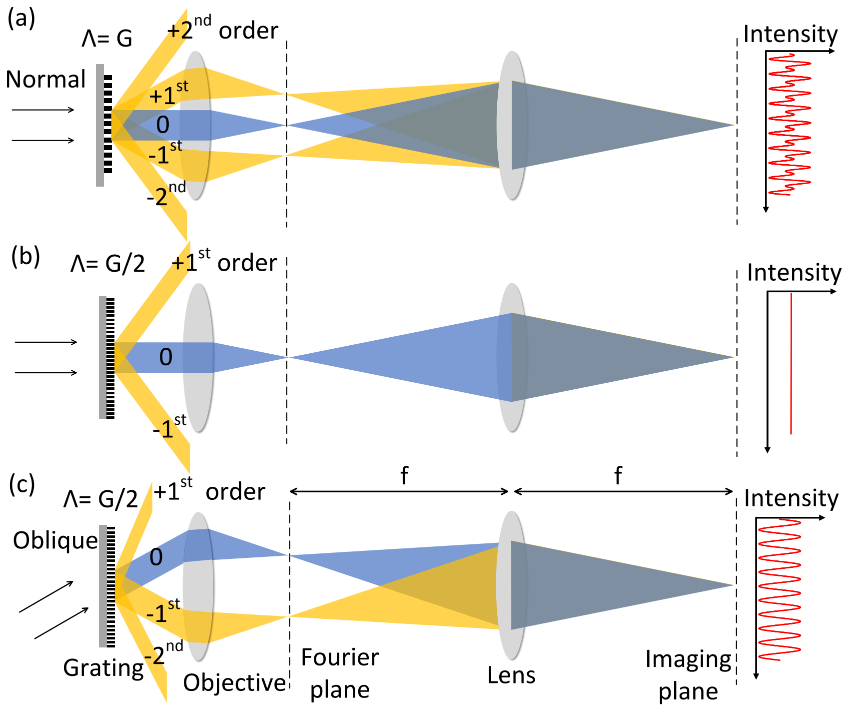

Figure 2.1: Schematic of image formation in coherent imaging using plane waves. (a-b) Grating pitches $\Lambda = G$ and $\Lambda = G/2$, respectively. The illumination beam is incident in a normal way. (c) Grating pitch $\Lambda = G/2$. The illumination beam is incident with an angle.

One way to explain the origin of the resolution limit is to use a grating structure as an object in the object plane of a microscope. A parallel coherent beam propagating along the optical axis of the instrument through the grating will be diffracted into several diffraction orders, the direction of which is set by the phase-matching condition at the grating surface:

$$\vec{k}_m = \vec{k}_{in} + m\vec{G}, \quad m \in \mathbb{Z} \tag{2.1}$$

where $\vec{k}_{in}$ is the wave vector of the incident beam, $\vec{G}$ is the reciprocal vector of the grating, and $\vec{k}_m$ is the wave vector of the diffraction order m, with m an integer. The wave vector of the incident beam is given by $\vec{k}_{in} = \vec{j}\frac{2\pi}{\lambda} \cdot n$, where n is the refractive index of the ambient medium, λ is the working wavelength in free space, and $\vec{j}$ is a unit vector. At the grating plane, the wave vectors are projected according to the angle between the wave vector and the optical axis of the microscope objective. It follows:

$$\frac{2\pi}{\lambda} \cdot n\sin(\theta_m) = \frac{2\pi}{\lambda} \cdot n\sin(\theta_{in}) + m\frac{2\pi}{\Lambda}, \quad m \in \mathbb{Z} \tag{2.2}$$

where Λ is the grating pitch. With an incident beam parallel to the optical axis of the microscope objective, the angle θ_{in} equals zero, as shown in Fig. 2.1(a) and (b). The relationship between the angle of the diffraction orders and the grating pitch is then given by:

$$n\sin(\theta_m) = \pm m\frac{\lambda}{\Lambda} \tag{2.3}$$

The numerical aperture (NA) of the microscope objective is set by $n\sin(\theta_{co})$, where θ_{co} is the maximum angle that can be collected. To recover the spatial information of the grating, at least two diffraction orders must be collected by the microscope objective. When θ_m is smaller than or equal to θ_{co}, the diffracted beam can be collected by the microscope objective, which forms an image at the imaging plane, as shown in Fig. 2.1(a). As shown in the equation 2.3, decreasing the grating pitch leads to a larger diffraction angle θ_m. When the angle θ_m is larger than the θ_{co}, only the zero-diffraction order is collected, which results in a profile with a constant intensity at the imaging plane, *i.e.* the information about the grating modulation is lost, see Fig. 2.1(b). Setting the diffraction order m to 1, the smallest grating pitch that can be resolved is obtained by:

$$\Lambda_{min} = \frac{\lambda}{n\sin(\theta_{co})} = \frac{\lambda}{NA_{co}} \tag{2.4}$$

This equation reveals the optical resolution of a microscope for coherent imaging with normal illumination. To increase the optical resolution of coherent imaging, oblique illuminations can be applied, as shown in Fig. 2.1(c). Defining the angle of the first-order diffraction beam by the numerical aperture of the microscope objective θ_m= θ_{co}, we can rewrite the equation 2.2 as:

$$\Lambda_{min} = \frac{\lambda}{n\sin(\theta_{co}) + n\sin(\theta_{in})} = \frac{\lambda}{NA_{co} + NA_{in}} \tag{2.5}$$

To work in a bright field, the zero diffraction order should be collected, implying the maximum numerical aperture of the incident beam NA$_{in}$equals NA$_{co}$ which results in a resolution of $\frac{\lambda}{2NA_{co}}$.

The resolution of the optical system can also be described by a transfer function formalism. In a coherent imaging system, the impulse response, namely the amplitude spread function $h(\vec{x})$, is the Fourier transform of the pupil function of the optical system $P(\vec{k})$. With normal illumination, the maximum spatial frequency which can be collected is determined by the aperture of the microscope objective, which is given by $k_{max} = \frac{2\pi}{\lambda} \cdot NA_{co}$. The one-dimensional intensity profile of the pupil function is illustrated in Fig. 2.2(b). The optical resolution of the optical system is given by $\Lambda = \frac{2\pi}{k_{max}} = \frac{\lambda}{NA_{co}}$. As the camera sensor records the intensity of the light field instead of amplitude, the response of light field $E_{in}(\vec{x})$ is given by:

$$\begin{aligned} I_{out}(x) &= E_{out}(\vec{x}) \cdot E^*_{out}(\vec{x}) \\ &= |E_{in}(\vec{x}) \otimes h(\vec{x})|^2 \end{aligned} \tag{2.6}$$

where $\otimes$ denotes the convolution. We define the electric field of two adjacent point sources $E_{in1}(\vec{x})$ and $E_{in2}(\vec{x})$. The response of these two point sources can be written by:

$$\begin{aligned} I_{out}(x) =& |(E_{in1}(\vec{x}) + E_{in2}(\vec{x})) \otimes h(\vec{x})|^2 \\ =& |E_{in1}(\vec{x}) \otimes h(\vec{x})|^2 + |E_{in2}(\vec{x}) \otimes h(\vec{x})|^2 \\ &+ E_{in1}(\vec{x}) \otimes h(\vec{x}) \cdot E^*_{in2}(\vec{x}) \otimes h^*(\vec{x}) \\ &+ E^*_{in1}(\vec{x}) \otimes h^*(\vec{x}) \cdot E_{in2}(\vec{x}) \otimes h(\vec{x}) \end{aligned} \tag{2.7}$$

The analysis of coherent imaging above still applies in incoherent imaging. When the temporal coherence of the light field is low, the light is considered as incoherent light, implying that the light field $E_{in1}(\vec{x})$ and $E_{in2}(\vec{x})$ are statistically independent over time. Therefore, the cross terms $E_{in1}(\vec{x}) \otimes h(\vec{x}) \cdot E^*_{in2}(\vec{x}) \otimes h^*(\vec{x})$ and $E^*_{in1}(\vec{x}) \otimes h^*(\vec{x}) \cdot E_{in2}(\vec{x}) \otimes h(\vec{x})$ turn to be zero after integrating the field over time in the camera sensor. The response of two adjacent point sources becomes:

$$I_{out}(x) = I_{in1}(\vec{x}) \otimes |h(x)|^2 + I_{in2}(\vec{x}) \otimes |h(\vec{x})|^2 \tag{2.8}$$

This equation states that the incoherent imaging system is linear and shift-invariant in intensity and the impulse response of the intensity of a point source is $|h(x)|^2$ which is also referred to as the point spread function ($PSF(x)$). The Fourier transform of the point spread function is the optical transfer function ($OTF(K)$) of the imaging system. Here, We use a capital letter K for the spatial frequencies of the intensity of the light field, and a lowercase letter k for the spatial frequencies of the complex amplitude of the light field. The optical transfer functions $OTF(K)$ is the normalized autocorrelation function of the pupil function $P(k)$. The relationship is given by the equation:

$$OTF(K) = \frac{P(\vec{k}) \otimes P^*(\vec{k})}{\int_{-\infty}^{\infty} |P(\vec{k})|^2 d(k)} \tag{2.9}$$

Figure 2.2(a) depicts the relationship between amplitude spread function $h(\vec{x})$, the pupil function $P(\vec{k})$, the point spread function $PSF(x)$, and the optical transfer function $OTF(K)$. The one-dimensional ideal intensity profile of the $OTF(K)$ is plotted in Fig. 2.2(a). With a normal illumination, the maximum spatial frequency which can be collected is $K_{max} = 2k_{max} = 2\frac{2\pi}{\lambda}NA_{co}$, which implies that the optical resolution of incoherent light imaging is two times larger than that of coherent light imaging. The optical resolution $\frac{\lambda}{2NA_{co}}$ is also referred to the diffraction-limited resolution. In the following sections, I will introduce super-resolved structured illumination microscopy to bypass the diffraction-limit resolution in an incoherent light imaging system. Besides, I will discuss a quantitative phase imaging method based on Kramers-Kronig relations to recover the phase of the coherent light which is lost due to the quadratic nature of intensity in a coherent imaging system.

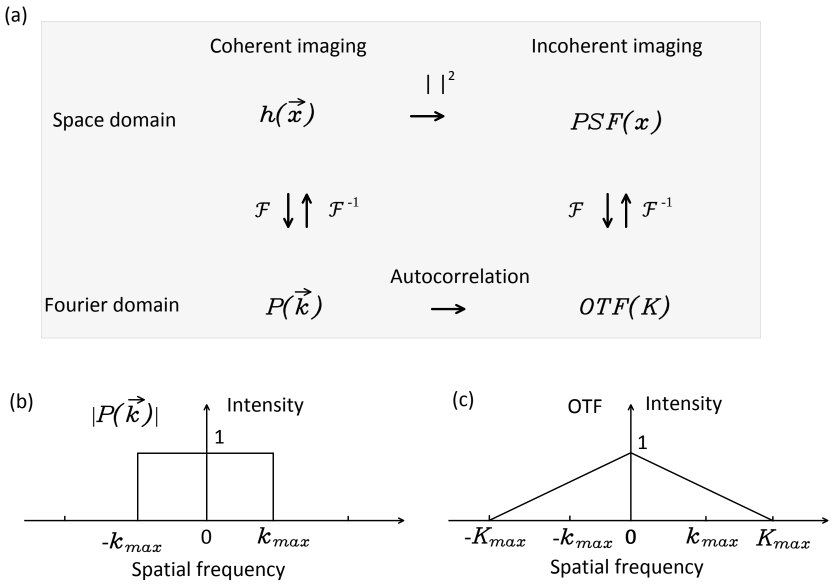

Figure 2.2: (a) Relationship between the transfer functions in coherent imaging and incoherent imaging. (b) Modulus of an ideal one-dimensional pupil function $P(\vec{k})$. $k_{max} = \frac{2\pi}{\lambda} \cdot NA_{co}$ (c) Intensity of an one-dimensional optical transfer function $OTF(K)$. $K_{max} = \frac{2\pi}{\lambda} \cdot 2NA_{co}$

2.2 Super-resolution structured illumination fluorescence microscopy

This section introduces the fundamental principles of two-dimensional structured illumination microscopy. As discussed in the previous section, incoherent imaging offers a higher optical resolution compared with coherent imaging in normal illumination. However, it is still limited by diffraction. At visible wavelengths, the optical microscopy resolution is limited to $\frac{\lambda}{2NA_{co}}$ where NA_{co} is limited to 1 in free space. Many efforts have been made to enhance the resolution and bypass the diffraction limit. Structured illumination microscopy is one of the super-resolution microscopy techniques, which is working in wide-field and is compatible with standard fluorescent dyes. A resolution enhancement by a factor of 2 has been achieved with this technique compared to conventional microscopy, by taking advantage of the incoherence of the fluorescence emission. The mechanism involved is presented below.

The structured illumination can be obtained by generating interference between two coherent beams. For simplicity, we write the relevant equations in one dimension as an example. Two monochromatic beams illuminate the sample with an angle θ and $-\theta$, respectively. The electric fields are written as: $\vec{E}_1 = E_{i1}e^{i(\vec{k}_x x+\phi_1)}$ and $\vec{E}_2 = E_{i2}e^{-i(\vec{k}_x x+\phi_2)}$, where $\vec{k_x}$ is the spatial frequency given by $\frac{2\pi}{\lambda}\sin(\theta)$ in free space. Then, the interference fringe pattern appears at the area where two beams overlap and the intensity can be expressed by:

$$\begin{aligned} I_{ex} &= |\vec{E}_{i1} + \vec{E}_{i2}|^2 \\ &= |E_{i1}e^{i(\vec{k}_x x+\phi_1)} + E_{i2}e^{-i(\vec{k}_x x+\phi_2)}|^2 \\ &= I_0\left(1+\frac{\nu}{2}e^{i(2\vec{k}_x x+\Delta\phi)} + \frac{\nu}{2}e^{-i(2\vec{k}_x x+\Delta\phi)}\right) \end{aligned} \tag{2.10}$$

where $I_0 = |\vec{E}_{i1}|^2 + |\vec{E}_{i1}|^2$ is the sum of the intensities of the two excitation beams and $\nu = \frac{\vec{E}_{i1}\vec{E}^*_{i2}+\vec{E}^*_{i1}\vec{E}_{i2}}{|\vec{E}_{i1}|^2+|\vec{E}_{i1}|^2}$ is the fringe visibility of the interference pattern. The phase difference $\Delta\phi = \phi_1 - \phi_2$ is referred as the phase of the structured illumination and it can be adjusted by introducing a relative optical delay between the two beams. In the general SIM system, the excitation path shares the sample objective with the collection, which means the numerical aperture of the excitation NA_{col} has the same value as the collection NA_{ex}. At the sample plane, structured illumination excites the fluorophores inside the sample and the fluorophores will emit incoherent light at a wavelength λ_{em} larger than the excitation. The detected fluorescence intensity $I^F = \rho \times \Gamma \times \frac{hc}{\lambda_{em}}$ depends on the spatial distribution of the fluorophores ρ, namely the object to image, on the fluorescence rate Γ and on the photon energy $\frac{hc}{\lambda_{em}}$ where c is the speed of light and h the Planck constant. Here, we discuss the linear SIM in which the excitation intensity I_{ex} is much smaller than the saturation intensity I_s of the fluorophores. It follows that:

$$\Gamma = \frac{1}{\tau_r} \frac{I_{ex}/I_s}{1 + I_{ex}/I_s} \simeq I_{ex}/(\tau_r I_s) \tag{2.11}$$

where τ_r is the fluorophore radiative lifetime. The constant $(hc/\lambda)/(\tau_r I_s)$ has been included in the distribution ρ in the following for simplicity. In incoherent imaging, the imaged intensity of the object can be obtained by:

$$\begin{aligned} I &= [I_{ex} \cdot \rho] \otimes PSF \\ &= [I_0 \left(1 + \frac{\nu}{2} e^{i(2\vec{k}_x x + \Delta\phi)} + \frac{\nu}{2} e^{-i(2\vec{k}_x x + \Delta\phi}\right) \cdot \rho] \otimes PSF \end{aligned} \tag{2.12}$$

It follows that the collected image at the camera plane is the superposition of three fluorescence intensity distributions: one corresponding to the standard uniform beam illumination and the two others with a relative spatial frequency shift of either $2\vec{k}_x$ or $-2\vec{k}_x$. The two extra terms include the high frequency of the object, but all the signals are entangled in one image. The two extra contributions resulting from the coherent structured illumination have an additional phase term $+\Delta\phi$ or $-\Delta\phi$, respectively. Setting $\Delta\phi$ at three different values enables disentangling the three intensity contributions from the measured image I and reconstructing the image intensity of the object ρ with a super-resolution. Such a reconstruction is conveniently implemented in the K space where the Fourier transform of image $\tilde{I}^F$ and of the object $\tilde{\rho}$ are connected by:

$$\tilde{I}^F(K) = I_0 \left[\tilde{\rho}_1(K) + \frac{\mathcal{V} e^{i\Delta\phi}}{2} \tilde{\rho}_2(K) + \frac{\mathcal{V} e^{-i\Delta\phi}}{2} \tilde{\rho}_3(K)\right], \tag{2.13}$$

with $\tilde{\rho}_1(K) = \tilde{\rho}(K) OTF(K)$ the part of the Fourier spectrum of the object that is located inside the transmission bandwidth of the microscope, and $\tilde{\rho}_2(K) = \tilde{\rho}(K + 2k_x) OTF(K)$ and $\tilde{\rho}_3(K) = \tilde{\rho}(K - 2k_x) OTF(K)$ the parts that have been shifted by $-2k_x$ and $+2k_x$ inside the transmission bandwidth, respectively. The resolution enhancement relies on the possibility of determining $\tilde{\rho}_2(K)$ and $\tilde{\rho}_3(K)$. A single intensity image $\tilde{I}^F(K)$ is a mixture of three unknown variables, namely $\tilde{\rho}_1(K)$, $\tilde{\rho}_2(K)$, and $\tilde{\rho}_3(K)$, which requires three intensity images to disentangle. Typically, the phase terms are set to 0^o, 120^o, and 240^o, respectively. These three equations can be written as :

$$\begin{bmatrix} \tilde{I}_1^F(K) \\ \tilde{I}_2^F(K) \\ \tilde{I}_3^F(K) \end{bmatrix} = M \begin{bmatrix} \tilde{\rho}_1(K) \\ \tilde{\rho}_2(K) \\ \tilde{\rho}_3(K) \end{bmatrix} \tag{2.14}$$

where

$$M = \begin{bmatrix} 1 & \frac{\nu}{2} e^{i\Delta\phi_1} & \frac{-\nu}{2} e^{-i\Delta\phi_1} \\ 1 & \frac{\nu}{2} e^{i\Delta\phi_2} & \frac{-\nu}{2} e^{-i\Delta\phi_2} \\ 1 & \frac{\nu}{2} e^{i\Delta\phi_3} & \frac{-\nu}{2} e^{-i\Delta\phi_3} \end{bmatrix} \tag{2.15}$$

The matrix M is known with the prior knowledge of the phase and visibility of the structured illumination. Then we can solve the equation and disentangle the three unknown frequency bands by:

$$\begin{bmatrix} \tilde{\rho}_1(K) \\ \tilde{\rho}_2(K) \\ \tilde{\rho}_3(K) \end{bmatrix} = M^{-1} \begin{bmatrix} \tilde{I}_1^F(K) \\ \tilde{I}_2^F(K) \\ \tilde{I}_3^F(K) \end{bmatrix} \tag{2.16}$$

Next, we shift the high frequency bands $\tilde{\rho}_2(K)$ and $\tilde{\rho}_3(K)$ to their right position by a spatial frequency of $-2\vec{k}_x$ and $+2\vec{k}_x$, respectively. Figures 2.3(a) and (b) compare the one-dimensional intensity profile of the optical transfer function and the synthetic transfer function of SIM microscopy. In the case of $K_{max} = 2|\vec{k}_x|$, the bandwidth of SIM is two times wider than that of conventional incoherent microscopy. In practice, the images are generally corrupted by noise. In the image reconstruction, many kinds of digital filters have been applied to minimize the artifacts induced by the noise, including the Wiener filter [2, 3], the total variance filter (TV) [4] and the Hessian filter [5]. In this work, I used the standard Wiener filter which requires no iteration so it is faster than the other methods. The Wiener filter was named after Norbert Wiener who proposed this method in 1940 [6]. In diffraction-limited incoherent imaging, the Wiener filter is given by:

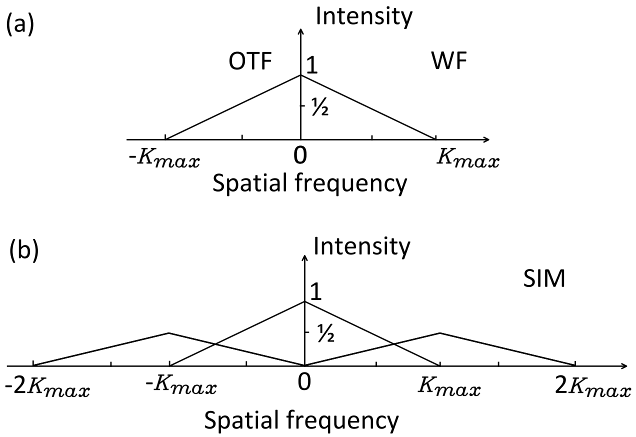

Figure 2.3: (a) One-dimensional intensity profile of optical transfer function. (b) One-dimensional intensity profile of the transfer function of structured illumination microscopy. $K_{max} = \frac{4\pi NA_{co}}{\lambda} = 2|\vec{k}_x|$.

$$\Phi = \frac{OTF^*}{OTF^2 + \frac{N^2(K)}{P_t^2(K)}} \tag{2.17}$$

where $N^2(K)$ and $P_t^2(K)$ represent for the spectrum power of the noise and of the true object. Given that the signal of the true object is unknown, the parameter $\frac{N^2}{P_t^2(K)}$ is given empirically according to the SNR ratio of the image. The noise power $N^2(K)$ is determined by averaging the intensity of the noise falling outside of the OTF bandwidth, assuming the noise in the system is white noise and its intensity is everywhere the same in K-space. The power of true signal $P_t^2(K)$ is approximated by the averaged intensity of the signal inside the OTF bandwidth.

Stitching the frequency bands and applying the deconvolution with a Wiener filter, the final reconstructed image in the Fourier domain is obtained:

$$\tilde{\rho}^r(K) = \frac{\sum_i (M_\phi^{-1})_i \tilde{I}_i^F(K) \cdot \sum_i OTF_i^*(K)}{\sum_i |OTF_i(K)|^2 + N^2(K)/P_t^2(K)} \tag{2.18}$$

where the OTF_i is the optical transfer function shifted by a spatial frequency of 0, $-2\vec{k}_x$, and $+2\vec{k}_x$, for i= 1, 2, and 3 respectively. The reconstructed super-resolved image in the space domain is obtained by applying an inverse Fourier transform of $\tilde{\rho}^r(K)$.

2.3 Quantitative phase imaging based on Kramers-Kronig relations

This section introduces the fundamentals of the quantitative phase imaging based on the Kramers-Kronig (K-K) relations. Different from the above-mentioned structured illumination microscopy which is based on incoherent imaging, this technique is based on coherent imaging. The K-K relations are named after Hans Kramers and Ralph Kronig, which was initially proposed to measure the dispersion of solid materials at X ray [7, 8]. It is also named Hilbert transform in mathematics. The relations link the real part of a complex function with its imaginary part if the function is analytic in the upper half-plane. In this thesis, we investigate the K-K relations in the spatial domain. It was initially applied for phase retrieval in electron microscopy in 1974 [9, 10] and recently extended to optical microscopy [11, 12]. To apply the spatial-domain K-K relations in the spatial domain, the complex function corresponding to the field $E(\vec{r})$ should fulfill two conditions: (1) it vanishes in one of the half-planes in the k-space, and (2) the complex function is analytical in the remaining half-plane.

There are two possible configurations to meet the first condition, see Fig2.4. The first approach is aperture shaping. As schematically illustrated in Fig. 2.4(a), the illumination is parallel to the optical axis of the microscope objective. Then, a spatial filter is placed at the Fourier plane of the imaging system to block the signals falling in the negative or positive part. The second method is beam shaping. Instead of applying an illumination parallel to the optical axis, the incident light

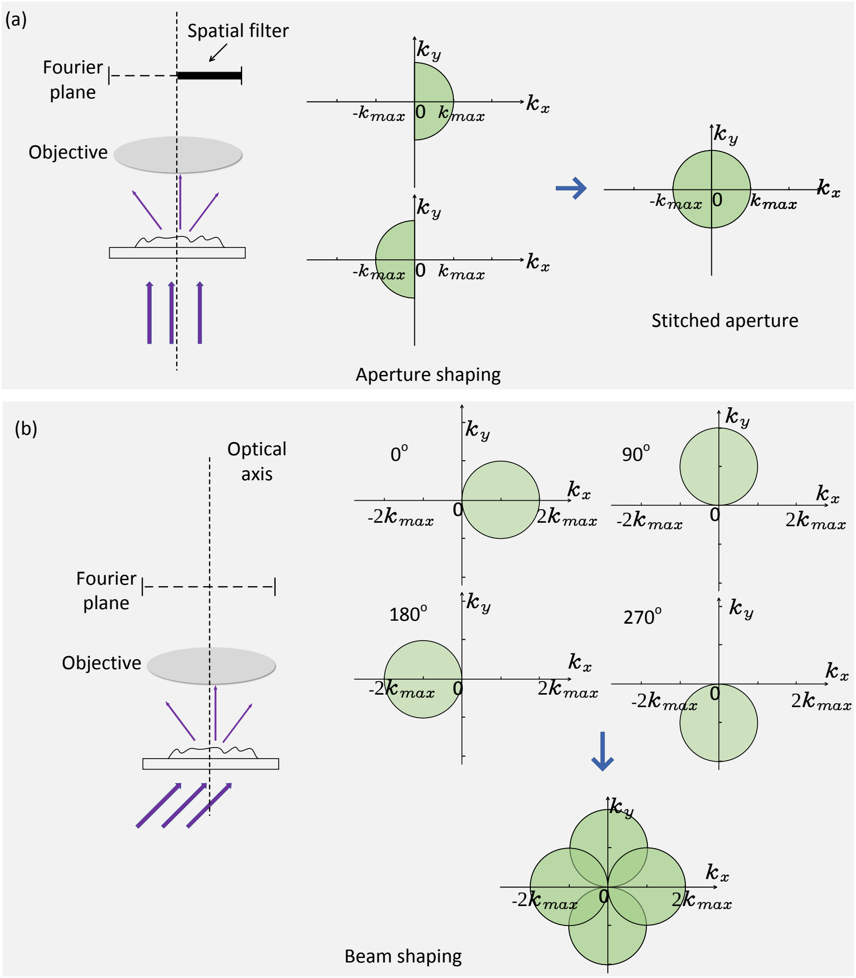

Figure 2.4: Implementation of K-K relations-based QPI engineered by (a) aperture shaping and (b) illumination beam shaping. $k_{max} = \frac{2\pi NA_{co}}{\lambda}$

illuminates the object at an angle that equals the maximum angle collected by the microscope objective, see Fig2.4(b). To simplify the derivation, we consider the scattered signal in one dimension along the x-axis and define $E(k)$ as the Fourier transform of the scattered total field $E(x)$. If condition (1) holds, we can write:

$$E_{co}(k) = E(k) \cdot U(k) \tag{2.19}$$

where $E_{co}(k)$ is the field collected by the microscope objective, $U(k)$ is a Heaviside step function in the Fourier domain:

$$U(k) = \begin{cases} 1, & k \text{ at the remaining half-plane} \\ 0, & k \text{ at the vanished half-plane} \end{cases} \tag{2.20}$$

The collected field in the space domain can be obtained by taking a Fourier transform, as follows:

$$E_{co}(x) = \int_{-\infty}^{\infty} E_{co}(k) e^{-ikx} dk \tag{2.21}$$

Since the $E_{co}(k)$ is band-limited function with the $k_{max} = \frac{2\pi}{\lambda} NA_{co}$, $E_{co}(k)$ turns to be zero at k approaching $+\infty$ or $-\infty$. If the function $E_{co}(k)$ is analytical, we can define the integration along a closed path l in the upper half plane, as follows [7, 8]:

$$\begin{aligned} \oint_l \frac{E_{co}(X)}{X-x} dX =& 0 \\ =& PV \int_{-\infty}^{\infty} \frac{E_{co}(X)}{(X-x)} dX - j\pi E_{co}(x) \end{aligned} \tag{2.22}$$

Where PV is the Cauchy principal value and the term $-j\pi E_{co}(x)$ is the production of the integration around the pole x according to the theory of residues. Rearrange the equation, we can obtain the equation below:

$$E_{co}(x) = \frac{1}{j\pi} PV \int_{-\infty}^{\infty} \frac{E_{co}(X)}{(X-x)} dX \tag{2.23}$$

The collected complex field $E_{co}(x)$ consists of the imaginary part $E_i(x)$ and the real part $E_r(x)$, respectively. Splitting the real and imaginary parts of the field, we can obtain the KK-relations:

$$E_i(x) = -\frac{1}{\pi} PV \int_{-\infty}^{\infty} \frac{E_r(X)}{(X-x)} dX \tag{2.24}$$

$$E_r(x) = \frac{1}{\pi} PV \int_{-\infty}^{\infty} \frac{E_i(X)}{(X-x)} dX \tag{2.25}$$

These equations 2.24 and 2.25 state that by knowing either the real part or the imaginary part we are able to retrieve the other. Given that the real objects are complicated and unpredictable, the analyticity of the image field is generally not guaranteed. Here, we discuss the case when the microscopy system is working in a bright field and the amplitude of the scattered light $|E_s(x)|$ is smaller than unscattered light the $|E_u(x)|$. The sum of the scattered and unscattered light equals the total image field, $E_{co}(x) = E_s(x)+E_u(x)$. To ensure the analyticity we define the following function:

$$\begin{aligned} \chi(x) &= \ln(E_{co}(x)) \\ &= \ln\left(1 + \frac{E_s(x)}{E_u(x)}) + \ln(E_u(x)\right) \end{aligned} \tag{2.26}$$

If the defined function is analytical, we are able to retrieve the imaginary part from the real part of the complex function $\chi(x)$. To verify its analyticity, we only need to demonstrate the analyticity of the term $\ln\left(1 + \frac{E_s(x)}{E_u(x)}\right)$ since the term $\ln(E_u(x))$ is a constant. Considering the $\frac{|E_s(x)|}{|E_u(x)|} < 1$, the analyticity of the first term in the equation 2.26 can be proved via its Taylor expansion:

$$\ln\left(1 + \frac{E_s(x)}{E_u(x)}\right) = \frac{E_s(x)}{E_u(x)} - \frac{1}{2}\left(\frac{E_s(x)}{E_u(x)}\right)^2 + \frac{1}{3}\left(\frac{E_s(x)}{E_u(x)}\right)^3 + ... \tag{2.27}$$

The real part and imaginary part of function $\chi(x)$ are the amplitude and phase of the image field, respectively. In coherent imaging, we can measure the real part of $\chi(x)$ by knowing the intensity of the image field $|E_{co}(x)|^2$. Therefore, we are able to recover the imaginary part of the function $\chi(x)$ from its real part via the K-K relations and then retrieve the phase of the image field. The real part of $\chi(x)$ can be expressed by:

$$\chi_r = \frac{1}{2}\ln\left(|E_{co}(x)|^2\right) \tag{2.28}$$

then, the imaginary part is obtained using the K-K relations 2.24

$$\chi_i = -\frac{1}{\pi}PV\int_{-\infty}^{\infty}\frac{\frac{1}{2}\ln(|E_{co}(X)|^2)}{x-X}dX \tag{2.29}$$

As a result, we can recover the complex image field:

$$\begin{aligned} E_{co}(x) &= e^{\chi_r + j\chi_i)} \\ &= e^{\left(\frac{1}{2}\ln(|E_{co}(x)|^2) - j\frac{1}{\pi}PV\int_{-\infty}^{\infty}\frac{\frac{1}{2}\ln(|E_{co}(X)|^2)}{x-X}dX\right)} \end{aligned} \tag{2.30}$$

After retrieving the complex field of each frame, $i.e.$ for different orientations of the illumination, the images are finally stitched together in the Fourier domain. Followed by a deconvolution and an inverse Fourier transform, the high-resolution complex image field $E_{co}(x)$ is obtained.

2.4 Conclusion

In this chapter, I have introduced the imaging principle when coherent or incoherent light is scattered or emitted from the object. With normal illumination, the incoherent imaging has an optical resolution of $\frac{\lambda}{2NA_{co}}$ which is two times higher that of coherent imaging $\frac{\lambda}{NA_{co}}$. To bypass the diffraction limit in incoherent imaging, the physical principle of super-resolved structured illumination microscopy is introduced. Taking advantage of the spatial frequency mixing induced by the fluorescence emission, SIM techniques achieve a super-resolution two times larger than the diffraction-limited resolution, which can not be applied in coherent imaging to bypass the diffraction limitation. One of the advantages of coherent imaging is the capability of quantitative phase imaging. I have presented the physical principle of the QPI based on the spatial-domain Kramers-Kronig relations. This technique requires the imaging system to fulfill two conditions, $i.e.$ working in the bright field and vanishing one of the half-planes. The knowledge of the principles discussed above is fundamental to developing the UV-PIC-based SIM technique and the UV-PIC-enabled QPI based on the K-K relations in chapter 4 and chapter 5.

References

[1] E. Abbe. *Beiträge zur Theorie des Mikroskops und der mikroskopischen Wahrnehmung*. Archiv für Mikroskopische Anatomie, 9(1):413–468, 1873.

[2] M. G. Gustafsson, L. Shao, P. M. Carlton, C. J. Wang, I. N. Golubovskaya, W. Z. Cande, D. A. Agard, and J. W. Sedat. *Three-dimensional resolution doubling in wide-field fluorescence microscopy by structured illumination*. Biophys J, 94(12):4957–70, 2008.

[3] Amit Lal, Chunyan Shan, and Peng Xi. *Structured Illumination Microscopy Image Reconstruction Algorithm*. IEEE Journal of Selected Topics in Quantum Electronics, 22(4):50–63, 2016.

[4] K. Chu, P. J. McMillan, Z. J. Smith, J. Yin, J. Atkins, P. Goodwin, S. Wachsmann-Hogiu, and S. Lane. *Image reconstruction for structured-illumination microscopy with low signal level*. Opt Express, 22(7):8687–702, 2014.

[5] Xiaoshuai Huang, Junchao Fan, Liuju Li, Haosen Liu, Runlong Wu, Yi Wu, Lisi Wei, Heng Mao, Amit Lal, Peng Xi, Liqiang Tang, Yunfeng Zhang, Yanmei Liu, Shan Tan, and Liangyi Chen. *Fast, long-term, super-resolution imaging with Hessian structured illumination microscopy*. Nature Biotechnology, 36(5):451–459, 2018.

[6] Cyberneticist Mathematician Norbert Wiener. *Extrapolation, interpolation, and smoothing of stationary time series: with engineering applications*, volume 113. Cambridge, MA: MIT press, 1949.

[7] R. de L. Kronig. *On the Theory of Dispersion of X-Rays*. Journal of the Optical Society of America, 12(6), 1926.

[8] H. A. Kramers. *La diffusion de la lumière par les atomes*. Atti Cong. Intern. Fisici, (Transactions of Volta Centenary Congress) Como., 2:545–557, 1927.

[9] D. L. Misell and A. H. Greenaway. *An application of the Hilbert transform in electron microscopy: II. Non-iterative solution in bright-field microscopy and the dark-field problem*. Journal of Physics D: Applied Physics, 7(12):1660–1669, 1974.

[10] D. L. Misell and A. H. Greenaway. *An application of the Hilbert transform in electron microscopy: I. Bright-field microscopy*. Journal of Physics D: Applied Physics, 7(6):832–855, 1974.

[11] YoonSeok Baek, KyeoReh Lee, Seungwoo Shin, and YongKeun Park. *Kramers–Kronig holographic imaging for high-space-bandwidth product*. Optica, 6(1), 2019.

[12] YoonSeok Baek and YongKeun Park. *Intensity-based holographic imaging via space-domain Kramers–Kronig relations*. Nature Photonics, 15(5):354–360, 2021.

3

Development of a UV-compatible integrated photonics platform

Varieties of photonic integration platforms have been developed for a tremendous number of applications. At present, there is no mature platform compatible with UV wavelengths because of two main issues: (1) high material absorption and (2) high scattering loss. To tackle these issues, we have investigated two kinds of materials so-called aluminum oxide (AlO_x) and hafnium oxide (HfO_x) grown by the thermal atomic layer deposition. In view of their high bandgaps of 6.2 eV [1] and 5.5 eV [2] respectively, AlO_x and HfO_x are potential candidates as waveguide layers to guide UV light with a low absorption loss. This chapter first presents the designs of waveguide geometry of single-mode waveguides compatible with the ALD-AlO_x and ALD-HfO_x thin films. Then, I discuss the optimization of the waveguide fabrication and investigate the types of masks and etching recipes. Finally, I describe the characterization of fabricated waveguides using a home-built measurement setup operating at UV wavelengths.

3.1 Design of UV single-mode waveguides

The propagation loss of integrated waveguides includes absorption loss, scattering loss, and radiation loss. The absorption is intrinsic to the material used for the waveguide core and cladding. For ideal semiconductors and insulators, the absorption occurs for light energy larger than the bandgap. The presence of defects or disorders modifies the density of the state leading to new discrete or continuous energy states inside the band gap. To minimize the absorption loss in the UV, using a large bandgap material is a prerequisite. AlO_x and HfO_x are two well-known candidates. Thermal oxidized SiO_2 on top of the silicon substrate is expected to have low absorption at UV wavelengths and be used as bottom cladding of waveguides. Besides, minimizing the imperfection of the defects/disorders is crucial and depends on the elaboration of the deposition technique. Therefore, followed by the optimization of the layer deposition, the material absorption loss can be minimized as much as possible. In view of the high index contrast between the AlO_x and SiO_2 or the HfO_x and SiO_2, the mode is well confined and the radiation loss is generally ignored for straight waveguides. In this case, the scattering loss is dominating the waveguide loss at UV wavelengths because the Rayleigh scattering is inversely proportional to λ^4 [3]. To minimize the scattering loss, we need to minimize the roughness and defects at the interface including the top surface and side walls. For planar waveguides, the top surface is generally much smoother than the side walls of the waveguide. It follows that the straightforward way to decrease the scatter loss is engineering the waveguide geometry to confine the light more inside the waveguide layer and minimize the interaction at side walls. Alternatively, decreasing the side wall roughness is an effective way but with a high technical requirement in processing. The side wall roughness is mainly introduced by the etching process. Compared with AlO_x or HfO_x, it is much easier to etch SiO_2 since it is often used as a waveguide cladding layer and the processing has been investigated massively.

3.1.1 Etch-free slot and rib-like waveguides

The target of the design is to engineer the waveguide geometry to achieve single-mode propagation and minimize scattering loss induced by the waveguide interface. The radiation loss is considered in the case of bend waveguides. Here we proposed two kinds of waveguides, namely slot and rib-like waveguides. In the simulation, there is an assumption that the materials are free of absorption. The TE-mode profiles of the slot and rib-like waveguide are shown in Fig.3.1, respectively. A large-scale thermal oxide silicon wafer is used as a substrate in these designs. The mode profile is simulated using the software COMSOL or Lumerical Mode solution. To avoid etching the core layer, the slot waveguides shown in Fig.3.1 are designed on pre-etched SiO_2, in view of improving the surface smoothness and further decreasing the scattering loss at the side walls. The rib-like waveguide shown in Fig.3.1(b) is designed by patterning a strip PECVD- or ALD-SiO_2 on top of a core layer of the ALD-AlO_x. The guided mode in the slot waveguide interacts strongly with the medium inside the slot, which can be attractive for on-chip Raman spectroscopy [4, 5]. Although the slot mode will also interact with side walls, the scattering loss is expected to be low because the surface of the etch-free ALD-deposited core layer is very smooth and the etched SiO_2 surface is expected to be smooth enough. The second design, namely the rib-like waveguide, can simultaneously achieve large waveguide dimensions and single-mode propagation, which not only provide a low light-matter interaction at the side-walls of the patterned SiO_2 but also relax the lithographic requirements, enabling standard UV contact lithography in place of e-beam lithography.

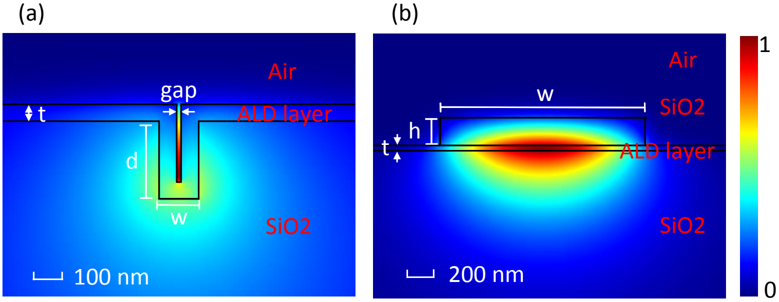

Figure 3.1: Cross-sections and simulated TE-mode intensity profiles of (a) slot waveguide and (b) rib-like waveguide.

Figures 3.2(a), (b) and (c) summarize the results of the slot waveguide structure simulated at a wavelength of 260 nm, 300 nm and 405 nm. Refractive indexes of 2.00 and 1.69 are chosen for simulation to be inline with HfO_x and AlO_x, respectively. To avoid any coupling between the guided mode and the possible surrounding slab modes, the thickness of the ALD layer is controlled to be less than the mode cutoff thickness. This constraint on thickness appears in the plot as the maximum thickness value for each shaded area. The shaded areas show the range where the TE or TM mode is guided and the dotted lines represent the cutoff of the slab mode. In this structure, many parameters would affect the light confinement such as the depth (d), the width (w), the slot width (gap), the thickness of the ALD layer (t), the working wavelength (λ) and the refractive index value of the ALD layer (n). To investigate the variables of interest (gap, t, λ and n), the width w and depth d are constrained by the following relationships: $aspectratio = \frac{d}{w}$ and $w = 2 \cdot t + gap$. Aspect ratios with values of 2 and $\frac{2}{3}$ have both been simulated, but the latter result is not plotted because no guided mode is found. The TE mode emerges earlier than the TM mode by increasing the thickness of the ALD layer when the slot is narrow, while the TM mode can be guided over a wider thickness range in the case of wider slots ($>$10 nm). In this structure, light is confined tightly in the slot where the analyte of interest is located, which can enhance the light-matter interaction dramatically. At λ= 260 nm, the single mode behavior for TE and TM ranges over an ALD thickness of 14 nm for n= 1.69, which plummets to a range of only 2 nm for n= 2.00. This result highlights the challenge of fabricating slot waveguides for $\lambda < 300$ nm and high index contrast.

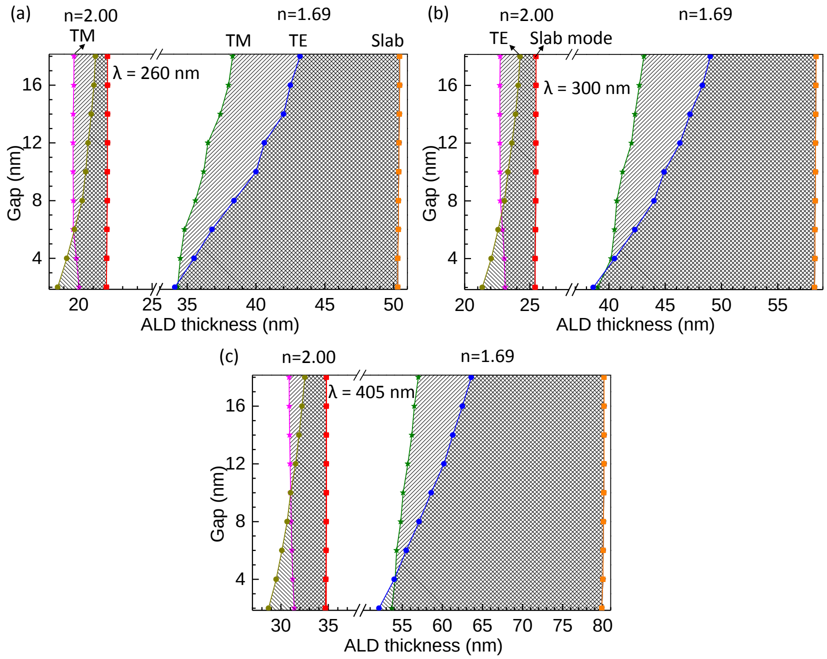

Figure 3.2: Simulated single mode map for the slot waveguide at three different wavelengths, (a) 260 nm, (b) 300 nm, and (c) 405 nm, respectively. In the case of index value n = 2.00, the cut-off of the fundamental TM, TE, and slab modes are indicated by purple, brown, and red dot lines, respectively. The green, blue, and orange dot lines represent the cut-off of the fundamental TM, TE, and slab modes in the case of n= 1.69. The aspect ratio of 2 is designed.

The simulated mode maps for the rib-like waveguide are given in Fig.3.3(a) and (b), respectively. Similar to the simulation of the slot waveguide, two refractive index values and three operating wavelengths are selected to reveal the evolution of the single-mode region. For the proposed rib-like waveguide, three geometrical parameters (h, w and t) affect the guided mode. To see the evolution of the TE single mode region with respect to the SiO_2 height and width, the thickness of the ALD layer is fixed in these cases. Moreover, as the layer thickness given by the cut-off of the slab mode varies with the index values, different thicknesses of 30 nm and 15 nm are selected for n= 1.69 and n= 2.00 respectively. The shaded regions between the dotted lines represent the TE single-mode range. The upper and lower lines of each shaded area represent the cutoff of the multi-mode and TE single-mode, respectively. From the figures, it can be easily seen that the constraints of height and width are stricter to implement TE single-mode propagation at a shorter wavelength. Furthermore, it is worth noting that no matter how large the h is, there is no multi-mode guided in the case of w= 1 µm and λ= 405 nm. In contrast, the h is limited to a range of 9 nm at λ= 260 nm for w= 2 µm and n= 2.00.

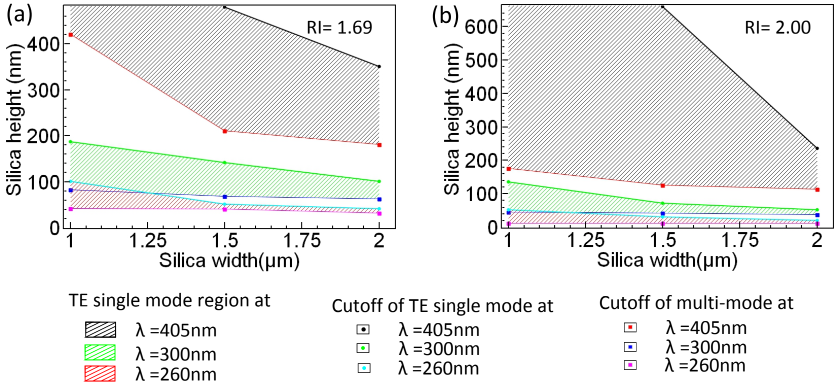

Figure 3.3: Simulated mode maps for rib-like waveguides at an ALD layer refractive index of (a) 1.69 and (b) 2.00, with an ALD thickness of 30 nm and 15 nm respectively. The cutoff of the TE single mode and multi-mode is given at three different operating wavelengths.

The rib-like waveguide is a promising geometry to provide low scattering loss. However, the radiation loss has to be taken into account at the bends, in view of their low light confinement. While smaller bend radii are required to keep the footprint of circuits as compact as possible, radiation losses increase as waveguide bend radii decrease. Fig.3.4 (a) and (b) compare the TE-mode profiles of the rib-like waveguide simulated without bending and with a bend radius of 300 µm. The geometry of the waveguide is selected from Fig.3.3 in the case of n= 1.69, t= 30 nm, W= 1500 nm and H= 150 nm. The working wavelength is 300 nm. Without bending the mode is well confined in the mid of the waveguide, while it is more confined close to the edge when the waveguide is bent. It is worth noting that the bend radius of 300 µm is relatively large compared with a radius of tens of µm for Si or SiN$_x$ platform, but the guided mode still suffers high radiation loss of 9 dB/cm. This radiation loss will considerably limit the application of such a waveguide in the design of compact circuits. By contrast, although the TE mode of the slot waveguide has a large bend loss of 92 dB/cm, the TM mode shows a low bend loss in order of 10^{-6} dB/cm at a bend radius of 200 µm, see Fig. 3.4(c) and (d). The geometry dimension of the slot waveguide is adopted from the simulated mode map in Fig. 3.2(a) in order to achieve single mode propagation at a working wavelength of 300 nm. The waveguide has a gap of 10 nm and a layer thickness of

45 nm. This result shows that the single-mode slot waveguide is a good candidate for routing waveguides.

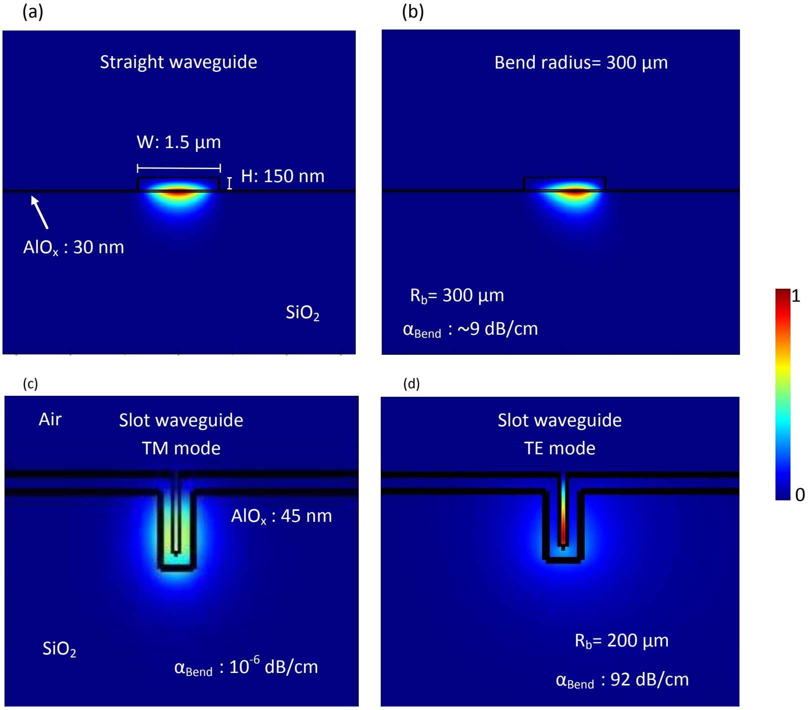

Figure 3.4: (a) TE-mode profile of the straight rib-like waveguide.(b) TE-mode profile of the bend waveguide with a radius of 300 µm*. (c) TM-mode and (d) TE-profiles of the slot waveguide with a gap of 10 nm, a ALD layer thickness of 45 nm and a bend radius of 300* µm*. The working wavelength λ is 300 nm.*

3.1.2 Standard strip waveguides

The strip waveguide is a kind of standard waveguide geometry, which is formed by selectively etching the waveguide layer to a rectangle shape on substrates, see Fig.3.5(a). The thermal SiO_2 and the air are used as the bottom and top cladding, respectively. Similar to etch-free waveguides, the AlO_x and HfO_x are investigated as the core layer. The ALD technique grows the layer at a very low growth rate, typically 0.1 nm per cycle, which means that it is very time-consuming to deposit a thick layer. In this simulation, we only consider the thin ALD-AlO_x and ALD-HfO_x layers with a thickness of 120 nm and 60 nm, respectively. The relationships between the dispersion curves and the designed waveguides are investigated using

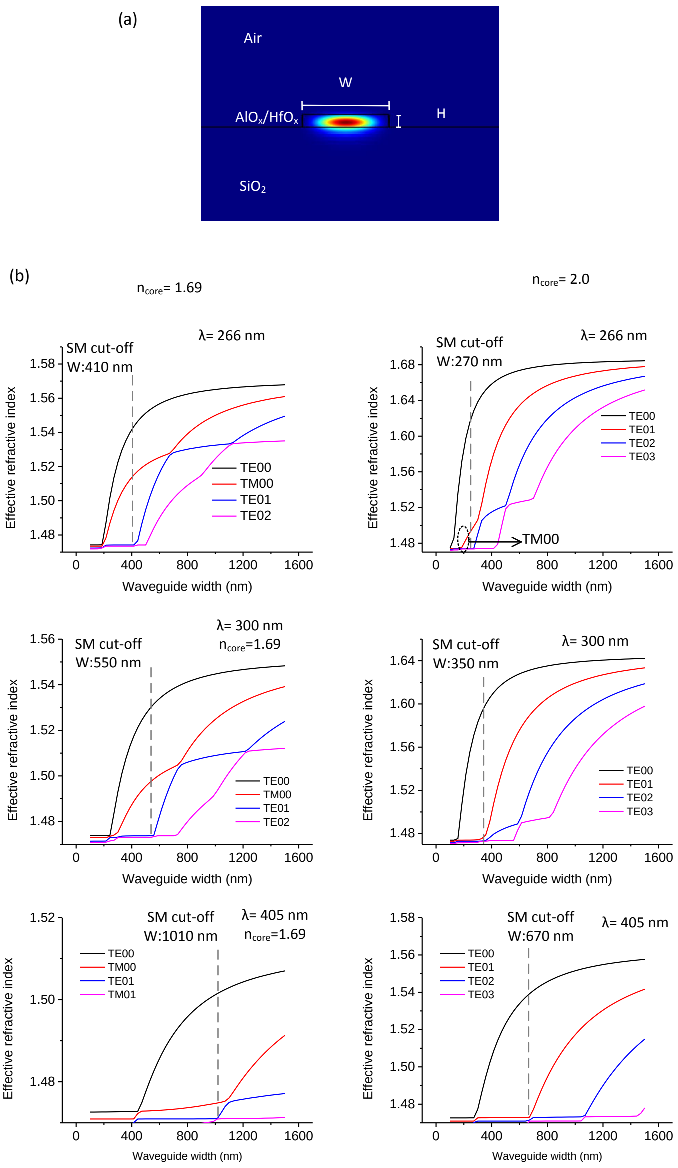

Figure 3.5: (a) TE00 mode profile a strip waveguide. The waveguide width W= 1.0 μm and height H= 120 nm at n= 1.69 or 60 nm at n= 2.0. (b) Relationship between the dispersion curves of guided modes (TE00, TM00,TE01, TE02) and the waveguide width. λ: working wavelength at 266 nm, 300 nm or 405 nm. n_{core}: refractive index of waveguide core with a value of 1.69 or 2.0.

the Lumerical Mode solution, see figure3.5(b). The waveguide geometries supporting single-mode propagation and low bend loss are desired. The dashed lines in the plots indicate the cut-off of the single-mode propagation. Decreasing the operating wavelengths from 405 nm to 266 nm, the waveguide widths of single-mode cutoff reduce from 1010 nm to 410 nm for the AlO_x layer and from 670 nm to 270 nm for the HfO_x layer, respectively. This reveals that a higher requirement on the resolution of lithography is required when the waveguide remains at single-mode propagation at shorter wavelengths. Besides, in the case of n= 1.69, there are two fundamental modes with either TE or TM supported in the range of single-mode propagation. By contrast, the fundamental TM mode is suppressed in the case of HfO_x, except at λ= 266 nm. Next, the bend loss of the strip waveguide is investigated. As an example, the waveguide with a width W= 500 nm and a height H= 120 nm is simulated with a bend radius of 50 µm. As shown in Fig.3.6, the mode profile is well confined in the center with such a small bend radius and the radiation loss is estimated to be 10^{-6} dB/cm, which leads to a negligible contribution in PICs in contrast to the rib-like waveguide.

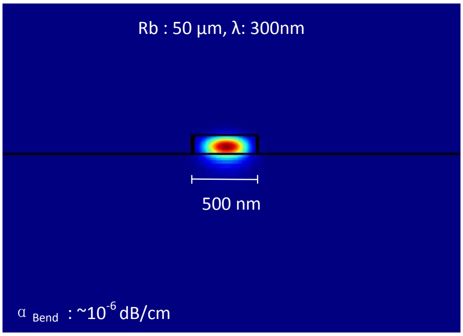

Figure 3.6: (a) TE mode profile the strip waveguide bent with a radius of 50 µm, in the case of n= 1.69, W= 500 nm and H= 120 nm.

Compared with the rib-like, the clear advantage of the strip waveguide and the slot waveguide is the lower radiation loss. In practice, the slot and strip waveguide will suffer scattering loss due to a higher interaction at side walls after etching. To minimize the scattering at side walls, the fabrication processes in particular the etching recipe should be carefully optimized to minimize the roughness. Considering that the geometry of the strip waveguide is easier to fabricate compared with the slot waveguide, we decided to use the strip waveguide to optimize the etching techniques at that stage.

3.2 Fabrication of integrated strip waveguides

This section investigates the fabrication of the AlO_x and HfO_x waveguides using layers deposited by ALD techniques. Their etching properties were investigated using reactive ion etching (RIE) and inductively coupled plasma-RIE (ICP-RIE) with a Fluorine-based and chlorine-based gas mixture, respectively.

3.2.1 Waveguide-core layer deposition via atomic layer deposition techniques

There are many ways to deposit AlO_x and HfO_x thin film, such as (plasma enhanced-) atomic layer deposition, chemical vapor deposition (CVD) [6], RF magnetron sputtering [7], electron beam sputtering [8, 9] and pulsed laser deposition (PLD) [10]. Among these techniques, RF-sputtering and ALD are promising to grow low-loss thin films at UV wavelengths. Combining the process of chemical mechanical polishing, the AlO_x thin film deposited by the former technique achieves a low loss of 0.6 dB/cm at a working wavelength of 377 nm [11]. Nevertheless, the ALD-AlO_x thin film deposited on fused silica substrates has been demonstrated to guide UV light at a shorter wavelength of 250 nm with a low propagation loss of 4 dB/cm at a wavelength [12]. Therefore, the ALD technique is employed to grow the AlO_x and HfO_x layers. The mechanism of ALD techniques is shown as an example in Fig.3.7, where the schematic depicts the process flow of the growth of the AlO_x layer using the two precursors, namely water (H_2O) and trimethylaluminum (TMA). Before loading the substrate into the ALD reactors, it is exposed to the air to be hydroxylated. A full cycle of deposition can be divided into four steps, as follows: (1) pulsing the precursor TMA to the chamber and the TMA reacts with the OH groups at the surface of the substrate, which creates the first Al monolayer with CH_3 bonds remaining exposed. (2) pumping the chamber to vacuum status to remove any remaining TMA precursor gas. In this step, an inset gas such as N_2 can be pulsed. (3) pulsing H_2O to remove the CH_3 bonds and leave OH bonds again on the surface. (4) pumping the chamber again to remove any remaining H_2O in the chamber. Each full cycle can grow the AlO_x layer with a thickness of 1 Å. Repeating steps (1-4) allow us to accumulate the layer gradually.

In this thesis, the AlO_x layers are deposited by cooperators, either the CMST group or Cocoon group at the University. At the CMST group, the layer is deposited by a commercial reactor, an Ultratech Savannah 200 instrument (Veeko). At the Cocoon group, the ALD reactors are home-built, and compatible with plasma enhanced-ALD. The ALD-AlO_x layers used in this thesis are all deposited by the precursors of TMA and H_2O. The ALD-HfO_x are grown with the precursors of tetrakis(dimethylamido)hafnium (TDMAH) and H_2O. The optical dispersion of the ALD-AlO_x and ALD-HfO_x measured by ellipsometry are shown in Fig. 3.8. The ALD-HfO_x shows a high refractive index of 2.1 at a wavelength of 400 nm,

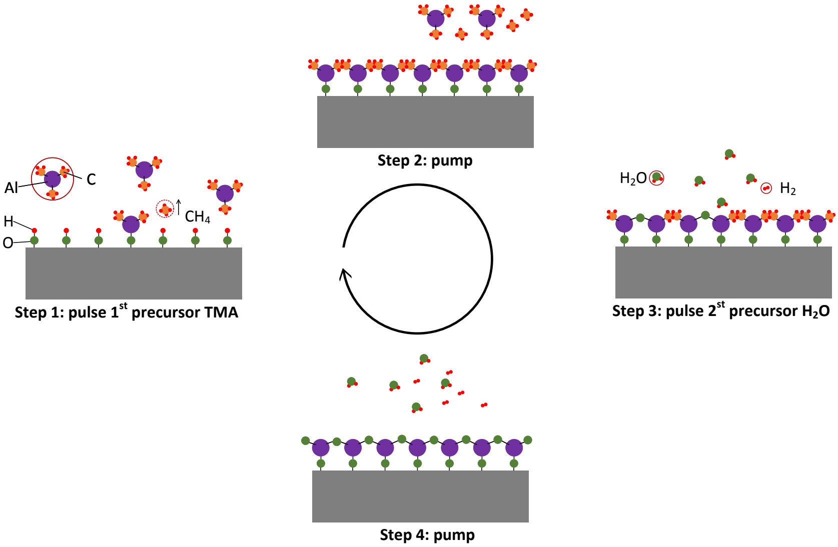

Figure 3.7: Schematic of the working principle of ALD techniques. Precursors of TMA and water are used as examples to show the deposition of AlO_x thin film layer-by-layer.

which allows the waveguide to confine the light in a more compact size compared with the ALD-AlO_x of n= 1.68.

3.2.2 Fabrication of aluminum oxide waveguides

The standard strip waveguides are produced by selectively etching the ALD layers with a patterned mask. The mask is generally made of varieties of polymers sensitive to UV light or electron beams. Given that the photoresist (PR) is prone to be deformed during dry etching in ICP applied with high power, the investigated materials of the mask are not only limited to polymers but also inorganic materials such as SiN_x.

3.2.2.1 Photoresist mask with a low etching selectivity

At the early stage of this project, the conventional photolithography using a mask aligner (MA6, Karl Suss) was employed to pattern a photoresist mask in view of its shorter processing cycle compared to that of E-beam lithography or extreme UV (EUV) lithography. Although the resolution of a conventional contact optical lithography is around 1 µm which is much lower than that of E-beam lithography or EUV lithography, the geometries of AlO_x waveguide can be properly designed to support single-mode propagation for a waveguide width larger than 1 µm. Con-

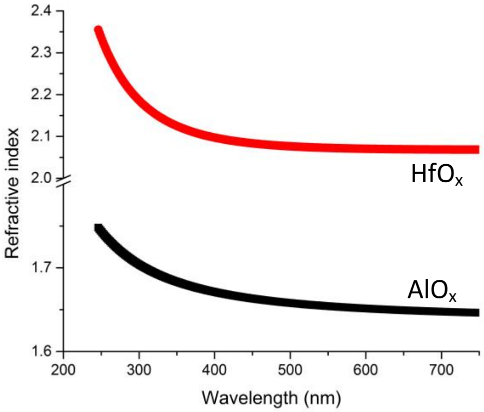

Figure 3.8: Optical dispersion curves of ALD-HfO$_x$ and ALD-AlO$_x$.

sidering the side wall roughness of the etched layers is generally high without the optimization of the process, the short processing time of photolithography allowed us to iterate the fabrication efficiently and shorten the total time to find the optimum parameters of dry-etching. The processing flow of the selective etching of AlO$_x$ is shown in the figure3.9. The process starts with a thermally oxidized silicon wafer (SiO$_2$/Si) ordered at UniversityWafer. A thick thermal oxide of 3 µm is selected to prevent any mode leakage introduced by the silicon substrate underneath. Prior to loading the substrate into the ALD reactor, the substrates are treated by wet and dry cleaning successively to remove any contamination on the surface. The wet cleaning is implemented by rinsing the substrate with acetone, isopropanol and water for 60 seconds for each step successively. The dry cleaning is implemented by 15-minutes O$_2$ plasma in Tepla GiGAbatch (PVA), which removes the organic residues that have not been removed during the wet cleaning. During the layer deposition in ALD reactors, a thin-film AlO$_x$ of 120 nm is grown after repeating the deposition cycles over 1200 times. It takes around 20 hours to finish the deposition, which is the reason why the ALD technique is not ideal for thick-layer deposition. Then, the wafer is diced into small pieces forming samples with a dimension of 2 cm by 2 cm for further processing. After dicing, samples are cleaned again before starting the optical lithography. In the process of optical lithography, the sample is firstly coated with a thick layer of TI prime for better adhesion between the photoresist and substrate. After baking the TI prime at 120 ^{o}C for 3 minutes, the sample is coated with photoresist AZ MIR 701 produced by

MicroChemicals. The rotation per minute (rpm), acceleration, and spin duration are set to 4000 rpm, 4000 rpm/s and 40s, respectively, which gives a 800 nm-thick photoresist layer. After 60s baking at 100 ^{o}C, the sample is loaded to an MA6 mask aligner for UV exposure. A Hg bulb and a band pass filter are used to select the exposure wavelength of 365 nm. The exposure time and exposure dose are optimized to 100s and 5 mW/cm^2 at the contact vacuum mode, respectively. A post-exposure bake is applied at 110 ^{o}C for 60s. The exposed sample is then immersed in the diluted developer solution of AZ-726:H_2O with a ratio of 2:1 for development. The etching phase is implemented by RIE or ICP-RIE. Finally, the photoresist mask is removed by 10-minute O_2 plasma or immersion in the acetone solution to obtain the strip waveguide on top of the Si/SiO_2 substrate with the air top cladding.

The selective etching of AlO_x in RIE or ICP-RIE is the combination of chemical etching and physical etching. The physical etching comes from the ion milling and the chemical etching is caused by the chemical reaction between the gas mixture and the AlO_x or HfO_x layers. Selecting a proper gas mixture is one of the keys to achieve not only a high selectivity between the waveguide layer and mask but also a high-etching rate of waveguide layer in RIE and ICP-RIE. There are two common categories of gas mixture used for dry-etching of AlO_x and HfO_x in RIE or ICP, either fluorine-based or chlorine-based gases. There are two goals during the optimization of dry etching. The first one is smooth side walls. As the scattering loss is inversely proportional to λ^4, the side-wall roughness of the patterned waveguides should be as low as possible in order to achieve low-loss waveguides, in particular, at UV wavelengths. The second is the high etching selectivity between the AlO_x and the mask. An ideal mask is used to protect the target layer and must not be deformed during etching and the etching selectivity between the mask and waveguide layer should be as high as possible. Since the mask will be removed after etching the waveguide layer, the mask will be slightly over-etched to avoid any residue of the mask layer. A higher selectivity results in a less waveguide layer to be etched during removing the mask layer. Besides, a higher selectivity allows us to use a thinner mask layer needed in high-resolution lithography. For instance, with an etching selectivity of 0.15, the thickness of the photoresist should be thicker than 800 nm, in order to fully etch a 120 nm-thick AlO_x layer. Such a thick mask leads to difficulties during patterning fine features like gratings with a line width below 100 nm.

I have first investigated the etching properties of ALD-AlO_x using fluorine-based gas mixtures. The common possible mixtures are carbon tetrafluoride (CF_4)/ hydrogen(H_2), (CF_4)/ (H_2)/ Sulfur hexafluoride(SF_6) and SF_6/ oxygen(O_2) respectively. The etching rate of AlO_x, photoresist and PECVD-SiN_x are summarized in the table 3.1. We can see that the etching rate of ALD-AlO_x is quite low $\leq$ 4 nm/min in all recipes, no matter the CF_4 dominated gas mixture or the

Table 3.1: Etching properties of ALD-AlO_x using gases of CF_4/SF_6 in RIE

Recipe No.	Gas mixture	RF power	AlO_x Etching rate	Photoresist etching rate	SiN_x etching rate
1	CF_4/H_2 80:3	210 W	3 nm/min	50 nm/min	80 nm /min
2	CF_4/H_2/SF_6 80:3:7	210 W	4 nm/min	50 nm/min	100 nm/min
3	SF_6/O_2 50:3	160 W	4 nm/min	100 nm/min	300 nm/min

SF_6 dominated gas mixture. The reason behind this is that one of the etching products AlF_3 generated by the chemical reaction between AlO_3 and CF_4/SF_6 is nonvolatile, which stops the chemical reaction between the AlO_x and F^- radicals. As a result, the etching selectivities of AlO_x/PR(AZ MiF 701) are all below 0.1, with the maximum value of 0.08 obtained by recipe No.2. For an 800 nm-thick photoresist, these recipes are not able to etch a strip AlO_x waveguide with a height of 120 nm due to the low selectivities.

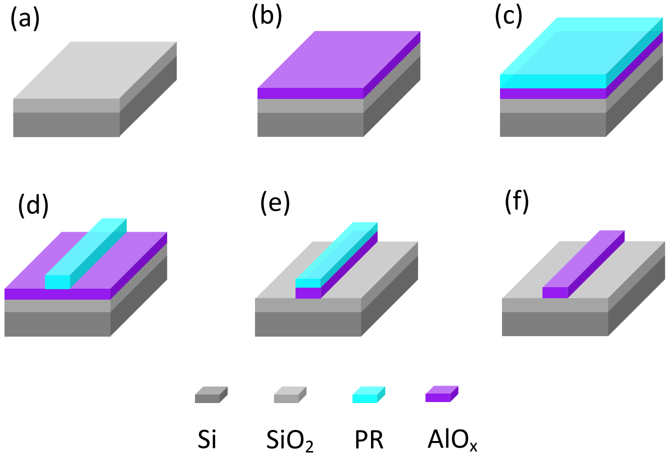

Figure 3.9: Process flow of the AlO_x strip waveguide with a photoresist mask. (a) Cleaned thermal oxidized silicon wafers. (b) Deposition of AlO_x layer via atomic layer deposition. (c) Spin coating photoresist. (d) Patterning photoresist via optical lithography. (e) Dry-etching of AlO_x layers in RIE or ICP-RIE. (f) photoresist removal via O_2 in RIE.

In this context, we replaced the F-based gas mixture with the Cl-based gases in order to achieve a higher etching selectivity. Two possible Cl-based gases in the cleanroom are chlorine (Cl_2)/ boron trichloride (BCl_3). The etching process is implemented in an ICP instrument where there are two chambers, namely the pumping chamber and the reaction chamber. The Cl-based gas mixtures are toxic and must be purged completely before the sample is sent out to the pumping chamber after etching. ICP power is an extra parameter in dry etching compared to RIE, which determines the density of the plasma in the reaction chamber. There are two kinds of possible products involved in the dry etching of AlO_x using BCl_3. One is the combination of nonvolatile B_2O_3 and volatile $AlCl_x$, the other is the combination of volatile $BOCl_x$ and $AlCl_x$ [13, 14]. The latter combination is desired to achieve a higher etching rate of AlO_X, because the volatile etching product will not hamper the chemical etching. The involved chemical reaction depends on the ratio between the radical Cl^- and O^-. Increasing the density of radical Cl^- is able to prevent the formation of B_2O_3 during etching. It follows that the parameters of ICP-RIE which determines the generation of Cl^- are significantly important for the etching of AlO_x layers. In the investigation of etching recipes, the pure BCl_3 gas with a flow rate of 20 sccm is used as the etching gas. The etching properties are investigated by sweeping the radio frequency (RF) power and ICP power. The RF power and ICP power refer to the electric power applied to the flat electrode and coil, which directly determine the energy of the accelerated ion and the density of the plasma, respectively. The parameters such as the chamber pressure, temperature and gas flow will also vary the etching properties but they are not changed during this optimization. The chamber pressure and temperature are set to common parameters, with a value of 20 mTorr and 18 ^oC for all etching in ICP-RIE, respectively.

The processing flow of AlO_x waveguides is the same as the previous one shown in Fig.3.9, except that the AlO_x thin layer is etched in ICP-RIE instead of RIE in step (e). The profile of the patterned photoresist prior to AlO_x etching is imaged in Fig.3.10 as the reference to compare with the profiles after etching, as shown in Fig. 3.11. The substrate used here is bare silicon instead of oxidized silicon wafers, in order to simplify the layer structures and precisely monitor the etching rate of photoresist and AlO_x layers as SEM images are of better quality (lower charging effect). The cross-section of the patterned photoresist in Fig. 3.10 corresponds to the profile obtained in step (d) in Fig. 3.9. The sample is mounted on a stage with a tilt of 48 ^{o}. The side wall is sloped due to the imperfection in the lithography process. In the case where a steep side-wall is required, the lithography process need to be carefully optimized. More details can be found from the supplier MicroChemicals [15]. Here, the slightly sloped side walls are not optimized, since they will not dramatically deviate from the waveguide geometry of a thin waveguide. The layer of AlO_x is highlighted by the false color in light purple. Without dry-etching, the photoresist is in good shape the roughness at the side walls comes from the lithography and development.

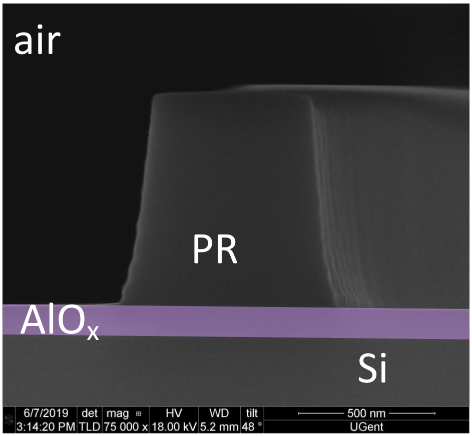

Figure 3.10: Cross-section of photoresist and AlO$_x$ layers on silicon, imaged by scanning electron microscopy.

The etching properties of the photoresist are investigated for different recipes. The RF and ICP powers of ICP-RIE are varied from 25W to 100W and 500W to 1500W, respectively. Figure 3.11 shows the cross-sections of the photoresist and AlO$_x$ layers etched by different parameters. Compared with the profile before etching in Fig.3.10, the photoresist masks are deformed in some cases, especially in the area above the dashed red line. The main reason is that the temperature of the generated plasma in ICP-RIE increases with the applied electric power of RF and ICP. The photoresist can not withstand the excessively high temperature, even though the carrier wafer is cooled with helium flow at the backside.

The etching rate and selectivity are summarized in the table3.2. Increasing ICP power at a given RF power will increase both the etching rate and selectivity since plasma density will be increased and more chemical etching will be involved. It is worth noting that the mask should remain intact after etching in order to achieve smooth side walls of AlO$_x$ waveguide. Therefore, I focused on the recipes below the red dashed lines, namely recipes S2-3, S6-8, S10 and S12, and analyze the etching rates of photoresist and AlO$_x$. All the recipes give relatively low selectivities of AlO$_x$/PR $\leq$ 0.26, which means the mask is etched much faster than the target material AlO$_x$. Considering that the processing flow should be compatible with a thinner PR mask to achieve a higher fabrication resolution, the polymer material is not good enough to be used as a mask for ALD-AlO$_x$ etching. We concluded to use an intermediate layer of SiN$_x$ as the hard mask in AlO$_x$ dry-etching as discussed in the following section.

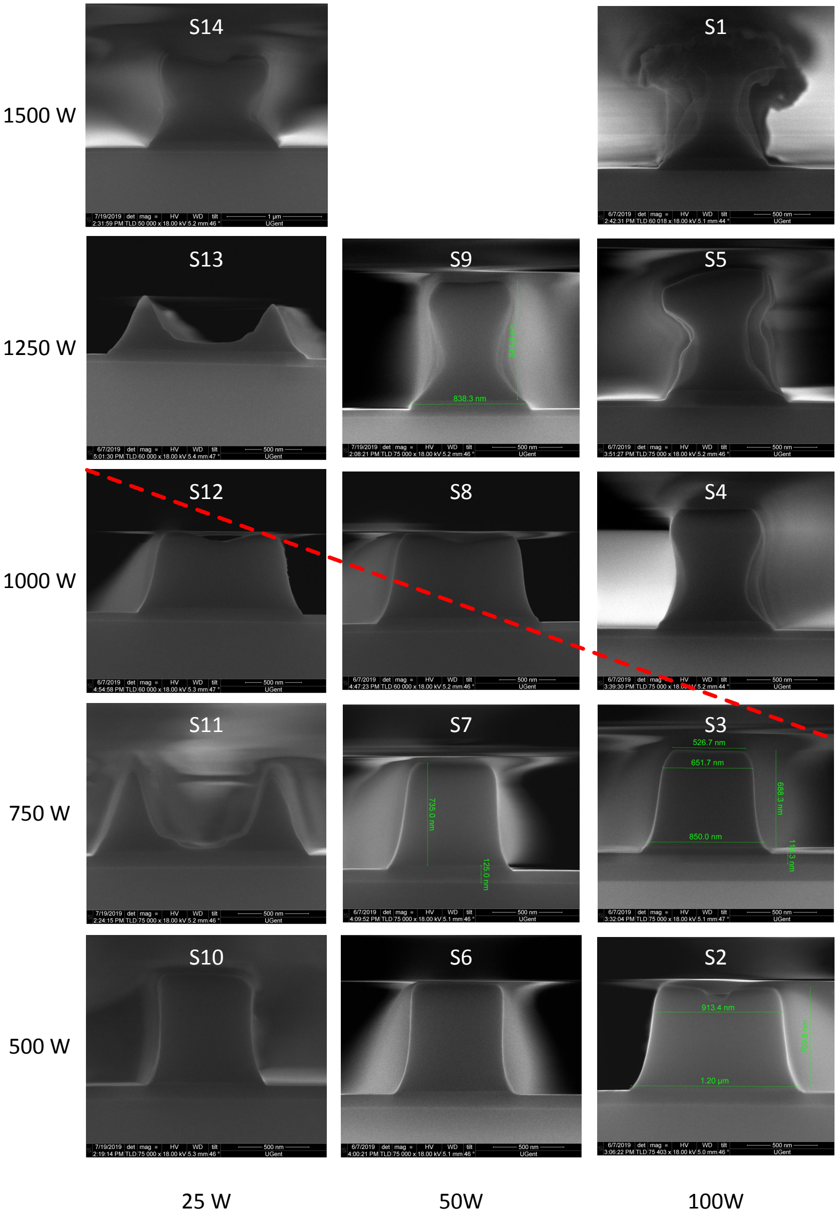

Figure 3.11: SEM images of cross-sections of photoresist and AlO_x layers patterned by different etching recipes.

Table 3.2: Etching properties of ALD-AlO$_x$ using BCl$_3$ in ICP-RIE

Recipe No.	RF power	ICP power	AlO$_x$ etching rate (nm/min)	selectivity AlO$_x$/RP
S1	100 W	1500 W	84	0.28
S2	100 W	500 W	16.5	0.1
S3	100 W	750 W	30	0.19
S4	100 W	1000 W	46	0.24
S5	100 W	1250 W	65.5	0.4
S6	50 W	500 W	12	0.08
S7	50 W	750 W	21.5	0.11
S8	50 W	1000 W	36.5	0.26
S9	50 W	1250 W	52	0.31
S10	25 W	500 W	14	0.08
S11	25 W	750 W	25	0.09
S12	25 W	1000 W	40	0.21
S13	25 W	1250 W	44	0.22
S14	25 W	1500 W	54	0.28

3.2.2.2 SiN$_x$ hard mask with a high-enough etching selectivity

Silicon nitride deposited by PECVD or LPCVD is developed for low-loss waveguides operating either at telecom wavelengths or visible wavelengths. In our group, the dry etching of SiN$_x$ has been well developed to achieve a low side-wall roughness [16, 17]. Besides, the selectivity of SiN$_x$/AlO$_x$ is as high as 75 using recipe No.3 in table 3.1. As a mask, it will be removed after etching of the waveguide layer, in which process the waveguide layer must be remain intact. The high selectivity between SiN$_x$/AlO$_x$ minimize the impact on the AlO$_x$ layer during the removal of the SiN$_x$ layer. These etching properties make the SiN$_x$ a good candidate as a hard mask for AlO$_x$ etching. The processing flow is depicted in Fig. 3.12. The processing starts with thermally oxidized silicon wafers. After the deposition of a ALD-AlO$_x$ layer, a layer of SiN$_x$is deposited with PECVD at a temperature of 270 ^{o}C. The NH$_3$ and N$_2$ gases are used as precursors. In order to balance the stress introduced to the deposited thin film, the applied RF signal can be iteratively switched between the high frequency 13.56 MHz and low frequency 100 kHz to generate the plasma during the deposition in a mixed frequency (MF) approach with an Advanced Vacuum Vision 310 PECVD instrument. In this work, both the MF- and LF-SiN$_x$ layers have been used as the hard mask and no clear difference was been observed between them in terms of side-wall roughness. Next, the PR is patterned using either optical lithography (MA6) or E-beam lithography (EBL). In the Ebeam lithography, the photoresist ARP6200.09 ordered from Allresist is coated on top of the sample with a spin rate of 4000 rpm and an acceleration of

1000 rpm/s, which results in a thickness of 400 nm. The photoresist is then exposed to electron beams with a dose of 160 $\mu C/cm^2$ and a column voltage of 50 kV using Raith Voyager. Followed by the dry etching of SiN_x in RIE using recipe No.1 in table 3.1, the hard mask is patterned. Then, the photoresist is removed via O_2 plasma in RIE before loading to the ICP-RIE chamber. The AlO_x etching is realized by the ICP-RIE using the BCl_3 gas with different RF and ICP powers applied. Finally, the SiN_x hard mask is removed in RIE to avoid any material absorption when the AlO_x waveguides operate at UV wavelengths.

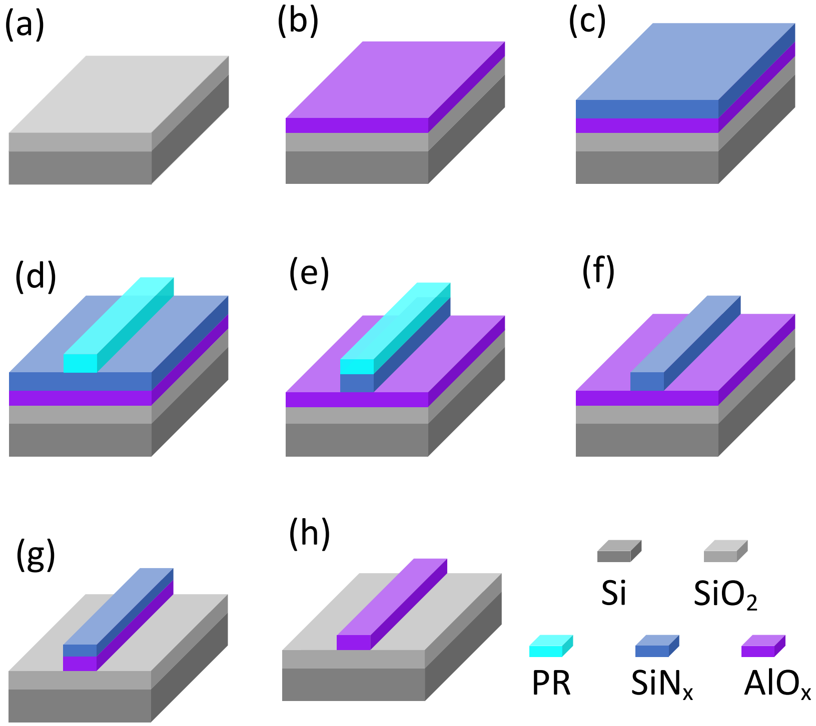

Figure 3.12: The processing flow of AlO_x waveguides using SiN_x as a hard mask. (a) Cleaned thermal oxidized silicon wafers. (b) Deposition of AlO_x layer via atomic layer deposition. (c) Deposition of AlO_x layer via PECVD. (d) Patterning photoresist via optical lithography or E-beam lithography. (e) Patterning SiN_x in RIE. (f) PR removal via O_2 plasma in RIE. (g) AlO_x etching in ICP-RIE. (h) SiN_x removal in RIE.

Nine different recipes have been investigated, whose etching propertios are summarized in the table 3.3. The gas argon (Ar) is added to the gas mixture to tune the ratio between chemical and physical etching. The RF and ICP powers are set to be 50W and 1000W, respectively. The concentration of BCl_3 in the gas

Table 3.3: Etching properties of ALD-AlO_x using SiN_x mask in ICP-RIE

Recipe No.	RF power	ICP power	gas mixture BCl_3/Ar	AlO_x etching rate (nm/min)	selectivity AlO_x/SiN_x
S1	50 W	1000 W	20/0	41	2.56
S2	50 W	1000 W	18/2	43	1.26
S3	50 W	1000 W	14/6	47.3	1.51
S4	50 W	1000 W	10/10	43.5	3.00
S5	50 W	1000 W	6/14	39	2.17
S6	25 W	1000 W	14/6	36.3	1.79
S7	75 W	1000 W	14/6	57	1.14
S8	25 W	750 W	14/6	27	1.93
S9	50 W	750 W	14/6	35.2	1.66

mixture of BCl_3/Ar decreases from 100% to 30%, which corresponds to recipes No.1-5. The etching rate fluctuates around 40 nm/min, with a peak etching rate of 47.3 nm/min in the case of BCl_3/Ar:14/6. Then, the gas mixture of BCl_3/Ar is kept at a ratio of 14/6 to sweep the RF and ICP powers in the recipes from S6-9. These recipes are in line with the trend that a higher RF power results in a higher etching rate but a lower selectivity. In all cases, the selectivity of AlO_x/ SiN_x is larger than 1, which means that the hard mask is etched slower than the target material AlO_x. As a hard mask, a 100 nm-thick SiN_x is generally sufficient for the full etching of a 120 nm-thick AlO_x layer.

It is important to make sure that the profiles of AlO_x waveguides are free of deformation after etching. The cross-section of the etched AlO_x layer is inspected by scanning electron microscopy (FEI Nova 600) shown in Fig.3.13. Since the AlO_x and buried thermal oxide SiO_2 are highly non-conductive, a relatively high voltage of 18 kV is applied to provide higher energy electrons for imaging. It should be noted that the sample will be damaged after long-term exposure to high-energy accelerated electrons, see an example at the left side of the AlO_x waveguide in S8. In all samples, the AlO_x waveguide is fully etched on top of SiO_2. In the image of S2, the patterned AlO_x is indicated with a false color of light purple. All recipes show a high anisotropy for AlO_x etching, with a steep angle as high as 85 ^{o}. The profile of the AlO_x waveguides is free of deformation, implying that the SiN_x hard masks should be remaining intact during and after etching. The properties of sufficient 'high' selectivity >1 and good anisotropy suggest that the SiN_x should be a good option as hard mask for the dry-etching of AlO_x layers. The propagation loss of the waveguides fabricated by the above recipes will be discussed in next section 3.3, which quantifies the etching quality in terms of sidewall roughness.

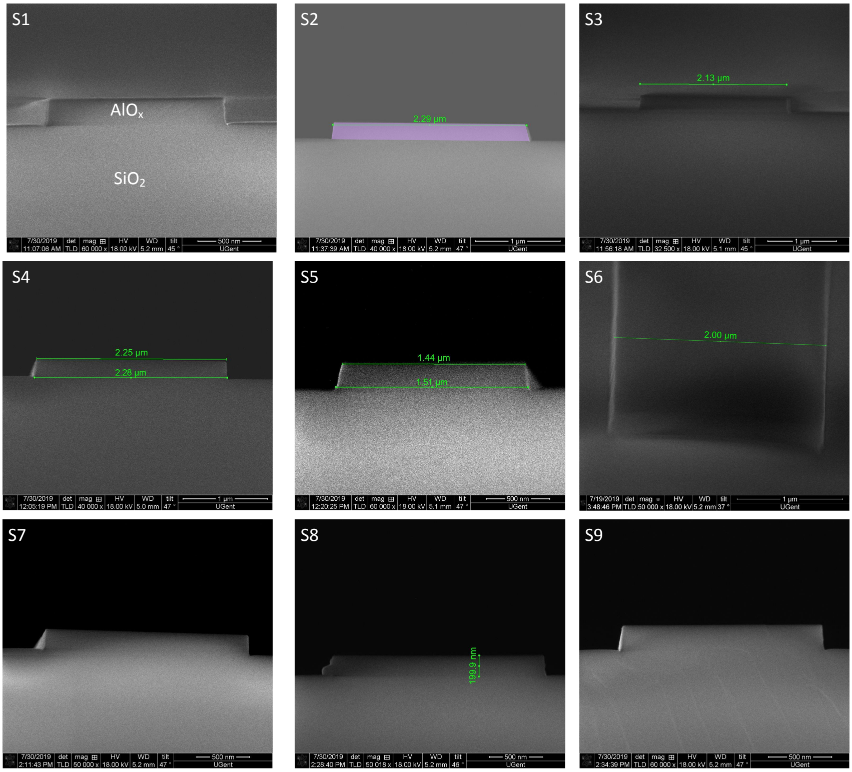

Figure 3.13: SEM images of the cross-section of AlO$_x$ layers patterned by different etching recipes, with the SiN$_x$ hard mask being removed.

3.2.3 Fabrication of hafnium oxide waveguide

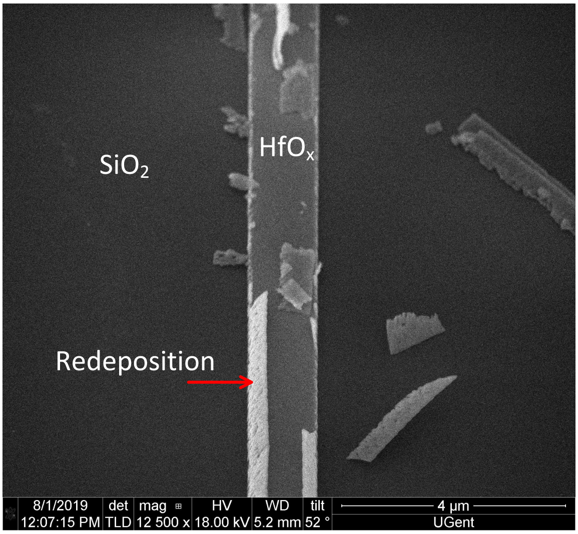

Figure 3.14: SEM images of the cross-section of HfO$_x$ layers patterned by RIE.

ALD-hafnium oxide (HfO$_x$) has a wide bandgap of 5.9 eV [18], which avoids the direct single-photon absorption of UV light. Combing its moderate refractive index n of 2.1 and potential second harmonic nonlinearity [19–21], this material is a good candidate for the waveguide core material operating at UV wavelengths. Although a higher n value allows the waveguide to confine the light in a more compact dimension, it will be more difficult to minimize the scattering loss because the Rayleigh scatter is scaled with the index contrast between the waveguide core and cladding. The processing flow of HfO$_x$ waveguides is the same as that of AlO$_x$ waveguides. Similarly, the dry etching of HfO$_x$ using fluorine- and chlorine-based gas mixtures is investigated in RIE and ICP-RIE, respectively.

Figure3.14 shows the top view of the patterned HfO$_x$ layer using a gas mixture of CF_4/ SF_6/ H_2 in RIE. A clear re-deposition of the etching residue appears at the side walls of the photoresist. After removing the photoresist with O_2, these nonvolatile products still remain on top of the HfO$_x$. The etching residue is expected to be HfF_4, which has a high sublimation point of 970 ^{o}C [22], which means that it is nonvolatile at room temperature. Therefore, the fluorine-based gas is also not a good option for HfO$_x$ etching.

By contrast, $HfCl_4$ has a sublimation point of 317 ^{o}C [22], implying that $HfCl_4$ is more volatile than HfF_4. The etching using a chlorine-based gas mixture is implemented in the ICP-RIE, using the SiN$_x$ as the hard mask. The gas mixture is

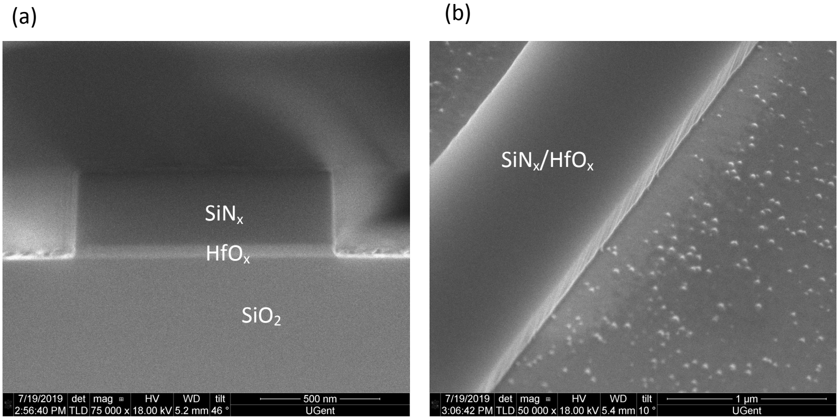

Figure 3.15: SEM images of top-view of a HfO$_x$ layer etched by fluorine-based gas mixture in RIE, with the PR mask being removed.

made of BCl_3/Ar with a ratio of 14:6. The RF and ICP powers are set to 100 W and 1250 W, respectively. The cross-section and angled top view of the etched HfO$_x$ with SiN$_x$ are imaged by scanning electron microscopy, see Fig. 3.15(a) and (b), respectively. As shown in the cross-section in Fig.3.15(a), the HfO$_x$ layer with a thickness of 60 nm is fully etched on top of the SiO_2/Si substrate and the SiN$_x$ hard mask has steep side walls after etching. Besides, the etching residue namely $HfCl_4$ does not build up along the hard mask. Compared with the fluorine-based gas mixture, the etching process using chlorine-based gas results in less redeposition at the top surface of the waveguide but more on the substrate. However, the nonvolatile residue still remains on the surface, which may lead to scattering or absorption losses.

3.3 Loss measurement of the fabricated waveguides

Characterizing the side-wall roughness is one way to quantify the quality of the dry-etching process. Although it can be measured by atomic force microscopy (AFM), the sample or the probe of the AFM needs to be tilted which makes the measurement extremely difficult. The optical loss of the waveguide that scales with the degree of roughness of the waveguide surfaces can be used to quantify the side-wall roughness introduced by the dry etching process. In this section, the fabricated waveguides are characterized by a home-built measurement setup.

3.3.1 Measurement setup operating at UV wavelengths

There are several ways to determine the propagation loss of waveguides, including the most common cut-back method [23], scattered light imaging [24], optical frequency domain reflectometry (OFDR) [25] and Q-factor measurement [26]. In this thesis, the propagation loss of the waveguides is measured by analyzing the decay of the intensity of the scattered light along the waveguides. The roughness introduced during etching process is assumed to be randomly distributed along the waveguide, so the intensity of the scattered light scales with the intensity of the guided light. By determining the relationship between the scattered light with the propagation length L, the propagation loss α of the waveguide can be retrieved, as follows:

$$\alpha L = 10log(\frac{I_1}{I_0}) \tag{3.1}$$

Where α is given in dB/cm, L in cm, I_1 and I_0 are the intensity of the light scattered from the waveguide at the input and the output, respectively. The intensity of the scattered light can be collected from the top of waveguides using a microscope.

The schematic of the measurement setup including the fiber-to-chip coupling system and imaging system is depicted in Fig.3.16(a). The fiber-to-chip coupling system is built to couple the UV laser light from free space to a single-mode fiber and control the polarization of the light via a fiber polarization controller (PC). The all-solid-state UV laser (UV-FN-360, CNIlaser) has a working wavelength of 360 nm and a maximum output power of 55 mW. The output mode of the laser is in quasi-TEM$_{00}$ with a beam diameter of 1.5 mm which is defined by $\frac{1}{e^2}$. A fiber port coupler (PAF2A-18A, Thorlabs) is used to couple the light from free space to fiber, in view of its transparency window at 360 nm. The embedded aspheric lens has a clear aperture of 5.5 mm. A beam expander which consists of two plano-convex lenses is used to expand the beam to match the aperture of the fiber port coupler. A neutral density filter (NDF) is placed in front of the laser output to adjust the power in the optical path. In this coupling system, the alignment of the aspheric lens mounted inside the fiber port coupler is critical to achieving high coupling efficiency. Since the pigtail single-mode fiber (SM300, Thorlabs) has a relatively small core of $\sim$2 µm and the focal spot of the fiber port coupler is 3.5 µm, a slight misalignment will lead to poor coupling efficiency. Optimizing the overlap between the guided mode of the fiber and beam at the focus of the coupling lens is not sufficient to enable good coupling efficiency. The numerical aperture of the coupling lens should match that of the fiber. Here, the NA of the embedded aspheric lens is 0.15 which roughly matches the value of 0.12-0.14 of the connected fiber. In the experiment, a maximum power of 26 mW has been coupled into the SM fiber with a power of 55 mW in the free space, which corresponds to a coupling efficiency of $\sim$ 3 dB. The polarization controller is used to control the polarization of the mode guided in the fiber. At telecom wavelengths or visible wavelengths, the end facet of the fiber is tapered to focus the light in a small spot size. However, it is difficult to process such a lensed fiber at UV wavelengths, since the effective mode area of a single mode fiber is already quite small ∼ 2.3 µm. In this setup, the light coupling from the fiber to the chip is realized by butt coupling using a standard SM fiber with a cleaved flat output.

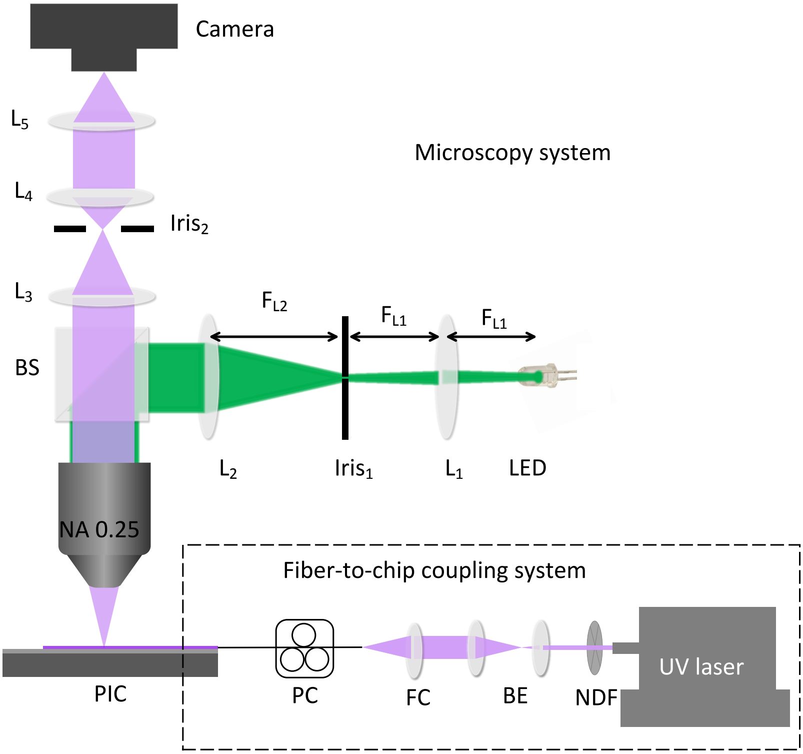

Figure 3.16: Schematic of the measurement setup. It includes lenses (L1-L5), a neutral density filter (NDF), a beam expander (BE), a fiber poet coupler (FC), a polarization controller (PC), a light emission diode (LED), a beam splitter (BS), a UV laser, a microscope objective and a camera.

To image the light scattered from the waveguides, I have adapted an home-build microscope that was designed to operate at visible and near-infrared wavelengths. Since the optical components used to those wavelengths have poor transparency at UV wavelengths, I have replaced them with components of high UV transmittance. As shown in Fig. 3.16, this system includes an illumination path (green) and a collection path (light purple). The illumination is provided by a light emission diode (LED) with a working wavelength of 450 nm or 375 nm. The lens

Table 3.4: Propagation loss of the AlO$_x$ waveguides fabricated with optical lithography

Recipes	S1	S2	S3	S4	S6	S7	S8	S9
Propagation loss (dB/cm)	15.7	20.4	11.2	6.5	5.0	10.5	24.3	8.0

L1 produces a homogeneous light field at the Iris1 which is projected on the sample via the lens L2 and a beam splitter (BS). The adjustable Iris1 is placed between these two lenses to adjust the beam profile. Here, a pellicle beam splitter (PB108, Thorlabs) is selected to minimize the ghost image. The split ratio is selected to be 92:8, which allows most of the scattered light to be collected by the camera. An aspherical lens of NA= 0.25 with a focal length f of 11 mm (C220TMD-A, Thorlabs) is used to collect the scattered light from the waveguide surface, whose transmittance at 360 nm is higher than 90 %. In the collection path, a lens L3 working as a tube lens with a focal length of 300 mm is placed after the beam splitter. The magnification of the image is defined by the ratio between the focal length of the lens L3 and the aspherical lens. A telescope consisting of two lenses L4 and L5 is inserted in the collection path to adjust the final magnification of the photonic circuits to fit the size of the used camera. A UV-enhanced camera (340UV, Thorlabs) is used to record and digitize the image. the image, which has a sensor dimension of 640 x 480 pixels and a pixel size of 7.4 µm.

3.3.2 low-loss single-mode ALD-AlO$_x$ waveguides

At the beginning of the project, a low-cost violet laser diode (CPS405, Thorlabs) was used to measure the loss. The laser has a working wavelength of 402 nm which is very close to the UV wavelength range defined between 200-400 nm. The AlO$_x$ waveguides fabricated by the parameters in table 3.3 are measured. The waveguides are straight lines with a waveguide width of 1 µm and a length of 1 cm. The summary of the propagation loss is presented in the table 3.4. Despite the cross-sections being similar for all waveguides according to the SEM images, the propagation loss varies considerably due to the different side-wall roughness introduced during the etching process. The maximum loss is as high as 24.3 dB/cm measured with the waveguide fabricated by the recipe S8, while a much lower loss of 5.0-6.5 dB/cm is measured with recipe S6 and S4. It is difficult to inspect the side-wall roughness by SEM due to its $\sim$ nm-scale residue and the charging effect of the SEM. However, the side-wall roughness of the wavegudies scales with the propagation loss which can be measured easily.

In this context, the parameter optimization of the etching recipes is continued based on recipes S4 and S6, in view of the relative low propagation loss of the waveguides processed by these two recipe. The extra Cl_2 gas is added into the gas mixture in order to increase the concentration of radical Cl^- which contributes more volatile $BOCl_x$ and reduces the nonvolatile etching residue of B_2O_3. Besides, the layout design of the waveguide has been improved by patterning spiral waveguides, see Fig.3.17(a). On the one hand, the designed spiral waveguide allows us to collect the scattered light over an entire filed-of-view of the imaging system, $i.e.$ without moving the microscope objective, which avoids stitching issues. On the other hand, the lead-in waveguide is separated from the spiral waveguide at a distance S of 1 mm to minimize spurious signals. Since the propagation loss is determined by the decay of the scattered light along the waveguides, any spurious light around the waveguide will introduce inaccuracies in determining the propagation loss. A lot of light is scattered at the input of the waveguide due to the mode mismatching between the on-chip waveguide and the SM fiber. The lateral shift between the input and the spiral waveguide can effectively minimize the spurious light collected by the microscope objective and improve the accuracy of the measured results. I have chosen a bend radius of 200 µm to minimize the impact of the bending loss. The total length of the spiral waveguide is 2.7 cm and the waveguide width varies from 0.8 µm to 2 µm. The optical image of the fabricated spiral waveguides is shown in Fig. 3.17(b).

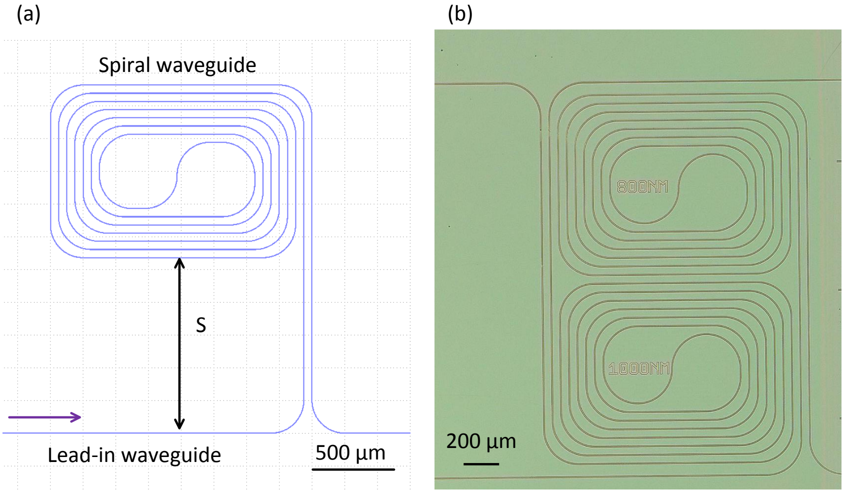

Figure 3.17: (a) Layout design of spiral waveguides. S is the spacing between the lead-in waveguide and spiral waveguide with a value of 1 mm. (b) Optical image of the fabricated spiral AlO_x waveguide.

The image of the light scattering from a spiral waveguide is presented in Fig 3.18(a). The details of the etching recipe of the waveguide can be seen in the recipe

No.4 in table 3.5. The intensity averaged over 10 pixels along the dashed red line is plotted at the top. It can be seen that the ratio between the scattered light and the background is high, which helps us to determine the propagation loss properly. The intensity of the scattered light decays along the propagation direction. Analyzing the relationship between the scattered intensity and propagation length, the waveguide loss is estimated to be 5.0 dB/cm. Considering that the optical lithography is not reliable when the designed line width is approaching the resolution limit of 1 µm. The actual waveguide widths may deviate from the designed value, so the actual widths of fabricated waveguides are measured by SEM. Figure 3.18(b) shows the cross-section of the fabricated AlO_x waveguides with a width measured to be 1.1 µm, while the designed width is 0.8 µm.

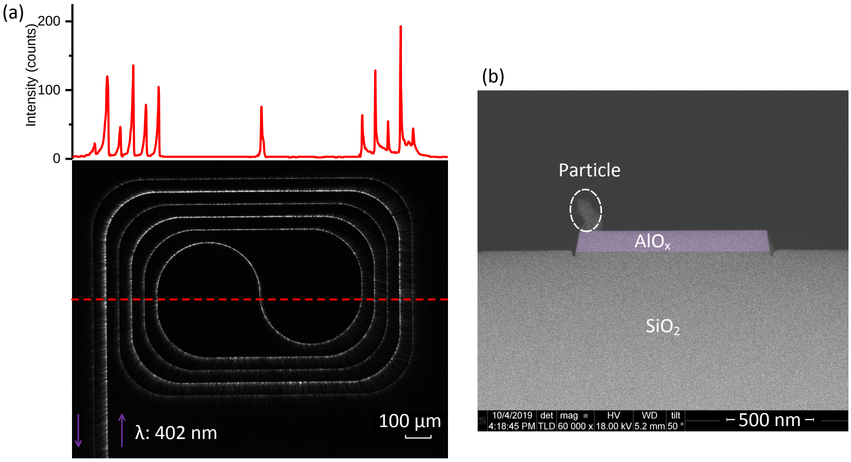

Figure 3.18: (a) Microscopy images of the scattered light from a spiral waveguide at a wavelength of 402nm. The plot above the image shows the averaged intensity profile of the scattered light along the dashed red line. (b) Cross-section of the measured AlO_x waveguide in (a) imaged by a scanning electron microscope.

Nine etching recipes based on the etching gas mixture of BCl_3/Ar/Cl_2 have been investigated and the results are summarized in Table 3.5. The high-resolution mask fabricated by Compugraphics has a resolution of 0.6 µm, which allows patterning a 0.8 µm-wide waveguide theoretically. However, it is not always robust. For contact lithography, where the photoresist surface should be in contact directly with the contact mask, working in a contact vacuum mode gives the highest resolution. Any imperfection in the process, such as non-uniformity of the photoresist or particle contamination on the surface, leads to a low vacuum between the sample and the mask, thus decreasing the resolution of the lithography. The knowledge of the actual waveguide width is of importance during the optimization of the waveguide processing, since the propagation loss is strongly dependent not only on the

Table 3.5: Relationship between the propagation loss of AlO$_x$ waveguides and etching recipes.

Recipe No.	RF power	ICP power	gas mixture $BCl_3/Ar/Cl_2$	propagation loss (dB/cm)	Measured width (μm)
S1	25 W	1250 W	10/10/0	6.5	1.04
S2	25 W	1250 W	10/10/3	6.8	0.86
S3	25 W	1250 W	10/7/3	6.0	1.00
S4	25 W	1250 W	10/10/5	5.0	1.10
S5	25 W	1250 W	10/10/10	14.6	0.87
S6	25 W	1500 W	10/10/5	8.5	1.00
S7	50 W	1250W	10/10/5	7.6	0.80
S8	75 W	1250 W	10/10/5	6.8	1.10
S9	10 W	1750 W	10/10/5	7.0	1.08

side-wall roughness but also on the waveguide width of waveguides. As a result, it is reasonable to measure the actual waveguide width using SEM instead of directly taking the value from the designed mask. As shown in the table, the waveguide width of 0.8 μm is designed for all waveguides but the actual waveguide width varies between 0.80 to 1.10 μm. As regards the waveguide loss, the minimum value of 5 dB/cm at λ= 402 nm is measured with the recipe S4. According to the simulation, the cut-off width of single-mode propagation is 1.19 μm, which means that the geometry of height = 120 nm and width = 1.1 μm is still in a single-mode regime. This value is good, compared with the latest record of $\sim$ 2 dB/cm at λ= 405 nm reported by [23]. Therefore, this recipe has been used for the processes. Propagating light at a shorter working wavelength of 360 nm, the value increases to 9 dB/cm due to a stronger side-wall scattering. The processing is expected to improve further by replacing the conventional contact photolithography with e-beam lithography, which can effectively decrease the side-wall roughness and scattering loss. Although it is possible to achieve smooth side walls of the photoresist with optical contact lithography after careful optimization, e-beam lithography has much better robustness and a higher resolution $\sim$10 nm.

The processing flow using E-beam lithography has been discussed in the section 3.2.2.2. Six different waveguide widths are designed in the layout ranging from 0.7 μm to 1.2 μm with a step of 100 nm. A laser with a working wavelength of 360 nm is used to characterize the propagation loss. A thinner ALD-AlO$_x$ layer of 100 nm is deposited at a deposition temperature of 150 ^{o}C, allowing a single-mode cut-off width of 1.15 μm at a working wavelength of 360 nm. The relationship between the propagation loss and the waveguide width is shown in Fig. 3.19. The 0.8 μm-wide waveguide was contaminated by the particles during the processing, which is why the corresponding loss value has not been measured. The waveguides with a width from 0.9 µm to 1.2 µm exhibit the same level of propagation loss, $i.\,e.$ 7 dB/cm, while the loss value jumps to 30 dB/cm at a width of 0.7 µm. The abnormally high loss of the 7 µm wide waveguide may be attributed to a radiation loss (0.5 dB/cm) and a large bending loss (38 dB/cm) according to simulation via Lumerical Mode. Besides, the scattering loss is expected to increase when the waveguide width decreases for a given sidewall roughness, as the field density of the mode at the side walls increases. Here, the loss is almost constant for waveguide width beyond 0.9 µm. This means that the scattering loss is negligible from a width >0.9 and that the material absorption dominates the propagation loss. Therefore, the absorption loss of the AlO$_x$ layer deposited at 150 ^{o}C is estimated to be a level of 7 dB/cm. Consequently, the deposition of the ALD-AlO$_x$ layer needs to be improved, in order to further decrease the waveguide loss. Besides, the photodarkening effect is observed when the guided power is more than $\sim$1 mW. Note that the absorption loss of this layer estimated by ellipsometry is negligible. This means that the result measured by the ellipsometer is not reliable with the current signal-to-noise ratio of the setup.

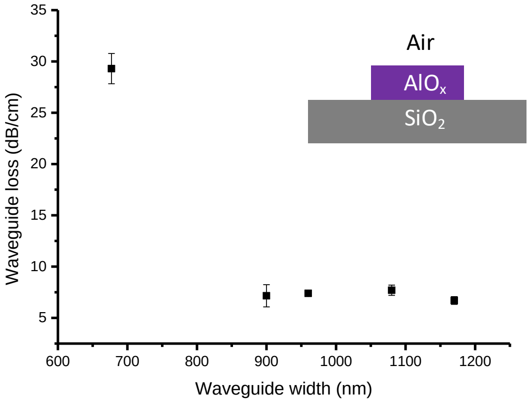

Figure 3.19: Relationship between the propagation loss of AlO$_x$ waveguide and the waveguide width. The AlO$_x$ is deposited at 150 ^{o}C. The insert shows the schematic of the cross-section of AlO$_x$ waveguides.

The optimization of the growth of ALD-AlO$_x$ layers was completed in collaboration with the CoCoon group. The parameters of the ALD technique that are critical are temperature, purge, pump time, as well as the choice of precursors. In this study, TMA and water are selected to be the precursors for all AlO$_x$ deposition. The loss introduced by the amorphous waveguide layer can be attributed to the surface scattering and the material absorption. The surface scattering can be directly determined by the surface roughness that can be measured by atomic force microscopy. As shown in Fig.3.20, the ALD-AlO$_x$ layer is very smooth. The root means square (RMS) of the layer surface is measured to be as low as 0.3 nm. Note that the surface roughness of the AlO$_x$ layer remains at the same level after the etching process. Therefore, the scattering loss introduced by the layer surface can be neglected and the absorption may dominate the loss of the material. In view of the compound of the precursors TMA Al(CH$_3$)3 and water H$_2$O, the possible impurity of carbon C and hydrogen H in the grown layer may lead to strong absorption of UV light. It has been demonstrated that increasing the deposition temperature from 150 ^{o}C to 300 ^{o}C can effectively decrease the amount of C and H [27]. The ALD-AlO$_x$ layer is, therefore, deposited at 300 ^{o}C and the AlO$_x$ waveguides are processed as above using E-beam lithography. Figure3.21(a) shows the image of the scattered light along the part of the spiral waveguide. The waveguide height H is 120 nm and the waveguide width varies from 600 nm to 1100 nm with a step of 100 nm. The propagation loss is obtained by analyzing the intensity decay of the scattered light. The intensity is extracted from the image via Matlab software. With the knowledge of position according to the designed layout, the propagation loss is obtained by the linear fitting of the relationship between propagation distance and the logarithm of the intensity of the scattered light, see Fig. 3.21(b). For each waveguide at a given width, the loss values are measured by three times at different positions. The standard deviation of these loss values gives the error bars in Fig.3.21. The propagation losses are below 5 dB/cm for all waveguides, with a minimum value of 2.5 dB/cm at a waveguide width of 1.0 µm. This suggests that the material absorption of the AlO$_x$ layer is equal or less than 2.5 dB/cm at λ= 360 nm, much lower than the value of 7 dB/cm obtained with the AlO$_x$ layer deposited at 150 ^{o}C. More importantly, a 3 dB/cm low-loss single-mode waveguide is achieved at a waveguide width of 800 nm, indicating that the scattering loss is also lower than 1 dB/cm. Besides, no photodarkening effect has been observed with this layer at a guided power as high as 3 mW.

To further improve the processing of the AlO$_x$ waveguide and decrease the propagation loss, the layer deposition should be further improved in view of the high absorption loss of 2.5 dB/cm. In this work, TMA and H$_2$O are used as precursors for the deposition of ALD-AlO$_x$ layers. However, there are more options for precursors. The dimethylaluminum isopropoxide (DMAI, (CH$_3$)$_2$AlOCH(CH$_3$)$_2$) and O$_3$ can be the replacement of TMA and H$_2$ [28, 29]. Besides, implementing O$_2$ plasma treatment on the surface may also be one of the possible ways to improve the layer deposition, which has been demonstrated to decrease the film stress [30]. It is known from this thesis that the ALD-AlO$_x$ layer deposited at a higher temperature shows higher transparency at UV wavelengths. The reason behind this is expected to lower the level of impurity [27]. Besides, the process

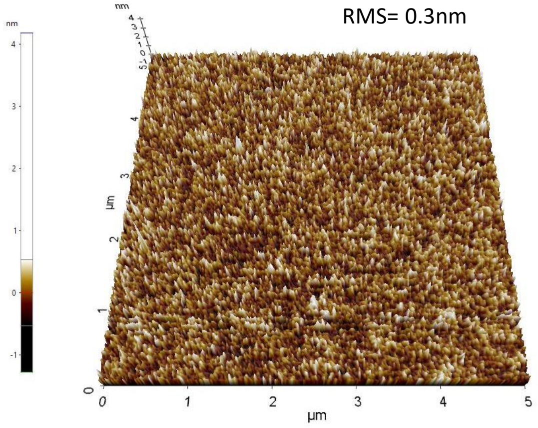

Figure 3.20: Height map of a blank ALD-AlO$_x$ layer measured by atomic force microscopy. The roughness is measured to be 0.3 nm.

of thermal reflow is expected to improve the sidewall roughness of the photoresist before implementing dry etching. This step can effectively reduce the roughness transferred from the photoresist mask to the waveguide.

3.3.3 ALD-HfO$_x$ waveguides

The ALD-HfO$_x$ waveguides are characterized by a 402-nm laser diode, using the same setup as above. Since the HfO$_x$ has a relatively higher refractive index of 2.1, a bend radius of 100 µm was chosen for spiral waveguides without introducing radiation loss. Figure 3.22(a) shows the measured scattered light from a spiral waveguide. The waveguide width of 2 µm is selected to minimize the impact of scattering at the side walls and investigate the material absorption loss. A propagation loss of 35 dB/cm is measured by analyzing the intensity decay along the waveguide. In view of their high bandgap of ∼5.5 eV, ALD-HfO$_x$ layers should have no absorption related to the direct bandgap at a working wavelength of 402 nm. The large absorption loss may be attributed to the oxygen vacancies and defects formed during the deposition [31]. The maximum output power of the continuous-wave laser in free space is 10 mW. After a continuous excitation with the 402 nm laser for a duration of 2 hours, the propagation loss of the waveguide drops to 19 dB/cm. Such an improvement may be explained by an absorption annealing effect [32]. Nevertheless, the absorption of ALD-HfO$_x$ is still too high compared to that of ALD-AlO$_x$ layers. The layer deposition has to be optimized to decrease the vacancies and defects before it can be considered as the core layer

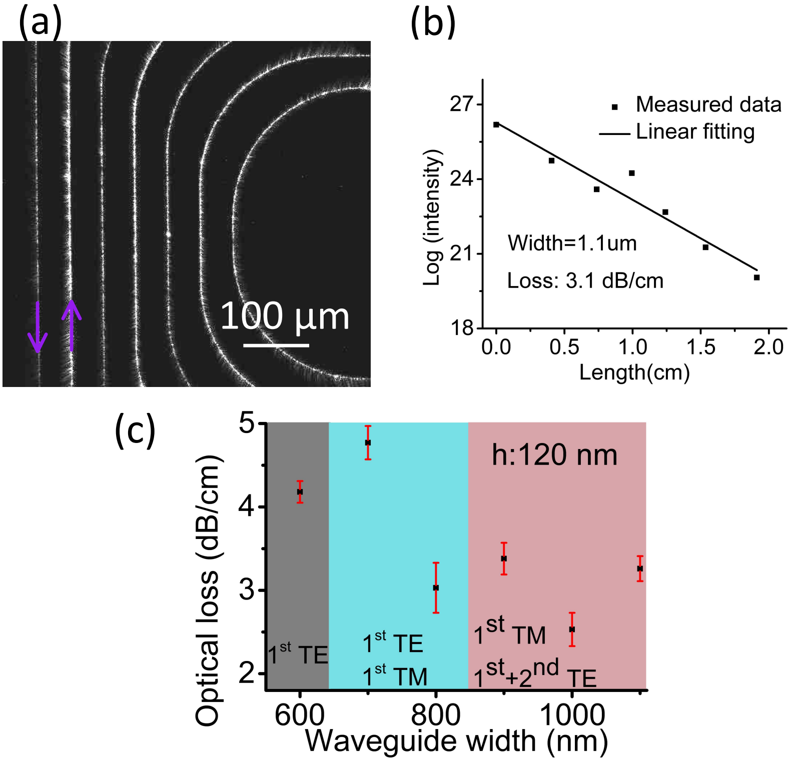

Figure 3.21: (a) Imaged of the scattered light from a part of spiral waveguide with the excitation wavelength of 360 nm. The waveguide width is 1.1 µm. (b) Linear fitting of the logarithm of the intensity of scattered light and propagation length. (c) Relationship between the propagation loss and waveguide width.

of waveguides operating at UV wavelengths. In this context, we have decided not to investigate further the ALD process of HfO$_x$ considering that the required efforts in material development were too much and that AlO$_x$ was mature enough to demonstrate relevant applications for UV-PIC.

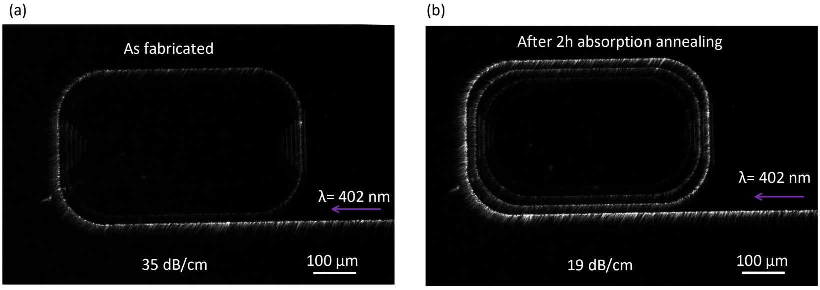

Figure 3.22: Optical image of the scattered light from the HfO$_x$ spiral waveguide (a) as deposited, (b) after a 2 hour continuous excitation of a 402 nm laser.

3.4 Conclusion

This chapter presents the investigation of two potential core layers, namely ALD-AlO$_x$ and ALD-HfO$_x$. Starting with the simulation of etch-free rib waveguides, etch-free slot waveguides, and standard strip waveguides, we have investigated the waveguide geometry which allows single-mode propagation. In view of the high bending loss of etch-free rib waveguide, the regular strip waveguide is used to study the etching process and the measured waveguide loss is used to quantify the quality of the etching process, since the scattering loss scales with the roughness of the side walls of the waveguide. The etching properties of the ALD-AlO$_x$ and ALD-HfO$_x$ are studied using the fluorine- and chlorine-based gas mixture in RIE or RIE-ICP, respectively. The chlorine-based gas mixture is demonstrated to be a better option for etching process, in terms of the volatile etching products. Next, the PECVD-SiN$_x$ as the hard mask is compared with the photoresist mask in the dry-etching of the AlO$_x$ layer. It turns out that the SiN$_x$ mask provides a larger selectivity that exceeds 1. and it is free of deformation after the dry-etching. Followed by the characterization of AlO$_x$ waveguides, I have demonstrated that the ALD-AlO$_x$ layer deposited at 300 ^{o}C shows an absorption loss of $\sim$2 dB/cm much lower than 7 dB/cm obtained by the layer deposited at 150 ^{o}C. By contrast, I have demonstrated that our current ALD-HfO$_x$ is an inappropriate material for the waveguide core layer, in view of its absorption loss as high as 19 dB/cm, which I attributed to the oxygen vacancies and defects inside the layer. Finally, my study has demonstrated that ALD-AlO$_x$ is a potentially good candidate for a UV-PIC platform. A low-loss single-mode AlO$_x$ waveguide of 3 dB/cm has been achieved, which value increases to $\sim$40 dB/cm at a shorter wavelength of 266 nm due to higher absorption and scattering loss. The platforms of single crystal AlN on sapphire and sputtering AlO$_x$ are alternative potential candidates, which still needs to be demonstrated. The multi-modal AlN/sapphire waveguide and the sputtered AlO$_x$ thin-film waveguide (with polishing) reported in literature [11, 26] exhibit a loss of 8 dB/cm at λ= 389 nm and a low loss of 0.6 dB/cm at λ= 377 nm, respectively. Nevertheless, the propagation loss of single-mode waveguides based on these platforms is expected to be higher than their current loss value due to a higher scattering loss. The technological development reported in this chapter was key to process complex optical circuits operating at a wavelength of 360 nm for imaging applications in the following chapters.

References

[1] V. V. Afanasev, M. Houssa, A. Stesmans, and M. M. Heyns. *Band alignments in metal–oxide–silicon structures with atomic-layer deposited Al2O3 and ZrO2*. Journal of Applied Physics, 91(5):3079–3084, 2002.

[2] J. Aarik, H. Mandar, M. Kirm, and L. Pung. *Optical characterization of HfO2 thin films grown by atomic layer deposition*. Thin Solid Films, 466(1-2):41–47, 2004.

[3] Robert A Meyers. *Encyclopedia of physical science and technology*. Academic, 2002.

[4] Yang Li, Haolan Zhao, Ali Raza, Stephane Clemmen, and Roel Baets. *Surface-Enhanced Raman Spectroscopy Based on Plasmonic Slot Waveguides With Free-Space Oblique Illumination*. IEEE Journal of Quantum Electronics, 56(1):1–8, 2020.

[5] Ananth Z. Subramanian, Eva Ryckeboer, Ashim Dhakal, Frédéric Peyskens, Aditya Malik, Bart Kuyken, Haolan Zhao, Shibnath Pathak, Alfonso Ruocco, Andreas De Groote, Pieter Wuytens, Daan Martens, Francois Leo, Weiqiang Xie, Utsav Deepak Dave, Muhammad Muneeb, Pol Van Dorpe, Joris Van Campenhout, Wim Bogaerts, Peter Bienstman, Nicolas Le Thomas, Dries Van Thourhout, Zeger Hens, Gunther Roelkens, and Roel Baets. *Silicon and silicon nitride photonic circuits for spectroscopic sensing on-a-chip [Invited]*. Photonics Research, 3(5):B47–B58, 2015.

[6] Toshiro Maruyama and Susumu Arai. *Aluminum oxide thin films prepared by chemical vapor deposition from aluminum acetylacetonate*. Applied Physics Letters, 60(3):322–323, 1992.

[7] O. Zywitzki and G. Hoetzsch. *Influence of coating parameters on the structure and properties of Al2O3 layers reactively deposited by means of pulsed magnetron sputtering*. Surface and Coatings Technology, 86-87:640–647, 1996.

[8] Priyanka Nayar, Atul Khanna, D. Kabiraj, S. R. Abhilash, Ben D. Beake, Yannick Losset, and Banghao Chen. *Structural, optical and mechanical properties of amorphous and crystalline alumina thin films*. Thin Solid Films, 568:19–24, 2014.

[9] K. S. Shamala, L. C. S. Murthy, and K. Narasimha Rao. *Studies on optical and dielectric properties of Al2O3 thin films prepared by electron beam evaporation and spray pyrolysis method*. Materials Science and Engineering: B, 106(3):269–274, 2004.

[10] A. Pillonnet, C. Garapon, C. Champeaux, C. Bovier, R. Brenier, H. Jaffrezic, and J. Mugnier. *Influence of oxygen pressure on structural and optical properties of Al 2 O 3 optical waveguides prepared by pulsed laser deposition*. Applied Physics A: Materials Science & Processing, 69(7):S735–S738, 1999.

[11] W.A.P.M. Hendriks M.P. Nijhuis Groen S.M. Garcia-Blanco S. Mardani, M. Dijkstra. *Low-loss chemical mechanically polished Al2O3 thin films for UV integrated photonics*. In European Conference on Integrated Optics (ECIO).

[12] M. M. Aslan, N. A. Webster, C. L. Byard, M. B. Pereira, C. M. Hayes, R. S. Wiederkehr, and S. B. Mendes. *Low-Loss Optical Waveguides for the Near Ultra-Violet and Visible Spectral Regions with Al(2)O(3) Thin Films from Atomic Layer Deposition*. Thin Solid Films, 518(17):4935–4940, 2010.

[13] Dong-Pyo Kim, Ji-Won Yeo, and Chang-Il Kim. *Etching properties of Al2O3 films in inductively coupled plasma*. Thin Solid Films, 459(1-2):122–126, 2004.

[14] Xeng Yang, Jong-Chang Woo, Doo-Seung Um, and Chang-Il Kim. *Dry Etching of Al2O3Thin Films in O2/BCl3/Ar Inductively Coupled Plasma*. Transactions on Electrical and Electronic Materials, 11(5):202–205, 2010.

[15] MicroChemicals. *www.microchemicals.com/products/photoresists*.

[16] Weiqiang Xie. *Development of passive and active integrated silicon nitride photonics*. Thesis, 2016.

[17] A. Z. Subramanian, P. Neutens, A. Dhakal, R. Jansen, T. Claes, X. Rottenberg, F. Peyskens, S. Selvaraja, P. Helin, B. DuBois, K. Leyssens, S. Severi, P. Deshpande, R. Baets, and P. Van Dorpe. *Low-Loss Singlemode PECVD Silicon Nitride Photonic Wire Waveguides for 532–900 nm Wavelength Window Fabricated Within a CMOS Pilot Line*. IEEE Photonics Journal, 5(6):2202809–2202809, 2013.

[18] Marie C. Cheynet, Simone Pokrant, Frans D. Tichelaar, and Jean-Luc Rouvière. *Crystal structure and band gap determination of HfO2 thin films*. Journal of Applied Physics, 101(5), 2007.

[19] J. Qin, F. Huang, X. Li, L. Deng, T. Kang, A. Markov, F. Yue, Y. Chen, X. Wen, S. Liu, Q. Xiong, S. Semin, T. Rasing, D. Modotto, R. Morandotti, J. Xu, H. Duan, and L. Bi. *Enhanced Second Harmonic Generation from Ferroelectric HfO2-Based Hybrid Metasurfaces*. ACS Nano, 13(2):1213–1222, 2019.

[20] M. Y. Ho, H. Gong, G. D. Wilk, B. W. Busch, M. L. Green, P. M. Voyles, D. A. Muller, M. Bude, W. H. Lin, A. See, M. E. Loomans, S. K. Lahiri, and Petri I. Räisänen. *Morphology and crystallization kinetics in HfO2 thin films grown by atomic layer deposition.* Journal of Applied Physics, 93(3):1477–1481, 2003.

[21] Jun-Dao Luo, He-Xin Zhang, Zheng-Ying Wang, Siang-Sheng Gu, Yun-Tien Yeh, Hao-Tung Chung, Kai-Chi Chuang, Chan-Yu Liao, Wei-Shuo Li, Yi-Shao Li, Kai-Shin Li, Min-Hung Lee, and Huang-Chung Cheng. *Improvement of ferroelectric properties in undoped hafnium oxide thin films using thermal atomic layer deposition.* Japanese Journal of Applied Physics, 58(SD), 2019.

[22] Lin Sha, Ragesh Puthenkovilakam, You-Sheng Lin, and Jane P. Chang. *Ion-enhanced chemical etching of HfO2 for integration in metal–oxide–semiconductor field effect transistors.* Journal of Vacuum Science & Technology B: Microelectronics and Nanometer Structures, 21(6), 2003.

[23] Gavin N. West, William Loh, Dave Kharas, Cheryl Sorace-Agaskar, Karan K. Mehta, Jeremy Sage, John Chiaverini, and Rajeev J. Ram. *Low-loss integrated photonics for the blue and ultraviolet regime.* APL Photonics, 4(2):026101–7, 2019.

[24] A. Layadi, A. Vonsovici, R. Orobtchouk, D. Pascal, and A. Koster. *Low-loss optical waveguide on standard SOI/SIMOX substrate.* Optics Communications, 146(1-6):31–33, 1998.

[25] S. Huang, M. Li, S. M. Garner, M. J. Li, and K. P. Chen. *Flexible photonic components in glass substrates.* Opt Express, 23(17):22532–43, 2015.

[26] Xianwen Liu, Alexander W. Bruch, Zheng Gong, Juanjuan Lu, Joshua B. Surya, Liang Zhang, Junxi Wang, Jianchang Yan, and Hong X. Tang. *Ultra-high-Q UV microring resonators based on a single-crystalline AlN platform.* Optica, 5(10):1279–1283, 2018.

[27] Oili M. E. Ylivaara, Xuwen Liu, Lauri Kilpi, Jussi Lyytinen, Dieter Schneider, Mikko Laitinen, Jaakko Julin, Saima Ali, Sakari Sintonen, Maria Berdova, Eero Haimi, Timo Sajavaara, Helena Ronkainen, Harri Lipsanen, Jari Koskinen, Simo-Pekka Hannula, and Riikka L. Puurunen. *Aluminum oxide from trimethylaluminum and water by atomic layer deposition: The temperature dependence of residual stress, elastic modulus, hardness and adhesion.* Thin Solid Films, 552:124–135, 2014.

[28] Wontae Cho, Kiwhan Sung, Ki-Seok An, Sun Sook Lee, Taek-Mo Chung, and Yunsoo Kim. *Atomic layer deposition of Al2O3 thin films using dimethylaluminum isopropoxide and water*. Journal of Vacuum Science & Technology A: Vacuum, Surfaces, and Films, 21(4):1366–1370, 2003.

[29] D. L. Caballero-Espitia, E. G. Lizarraga-Medina, H. A. Borbon-Nuñez, O. E. Contreras-Lopez, H. Tiznado, and H. Marquez. *Study of Al2O3 thin films by ALD using H2O and O3 as oxygen source for waveguide applications*. Optical Materials, 109, 2020.

[30] S. , A. Bingel, P. Munzert, L. Ghazaryan, C. Patzig, A. Tunnermann, and A. Szeghalmi. *Mechanical, structural, and optical properties of PEALD metallic oxides for optical applications*. Appl Opt, 56(4):C47–C59, 2017.

[31] A. S. Foster, F. Lopez Gejo, A. L. Shluger, and R. M. Nieminen. *Vacancy and interstitial defects in hafnia*. Physical Review B, 65(17), 2002.

[32] Semyon Papernov, Alexei A. Kozlov, James B. Oliver, Terrance J. Kessler, Alexander Shvydky, and Brenda Marozas. *Near-ultraviolet absorption annealing in hafnium oxide thin films subjected to continuous-wave laser radiation*. Optical Engineering, 53(12), 2014.

4

UV-PICs for structured illumination microscopy

4.1 Introduction

In the previous chapter, we developed the photonic integrated waveguides operating at UV wavelengths, which can benefit many fields including quantum information [1], quantum computing [2], biosensing, [3] and microscopy [4]. In the context of biological and chemical sensing, the UV wavelength range is particularly interesting as most of the biological and chemical molecules exhibit strong absorption in this range. A large fraction of these molecules, among others the three amino acids, tryptophan, tyrosine, and phenylalanine, and the nicotinamide adenine dinucleotide (NADH) coenzyme also provide fluorescence, which could be used advantageously for implementing label-free super-resolved microscopy techniques [5]. UV super-resolved microscopy techniques are still in their infancy, awaiting a technological breakthrough to allow their widespread use. One of the challenges facing standard UV bulk optics to achieve this goal is the lack of low-cost and aberration-free imaging lenses combining good transmission and high numerical aperture at UV and visible wavelengths. Moreover, shaping and steering UV beams is crucial, in particular for structured illumination microscopy, which is generally implemented with spatial light modulators (SLM) or digital micro-mirror devices (DMD), but only at wavelengths larger than 365 nm [6–9]. Photonic integrated circuits offer robust, compact, and low-cost solutions for implementing complex optical functions that are hardly achievable at the same level of performance as standard bulk optics [10]. In particular, bulk optics cannot compete with the large-scale manufacturing capabilities offered by silicon photonics platforms [11, 12]. This chapter presents a UV-PIC-based label-free super-resolved SIM technique, making use of a photonic integrated circuit and being the first application of the developed alumina UV photonic integration platform. We start discussing the design of the integrated optical circuits which includes beam splitters, adiabatic tapers, grating out-couplers, and thermal phase shifters. Next, I describe the fabrication and the optical characterization of the performance of the photonic chip. Finally, I demonstrate that the UV-PIC can be advantageously implemented for super-resolved structured illumination microscopy with homemade objects and biological cells.

4.2 Design of UV-PICs for structured illumination microscopy

The design of UV-PICs is carried out by simulating each optical component in the Lumerical software and the COMSOL software. The simulation of the grating coupler is simulated by the 2D-FDTD method. The Eigen mode expansion (EME) method is ideal for simulating light propagation over long distances, which is chosen to simulate adiabatic taper and multi-mode interferometers (MMI). The heater design involves multi-physics of optics and thermodynamics, which is simulated in COMSOL. All the optimized components are gathered together in a single layout and connected by low-loss waveguides. The layout drawing is carried out using Ipkiss 3.1.3 (Luceda). The waveguide width and height are designed to be $\sim$800 nm and 120 nm respectively, which supports single-mode propagation and inhibits multi-mode propagation.

4.2.1 Design of integrated photonic components necessary for SIM

To describe a structured illumination pattern, parameters such as phase, illumination orientation, and spatial frequency should be known. As presented in Chapter 2, all the parameters of the structured illumination pattern need to be precisely estimated, in order to reconstruct a super-resolved image properly. That is why the photonic integrated circuit should include several components with different optical functionalities and these components are connected by low-loss single-mode waveguides. The optical components necessary to achieve a useful structured illumination will be described in this section, including adiabatic tapers, grating out-couplers, and MMI 1x2 beam splitters.

4.2.1.1 multi-mode interferometer 1x2 beam splitters

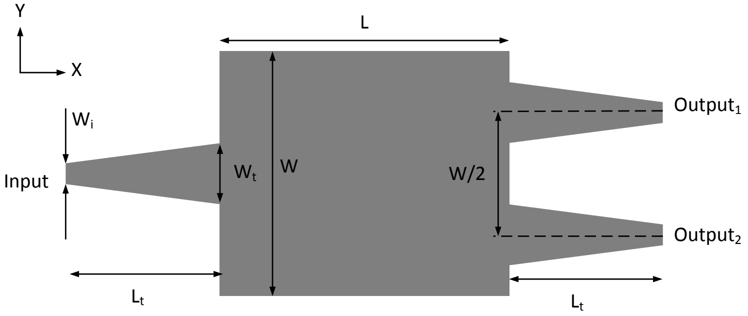

Figure 4.1: General geometry of a multi-mode interferometer (MMI). L: MMI length, W: MMI width, W_i: input waveguide width, W_t: expanded taper width.

The purpose of using 1x2 beam splitters in photonic circuits is to split the coupled light into two paths with a given split ratio, which needs to be 50:50 for the current application. Since the visibility of the interference fringe is given by $\frac{2\sqrt{I_1 I_2}}{I_1+I_2}$, any imbalance of the intensity between two output beams will lead to a decrease of the visibility. In silicon photonic platforms, there are two common solutions for 1x2 beam splitters, namely directional couplers (DC) and multi-mode interferometers. Directional couplers allow the guided light to couple between two adjacent waveguides via an evanescent field ideally without introducing insertion loss. However, the actual split ratio is very sensitive to any deviation of the waveguide width or of the spacing between the waveguides, resulting from residual errors intrinsic to the fabrication. Therefore, multi-mode interferometers are chosen for a robust beam split ratio, although the variation of the geometry will lead to extra optical loss. As its name suggests, the mechanism behind the MMI is the interference process between the guided modes. A schematic of a 1x2 MMI beam splitter is shown in Fig. 4.1. The 1x2 MMI is designed to be symmetric with respect to the Y axis. At the input, the routing single-mode waveguide is expanded from 0.8 µm to W_t= 1.4 μm over a length L_t= 10 µm, to maximize the coupling efficiency between the waveguide and beam splitter. The dimensions of the MMI are first estimated with the analytical solution as a starting point and then more accurately determined with a numerical method. In the MMI waveguide, The lateral wavenumber k_{ym} and propagation constant β_m are determined by the effective MMI width W_e and refractive index n_{co} of the waveguide, as follows:

$$k_{ym}^2 + \beta_m^2 = k_o^2 n_{co}^2 \tag{4.1}$$

Where $k_{ym} = \frac{(m+1)\pi}{W_e}$, k_0 is wave vector in free space given by $\frac{2\pi}{\lambda_0}$, and m is the order of the guided mode. Since the term, $k_{ym}^2 \ll k_o^2 n_{co}^2$, the propagation constant of a given order of mode is approximated by:

$$\begin{aligned}\beta_m &= \sqrt{k_o^2 n_{co}^2 - k_{ym}^2}\\ &\simeq k_0 n_{co} - \frac{(m+1)^2\pi\lambda_0}{4n_{co}W_e^2}\end{aligned}$$

We define L_π as the beating length of the two lowest-order modes supported by the multi-mode waveguides:

$$L_\pi = \frac{\pi}{\beta_0 - \beta_1} \approx \frac{4n_{co}W_e^2}{3\lambda} \tag{4.2}$$

where β_0 and β_1 are the propagation constants of the two lowest-order modes, n_{co} is the refractive index of the core layer, W_e is the effective width of the MMI taking into account the evanescent field and λ is the working wavelength. The W_e is approximated by the designed width of MMI W, since the penetration depth is much smaller than the designed waveguide width. Assuming no radiative mode is excited, the input mode profile Φ_0 excites the multiple guide modes $\Phi_m(0)$ with a given coupling efficiency C_m: $\Phi_0 = \sum_m C_m\Phi_m(z)$. At a given propagation distance L, the superposition of the mode profile can be written as:

$$\begin{aligned}\Phi_0 &= \sum_m C_m\Phi_m(z)e^{j(\beta_0-\beta_m)L} \qquad (4.3)\\ &= \sum_m C_m\Phi_m(z)e^{j(\frac{m(m+2)\pi}{3L_\pi})L} \qquad (4.4)\end{aligned}$$

It is clear that the profile of the field will be reproduced when the phase term $e^{j\frac{m(m+2)\pi}{3L_\pi}L} = 1$, $i.e.$ at a propagation length $L = 3nL_\pi$ with $n = 0, 1, 2, ...$ At half of this length $L = \frac{3nL_\pi}{2}$, a pair of mirrored images can be founded [13]. This is the optimum length used for 1x2 beam splitters. When the input is positioned in the center along the Y-axis, the odd modes are not excited and $C_m = 0$ (m=1,3,5,...) so the length of MMI can be four times shorter to make the phase term equal to zero. In this way, a 1x2 50:50 MMI beam splitter with a centered input can be obtained at a length L given by:

$$L = \frac{3L_\pi\pi}{8} \tag{4.5}$$

For a given width W of 8 µm, the 1x2 MMI length is estimated to be 149 µm. Next, we sweep the length around this value and monitor the output power with the EME method.

The fundamental TE mode is injected at the input port. As the two outputs are expected to share the same amount of power, the normalized intensity here shows the power recorded at one of the outputs. The simulated evolution of the normalized intensity versus the MMI length reveals that the peak coupling efficiency reaches a maximum of 0.49 at a length L= 133 µm, see Fig. 4.2(a). With the optimized geometry, the intensity profile of the guided light in the MMI shows two balanced outputs, see Fig. 4.2(b), which shows that the MMI length L= 133 µm is the shortest length to achieve simultaneously a split ratio of 50:50 and a low insertion loss, with a waveguide width W= 8µm, a taper width W_t= 1.4 µm, and a taper length L_t= 10 µm.

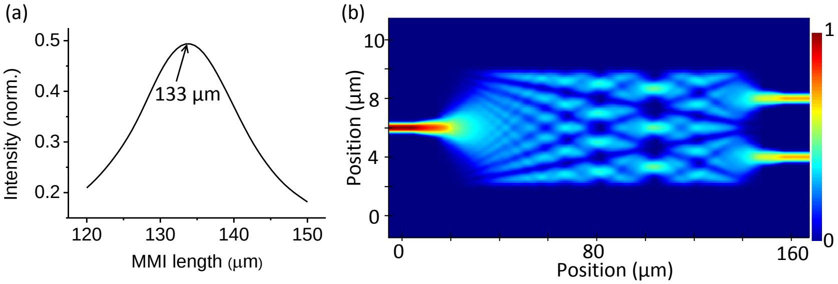

Figure 4.2: (a) Relationship between the normalized intensity at one of the outputs and the MMI length. (b) Intensity profile of the interference pattern inside the optimized MMI. MMI length L= 133 µm. The color bar is in a linear scale.

4.2.1.2 Low-loss adiabatic tapers

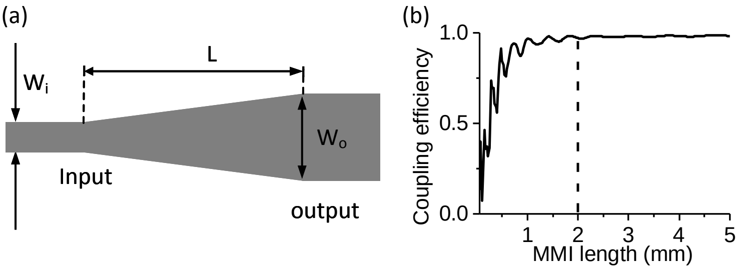

Figure 4.3: (a) General geometry of an adiabatic taper. L: taper length, W_i: input waveguide width, W_o: expanded waveguide width. (b) Relationship between the normalized intensity of the fundamental TE mode at the output and the length of MMI.

In photonic circuits, adiabatic tapers are used to gradually expand or scale down waveguides in width, simultaneously keeping light propagating in the same mode at the input and output. The device is expected to be as compact as possible without introducing extra insertion loss. Here, two adiabatic tapers are designed, one for expanding the single-mode waveguide width to match a 20 µm-wide grating out-coupler used for illuminating an object and another one for scaling down a 3 µm-wide waveguide to single-mode waveguide width. The typical schematic of adiabatic tapers is shown in Fig. 4.3(a). The length is optimized by using the EME method with the Lumerical software. The thickness of the AlO_x layer is set to 120 nm. Generally, the minimum length of an adiabatic taper scales with the index contrast between the waveguide core and cladding. In view of the relatively low index of ALD-AlO_x $\sim$1.69, the taper length L is swept from 50 µm to a relatively long length of 5 mm. The relationship between the normalized intensity of the fundamental TE mode at the output and the length of adiabatic tapers is simulated and plotted in Fig. 4.3(b). The transmitted power increases with increasing length and saturates around a length of 2 mm. In view of the trade-off between the loss and compactness, I have chosen a length of 1 mm corresponding to a transmittance of $\sim$96%.

The width of the single-mode waveguide is as narrow as 800 nm, while the mode profile of single-mode fibers (SM300, Thorlabs) is as large as $\sim$2.0-2.4 µm at an operating wavelength of 350 nm according to the manufacture [14]. This implies that a large coupling loss appears in a butt coupling configuration due to the mode profile mismatch between the fiber and waveguide. In this context, larger waveguide widths are designed at the input in order to match better the mode profile of SM fibers at least in the direction coplanar with the chip.

To optimize the width of the input waveguide, I used FDTD simulation with the model in Fig. 4.4(a). In view of the previous simulation, the insertion loss of an adiabatic taper is negligible when the length is sufficiently long, $i.e.$ larger than 3 mm in our case. Therefore, no adiabatic taper is not included in this simulation. Here, I assume the fundamental TE mode of an expanded waveguide can be converted to the fundamental TE mode of a single-mode waveguide without introducing an extra loss. The refractive indexes of the fiber core and cladding are set to be 1.475 and 1.472, respectively. The diameter of the fiber core is set to be 2.2 µm, which approximately matches the mode profile of the UV single-mode fiber. The fundamental TE mode of the SM fiber is used as the input source. The normalized power coupled to the fundamental TE waveguide mode, namely the coupling efficiency, increases from 0.14 to 0.25 ($\sim$ 6 dB) for a waveguide width increasing from 0.80 µm to 3.75 µm but slightly decreases with a waveguide width beyond 3.75 µm, see Fig.4.4(b). By expanding the waveguide width at the input, the coupling efficiency is almost doubled. The improvement of the coupling efficiency is attributed to a better overlap between the fundamental TE modes in the fiber and waveguide, while the decrement at widths beyond 3.75 µm may be caused by the increment of the number of higher-order modes.

Using the adiabatic taper, we are able to not only maximize the coupling between a single-mode fiber and an integrated waveguide but also keep the single-mode propagation of expanded waveguides. The single-mode propagation is the key to allow grating out-couplers to scatter beams at only one angle and maximize the radiation intensity.

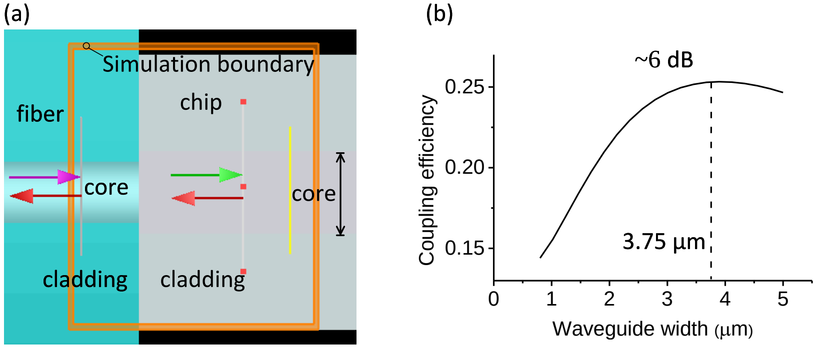

Figure 4.4: (a) Model of the butt coupling between a cleaved SM fiber and an AlO$_x$ waveguide. (b) Relationship between the coupling efficiency and waveguide width.

4.2.1.3 High-radiance and large-FoV grating out-couplers

Grating out-couplers are used to couple the on-chip guided light to a far-field beam and in our case to generate structured illuminations. To couple on-chip guided modes with a specific mode propagating in free space with a wavevector $\vec{k}_{out}$, the phase matching condition needs to be fulfilled, in particular for a grating of pitch Λ:

$$\vec{k}_{out} = \vec{k}_{in} \pm p\vec{G}, \;\; p \in \mathbb{Z} \tag{4.6}$$

where p is an integer, $\vec{G}$ is the grating vector given by $\frac{2\pi}{\Lambda}$. The wave vector of the guided mode $\vec{k}_{in}$ is related to the effective refractive index n_{eff} of the guided mode by

$$\vec{k}_{in} = n_{eff}\frac{2\pi}{\lambda_{ex}}\vec{j} \tag{4.7}$$

where λ_{ex} is the excitation wavelength and $\vec{j}$ is a unit vector in the direction of the mode propagation. To achieve a high coupling efficiency in a unique specific scattering angle, the grating out-coupler is designed to couple only the negative 1^{st} diffracted order into the free space. It follows that the scattering angle θ is given by:

$$sin(\theta) = n_{eff} - \frac{\lambda_{ex}}{\Lambda} \tag{4.8}$$

where θ is the angle between the $\vec{k}_{out}$ and the axis perpendicular to the chip surface. Instead of specifying the angle, we will use later the numerical aperture NA$_{ex}$

to specify the illumination beam. As the numerical aperture of the excitation beam is defined by $NA_{ex} = n \cdot sin(\theta)$ and in free space n= 1, it is directly linked to the grating parameters via:

$$NA_{ex} = \frac{\lambda_{ex}}{\Lambda} - n_{eff} \tag{4.9}$$

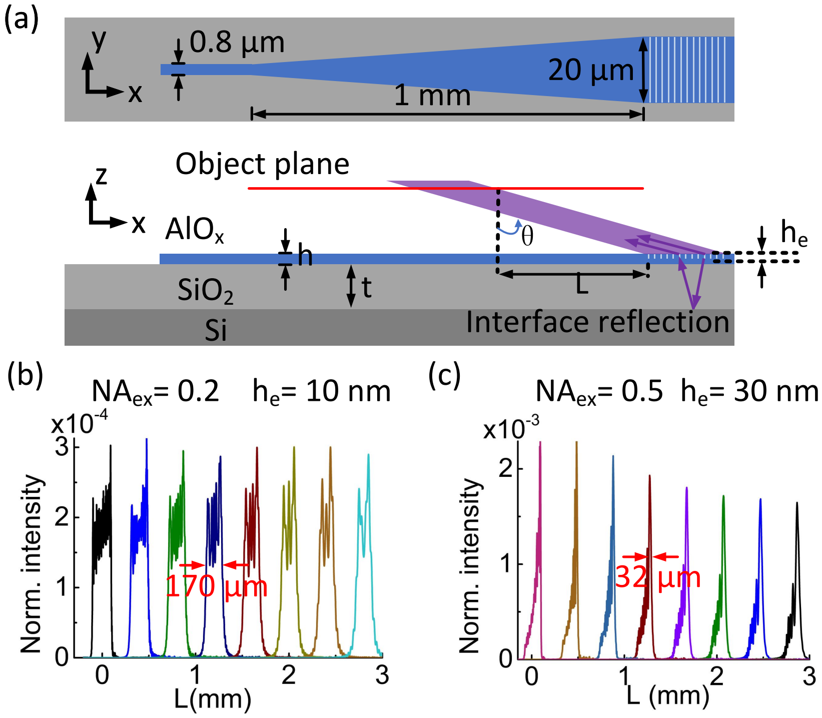

Figure 4.5: (a) Schematic of AlO$_x$ grating out-couplers on a SiO$_2$/Si substrate. (b-c) Evolution of the intensity profile of diffracted beams over the projection of the propagation distance L, in the case of p= 180 nm, h_e= 10 nm and p= 210 nm, h_e= 30 nm, respectively.

Each grating out-coupler is patterned on a 20 µm-wide alumina waveguide that is connected to a 0.8 µm-wide single-mode waveguide via an adiabatic taper of length 1 mm. The taper allows that only the fundamental TE mode is propagating in the corrugated waveguide. In the case of λ_{ex}= 360 nm and an alumina film thickness h= 120 nm, the mode effective index n_{eff} of the fundamental Bloch mode propagating in the corrugated waveguide has a value of ∼1.5, which is simulated by using a finite difference eigenmode solver (MODE, Lumerical). In this thesis, three gratings with different grating pitch Λ of 210 nm, 180 nm, and 150 nm were designed with 1000-grating periods, in order to target numerical aperture values NA_{ex} of 0.2, 0.5, and 0.9, respectively. The gratings are formed by partially etching the waveguide with a depth h_e of either 10 nm or 30 nm, which generates weak modulations on the waveguide and allows large-FoV of the diffracted beams. The 2D-FDTD method was used to simulate the beam profile diffracted by the gratings. Figure 4.5(a) shows the schematic of the grating coupler made of ALD-AlO$_x$ on top of a SiO$_2$/Si substrate. The thickness t of buried oxide (BOX) SiO$_2$ is set to 3 µm. To minimize scattering loss induced by mode-mismatch at the input of gratings, the fill factor f of 0.75 was chosen. Each grating is designed: 1) to diffract only one mode in the far field with a desired numerical aperture $NA_{ex} = n \cdot sin(\theta)$, 2) to minimize the divergence of the diffracted beam, 3) to provide a far-field field pattern as homogeneous and wide as possible, and 4) to optimize the coupling efficiency from chip to free space. The intensity profile of the diffracted beam in the far field must be monitored during the simulation, in order to achieve a beam with a large FoV and good homogeneity. The object plane is generally several millimeters above the photonic chip, which implies that we need to simulate the beam propagation of the diffracted light in mm-scale. However, a large simulation area will consume a lot of computation energy with FDTD and lead to a long simulation time. Alternatively, instead of simulating the whole field, the model is designed and built to record the distribution of the complex electric field ($\vec{E}$) of the diffracted beam at a plane 1-µm above the grating coupler. Knowing the field profile of the diffracted beam at a given position of the free space, its field profile at any position along the propagation can be recovered using the far-field projection method [15]. Here, I use the distance L to describe the propagation length of the diffracted beam along x-axis, which in the following sections corresponds to the spacing between grating pairs used to generate structured illumination patterns in the far-field. Figures 4.5(b) and (c) show the relationship between the beam profile and the distance L at a numerical aperture of 0.2 and 0.5, respectively. On the one hand, the grating with a etch depth h_e= 10 nm exhibits a much lower divergence than of h_e= 30 nm, due to the longer effective grating length provided by the weaker coupling efficiency. Increasing the propagation length from 0.7 mm to 2.7 mm, the full-width-at-half-maximum (FWHM) of the intensity profiles varies from 190 µm to 160 µm and from 23 µm to 41 µm, for the etching depth of 10 nm and 30 nm respectively. On the other hand, the deeper etched gratings exhibit higher coupling efficiencies or radiant intensities, see Fig. 4.6. As depicted in Fig. 4.5(a), the beam diffracted towards the substrate will be partially reflected back at the interface of the BOX layer and the silicon substrate. As the index contrast is larger than 5 at the working wavelength of 360 nm, about 40$\%$ of the light will be reflected back and interfere with the light directly diffracted in the opposite direction of the silicon substrate. As a consequence, the phase difference between these two beams, which is given by the BOX thickness and the scattering angles, will have an impact on the output power value. As shown in Fig. 4.6(a), the coupling efficiency oscillates at a period of ~61 nm, which approximately matches the result of 53 nm obtained by using geometry optics. In the case of h_e= 10 nm and p= 210 nm, the coupling efficiency varies dramatically from 0.02 to 0.42 with the BOX thickness ranging from 2.95 μm to 3.05μm, see Fig. 4.6(a). A deeper etch depth of 30 nm shows a higher coupling efficiency of up to 0.73. A similar maximum coupling efficiency is observed in the case of p= 180 nm, see Fig. 4.6(b). Ideally, the BOX thickness should be optimized to maximize the coupling efficiency according to a given diffraction angle of grating couplers during the process, but it must be done before the deposition of ALD AlO_x. Considering the deposition of ALD-AlOx is quite time-consuming, the optimization of BOX thickness has not been done in this thesis. Although the target BOX thickness is 3μm on $\mathrm{SiO_2}$/Si wafers, the actual value varies from wafers to wafers with an accuracy of ~ ±50 nm, which leads to the variation of radiant intensity of grating out-couplers from samples to samples.

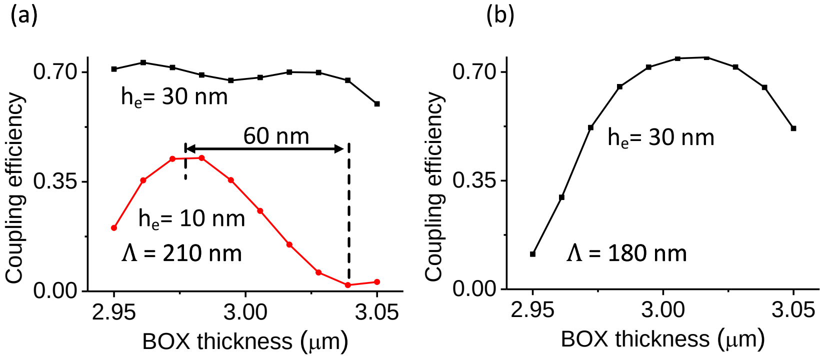

Figure 4.6: Evolution of the coupling efficiency of grating out-couplers over the thickness of buried $\mathrm{SiO_2}$. (a) Grating pitch Λ= 210 nm, h_e= 10 nm and 30 nm, (b) p= 180 nm and h_e= 30 nm.

As shown in Fig. 4.5(b) and (c), the beam profiles are not perfectly homogeneous inside the FoV. In addition to the homogeneity of the beam profile, the visibility of interference fringe patterns is another important factor for structured illumination. The schematic of the concept to generate structured illumination in the far field is shown in Fig. 4.7, using a pair of grating out-couplers. Since the model is too large to be simulated efficiently with FDTD, the interference pattern is investigated with the far-field projection method. One of the diffracted beams is determined with FDTD and flipped around the symmetry axis of the photonic structure to generate the second beam. The intensity of the interference fringe pattern is then obtained by taking the modulus square of the superposition of these two light fields. As shown in Fig. 4.7(a) and (b), the visibility of the interference pattern is as high as 0.97 and 0.99 for the grating of p= 180 nm and p= 210 nm, respectively, despite slight intensity variation inside the FoV.

The oscillation features in the beam profile are attributed to the short propagation distance in the far field. As the grating aperture is designed to be $\sim$200 μm long, the object plane is expected to be located at a position corresponding to a transition between the Fresnel and Fraunhofer diffraction regimes. A uniform pattern can be achieved by increasing the spacing between the grating pairs in order to increase the propagation length at a given angle or by decreasing the grating length. The first case requests a larger circuit footprint that is more challenging to fabricate. The second case leads to a smaller FoV, which is less interesting for imaging applications like SIM.

Here, I have optimized the design of grating out-couplers and achieved structured illumination patterns in the far field with a large enough FoV and high visibility, which are essential to implement the UV-PIC-based SIM technique. Next, we need to adjust the phase of structured illumination patterns. One of the solutions is the on-chip thermal phase shifter, which will be investigated in the next subsection.

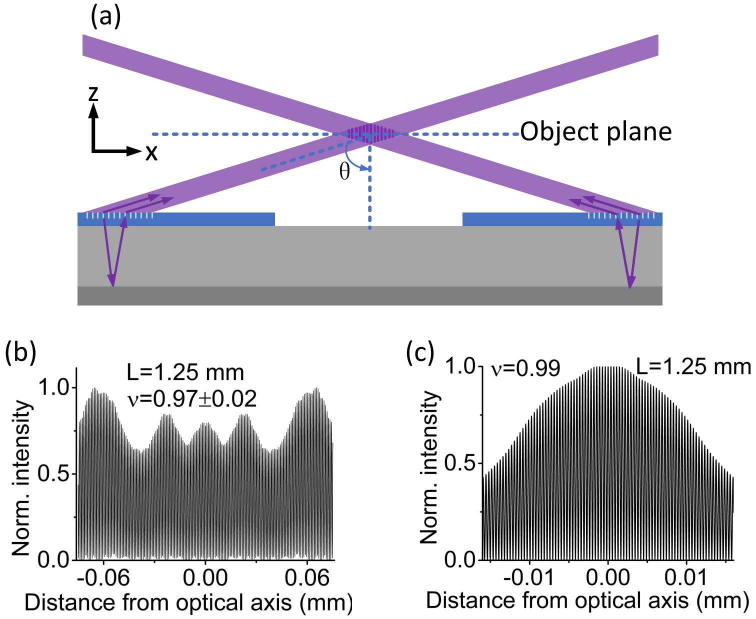

Figure 4.7: (a) Schematic of a grating out-coupler pair for the generation of structured illumination. (b-c) Simulated interference fringe patterns in the cases of p= 210 nm, h_e= 10 nm and p= 180 nm, h_e=30 nm, respectively.

4.2.1.4 Thermal phase shifter

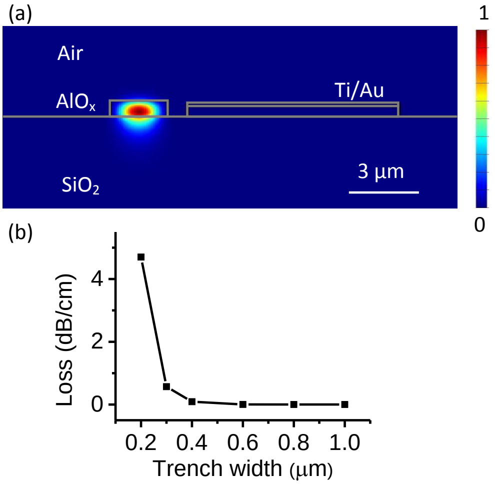

Figure 4.8: (a) Mode profile of single-mode AlO_x *waveguide adjacent to a thermal heater. The gap width is 300 nm. (b) Relationship between the absorption loss of* AlO_x *waveguides and gap width.*

On-chip thermal phase shifters are widely used in photonic integrated circuits, for tuning the phase of the guided mode based on the thermo-optic effect. Compared to other methods, the easiest way to locally change the refractive index of the amorphous AlO_x waveguide is thermal tuning. Applying electric injection to the thermal phase shifter will locally heat up the adjacent waveguide and change the refractive index of the material. The thermo-optic coefficient of ALD-AlO_x has been reported to be as low as 1.68 x 10^{-5} RIU/^{o}C in the literature [16]. In order to achieve a 2π phase shift, the effective index of the guided waveguide mode has to be varied by 3.6 x 10^{-4} RIU for a propagation length of 1 mm, which implies a temperature shift of 21.4 ^{o}C. The thermal phase shifter is designed on the side of the waveguide since the alumina platform has an air top-cladding currently. The gap width between the AlO_x waveguide and the heater is designed as small as possible to minimize the absorption loss induced by metals. The heater is made of 80 nm thick Titanium (Ti) and 20 nm gold (Au) with a width of 3 µm. The Ti layer is first deposited on top of the sample in view of its better adhesiveness. Figure 4.8(a) shows the mode profile of the AlO_x waveguide with a gap width set to 300 nm. The fundamental TE mode is well confined inside the AlO_x. The relationship between the gap width and absorption loss of the waveguide is simulated by the MODE solution in Lumerical and plotted in Fig. 4.8(b). With a gap width larger than 0.6 µm, the absorption loss introduced by the thermal heater is negligible. However, efficient heating of the waveguide requires the smallest possible gap. Taking into account the precision of the overlay in E-beam lithography ($\sim$ 200 nm), a gap width of 1 µm is chosen in the circuit design.

I have simulated the heat transfer of thermal heaters with finite element analysis in 2D using the COMSOL5.4 software. The temperature map of the model is shown in Fig. 4.9. With an applied power of 170 W, the heater temperature increases from room temperature 293 K to 358 K, which heats up the waveguide to 315 K to an increment of 22 ^{o}C. In the 2D model, the length of the structures is simulated with a unit of length, which is given in meters (m). The consumed electric power will be 170 mW to heat up the metal stack over a length of 1 mm, which results in a 2π-phase shift to the AlO$_x$ waveguide. Such as $P_{2\pi}$ is relatively high, mainly due to the low thermo-optic coefficient of AlO$_x$. To further improve the efficiency of thermal phase shifters, one possible approach is to undercut the heaters and the waveguides [17].

We have completed the design of all the optical components necessary to achieve PIC-based structured illumination in the far field. Next, I will design photonic circuits to place the optical components in the proper positions according to their functionalities and use low-loss single-mode waveguides to connect these components without crossing.

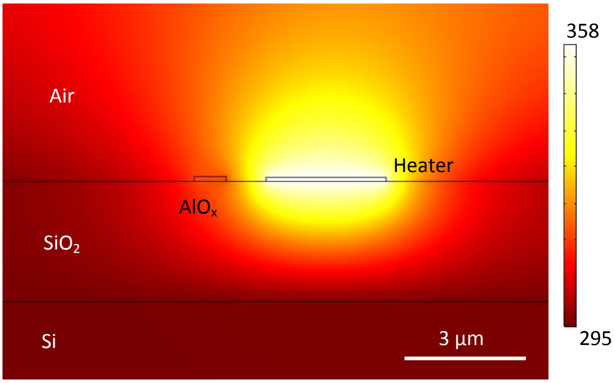

Figure 4.9: Temperature map of an on-chip thermal phase shifter on a SiO$_2$/Si substrate. The electric power applied on the phase shifter is 170 W in the 2D model. Gap width = 1 µm.

4.2.2 Layout design of UV-PICs for SIM

Our photonic integrated circuits combine all the previously optimized components together by connecting them with single-mode waveguides. This allows us to integrate complex optical functionalities on a single chip. One of our circuits is designed to experimentally highlight the physics behind structured illumination microscopy. This circuit is as simple as possible by using only one orientation of structured illuminations. The other one is designed for label-free super-resolved two-dimensional imaging in particular of biological cells. The respective layouts of the design are presented in Figures 4.10(a) and (b). In Fig. 4.10(a), a UV laser operating at a wavelength of 360 nm is coupled to the lead-in single-mode waveguide. The guided mode is split into two paths via the 1x2 MMI beam splitter with a split ratio of 50:50. Then, the waveguide is expanded from 0.8 µm to 20 µm via a 1 mm-long adiabatic taper before the light is coupled to free space at a given angle. The gratings are placed opposite to each other with an angle of 180 degrees, to maximize the spatial frequency of the structured illumination. The spacing between the gratings is set to 2.5 mm. The phase of the structured illumination pattern, $i.e.$ the phase difference between two diffraction beams, is controlled by a 1 mm-long thermal phase shifter which is placed beside the adiabatic taper with a gap width of 3 µm.

In Fig. 4.10(b), the design for 2D structured illumination is made of three individual photonic circuits for a total footprint of $\sim$5 mm by 5 mm. Each circuit generates a structured illumination in one specific direction and at a given orientation. The circuits are designed with no crossing between the waveguides to avoid any cross-talk between circuits. The paths split by each MMI have the same total length for all individual circuits, which keeps the propagation loss of all the guided modes at the same level before being diffracted by the grating out-couplers and maximizing the visibility of the interference fringe pattern. The lead-in waveguide has a waveguide width of 3 µm and is tapered down to 0.7 µm, with a taper length of 3 mm. The total length of the thermal heater is 700 µm for each circuit, which is placed 1 µm away from the edge of the waveguide. The spacing between the grating pairs is 2.8 mm.

These layout designs are generated by using the Ipkiss software (Luceda) and used as the patterns to define the exposure area in e-beam lithography during the fabrication of UV-PICs.

4.3 Fabrication of UV-PICs for SIM

The designed UV-PICs are fabricated on the alumina platform that we have developed in our cleanroom at UGent. Three different mask layers in the previous design are processed one after another one, including the full etching of AlO_x layers, shallow etching of the grating coupler, and lift-off of thermal phase shifters, respectively.

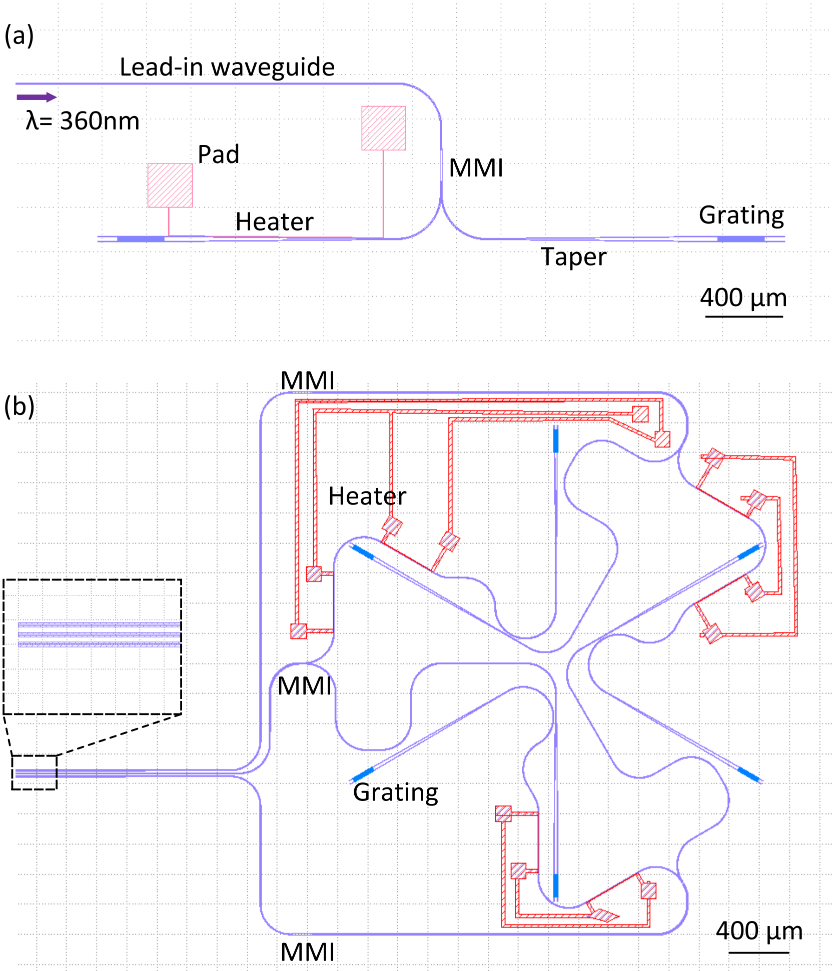

Figure 4.10: Layout design of the UV-PIC for (a) one-dimensional super-resolved structured illumination microscopy. (b) two-dimensional super-resolved structured illumination microscopy.

4.3.1 Patterning routing photonic circuits on ALD-AlO$_x$ layers

The first layer in the design is used to fully etch the AlO$_x$ layer deposited by the ALD technique, to form the single-mode routing waveguides, the adiabatic tapers, and the MMI 1x2 beam splitters. The process starts with the cleaning of a 4-inch SiO$_2$/Si wafer in a standard way (acetone, IPA, and DI water), followed by a 15-min oxygen plasma in an instrument (Tepla). Then, the wafer is packaged inside a wafer box and transferred to the Cocoon group at UGent. Since the ALD reactor is built in the open air outside a cleanroom environment, the clean wafer suffers from contamination once the package box is opened. Therefore, it is necessary to do another 15 minutes of oxygen plasma again after opening the box and loading the sample into the ALD reactor, which minimizes the impact of the contamination by the dust particles. Using the atomic layer deposition with TMA and water precursors, a 120 nm-thick AlO$_x$ is grown at a substrate temperature of 300 ^{o}C. Next, the wafer is transferred back to the UGent cleanroom and carefully cleaned successively with via acetone, IPA, and DI water, before being loaded in the PECVD instrument for growing a 100 nm-thick hard mask of MF/LF SiN$_x$. The deposition of the hard mask is carried out with a gas mixture of SiH$_4$, NH$_3$, and N$_2$ as precursors at a substrate temperature of 270 ^{o}C. The wafer is then cleaved into small pieces of 2.5 cm by 2.5 cm, and each piece is cleaned in an ultrasonic water bath for 10 minutes to remove large particles on the surface and with 15 minutes-O$_2$ plasma to remove any organic residue. At this stage, each piece is treated separately as a unique sample. A 200 nm-thick layer of positive photoresist (ARP6200.09) is coated on top of the sample via a spinner at a speed rate of 4000 rpm. After baking at 120 ^{o}C on a hotplate, the sample is coated with a layer of Electra92 for better electric conduction during e-beam lithography. After baking at 90 ^{o}C for 2 minutes, the sample is loaded into our Voyager (Raith) E-beam lithography tool. The photoresist is exposed by electron beams with an exposure dose of 160 μC/cm^2. Next, the sample is rinsed with DI water to remove the layer of Electra92 (AR-PC 5090.02), developed in n-amyl acetate at room temperature for 60 seconds and immersed in isopropyl alcohol (IPA) to stop the development. The sample is inspected using an optical microscope to be sure no errors occurred during the lithography and development. Then, the sample is etched in RIE with a gas mixture of CF$_4$/H$_2$ (80:3 sccm) at an RF power of 210 W. The 100 nm-thick SiN$_x$ hard mask is slightly over-etched with an etching time of 1m40s, which ensures complete removal of the SiN$_x$ mask where the AlO$_x$ needs to be etched. Followed by an oxygen plasma in RIE for 3 minutes, the remaining ARP6200 photoresist is totally removed. The etched SiN$_x$ profile is inspected by a surface profilometer (Veeco Dektak 150) to check if the height of the etched SiN$_x$ structure matches the expected layer thickness. The AlO$_x$ etching is then performed in ICP-RIE with a gas mixture of 10:5:10 BCl$_3$/Cl$_3$/Ar at a temperature of 18 ^{o}C. The ICP and RF power are set to 1250 W and 50 W for 2m10s to fully etch the AlO$_x$ layer. Figures

4.11(a) and (b) show the optical images of an array of optical circuits for 1D-SIM and the zoom-in of a 1x2 MMI beam splitter, respectively. The thickness of the remaining SiN$_x$ is inspected by a thin-film analyzer (Filmmmetric). The SiN$_x$ layer is estimated to be 35±5 nm after AlO$_x$ etching, and it will be used in the next step to process grating out-couplers.

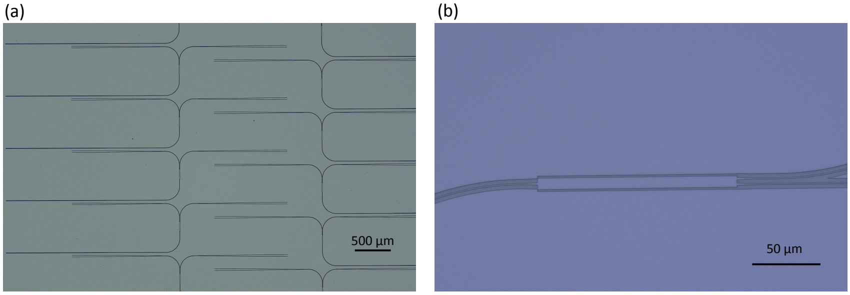

Figure 4.11: Optical images of (a) UV-PIC for 1D-structured illumination microscopy, (b) zoom-in 1x2 MMI beam splitter.

4.3.2 Patterning grating structures for grating couplers

This section focuses on the process of shallow-etched grating out-couplers on top of 20 µm-wide waveguides. The sample is coated with a 200 nm-thick layer of ARP6200.09 photoresist and baked at 120 ^{o}C for 60 seconds. After coating a second thin film of Electra92 with a spin rate of 2000 rpm, the sample is baked at 90 ^{o}C for 2 minutes. To pattern features on top of the etched AlO$_x$ waveguides, the mask design needs to be accurately aligned with the existing structures. This is enabled by "L" shape alignment markers of size 20 µm by 20 µm that are located at the corners of the circuits. Since the depth of the markers is as small as around 155 nm, the contrast of the image in E-beam lithography is very weak. Each image is acquired with a relatively long exposure of 7 μs in order to increase the SNR. As a filling factor of 0.75 is chosen, the grating lines have a width narrower than 50 nm for a grating pitch lower than 200 nm. It follows that proximity effects need to be taken into account during the EBL exposure and the exposure dose needs to be optimized. With the standard exposure dose of 160 μC/cm^2, the photoresist is underexposed. After the optimization, a dose factor of 1.3 is applied to optimize the lithography. After removing the layer of Electra92 layer by rinsing with DI water, the photoresist is developed in n-amyl acetate solution for the 60s. Then, the SiN$_x$ etching is performed in RIE using a gas mixture of CF$_4$/H$_2$ for 1 minute. After removing the photoresist via oxygen plasma for 3 minutes in RIE, the AlO$_x$ etching is implemented in ICP-RIE for 15s or 40s to realize a shallow-etching of 10 nm or 30 nm, respectively. Finally, the SiN_x is removed by RIE etching using a gas mixture of $BCl_3/Cl_3/Ar$ for 40s. Figure4.12(a) and (b) shows the SEM images of the AlO_x grating fabricated with a standard dose factor of 1 and 1.3, respectively. Some of the grating lines are partially open in the first case, while the lines are well-defined in the latter case. The grating profile can also be inspected after the development, although the grating features are too small to observe with standard optical microscopy. The profile of the grating is expected to be homogeneous after the development of grating, see Fig.4.12(c). Otherwise, the lithography of the grating is expected to be failed.

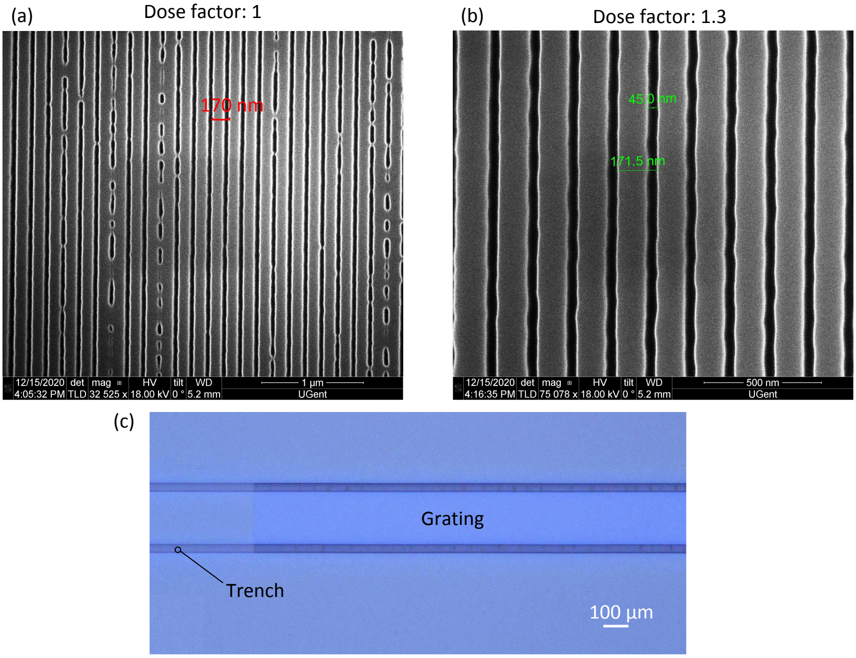

Figure 4.12: (a-b)Scanning electron images of AlO_x gratings. The exposure dose factor is 1.0 in (a) and 1.3 in (b). Grating pitch= 170 nm, filling factor= 0.75. (c) Optical images of the photoresist grating after development. Grating pitch= 180 nm, filling factor= 0.75.

4.3.3 Patterning metallic layers for thermal phase shifters

The fabrication of passive optical components is completed, after removing the SiN_x hard mask. The third layer in the design (red) in Fig. 4.10 is the metal layer designed for the thermal phase shifters. The width of the metallic strip is larger than 3 µm. As the alignment between the waveguide and phase shifter is critical in view of the targeted short spacing of 1 µm, it requires also E-beam lithography instead of contact photolithography. The lift-off process is adopted as a strategy for structuring the metal, for which the patterned photoresist should be generally 3 times thicker than the metal layer. This suggests that the photoresist thickness should be larger than 300 nm for a 100 nm-thick layer of metal. Therefore, a photoresist ARP6200.13 was selected to provide a 400 nm-thick layer of photoresist on top of the sample for a spin rate of 4000 rpm. After baking at 120 ^{o}C for 1 minute, the sample is coated with a layer of Electra92 at a spin rate of 2000 rpm and baked at 90 ^{o}C for 2 minutes. After aligning the mask layer with the patterned alumina structures on the chip, the photoresist is slightly overexposed with a dose of 170 μC/cm^2 in order to create undercut features which helps release the metal layer during lift-off. After a standard development (DI water rinsing, the 60s in n-amyl acetate, and 1 minute in IPA), the sample is inspected under an optical microscope. Next, the metalization is performed via a Leybold Univex sputtering system. The layers of 80 nm Ti and 20 nm Au are successively deposited via thermal evaporation. The sample is then immersed in the photoresist remover solution (ARP600-71) for 2 hours until the metal stack layer is detached from the sample surface. The lift-off process is completed after rinsing the sample with acetone, IPA, and water, and drying in a N_2 flow. Figures 4.13 (a) and (b) show the optical images of the fabricated photonic integrated circuits for 1D and 2D SIM after lift-off processing, respectively.

At this stage, I have completed the fabrication of the photonic integrated circuits. After cleaving the sample along the crystal axis of the silicon substrate to expose the waveguide facet for butt-coupling, the sample is ready for optical characterization and the application of structured illumination microscopy. To quantify the performance of the UV-PIC-based SIM, I will design and fabricate fluorescent objects in the following sections.

4.4 Fluorescent resolution target for the characterization of SIM techniques

4.4.1 Pattern design of 1D gratings and a Siemens star target

The UV-PIC-based SIM technique aims to enhance the optical resolution of conventional microscopes. To characterize the performance of this technique, a proper object needs to be designed and fabricated. One-dimensional grating structures with different periods are chosen to unveil experimentally the working principle of the super-resolved SIM technique, namely the spatial frequency mixing, see Fig. 4.14(a). Furthermore, a Siemens star target (spoke target) whose spatial frequency gradually increases from the outer part to the inner part is designed to determine the optical resolution, see Fig. 4.14(b). One of the key ingredients of the SIM technique is fluorescence. This incoherent signal generates a spatial frequency mixing

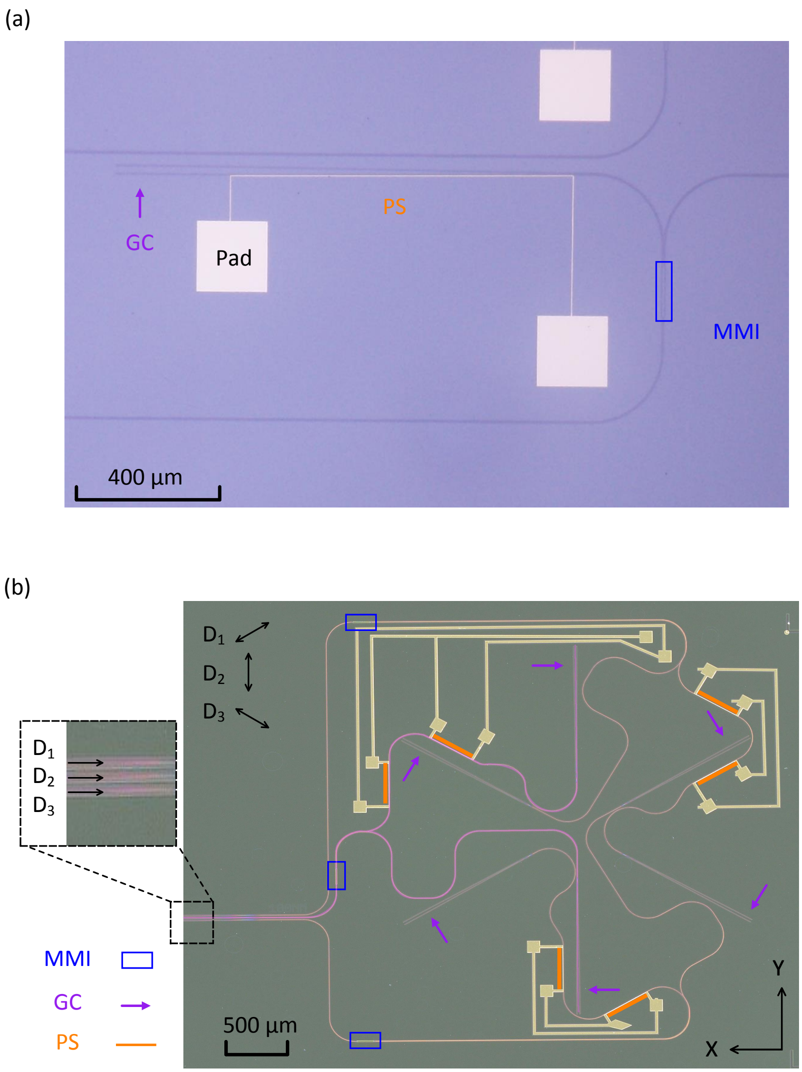

Figure 4.13: Optical images of the fabricated photonic integrated circuits after lift-off process for (a) 1D-SIM and (b) 2D-SIM. MMI: multi-modal interferometer (blue), GC: grating out-coupler (violet) and PS: thermal phase shifter (orange)

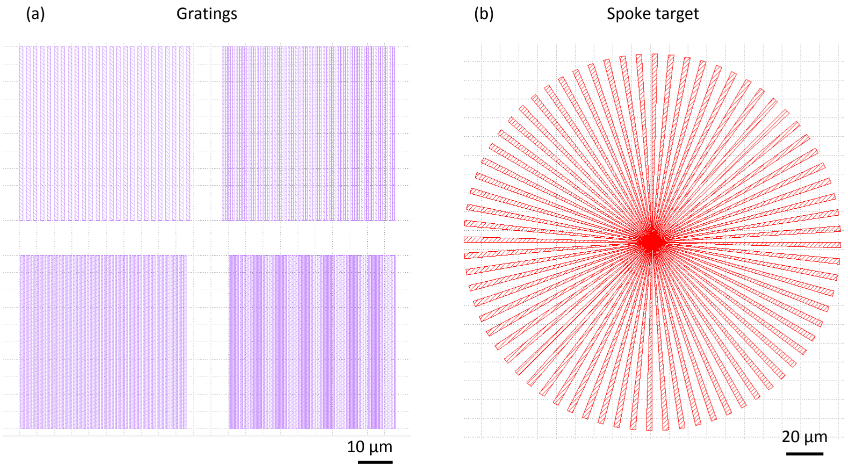

Figure 4.14: Layout design of (a) one-dimensional grating arrays and (b) Siemens star target.

between the fluorophore distribution and the structured illumination.

There are two steps to produce the fluorescent object: (1) fabricating metallic structures either gratings or spoke targets via a lift-off process on top of a transparent substrate such as borosilicate glass. The area covered by a stack of Ti/Au absorbs strongly UV light and prevents light propagation, while blank areas allow the UV light to transmit. In this way, the pattern metal layer is used as a mask. (2) Coating a layer of fluorescent dye on top of the sample. The fluorescent dye emits visible fluorescence when excited with UV light. Figure 4.15(a) and (b) show the schematic of the fluorescent grating and fluorescent spoke target, respectively. Gratings are designed with different grating pitches Λ, including the pitches smaller and larger than the optical resolution of the microscopy system.

4.4.2 Fabrication of the designed fluorescent resolution target

The process flow used to fabricate the fluorescent objects is described in Fig.4.16. The fluorescent objects are fabricated on top of 525 µm-thick borosilicate glass substrates, the surface size of which is 2.5 cm x 2.5 cm. The thickness is measured to be 525 µm. A 400 nm-thick layer of photoresist (ARP6200.13) is coated on top of the surface with a spin rate of 4000 rpm. After baking at 120 ^{o}C for 1 minute, the sample is coated with a layer of Electra92 and then baked at 90 ^{o}C for 2 minutes. Then, the photoresist is exposed to e-beam lithography. A dose factor of 0.8 is applied with a standard exposure dose of 160 $\mu C/$ cm^2, which allows us to process a grating with a grating pitch of 200 nm and a filling factor of 0.4.

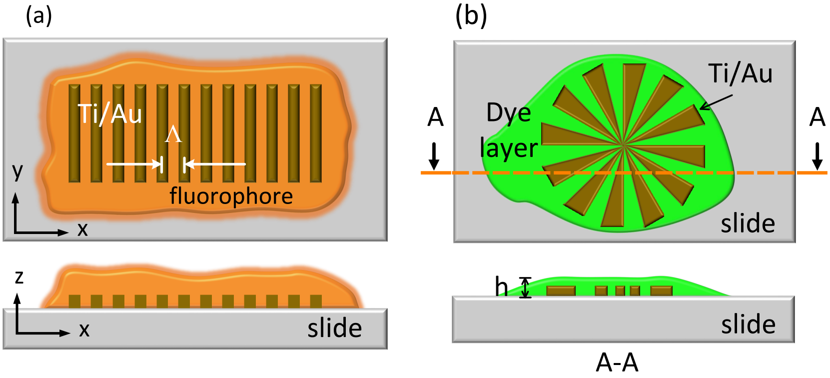

Figure 4.15: Schematic of (a) the metal grating with orange fluorescent dyes coated on top and (b) the sector star target with green fluorescent dyes coated on top.

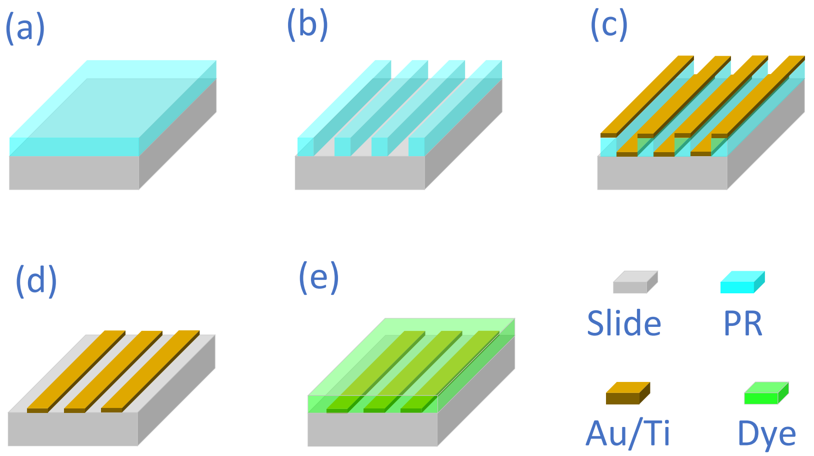

Figure 4.16: Process flow of fluorescent objects. (a) spin coating photoresist on top of borosilicate glass, (b) patterning the photoresist via EBL, (c) metal deposition via electron beam evaporation, (d) lift-off process, (e) coating and evaporation of dye solution.

As the substrate of borosilicate glass is quite different from the previous SiO_2/Si substrate, the amount of back reflection of the electron beam is strongly modified. Consequently, the exposure dose needs to be adjusted in order to process fine features with typical sizes below 100 nm. The metalization is implemented via an electron beam evaporator (Leybold L560) to produce a metal stack of Ti/Au 20 nm:80 nm. The thin layer of Ti gives a better adhesion between the metal layer and the glass substrate. Followed by 30 minutes of immersion in photoresist remover solution (ARP600-71), the sample is rinsed with acetone, IPA, and DI water to complete the lift-off process. Figure 4.17(a) and (b) shows the SEM images of metallic gratings of pitches 200 nm and 300 nm, respectively. Although a relatively low electron voltage of 2 kV in SEM is optimized to minimize the charging effect induced by the glass substrate, the signal coming from the metal strips is inhomogeneous with the presence of spikes attributed to charging effects. The profile of the red lines indicates the integration of the intensity along the vertical direction of the SEM image in Fig. 4.17(b). This distortion of the intensity profile limits the accuracy of the grating period to ± 5 nm in the measurement. The SEM image of the fabricated spoke target is presented in Fig. 4.17(c). This object gives access to a continuous sweep of the spatial frequency of the input light field from its outer part to its inner part, with a line spacing lower than 100 nm at the center. Decreasing further the line spacing isotropically requires optimizing the process including the exposure dose of the e-beam lithography and the thickness of the photoresist. I have not decided to optimize further the process, since the spacing of 100 nm is small enough to characterize the current UV-PIC-based SIM technique. Finally, a layer of organic dye is coated on top of the sample. As a simple example from everyday life, we used the ink of an orange or green highlighter that is made of a mixture of a xanthene dye and a coumarin dye or a mixture of Triphenylmethane dye and pyrene-based dye, respectively. A UV laser operating at a wavelength of 360 nm is used to excite the fluorescence dyes. The fluorescence spectra of the orange and green dyes are shown in Fig. 4.18 (a) and (b), respectively. The orange and green dyes emit fluorescence at a central wavelength of 585 nm and 511 nm, respectively. The optical spectrum of the orange dye exhibits a full-width-at-half-maximum (FWHM) of 34 nm, which is slightly narrower than the value of 53 nm in the case of the green dye. The dye solution is diluted with DI water with a ratio of 1:3 to form a thin layer. The mixture is coated in the liquid phase on the surface of the sector star target, resulting in a 325 nm-thick solid layer after evaporation of the solvent. At this stage, the fabrication of the fluorescent objects has been completed. These objects will be used to characterize the optical resolution of the conventional wide-field microscopy and the proposed UV-PIC-based SIM in the following section.

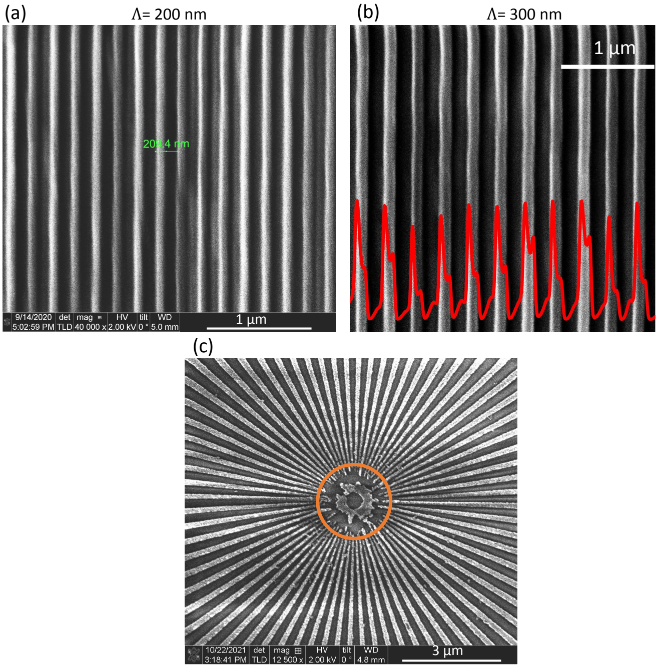

Figure 4.17: Scanning electron images. (a) 200 nm metal grating. (b) 300 nm metal grating. (c) Metal Siemens star target. The orange solid circle points out the position where the grating pitch along the circle equals 100 nm.

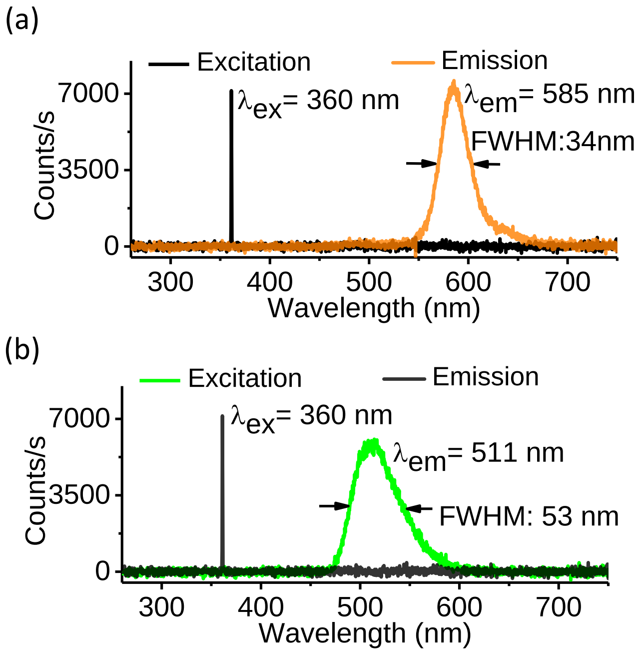

Figure 4.18: Optical spectra of the UV exciting beam and the fluorescent dyes. (a) Orange dye. (b) Green dye. λ_{ex}*: excitation wavelength,* λ_{em}*: emission wavelength.*

4.5 Implementation of UV-PICs based SIM technique

This section first explores the working principle of structured illumination experimentally, namely the spatial frequency mixing, using the 1D structured illumination generated by UV-PICs. Next, after characterizing the optical resolution by using the fluorescent spoke target, label-free super-resolved imaging of biological cells is implemented with the UV-PIC-based 2D-SIM.

4.5.1 Unveiling experimentally the working principle of SIM with UV-PICs

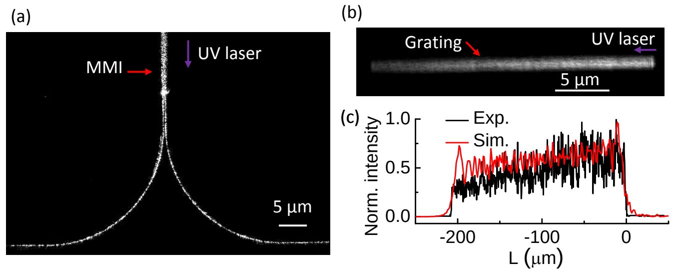

Figure 4.19: (a) Optical image of the diffracted light from a 1x2 MMI. (b) optical image of the diffracted light from a grating with a grating pitch of 210 nm. (c) intensity profile of the diffracted light at the near field of gratings. Exp.: experimental data, Sim. simulated data.

The setup depicted in Fig. 3.16 in Chapter 3 was used to characterize the fabricated photonic integrated circuits. A UV laser operating at a wavelength of 360 nm is used to characterize the PIC and excite the fluorescent objects. An aspheric lens of NA= 0.25 images the chip plane to inspect the SM fiber and the photonic chip to maximize the coupling between the fiber and on-chip lead-in waveguide. The first optical component connected to the lead-in waveguide is a 1x2 MMI beam splitter, as illustrated in Fig. 4.10. The light diffracted from the MMI and output SM waveguides is recorded by a UV-enhanced CCD camera, see Fig. 4.19(a). The balanced intensity of the light diffracted from the output waveguides implies that the actual split ratio is in line with the designed value of 50:50. The routing waveguide starting at the input is expanded by an adiabatic taper, to reach the grating out-couplers which diffract guided light. Figure 4.19(b) shows the diffracted light in the near field of grating out-coupler. The intensity profile of the diffracted light decays gradually along the propagation direction, which is compared with the simulated result in Fig. 4.20(c). The light intensity decays slightly faster in the experimental result than the simulation using FDTD, which may be attributed to the presence of propagation losses in the fabricated

AlO_x waveguide other than the grating loss due to the diffraction. As defined in Fig. 4.5(a), the negative sign of L is referred to the direction towards the negative x-axis, which is opposite to the propagation direction of diffracted beams along the x-axis.

Supported by the smooth operation of the MMI and the grating out-couplers, we investigate now the beam profile of the diffracted beam and the fringe pattern of two-beam interference is investigated at the far field where the two beams cross, namely the object plane. The focal plane of the aspheric lens is lifted up to at a distance given by $\frac{L}{tan(\theta)}$, where L= 1.25 mm, θ= 11.7. By blocking one of the beams, the profile of the intensity diffracted by a single grating is measured. The schematic of the measurement setup is illustrated in Fig. 4.20(a). Figure 4.20(c) shows the intensity profile of the diffracted UV beam with a large field-of-view of 150 µm x 200 µm. The experimental intensity variation (red line in Fig. 4.20(e)) is in line with that obtained with a 2D-FDTD simulation (blue line in Fig. 4.20(e)). The intensity variation is estimated to be 20% inside the FoV and is attributed to the short propagation distance of the diffracted beam. At the imaging plane, the experimental radiant intensity is 0.27 mW for one of the beams and 0.22 mW for the other. Considering the theoretical coupling efficiency, it implies that the current single-mode AlO_x waveguides can sustain at least 3.16 mW of CW laser light at λ= 360 nm. To record the fringe pattern generated by two-beam interference, the mechanical shutter blocking one of the beams is removed, see the schematic in Fig. 4.20(b). Figure 4.20(d) shows the intensity profile of the interference fringe pattern with a fringe spacing of 877 nm. The visibility of the interference fringes $\mathcal{V}$ is equal to 0.83 ± 0.04. This value is obtained by averaging the visibility over 85 $\mu m\times$ 60 µm field of view and ± 0.04 stands for the standard deviation (see Fig. 4.20(d) and 2(f)). This value can reach 0.97 ± 0.02 by averaging over the whole beam profile in simulation, despite the slightly unbalanced intensity due to the different local variations of the diffracted beam (see Fig. 4.7(b)). The lower visibility value in the experiment results from the residual disorder at the gratings and imperfection during the fabrication, which results in a slightly unbalanced intensity between the two diffracted beams.

The SIM technique relies on the incoherent light emitted from the object to be imaged and on its modulation via a coherent structured illumination. In the case of incoherent light imaging, the optical transfer function (OTF) of the optical system sets the optical resolution. The OTF defines the transmission of the spatial frequencies of the intensity of the emitted field: for emission at λ_{em}, only the spatial frequencies that have a modulus $K \leqslant (4\pi/\lambda_{em})NA_{col}$ are transmitted, where NA_{col} is the numerical aperture of the collecting lens, see discussion in Chapter 2. It contrasts with the case of a coherent field emission where the pupil of the optical system limits the modulus k of the transmitted spatial frequencies of the complex amplitude of the field to a bandwidth defined by $k \leqslant (2\pi/\lambda_{em})NA_{col}$.

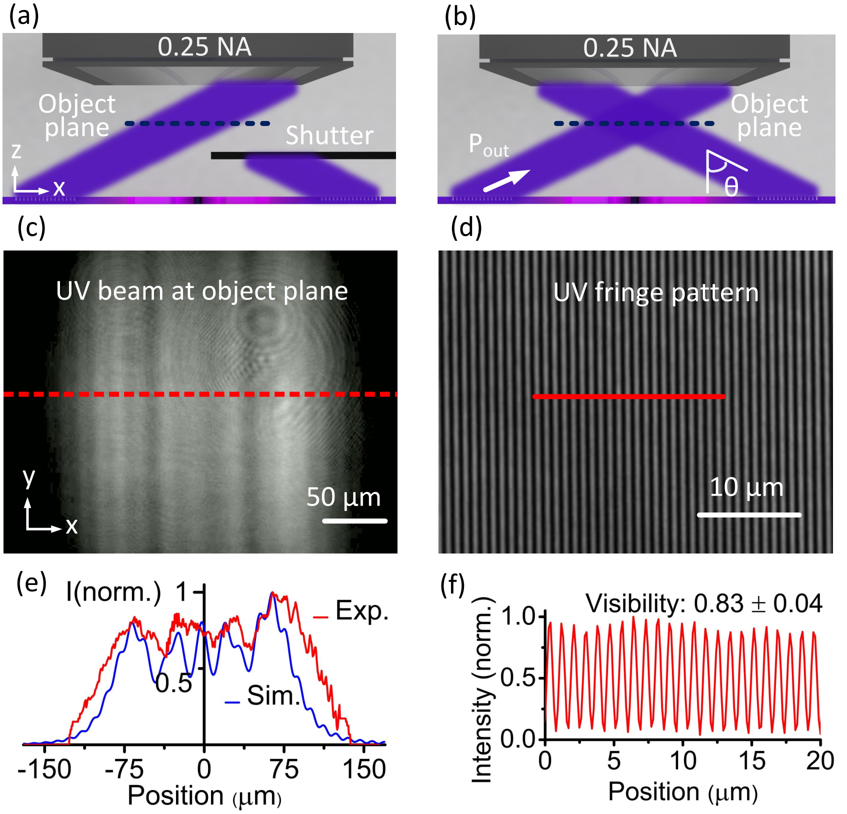

Figure 4.20: (a) Schematic of the UV photonic chip illumination and microscope objective collection in the case of a one-beam illumination. (b) Same as (a) but for a two-beams illumination as required for structured illumination microscopy. (c) Optical image of the beam profile projected in the object plane by a single on-chip grating of pitch 210 nm (λ= 360 nm). (d) Optical image of the interference fringe pattern at the object plane produced by two UV beams diffracted from on-chip gratings of pitch 210 nm. Fringe spacing of 877 nm. (e) Simulated and experimental normalized intensity profiles along the red dashed line of the beam image in (c). (f) Normalized intensity profile along the red segment of the interference fringe pattern in (d).

There is an even more striking difference between coherent and incoherent imaging: Imaging with incoherent light leads to a mixing of the spatial frequencies of the intensity distributions of the object and of the illumination due to the nonlinear quadratic dependence of the intensity on the field amplitude. This effect is at the heart of the enhanced optical resolution achieved with the SIM technique, which is investigated here using the generated 1D-structured illumination and fabricated fluorescent grating of Fig. 4.15.

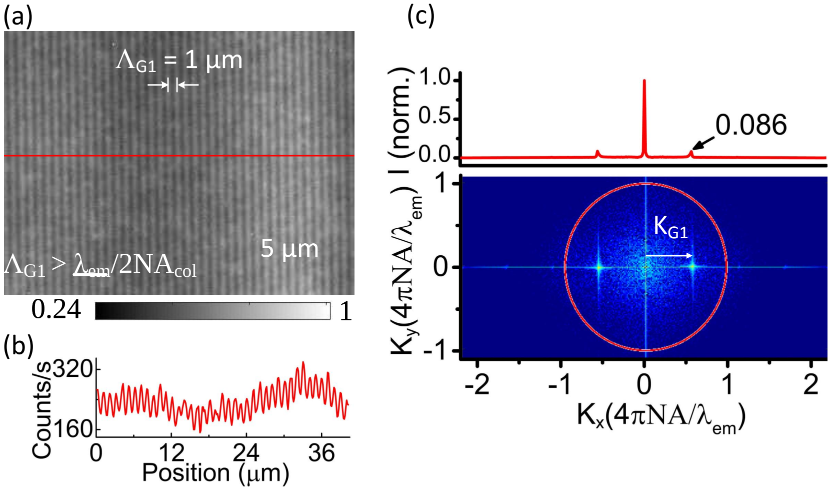

Figure 4.21: (a) Optical microscopy image of a fluorescent grating with a pitch of 1 µm and illuminated in a conventional way with one UV laser beam. Magnification ×60 and NA_{col}= 0.5. Normalized gray color scale. (b) Intensity profile along the red line. (c) Fourier transform of the image in (a) with on the top the intensity profile along the K_x axis.

A fluorescent grating $G1$ with a grating pitch Λ of 1 µm is used to investigate conventional fluorescent microscopy using a visible microscope objective of NA$_{col}$= 0.5. As shown in Fig. 4.21, mainly the dye molecules inside the grooves of the grating are excited due to the strong UV absorption of the gold. The grating pitch is such that $\Lambda_{G1} \geqslant \frac{\lambda_{em}\pm\Delta\lambda_{em}}{2NA_{col}}$=585 nm±34 nm, where $\triangle\lambda_{em}$ is the line width at half maximum of the fluorescence spectrum of the dyes (see Fig. 4.18(a)). The intensity profile along the red line in Fig. 4.21(a) is plotted in 4.21(b), in which the periodical modulation of 1 µm is clearly resolved. The Fourier transform of the Fig. 4.21(a) shown in Fig. 4.21(c), namely the K-space, enables to locate the spatial frequencies $\pm K_{G1}$ corresponding to the periodic modulation inside the bandwidth (red circle) of the OTF of the collecting lens. It also allows determining the average contrast $\mathcal{C}$ of the grating fluorescence modulation: $\mathcal{C}$= 0.138 is given by two times the intensity ratio 0.045 of the peaks at K_x= K_{G1} and K_y= 0 multiplied by a correction factor 1.53. The correction factor takes into account the so-called scalloping loss error resulting from the combination of the discrete nature of the FFT and the finite size of the image that is not a multiple of the grating period. Considering the value 0.3 of the ideal modulation transfer function (MTF), *i.e.* the modulus of the OTF of a conventional microscope, at $(K_x = K_{G1}, K_Y = 0)$, the actual value of the contrast is C_{G1}= 0.46.

As illustrated in Fig. 4.22(e), the fluorescent grating $G1$ is excited with a single coherent beam whose spatial wave vector components are given by $k_x = (2\pi/\lambda)sin(\theta_{180}) \simeq 8.6\ \mu m^{-1}$ and $k_y = 0$ in a plane transverse to the optical axis. For the same illumination, but a fluorescent grating with a period Λ_{G2}= 300 nm, the intensity modulation pattern is lost in the image (Fig. 4.22 (a)) as expected in view of $\Lambda_{G2} < \lambda_{em}/2NA_{col}$. On the other side, when this fluorescent grating is excited by a structured illumination formed as in Fig. 4.22 (f) with two coherent beams containing the transverse spatial frequencies $(k_x = (2\pi/\lambda)sin(\theta_{180}), k_y = 0)$ and $(k_x = -(2\pi/\lambda)sin(\theta_{180}), k_y = 0)$, a new intensity modulation of period $\Lambda_{Moiré} = 1.575\ \mu m$ appears in the spatial domain as unveiled in Fig. 4.22 (b).

The physical process of the optical resolution enhancement or spatial frequency mixing is illustrated in the K-space in Fig. 4.22(d): The high spatial frequencies, e.g. $K_{G2} = 2\pi/\Lambda_{G2}$, are folded into the transmission bandwidth of the OTF (red circle). It results in new transmitted spatial frequency $K_{Moiré}$ according to $K_{Moiré} = K_{G2} - 2k_x$ that are absent in Fig. 4.22(a) for the conventional illumination. The ability to retrieve $K_{G2} = 1.95(2\pi/\lambda_{em})$ is in line with a synthetic numerical aperture $NA_s = 0.98$ in the x direction, which corresponds here to a doubling of the numerical aperture. With the current structured illumination pattern a maximum synthetic numerical aperture $NA_s = NA_{col} + \frac{\lambda_{em}}{\lambda} NA_{ex} = 1.3$ corresponding to $K_{G2} = (2\pi/\lambda_{em})2NA_{col} + 2k_x$ is theoretically achievable by neglecting the background noise of the camera sensor.

Enhancing spatial resolution by probing spatial frequencies beyond the OTF cut-off is one of the key ingredients to achieve super-resolved microscopy. Another crucial parameter is the retrieved contrast. It impacts how clearly the different features of the object will present themselves in reconstructed images. It also needs to match the actual contrast of the sample for quantitative analysis. In this experiment, the actual contrast of the grating C_{G2} can be retrieved from the Moiré pattern in Fig. 4.22(d) since the contrast of the Moiré pattern depends on C_{G2} as $C_{Moiré} = C_{G2} \times \frac{\mathcal{V}}{2} \times MTF(K_x = K_{Moiré}, K_y = 0)$. The experimental value of $C_{Moiré}$ is $2 \times \alpha \times 0.021$ (see Fig. 4.22(d)) with $\alpha = 1.37$ the scaling factor related to the scalloping loss error (here related with the image not being a multiple of the Moiré period), and $MTF(K_x = K_{Moiré}, K_y = 0) = 0.54$. The fringe visibility $\mathcal{V}$ generated by the θ_{180} gratings is estimated to be 0.93. This value is higher than the θ_{210} gratings due to fewer residual fabrication imperfections. It follows that $C_{G2} = 0.23$.

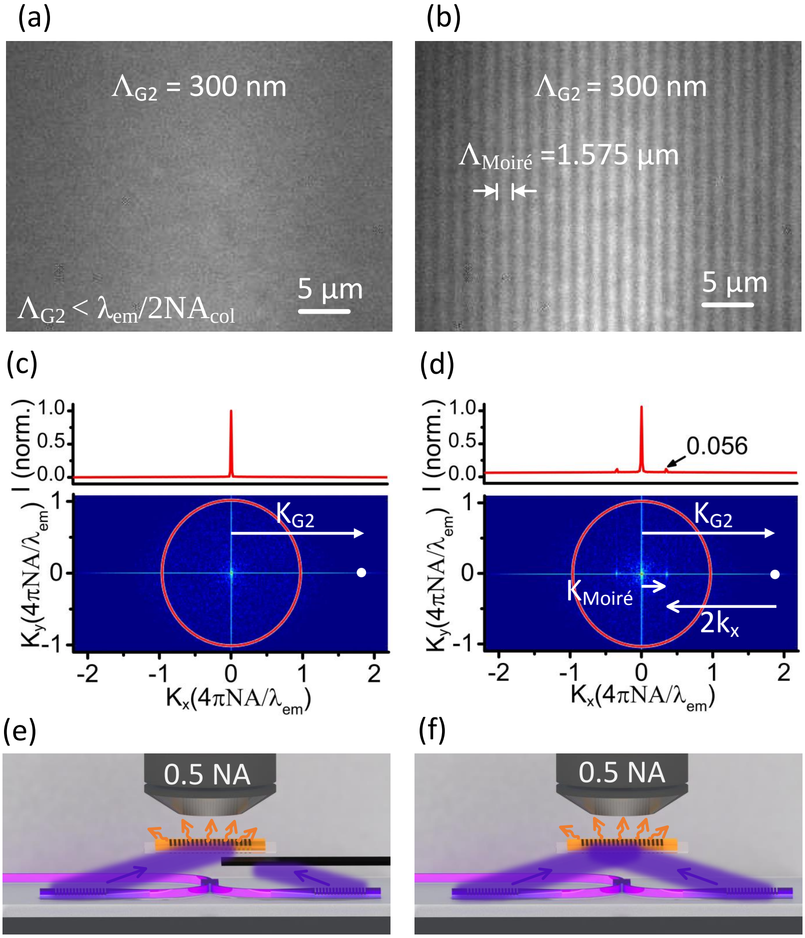

Figure 4.22: (a) Optical microscopy images of a fluorescent grating with a pitch of 300 nm illuminated with one UV laser beam (see schematic (e)). Magnification ×60 and NA_{col}=0.5. (b) Same as (a) but for a two coherent UV beam illumination (see schematic (f)) generating a Moiré fringe pattern. (c) and (d) fast Fourier transform (FFT) of the images in (a) and (b). The red circles represent the spatial frequency cut-off of the transmission bandwidth of the 0.5 NA collecting microscope objective, the red curves on the top are the intensity profiles of each FFT image along the K_x axis. (e) and (f) schematics of the single-beam illumination and the two-beam illumination, respectively.

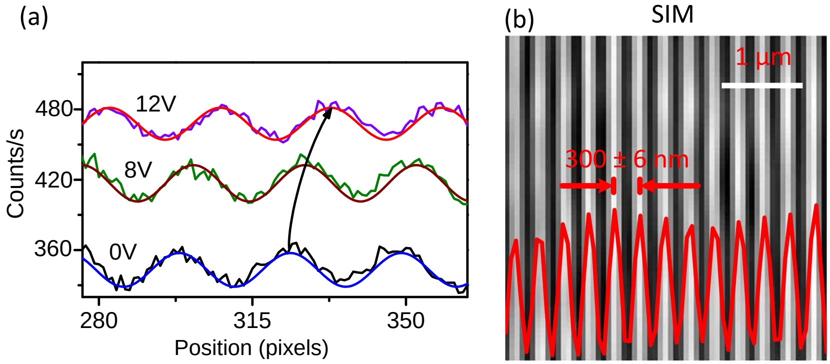

Figure 4.23: (a) Profiles of the Moiré pattern for different voltages, with the profiles labelled as 8V and 12V vertically shifted by 60 counts/s. (b) Super-resolved reconstructed SIM image from the same grating but with fluorophores. Magnification ×120, NA_{col}= 0.5, pixel size of the image 62 nm.

Inspecting successfully the Moiré pattern reported in Fig 4.22(b) in the experiment suggests that the high frequencies outside the OTF bandwidth are folded back and mixed with the low frequency, as depicted in Chapter 2 the equation 2.13. It should be noted that disentangling these frequencies is one of the keys to reconstruct the artifact-free super-resolved image. Three raw images illuminated with different phases, typically 0, $\frac{2\pi}{3}$ and $\frac{4\pi}{3}$, are required to solve the matrix in Chapter 2 2.16. Here, the phase shift is set by the integrated thermal phase shifter and can be precisely estimated by tracking the movement of the Moiré pattern. A voltage source varies locally the temperature of the waveguide by ohmic dissipation at the metal contact. Increasing the voltage V results in a translation of the Moiré pattern toward the positive $+x$ (see Fig. 4.23(a)), whereas the excitation fringe pattern moves in the opposite direction, as here $\Lambda_{ex} > \Lambda_{G2}$. If follows from the direction of the motion of the Moiré pattern that the induced phase shift $\Delta\phi$ is positive, *i.e.* the thermo-optic coefficient of the waveguide is positive in line with the result obtained in [16].

The true super-resolved image of the grating G2 is recovered by stitching all the frequency bands in the Fourier domain and taking an inverse Fourier transfer, after shifting the frequency bands to their right position. In practice the raw images are generally corrupted by noise. To overcome the ill-conditioned Fourier inversion due to the presence of noise N, Wiener filtering is applied, which is widely used in SIM techniques [18, 19]. As depicted in Chapter 2 the equation 2.17, the Wiener parameter $\frac{N^2(K)}{P_t^2(K)}$ requires the knowledge of the power of the true signal, while it is unknown. With a simple grating structure, the signal in K-space is sparse inside the transmission bandwidth. The signal of the true signal P_t is approximated by $OTF \times \tilde{\rho}_i(K)$, which corresponds to approximate the object by its noisy image in the Wiener filter. Besides, considering that the thermal noise of the camera sensor is larger than the shot noise, we have assumed that the noise contribution is constant over all the K-space, namely $N(K)^2$ is equal to the power spectrum of the noise. The power spectrum is estimated in the K-space by averaging the noise signal $N(K)^2$ outside the transmission bandwidth. The reconstructed image of the fluorescent grating G2 is shown in Fig. 4.23(b). The measured period of 300 nm matches well with the result obtained by the SEM image. Note that the reconstructed SIM image is free of charging effect in contrast to the SEM image. After successfully revealing the spatial frequency mixing which is the key to the SIM technique and demonstrating the super-resolved imaging with 1D fluorescent grating, I have investigated more complex samples in two-dimension, which will be presented in the following section.

4.5.2 Characterization of resolution enhancement with 2D-SIM

To implement super-resolved imaging with two-dimensional objects, I used the UV-PICs processed with the design depicted in Fig. 4.10(b). These UV-PICs are designed to deliver structured illumination over three different orientations which are generously required for 2D-SIM. Considering the limited power of the employed UV laser (50 mW) and a higher propagation loss induced by the larger footprint of UV-PICs compared to the last design, I have chosen a etch depth of 30 nm to maximize the coupling efficiency of grating out-couplers. Besides, to achieve high optical resolutions, I have chosen higher excitation numerical apertures of $NA_{ex} = 0.5$ and $NA_{ex} = 0.9$, corresponding to a grating pitch of Λ_G=180 nm and Λ_G=150 nm respectively. Before imaging the fluorescent Siemens star targets, the profile of the generated structured illumination is measured without any object. A microscope objective with a NA$_{col}$= 0.95 is used to image the profile of the structured illumination with a NA$_{ex}$= 0.5 or 0.9. The optical fiber is mechanically translated at the cleaved facet of the chip to activate the photonic circuits one after another, in order to switch the orientation of the structured illumination (namely, D_1, D_2 and D_3), see Fig. 4.13(b). Fig. 4.24 (a-c) shows the interference fringe patterns with different orientations generated by the on-chip grating pairs with a grating pitch of 180 nm. The measured fringe spacing of 362 nm matches well with the designed numerical aperture NA$_{ex}$= 0.5, which validates the robustness of the simulation and the well-controlled fabrication technique. Averaging the visibility over the field-of-view, results in values as high as 0.883, 0.889 and 0.911 for directions D_1, D_2 and D_3, respectively. Their standard deviation values as low as 0.004 are in line with the homogeneity of the beam profile inside the FoV. Such an FoV is estimated to be 32 µm by 32 µm, as defined by the FWHM of the quasi-Gaussian profile of the diffracted beams. The grating out-coupler is designed to reach both a high irradiance and a large FoV by optimizing the grating modulation etch depth. To further validate the flexibility of the UV-PICs in terms of the direction of the diffracted beam, we have designed grating out-couplers with a grating pitch of 150 nm to achieve a numerical aperture NA_{ex} as high as 0.9. Due to the imperfection in the MMI and grating fabrication, the imbalanced intensity coupled out from the two gratings of each pair leads to relatively lower but high enough visibilities for the different orientations D_1,D_2 and D_3, with values of 0.730±0.005 , 0.773±0.008 and 0.737±0.003 respectively (see Fig. 4.24(e-f)). The field of view of 30 µm by 30 µm is similar to that of the diffracted beam with numerical aperture NA_{ex}= 0.5 and the lower fringe spacing of 199 nm agrees with numerical aperture NA_{ex}= 0.9.

Once the generated structured illumination is well characterized, the implementation of the SIM can take place. The properties of flexible beam manipulation and intrinsic compact size make UV photonic chips compatible with any conventional optical microscope, as illustrated in Fig. 4.25(a). The chip is mounted on a printed circuit board (PCB) and positioned below the object for illumination. The PCB enables the electrical current injection of the thermal heaters and offers convenient handling of the photonic chip, see Fig. 4.25(c). The side view of the schematic is shown in 4.25(b). For excitation numerical apertures NA_{ex}= 0.5 and NA_{ex}= 0.9, the distances from the surface of the chip to the object are W_C= 2.75 mm and W_C= 1.33mm, respectively. The Siemens star target is fixed on a translation stage as commonly used and placed at the imaging plane below the microscope objective with a spacing W_D. The part of the set-up above the object is standard for all optical microscopes. The fluorescence of the object that is excited by the UV coherent structured illumination produced by the photonic chip is here collected by a microscope objective of high numerical aperture NA_{col}= 0.95. To filter the UV laser and collect only the fluorescence signal, a long-pass filter (Semrock, FF01-380/LP) is inserted into the imaging path. The magnification of the entire imaging system is 66× for the objective lens of numerical aperture 0.95. With the physical pixel size of 4.54 μm at the camera sensor (Retiga R3, Qimaging), the sizes of the optical sampling in the plane of the object are 68.6 nm. The diffraction-limited optical resolutions are expected to be 269 nm for NA_{col}= 0.95, i.e. more than two times the optical sampling size, which assures that the Nyquist criterion is fulfilled.

As highlighted in Fig. 4.26 (a), (b), and (c), the fringe pattern of the UV field is mapped on the fluorescent intensity field in the three illumination orientations and Moiré patterns are also present as expected. The Fourier transfer of Fig. 4.26 (a), (b), and (c) are shown in (d), (e) and (f), respectively. The peaks are clearly observed at the location corresponding to the spatial frequency of the structured illuminations. Using an extended object such as the current fluorescent sector star target is advantageous compared to conventional single point objects in terms of

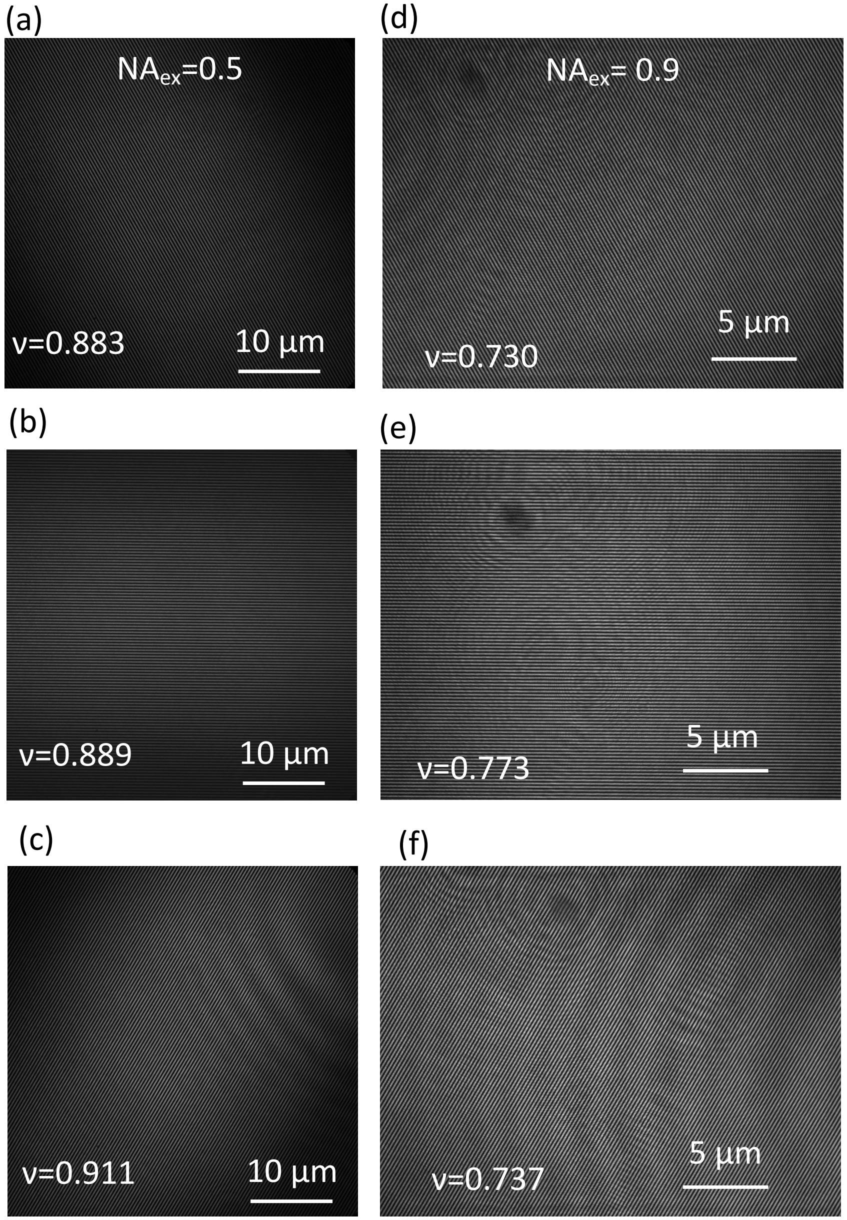

Figure 4.24: Optical images of the interference fringe pattern at the object plane produced by two UV beams coupled out from the on-chip grating pairs along different orientations, namely D_1, D_2 and D_3 respectively. (a-c) A grating pitch of 180 nm corresponding to NA_{ex} = 0.5 results in a fringe spacing of 362 nm and a field of view (FoV) = 32 µm × 32 µm. (d-f) A grating pitch of 150 nm corresponding to NA_{ex} = 0.9 results in a fringe spacing of 199 nm and FoV = 30 µm × 30 µm.

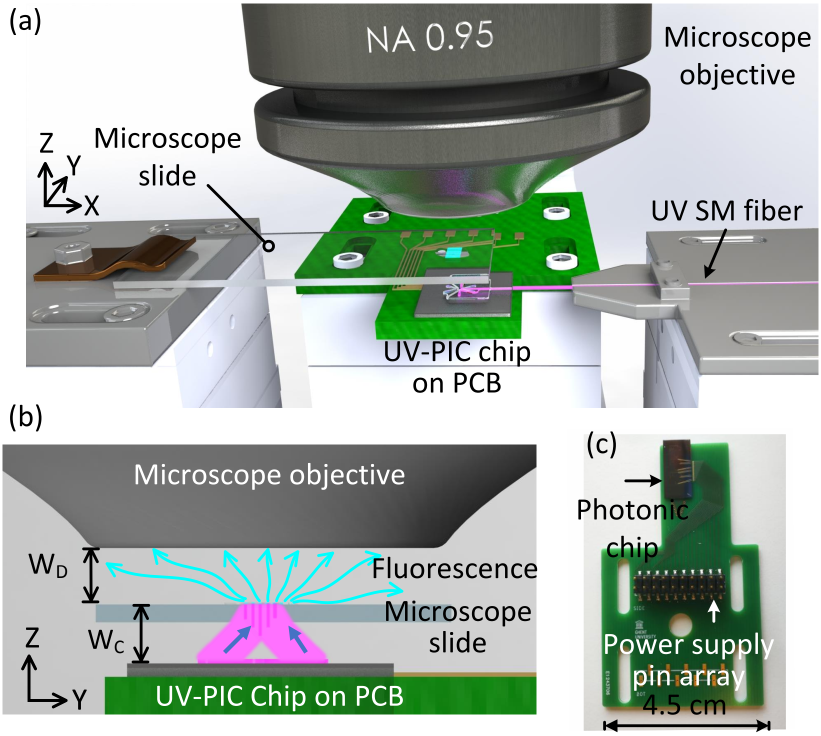

Figure 4.25: (a) Schematic of the chip-based far-field SIM set-up including a conventional microscope. (b) Working principle of the UV PIC-based SIM technique. W_D: working distance of the microscope objective, W_C distance between the top surface of the photonic chip and the sample. The blue and violet arrows illustrate the fluorescence and the UV excitation light, respectively. (d) Picture of the photonic chip mounted on an electric printed circuit board with gold wire connections.

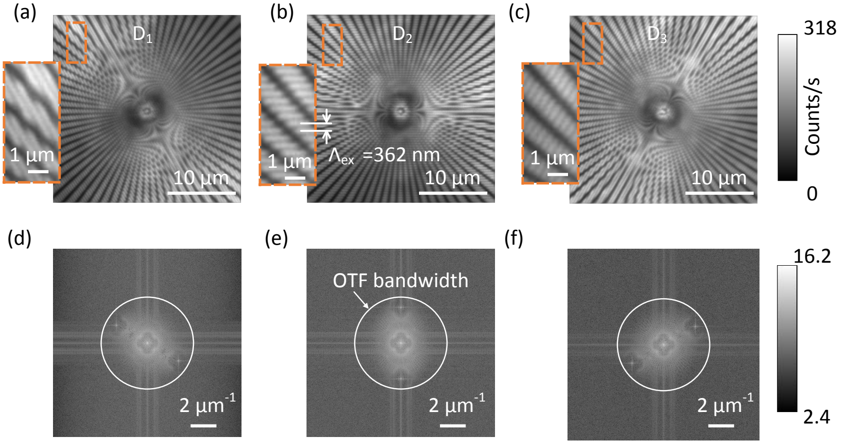

Figure 4.26: (a-c) Fluorescence images of the sector target illuminated by structured light for the D_1, D_2 and D_3 orientations, respectively. Λ_{ex} : modulation period of the fringe pattern. (d-f) Fourier transform of (a-c) in log scale, respectively.

signal-to-noise ratio (SNR) to infer the optical resolution, as ideal point sources have a limited number of fluorescent molecules and therefore a limited fluorescence rate. In addition, the phase of the OTF, i.e. the phase transfer function (PTF) is directly retrieved from the distortions of the pattern of lines constituting the sector star target. Such distortions have not been detected here.

To reconstruct a super-resolved SIM image using the raw images shown in Fig. 4.26, the prior knowledge of the OTF of the conventional collecting microscope objectives is needed. The phase of the OTF, i.e., the phase transfer function (PTF) is directly retrieved from the distortions of the pattern of lines constituting the sector star target. Such distortions have not been detected here, see Fig. 4.29 (a). As a result, the OTF can be directly retrieved from the knowledge of the MTF. To experimentally determine the MTF, we have built a setup that acquires the intensity of the squared pupil function $P^2(\vec{k})$, with $\vec{k}$ the wave vector in the plane perpendicular to the optical axis. This measurement setup is similar to the one used in ref. [20], except that a mirror replaces the opposite microscope objective and an extra lens images the back focal plane of the microscope objective, as illustrated in Fig. 4.27(a). Besides, the lens L1 focuses the emission from a green laser on a 10 µm-diameter pinhole in order to generate a Gaussian beam. The laser operates at a wavelength of 532 nm close to the emission wavelength of the fluorophores described previously in Fig. 4.18. The second lens L2 collimates the central spot of the field diffracted by the pinhole to provide a homogeneous illumination pattern. This beam is reflected by a 50:50 beam splitter and focused on the mirror by the microscope objective. The Fourier transform $\widetilde{E}_{in}(\vec{k})$ (up to a phase term) of the

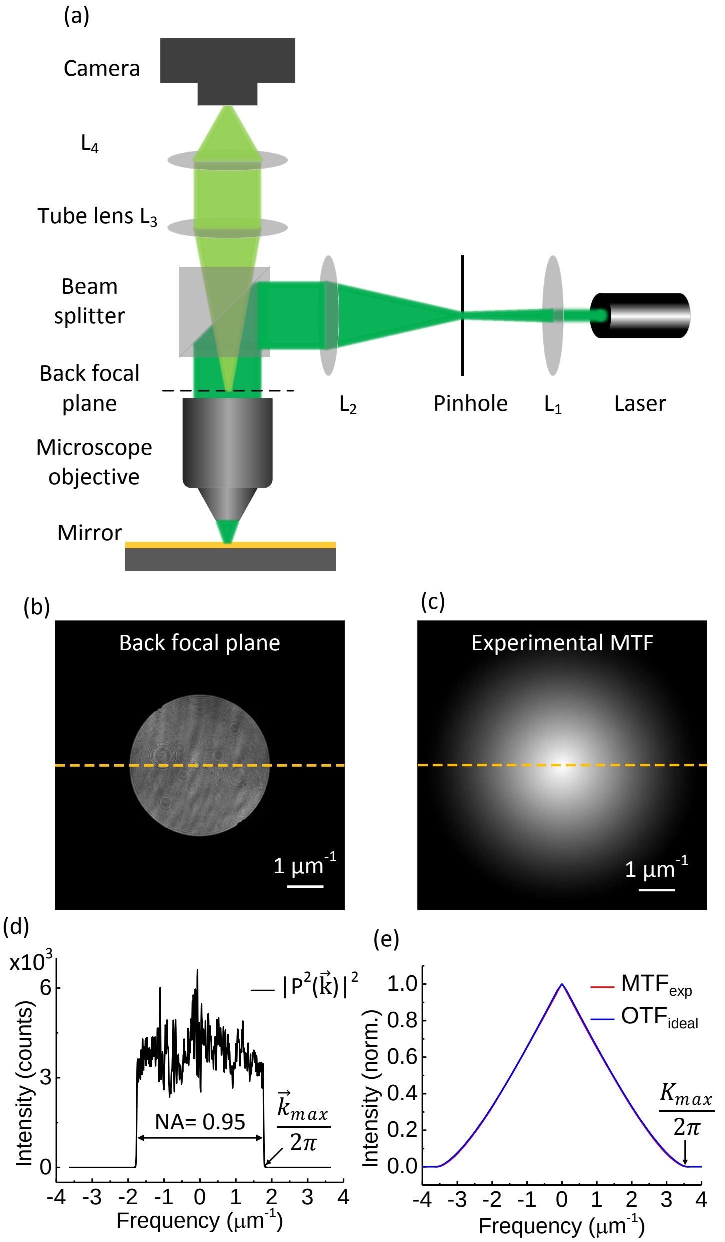

Figure 4.27: Modulation transfer function (MTF) measurement. (a) Schematic of the experimental setup used to determine the MTF. The numerical aperture of the microscope objective is NA_{col}=0.95 and the working wavelength λ= 532 nm. (b) Intensity profile of the squared pupil function measured in the back-focal plane, namely $|P^2(\vec{k})|^2$, with $P(\vec{k})$ the complex pupil function and $\vec{k}$ the wave vector in the plane perpendicular to the optical axis. (c) Retrieved MTF of the microscope objective. (d) Profile in linear scale along the dashed orange line in (b) with the bandwidth given by $\vec{k}_{max} = \frac{2\pi}{\lambda} NA_{col}$. (d) Normalized intensity profiles of the theoretical optical transfer function (blue) and the measured MTF (red), with the maximum of the bandwidth given by $K_{max} = \frac{2\pi}{\lambda} 2 \times NA_{col}$.

field located at the pinhole is retrieved in the back-focal plane of L2, which is also the back-focal plane of the microscope objective. As the beam reflected by the mirror passes through the objective twice, the output field in the back focal plane is given by $\widetilde{E}_{out}(\vec{k}) = P(\vec{k}) \cdot P(\vec{k}) \cdot \widetilde{E}_{in}(\vec{k})$. As the input beam is homogeneous and much larger than the aperture size of the objective, it is considered as constant inside the pupil, and consequently $\widetilde{E}_{out}(\vec{k}) = P^2(\vec{k}) \cdot \widetilde{E}_{in}$. In the imaging path, a telescope made of two lenses, namely the tube lens L3 and the lens L4, images the back-focal plane of the microscope objective. As cameras provide the intensity of the field, the acquired image corresponds to the intensity of squared pupil function, namely $|P^2(\vec{k})|^2$ (see Fig. 4.27(b)). Excluding small intensity fluctuations resulting from residual imperfections of the optical components of the set-up, the experimental intensity profile in the back-focal plane is in line with the ideal pupil function (see Fig. 4.27(d)). Considering that the phase of the experimental OTF is constant, the phase of the pupil function $P(\vec{k})$ can also be taken as constant. As a result, the normalized $MTF = \frac{|P(\vec{k}) \otimes P^*(\vec{k})|}{\int |P(\vec{k})|^2 d\vec{k}}$, where $\otimes$ represents for convolution operator and $P^*(\vec{k})$ is the complex conjugate of $P(\vec{k})$. From the modulus of the pupil function, we can then retrieve the MTF as shown in Fig. 4.27(c) which matches well with the ideal one and justifies the use of the ideal OTF in the SIM reconstruction process.

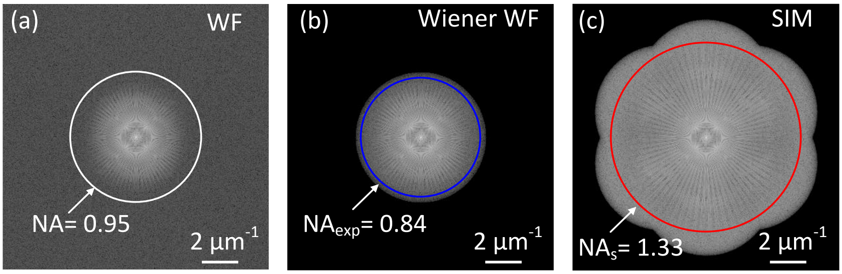

Figure 4.28: Fourier domain images of the sector star target with fluorescent dyes were obtained through fast Fourier transform (FFT) from real space domain images. (a) The real space image is acquired by wide-field (WF) microscopy and subjected to experimental noises. (b) WF image with the implementation of a Wiener filter to minimize the impact of the experimental noise. The white circle in (a) locates the ideal spatial frequency bandwidth of the NA= 0.95 microscope objective. (c) Reconstructed super-resolved SIM image.

The high quality of the structured illumination generated by the UV-PICs is expected to achieve 'artifact-free' super-resolved image reconstruction in SIM microscopy. Any inaccuracy in the estimation of the parameters, such as the spatial frequency of the excitation beams, the relative phase of the beams and the visibility of structured illumination for each frame contribute however to artifacts in the reconstructed image. Among these factors, the relative phase error contributes to the incomplete disentanglement between low and high-frequency bands and then leads to periodical artifacts stemming from the structured illumination. It is convenient to inspect the artifacts in the Fourier domain by monitoring the corresponding residue peaks in the disentangled frequency bands ($\tilde{\rho}_i(K)$ in the equation 2.16). Besides, it is convenient to estimate the noise level of the images acquired in the experiment. The signal-to-noise ratio (SNR) of each acquired frame determines the experimental resolution limit in microscopy. As shown in Fig. 4.28(a), the strong bandwidth-limited signal of the wide-field (WF) image in the Fourier domain can be easily seen in the center part of the white circles and the noise level can be estimated at the outer part. The white circle indicates the theoretical bandwidth of the microscope objective with NA= 0.95. The signal outside the bandwidth is attributed to the noise in the imaging system. To minimize the impact of the noise and properly estimate the spatial resolution limit for the conventional WF microscopy, the WF image is filtered through a conventional Wiener filter. The Wiener parameter ω^2 is set to 0.001, which is considered constant and empirically adjusted. The blue circle in Fig. 4.28(b) indicates the actual bandwidth achieved with the NA= 0.95 microscope objective in the experiment, which corresponds to that of a microscope objective of NA= 0.84 due to the presence of noise. The achieved resolution limit is indicated by the blue circle of radius 3.27 $\mu\mathrm{m}^{-1}$ in Fig. 4.28(b), corresponding to a minimum resolvable spacing of 305 nm in the real space domain. Figure 4.28 (c) shows the reconstructed Fourier domain of the super-resolved SIM image. The features of the sector star target are clearly extended in the expanded bandwidth of the UV-PIC-based SIM microscopy. The maximum resolved spatial frequency is highlighted by the red cycle, corresponding to the bandwidth of an objective with synthetic numerical aperture NA_S= 1.33. It is worth noting that there are no visible residue peaks located at the spatial frequency of structured illumination, which reveals the high accuracy in parameter estimation, the high quality of the structured illumination and the artifact-free reconstruction of the image. The reconstruction algorithm for the super-resolved SIM image is attached in Appendix A.

In Fig. 4.29, we compare the images of the fluorescent sector star target in the case of the WF and the SIM configurations. Switching from SIM to WF is possible by enabling only one grating out-coupler to irradiate the object. The SIM image is obtained by recording nine frames that correspond to three different relative phases between each pair of grating out-couplers, or equivalently to three different settings of the applied current in the thermal phase shifters associated with each direction D_i. The acquisition time for each frame is 500 ms, which is chosen according to the current SNR of the camera. The reconstruction of the final SIM image makes use of a standard Wiener-filter-based reconstruction algorithm [6, 8] with the Wiener parameter set to 0.001. The reconstruction algorithm requires

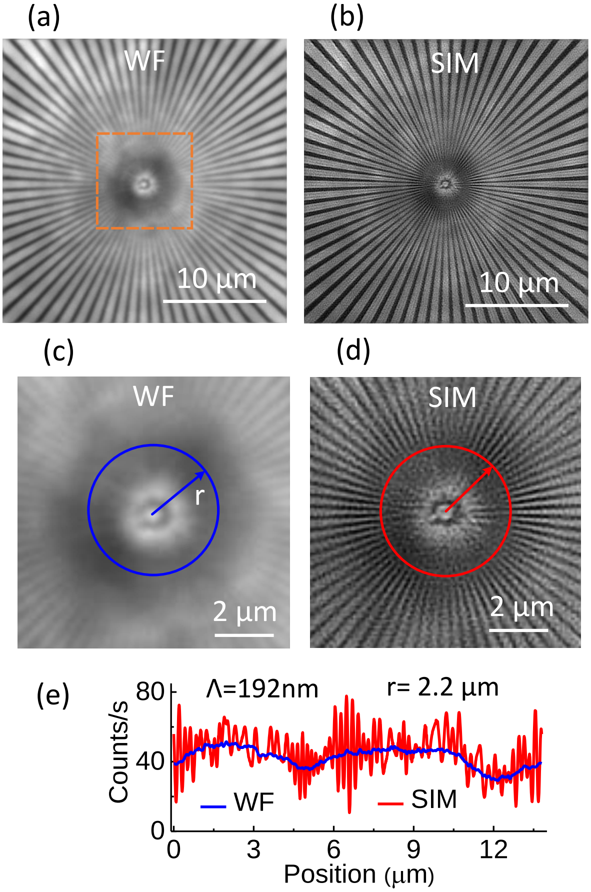

Figure 4.29: (a)Standard (raw data) wide-field (WF) image and (b) reconstructed super-resolved SIM image of the fluorescent sector star target in the case of an excitation numerical aperture NA_{ex}=0.5. (c) and (d) Magnified images of the area inside the dashed orange box in (a) and (d), respectively. The blue and red circles have a radius r=2.2 µm which corresponds to a grating pitch of 192 nm. (e) Intensity profiles were extracted along the circles in (c) and (d). Λ: spatial period.

knowledge of the OTF of the WF microscope. Here, the ideal OTF is used to reconstruct the SIM images, as the measured MTF matches well with the ideal one. Taking the intensity profiles of each image along concentric circles of radius r and of the same center as that of the sector star target, we identify the largest spatial frequency K_{Max} present in the image. The relationship between the r value and the K value is cross-checked with the value of the modulation period of the SEM image. K_{Max} corresponds to the circular profile for which the frequency peaks of the modulation are drowned in the noise of the fast Fourier transform of the profile, see Fig. 4.30. A threshold level of 0.03 in the normalized FFT is used to define the undistinguishable nature of the signal. The red circle in the zoomed SIM image (Fig. 4.29(d)), for which r=2.2 µm pinpoints the location of the largest spatial frequency $K_{Max} = 5.2\,\mu m^{-1}$. The associated red profile in Fig. 4.29(e) exhibits fast variations of spatial period Λ=192 nm. In the case of the WF image, the r=2.2 μm circle is located in a region of the sector star target where the high spatial frequencies of the fluorescent object are not visible. The intensity profile, blue curve in Fig. 4.29(e), and its FFT in Fig. 4.30, confirm the absence of fast variations in the detected signal. The experimental optical resolution achieved with the WF configuration is 305 nm. Considering that the optical resolution of our SIM approach is 192 nm, an enhancement factor of 1.58 has been achieved with NA_{ex}=0.5. The theoretical values of the optical resolution are 269 nm and 154 nm in the WF and SIM cases, respectively, which implies an ideal enhancement factor of 1.75. The difference between the experimental and theoretical optical resolutions is attributed to the current SNR. Using a deep-cooled scientific camera, which is generally used in SIM microscopes, instead of the more conventional and low-cost $20\,^{o}C$-cooled CCD camera that is used here, will reduce this difference. As a salient feature, our results highlight that even with non-specialized equipment, the UV-PIC can boost the performance of a microscope.

With Fig. 4.30 we stress the relative position of the ideal optical transfer functions and of the experimental transmitted spatial frequency spectra of intensity profiles at several r values for the WF (blue curves) and SIM (red curves). As revealed in Fig. 4.28(c), the optical transfer function is not isotropic as only three different orientations are used for the one-dimensional structured illumination. The OTF bandwidth is maximum in the direction of the structured illumination, with the limit K^{SIM}_{Max1}=6.49 µ m^{-1}, and minimum in the perpendicular direction, with the limit $K^{SIM}_{Max2} = 5.83\,\mu m^{-1}$, see red and orange curves in Fig.4.30, respectively. When averaged over all directions, the largest spatial frequency retrieved in the SIM image is close to K^{SIM}_{Max2}. The identification of the frequency peaks is confirmed with the associated FFT of the circular profiles of the SEM image, in particular for the largest spatial frequency where the radius is r=2.2µ m.

The Wiener filter removes the noise outside the bandwidth of the OTF and

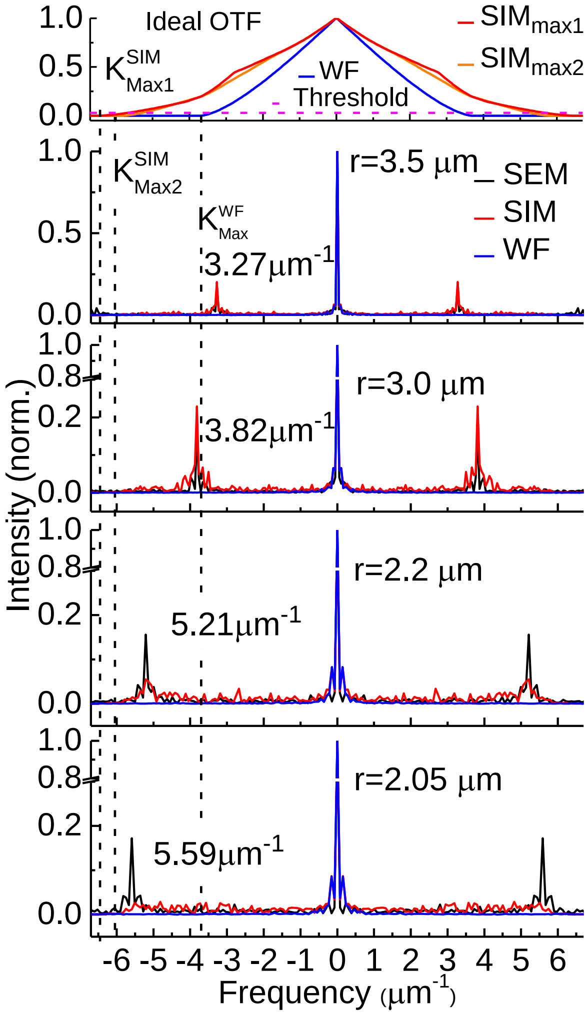

Figure 4.30: Fast Fourier transform of the intensity profiles extracted from the WF (blue), SIM (red) and SEM (black) images along circles of radii r=3.5 μ m, 3.0 μm, 2.2 μm, and 2.05 μm. The theoretical profiles of the optical transfer function (OTF) for the WF and SIM configurations are plotted at the top where the dashed purple line sets the intensity threshold over which the signal is detectable. The vertical dashed black lines locate the maximum spatial frequencies: K^{WF}_{Max} for the WF configuration, K^{SIM}_{Max1} and K^{SIM}_{Max2} for the SIM configuration, where the two values result from the anisotropy of the OTF.

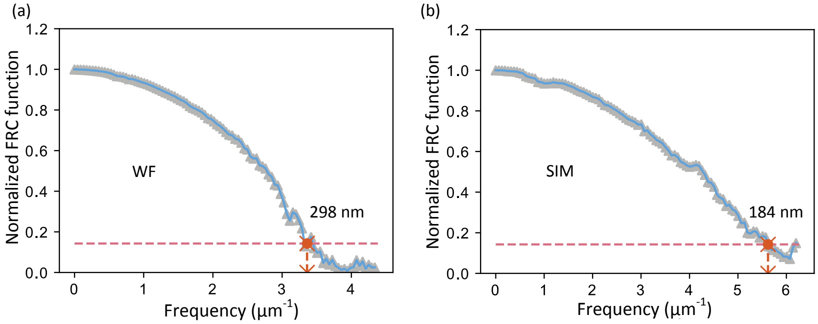

Figure 4.31: Fourier ring correlation curves. (a) WF image in Fig. 4.29(a), (b) SIM image without deconvolution in Fig. 4.29(b). The red dash line indicates a threshold of $\frac{1}{7}$.

enhances the contrast of the high-frequency signal and no impact is expected on the optical resolution limit here. To confirm the resolution limit of WF and SIM images, the Fourier ring correlation (FRC) method [21] which is a standardized approach in the field of microscopy is implemented. The FRC curves of WF and SIM images without applying deconvolution are plotted in Fig. 4.31(a) and (b), respectively. The optical resolutions that are extracted by the intersections between the FRC curves with a conventional threshold of $\frac{1}{7}$ are 298 nm and 184 nm for WF and SIM images, respectively. The $\frac{1}{7}$ cutoff is the most commonly used threshold for the resolution estimation of cryo-electron microscopy, the original application of the FRC method. The results are in line with the resolutions determined by the FFT peak analysis in Fig. 4.32, namely resolutions of 305 nm and 192 nm, respectively.

To illustrate the flexibility of UV-PICs, we have designed chips for which the grating out-couplers enable an excitation numerical aperture as large as NA_{ex}= 0.9. The WF and SIM image are compared in Fig. 4.32(a) and (b). Figure 4.32(c) shows the intensity profiles along the solid circles in Fig. 4.32(a) and (b) at different radii. The intensity profiles at r= 3.0 μm, 2.6 μm and 2.2 μm demonstrate that the oscillations with different frequencies are observable in the SIM images but indistinguishable in WF images. The optical resolution limit of the UV-PIC-based SIM technique is determined to be as low as 166 nm measured at a radius r= 1.9, implying an optical resolution enhancement factor of 1.84.

In order to check the reliability of the reconstruction outcome, the Fourier transforms of the intensity profiles of the WF and SIM images are compared with those of the SEM images. As shown in Fig. 4.33, the position of the peak maximum of the SIM curve (red) matches well with that of SEM (black), validating that the SIM approach retrieves properly the true profile of the object. In con-

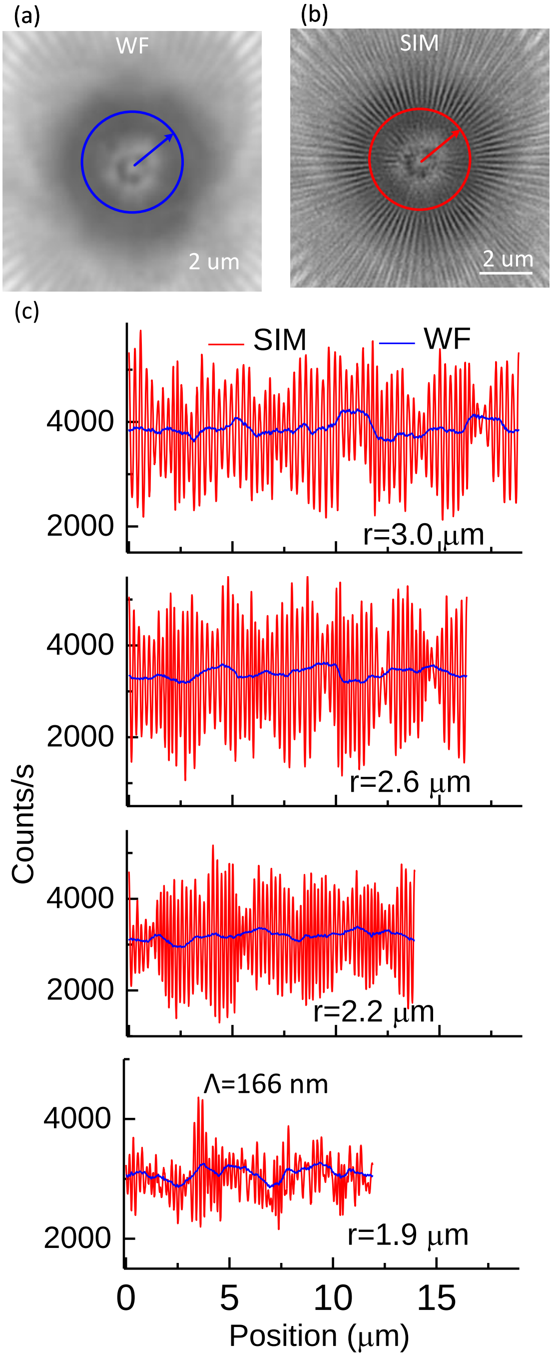

Figure 4.32: (a) WF image, (b) SIM image, NA_{ex}= 0.9. (c) Intensity profiles along different circular cross-sections of the optical images of the sector star target acquired by WF (blue) and SIM (red) microscopy with a NA_{col}= 0.95 objective and NA_{ex}= 0.9.

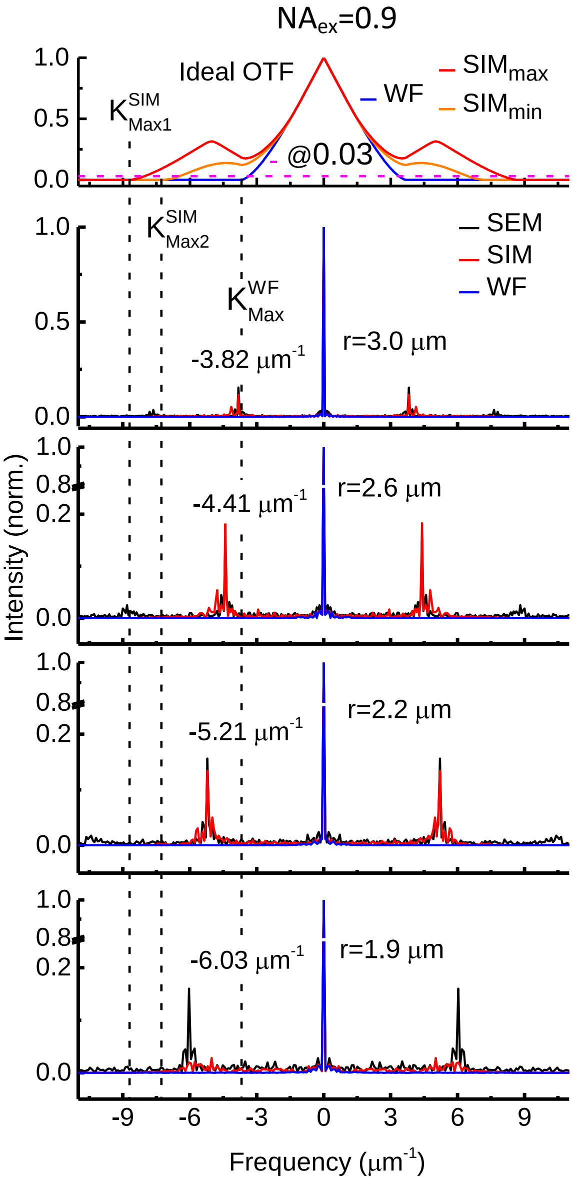

Figure 4.33: Fourier transforms of the line profile in Fig. 4.32(c). The profiles of the ideal optical transfer function (OTF) in the WF and UV-PICs based SIM microscopy are plotted at the top, where K^{WF}_{Max}, K^{SIM}_{Max1} and K^{SIM}_{Max2} are defined by the maximum bandwidths in the WF microscopy, in the SIM microscopy along the illumination orientation and along the direction perpendicular to illumination orientation respectively. The dashed purple line sets the intensity threshold over which the signal is detectable.

trast, no peak can be observed in the WF images (blue) since the grating features along these circular cross-sections oscillate at frequencies beyond the maximum bandwidth in the WF microscopy.

Even if the enhancement factor of 1.84 is larger than for the case of NA_{ex}= 0.5, the difference with the expected theoretical value 2.35 is quite significant. The theoretical enhancement factor is given by $1 + \frac{\lambda_{em}}{\lambda_{ex}} \frac{NA_{ex}}{NA_{col}}$. In addition to the contribution of the limited SNR of the camera, we attribute this difference to a less dense and less homogeneous distribution of the fluorescent dyes when the spacing between the sectors shrinks. The possibility to optically resolve the sector spacing for some limited parts of the intensity profiles of the circular cross-sections when the radius is lower than r=1.9 μm supports this last point. Using index-matching liquids between the chip and the borosilicate microscope slide, the refractive index of which (n=1.54) is smaller than that of aluminum oxide (n=1.69) at λ_{ex}=360 nm, even enhancement factors as large as 3.3 are in principle reachable. Note also that the larger the emission wavelength relative to the excitation wavelength, the larger the enhancement factor.

4.5.3 Demonstration of label-free super-resolved SIM with biological cells

Having assessed the performance of the UV-PIC for structured illumination microscopy with an artificial sample made of fluorescent dyes, we apply our technique to a label-free biological sample using one and three spatial directions of structured illumination, respectively.

As, unlike an artificial sample, there is no prior knowledge about the dimensions of the biological object, the increased quality of the SIM images is only revealed by comparing them with those obtained with standard WF microscopy. Here, I used yeast cells as an example of biological cells, which are considered model organisms for cell biology and consequently of high interest for biological research. The auto-fluorescence is provided by the intracellular nicotinamide adenine dinucleotide (NADH) coenzyme. This molecule exhibits a strong absorption at the excitation wavelength λ=360 nm and provides fluorescence in the blue with a peak maximum at λ_{em}=480 nm, see Fig. 4.34. Imaging the fluorescence of such molecules has already proved to be important for monitoring mitochondrial toxicity in cells [22]. The yeast strain is ordered from DSMZ (Braunschweig, German) and cultured for 24 hours in nutrient broth at 28^oC. A droplet of the yeast solution is taken and dropped on the glass substrate. The sample is ready for imaging after oil immersion and without using any coverslip. The low autofluorescence immersion oil (IMMOIL-F30CC, Olympus) is chosen to minimize the autofluorescence background at UV excitation.

SIM is generally implemented with structured illumination in at least three spa-

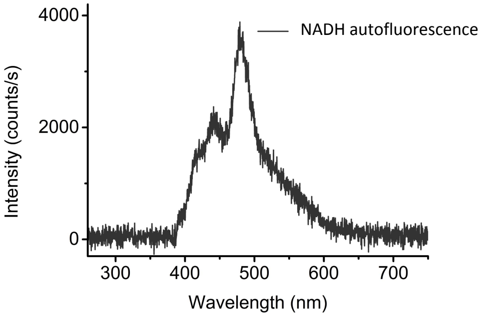

Figure 4.34: Fluorescence spectrum of yeast cells with UV excitation at λ= 360 nm.

tial directions. However, for some applications such as fast cell screening requiring high spatial resolution to discriminate slight cell phenotypes, it might be advantageous to use only one spatial direction for the structured illumination. Using one spatial direction for the structured illumination will enhance the optical resolution along the illumination direction and cause the anisotropic optical resolution in the reconstructed image, which will not impact the fidelity of the reconstructed image. In this context, I implemented the UV-PIC-based 1D SIM to achieve super-resolved imaging with yeast cells. In Fig. 4.35(a), the UV structured illumination that excites the yeast cells are generated by grating out-couplers with a grating pitch of 180 nm and an etch depth of 10 nm. The autofluorescence is collected via an oil immersion microscope objective with NA_{col}=1.32. The signal is imaged with a -20 degrees Celsius cooled CCD camera with a pixel size of 4.54 μm × 4.54 μm (QImaging Retiga R3). To minimize the bleaching of the fluorophores, each image is acquired with an integration time of 4.5 s under a 0.3 mW low excitation power. The autofluorescence clearly reveals, over a wide field, not only the presence of cells but also the underlying structured illumination (see zoom box in Fig. 4.35(a)). The periodic modulation of the fluorescence with a 370 nm period can indeed be observed here as $NA_{col} > NA_{ex}$. Phase shifting the structured illumination and performing image reconstruction, a super-resolved SIM image is obtained, a part of which is zoomed in Fig. 4.35(c). The SIM image reveals biological features that are indistinguishable from the standard wide-field microscopy image in Fig. 4.35(b), *i.e.* with a single beam excitation. For instance, the arrow in Fig. 4.35(c) pinpoints vesicle-like features. Note that the total excitation power is the same for Fig. 4.35(b) and Fig. 4.35(c) in order to compare the two cases under the same noise conditions. The theoretical diffraction-limited resolution for the standard wide-field microscopy image is 180 nm whereas it drops to 120 nm in the SIM case, which corresponds to a 1.5 resolution enhancement in favor of the SIM image. As shown in Fig. 4.35(d), such a resolution enhancement results in the appearance of several peaks in the straight A to B cross-section, with a peak contrast as high as 0.24. This result demonstrates that, even with only one direction of illumination, the UV-PIC-based SIM is a relevant approach for super-resolution label-free imaging of crucial biological samples.

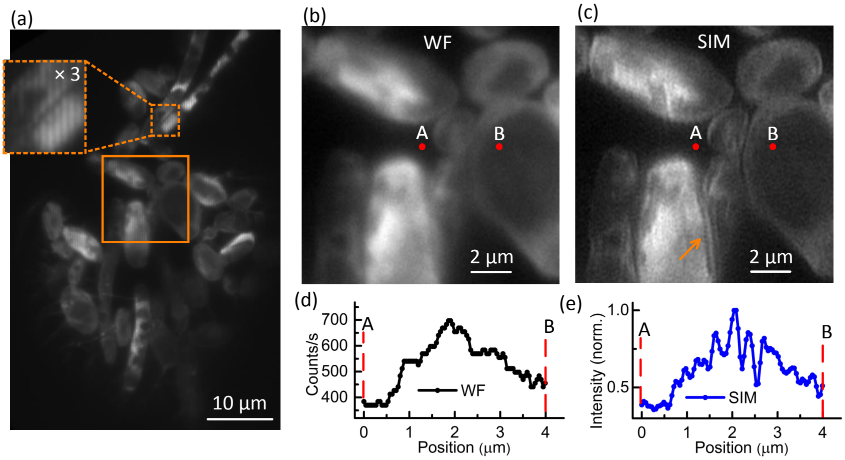

Figure 4.35: (a) Autofluorescence image of NADH in yeast cells under UV structured illumination. The insert is a 3 times magnified zoom of the area defined by the orange dotted contour to highlight the modulation pattern of fluorescence resulting from the structure illumination. (b) Standard wide-field (WF) and (c) SIM zoomed images of the area delimited by the orange rectangle in (a). The orange arrow in fig. 6(c) pinpoints vesicle-like structures that are indistinguishable in (b). (d) and (e): Cross-section along the same segment $[AB]$ in (b) and (c), respectively. The distance between two data points, corresponding to two pixels, is 44 nm

To successfully implement the SIM technique, the fringe pattern of the structured illumination should be stable and distortion-free during the acquisition of raw images. In some cases, the object showing a high refractive index than the ambient medium will lead to the distortion of the fringe pattern. As shown in Fig. 4.36(a), the fringe pattern of the UV structured illumination is distorted by the dried yeast cells when a dry objective of NA$_{col}$= 0.95 is used to image. The index contrast between the object and ambient air is as high as $\sim$0.35. The UV-structured illumination is severely distorted due to the refraction and strong phase difference. As a result, compared with the real signal, the reconstructed SIM image is corrupted by artifacts, see Figures 4.36(b) and (c).

Furthermore, we demonstrate the structured illumination autofluorescence microscopy using three spatial directions of structured illuminations which are generated by three pairs of grating out-couplers. The UV-PIC designed for NA_{ex}=

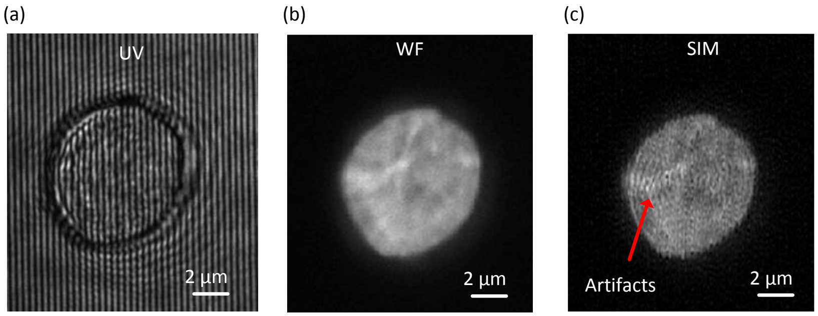

Figure 4.36: (a) Optical image of the fringe pattern of the UV structured illumination distorted by a dried yeast cell. (b) Fluorescent image of a yeast cell captured with WF microscopy. (c) Reconstructed SIM image of a yeast cell corrupted with artifacts.

0.5, which exhibits higher visibility, is used to provide the UV structured light and the autofluorescence is collected via an oil immersion microscope objective with NA_{col}= 1.32 in order to maximize the collected signal. The grating pitch and etch depth of the grating out-coupler are 180 nm and 30 nm, respectively. Note that endogenous fluorescence is much weaker and more prone to fast quenching than well-engineered exogenous dyes. The use of immersion oil also minimizes phase jumps at the interfaces between the cells and the surrounding medium, which otherwise leads to distortion of the structured illumination and produces artifacts in the reconstructed SIM images. The irradiance is set to a value of 3 $\mathrm{W/cm^2}$ to avoid damaging the cells. This light intensity is relatively low compared with typical values of 1-10^2 $\mathrm{W/cm^2}$ for SIM microscopy. Each image is acquired over an integration time of 4 s with a -20 degrees Celsius cooled CCD camera using the software µManager 2.0. In such experimental conditions, the autofluorescence clearly reveals not only the presence of cells but also a mapping of the underlying structured illumination without any deformation, see zoom boxes in Fig. 4.37(a), (b) and (c). The periodic modulation of the fluorescence is measured to be 362 nm. The low fluorescence quantum yield Φ=0.019 of the NADH molecules [23] compared to that of fluorescent probes such as green fluorescent molecules for which Φ=0.8 explains the relatively long exposure time. Like the majority of biological fluorophores, NADH molecules are also prone to photobleaching: the intensity of the NADH autofluorescence is decreased by a factor of 2 after 4 minutes of continuous 30 $\mathrm{mW/cm^2}$ UV excitation. Using a deep-cooled scientific camera is expected to further decrease the acquisition time down to tens of milliseconds.

Shifting the phase of structured illumination and implementing image reconstruction, we obtained the super-resolved SIM image in Fig. 4.37(e), a part of which is zoomed in Fig. 4.37(g). Compared with the WF image in Fig. 4.37(d),

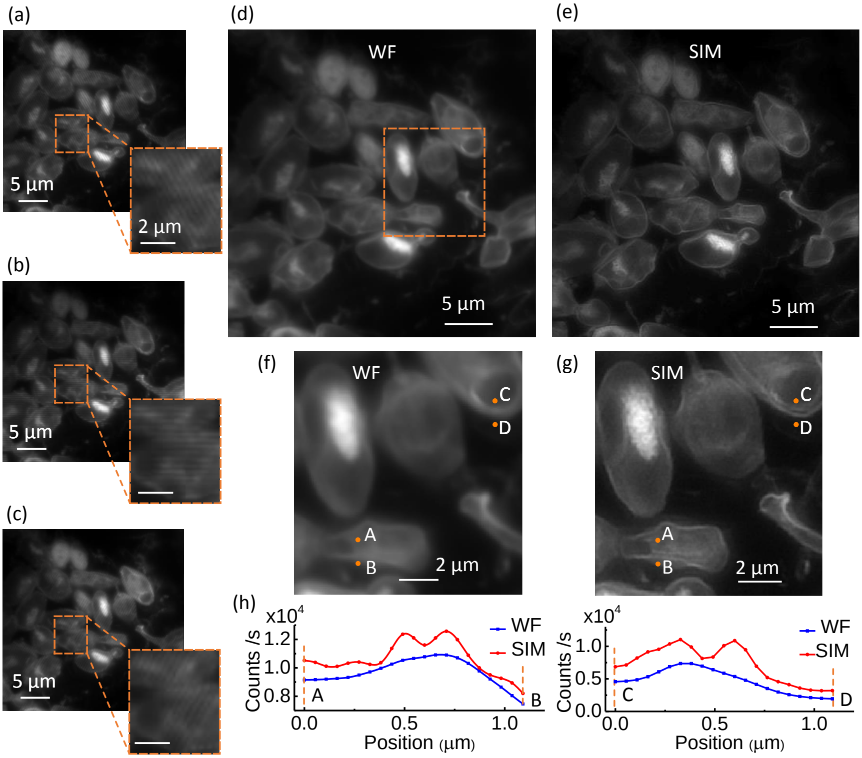

Figure 4.37: (a-c) Autofluorescence image of NADH in yeast cells under UV structured illumination with D_1, D_2 and D_3 orientations, respectively. The insert is a 3 times magnified zoom of the area defined by the orange dotted contour to highlight the modulation patterns of fluorescence intensity resulting from the structured illumination. (d) Standard wide-field and (e) reconstructed SIM images of NADH in yeast cells. The experiment is independently repeated three times for (a-e) on different samples. (f) and (g) zoomed images of the area delimited by the orange rectangle in (d) and (e), respectively. (h-i) Cross-section profiles in (f-g) along the segment [AB] and [CD], respectively.

more biological features are present in the SIM image: dual membranes of cells are clearly visible in the SIM image (see Fig. 4.37(g)) but indistinguishable in the WF image (see Fig. 4.37(f)). The theoretical diffraction-limited resolution for the standard wide-field microscopy image is 182 nm whereas it drops to 121 nm in the SIM case, which corresponds to a theoretical 1.5 resolution enhancement in favor of the SIM image. Using the FRC method, the wide-filed and SIM resolutions are determined to be 262 nm and 166 nm, respectively. The expected resolution enhancement results in the appearance of two peaks in the profile of the straight lines A to B and C to D cross-sections of the SIM image (see Fig. 4.37(h-i)), with a peak contrast of $\sim$ 0.03.

This result demonstrates that the UV-PIC SIM is a useful approach for super-resolution label-free imaging of crucial biological samples. Importantly, the technique does not modify the standard usage protocols for biological wide-field fluorescence imaging as the photonic chip is decoupled from the sample and from the collecting lens of the microscope: the UV-PIC is a plug-and-play add-on. Whether the setup can be built cost-effectively is one of the most frequently asked questions for the SIM technique [24]. Moreover, it is a burning issue for any kind of UV-based microscopy technique, as UV-enhanced components are much more expensive than those at visible wavelengths. The proposed UV-PICs are expected to provide a solution to this issue, in view of their robustness, multi-functionalities, and compatibility with large-scale fabrication methods.

This UV-PIC-based SIM technique can be improved by integrating on-chip switches to increase the temporal resolution which is currently limited by manually switching photonic circuits ($\sim$ minutes). The algorithmic processing time is in order of a few seconds, which will be the bottleneck after using the on-chip switch.

4.6 Conclusion

To conclude, I have developed photonic integrated circuits working at UV wavelength including optical components of 1x2 MMI beam splitter, adiabatic taper, and grating out-couplers. The UV-PICs for 1D-SIM are used to experimentally unveil the spatial frequency mixing in incoherent microscopy, which is the key ingredient to implement the SIM technique. Besides, combed with customized fluorescent Siemens star targets, the UV-PIC for 2D-SIM achieves super-resolved imaging with an enhancement factor of 1.84, compared with conventional microscopy. More importantly, I have also demonstrated that the UV-PIC is capable of label-free super-resolved imaging of biological cells. It is used as an add-on module to conventional microscopes without the need for modification on imaging systems. This novel UV-PIC has a strong potential for improving pathology inspections and diagnostics, triggering the discovery of therapeutic targets, and consequently enhancing the throughput of drug development.

References

[1] Zak David Romaszko, Seokjun Hong, Martin Siegele, Reuben Kahan Puddy, Foni Raphaël Lebrun-Gallagher, Sebastian Weidt, and Winfried Karl Hensinger. *Engineering of microfabricated ion traps and integration of advanced on-chip features*. Nature Reviews Physics, 2(6):285–299, 2020.

[2] R. J. Niffenegger, J. Stuart, C. Sorace-Agaskar, D. Kharas, S. Bramhavar, C. D. Bruzewicz, W. Loh, R. T. Maxson, R. McConnell, D. Reens, G. N. West, J. M. Sage, and J. Chiaverini. *Integrated multi-wavelength control of an ion qubit*. Nature, 586(7830):538–542, 2020.

[3] L. Liu, D. Shan, X. Zhou, H. Shi, B. Song, F. Falke, A. Leinse, and R. Heideman. *TriPleX waveguide-based fluorescence biosensor for multichannel environmental contaminants detection*. Biosens Bioelectron, 106:117–121, 2018.

[4] Øystein Ivar Helle, Firehun Tsige Dullo, Marcel Lahrberg, Jean-Claude Tinguely, Olav Gaute Hellesø, and Balpreet Singh Ahluwalia. *Structured illumination microscopy using a photonic chip*. Nature Photonics, 14(7):431–438, 2020.

[5] A. Ojaghi, G. Carrazana, C. Caruso, A. Abbas, D. R. Myers, W. A. Lam, and F. E. Robles. *Label-free hematology analysis using deep-ultraviolet microscopy*. Proc Natl Acad Sci U S A, 117(26):14779–14789, 2020.

[6] M. G. Gustafsson. *Surpassing the lateral resolution limit by a factor of two using structured illumination microscopy*. J Microsc, 198(Pt 2):82–7, 2000.

[7] J. T. Frohn, H. F. Knapp, and A. Stemmer. *True optical resolution beyond the Rayleigh limit achieved by standing wave illumination*. Proc Natl Acad Sci U S A, 97(13):7232–6, 2000.

[8] Florian Strohl and Clemens F. Kaminski. *Frontiers in structured illumination microscopy*. Optica, 3(6), 2016.

[9] R. Heintzmann and T. Huser. *Super-Resolution Structured Illumination Microscopy*. Chem Rev, 117(23):13890–13908, 2017.

[10] W. Bogaerts, D. Perez, J. Capmany, D. A. B. Miller, J. Poon, D. Englund, F. Morichetti, and A. Melloni. *Programmable photonic circuits*. Nature, 586(7828):207–216, 2020.

[11] Bahram Jalali and Sasan Fathpour. *Silicon Photonics*. Journal of Lightwave Technology, 24(12):4600–4615, 2006.

[12] David J. Moss, Roberto Morandotti, Alexander L. Gaeta, and Michal Lipson. *New CMOS-compatible platforms based on silicon nitride and Hydex for nonlinear optics.* Nature Photonics, 7(8):597–607, 2013.

[13] L. B. Soldano and E. C. M. Pennings. *Optical multi-mode interference devices based on self-imaging: principles and applications.* Journal of Lightwave Technology, 13(4):615–627, 1995.

[14] Thorlabs. *https://www.thorlabs.com/thorproduct.cfm?partnumber=SM300.*

[15] Ansys Lumerical. *https://optics.ansys.com/hc/en-us/articles/360034914713.*

[16] Gavin N. West, William Loh, Dave Kharas, Cheryl Sorace-Agaskar, Karan K. Mehta, Jeremy Sage, John Chiaverini, and Rajeev J. Ram. *Low-loss integrated photonics for the blue and ultraviolet regime.* APL Photonics, 4(2):026101–7, 2019.

[17] Z. Yong, H. Chen, X. Luo, A. Govdeli, H. Chua, S. S. Azadeh, A. Stalmashonak, G. Q. Lo, J. K. S. Poon, and W. D. Sacher. *Power-efficient silicon nitride thermo-optic phase shifters for visible light.* Opt Express, 30(5):7225–7237, 2022.

[18] Amit Lal, Chunyan Shan, and Peng Xi. *Structured Illumination Microscopy Image Reconstruction Algorithm.* IEEE Journal of Selected Topics in Quantum Electronics, 22(4):50–63, 2016.

[19] M. G. Gustafsson, L. Shao, P. M. Carlton, C. J. Wang, I. N. Golubovskaya, W. Z. Cande, D. A. Agard, and J. W. Sedat. *Three-dimensional resolution doubling in wide-field fluorescence microscopy by structured illumination.* Biophys J, 94(12):4957–70, 2008.

[20] Thomas Sure Joachim Wesner, Joachim Heil. *Reconstructing the pupil function of microscope objectives from the intensity PSF.* In International Symposium on Optical Science and Technology, volume 4767, pages 32–43.

[21] S. Koho, G. Tortarolo, M. Castello, T. Deguchi, A. Diaspro, and G. Vicidomini. *Fourier ring correlation simplifies image restoration in fluorescence microscopy.* Nat Commun, 10(1):3103, 2019.

[22] R. M. Rodrigues, P. Macko, T. Palosaari, and M. P. Whelan. *Autofluorescence microscopy: a non-destructive tool to monitor mitochondrial toxicity.* Toxicol Lett, 206(3):281–8, 2011.

[23] Charles R. Cantor Schimmel and Paul. *Biophysical Chemistry: Part II: Techniques for the Study of Biological Structure and Function.* W. H. Freeman, 1st edition, 1980.

[24] K. Prakash, B. Diederich, S. Reichelt, R. Heintzmann, and L. Schermelleh. *Super-resolution structured illumination microscopy: past, present and future*. Philos Trans A Math Phys Eng Sci, 379(2199):20200143, 2021.

5

UV-PICs for quantitative phase imaging

5.1 Introduction

In the previous chapter, I have shown that the photonic chip works as a powerful module to enhance the optical resolution of conventional microscopes and achieve label-free fluorescence imaging of NADH molecules inside biological cells. On the one hand, the SIM technique takes advantage of fluorescence for enhancing optical resolution via spatial frequency mixing. On the other hand, fluorescence-based imaging techniques suffer from the intrinsic issues of photobleaching that result in low SNR. By contrast, imaging techniques that are based on the elastic scattering of a coherent field are immune to photobleaching issues. It implies that an object can be illuminated with high irradiance and over a long acquisition time. If the illuminating beam can be filtered out from the signal, very high SNR ratios can be reached. Besides, when coherent illumination is used and scattering is weak, it is possible to quantify the optical phase delay introduced by the imaged object and allow us to retrieve the thickness if the refractive index n is known. In this chapter, I propose and implement a UV-PIC to upgrade a conventional microscope to a quantitative phase microscope. This approach relies on the space-domain Kramers-Kronig relations. Compared to traditional interferometry-based quantitative phase imaging techniques, such a KK-relations-based quantitative phase imaging technique enables a more robust way to recover the phase information from intensity images [1–5]. First, I study numerically the quantitative phase imaging making use of the KK-relations. This study is implemented with FDTD simulation (Lumerical) and an algorithm that I have developed from the Matlab software. Secondly, I discuss the optimization of photonic components such as 2x2 multi-mode interferometers and grating out-couplers, which are key to implement the concept of the UV-PIC-based QPI technique. After designing and fabricating the photonic chips, I experimentally validate this concept and characterize the performance of this technique with customized pure phase objects.

5.2 Simulation of KK-relations-based QPI

As described in Chapter 2, applying the KK-relations-based QPI technique allows us to recover the phase information from the intensity images. The conditions to apply the KK-relations are perfectly matching the numerical apertures between the excitation beam NA_{ex} and collection objectives NA_{co}. The numerical study of this technique is divided into two steps: 1) Generation of the raw intensity images. Prior to starting the image reconstruction using the algorithm, we need to properly generate the raw-intensity images. The light propagating through a pure-phase object is simulated via a 3D-FDTD method to obtain the complex electric field of the transmitted light. In the simulation, the monitor without band limitation collects the scattered light over all spatial frequencies, which is however not in line with the practice. Therefore, the recorded field is then further processed in the Matlab software by applying a low-pass spatial filter, in order to generate the band-limited amplitude and intensity images. Besides, the simulated complex object function is used as the ground truth to check the reconstructed results obtained with the algorithm. 2) Image reconstruction using the algorithm in the Matlab software. After applying the low-pass spatial filter at a maximum transmitted frequency given by the $\frac{2\pi}{\lambda}NA_{ex}$, the band-limited intensity is obtained by taking the square of the filtered field. This intensity is used in the algorithm to retrieve the phase.

This section starts with the simulation of the light propagation in a pure-phase object in order to generate the ground truth of the complex object function. Next, the development of the reconstruction algorithm will be discussed step by step using the simulated intensity images as input data. Finally, I will numerically analyze the impact on the phase retrieval induced by non-ideal conditions, such as the mismatching of numerical apertures between excitation and collection, the linewidth broadening, and the beam divergence of the illuminating beam.

5.2.1 Simulation of light propagation in pure-phase objects

The FDTD method is a powerful numerical tool to precisely infer beam propagation in three dimensions (3D). This method is used to simulate light propagation in a pure-phase object with inclined incident beams of different orientations. As

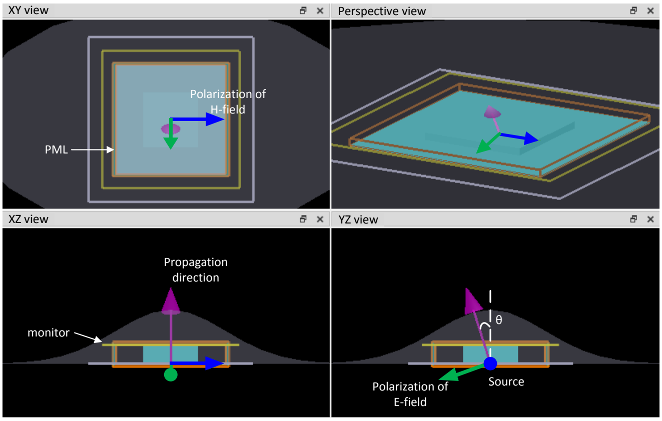

Figure 5.1: FDTD model of oblique illumination for KK-relations-based phase imaging

an example, a simple square pillar structure is chosen as the geometry of the pure phase object. Considering the trade-off between the precision and the consumed computation time, I built the 3D model in a small but large enough simulation volume of 20 x 20 μm^2 in the XY plane and 200 nm in the Z axis with the mesh size of 50 nm in the XY plane and 5 nm in the Z axis, respectively, see Figure 5.1. The simulation boundary is indicated with a solid orange square. The simple square pillar structures have a dimension of 5x5 μm^2 in the XY plane and depths varying from 10 nm to 200 nm. In the experiment, square pillar structures are formed by directly etching with RIE a standard glass coverslip (Schott D263M) whose refractive index equals 1.547 at a working wavelength of 360 nm. With an air ambient, it follows that the refractive index difference is 0.547. The purple arrow indicates the propagation direction of the source. The blue and green arrows are the polarization of the H- and E-fields of the source, respectively. In the concept of the KK-relations-based QPI, illumination beams should be inclined with respect to the optical axis of the microscope objective (Z axis) and the effective numerical aperture of the illumination NA$_{ex}$ should match with that of the microscope objective NA$_{co}$. In the simulation, NA$_{ex}$ is defined to be 0.45 and the NA$_{co}$ will be defined by its associated low-pass filter in the Matlab software. Taking into account the numerical aperture $NA = nsin(\theta)$ and refraction, the angle θ between the illumination beam and the optical axis of the objective is 16.91 degrees inside the coverslip. A monitor is placed at the top of the square pillar to collect the complex field of the transmitted and scattered light.

As discussed in Chapter 2, the oblique illumination exhibits a higher optical spatial resolution in coherent imaging than normal plane wave illumination along the illumination orientation, with an enhancement factor of $\frac{NA_{ex}+NA_{co}}{NA_{ex}}$. However, it also introduces an anisotropic spatial resolution in a 2D image. To minimize this effect, at least four frames acquired with four different illuminations rotated by 90 degrees are needed, which are stitched in the Fourier domain. Figures 5.2(a-d) and (e-h) show the amplitude images of the recorded complex field in linear scale and the amplitude images of their Fourier transforms in log scale, respectively. As shown in Fig. 5.2 (e-h), the monitor records the complex field in all scattered spatial frequencies. Microscope objectives are only able to collect light with the angle limit defined by its numerical aperture NA_{co}. Therefore, the complex fields recorded in the simulation are filtered by a digital low-pass spatial filter in the Matlab software. The relevant post-processing of the simulation data and reconstruction will be discussed later in the section 5.2.2.1.

5.2.2 Reconstruction algorithm development

In this subsection, I first post-process the simulated field images obtained in the previous section to generate band-limited intensity raw images and use them as raw data to develop the reconstruction algorithm for the KK-relations-based quantitative phase imaging. With this algorithm, we can reconstruct the phase of the field scattered by the object, either from the experimental raw intensity images captured by the camera or from the simulated band-limited intensity images. This validates the robustness of the developed algorithm. Secondly, I explore the effects of non-ideal conditions on the reconstruction to predict the potential issues in the experiment.

5.2.2.1 Simulation of coherent imaging with a limited-bandwidth

The complex wave function of a plane wave illumination at normal incidence can be written as :

$$E_{inc}(\vec{r}) = |E_{inc}|e^{i\vec{k}_{inc}\cdot\vec{r}} \tag{5.1}$$

where $\vec{k}_{inc}$ is wave vector of the illumination beam. The collected beam includes the unscattered field $E_u(\vec{r})$ and scattered field $E_s(\vec{r})$ after interacting with the object, recorded by the monitor without band limitation $E(\vec{r}) = E_s(\vec{r}) + E_u(\vec{r})$. Microscope objectives remove all the high-frequency signals of the scattered field which fall beyond the transmission bandwidth, which can be simulated with the Matlab software. For coherent imaging, the transfer function which is also named pupil function in the Fourier domain can be written as:

$$P(\vec{k}) = \begin{cases} 1, |\vec{k}| \leq k_{co} \\ 0, |\vec{k}| > k_{co} \end{cases} \tag{5.2}$$

where k_{co} is the maximum spatial frequency that can be collected by the microscope objective, which is given by the $\frac{2\pi}{\lambda_{co}}NA$. It follows that the band-limited

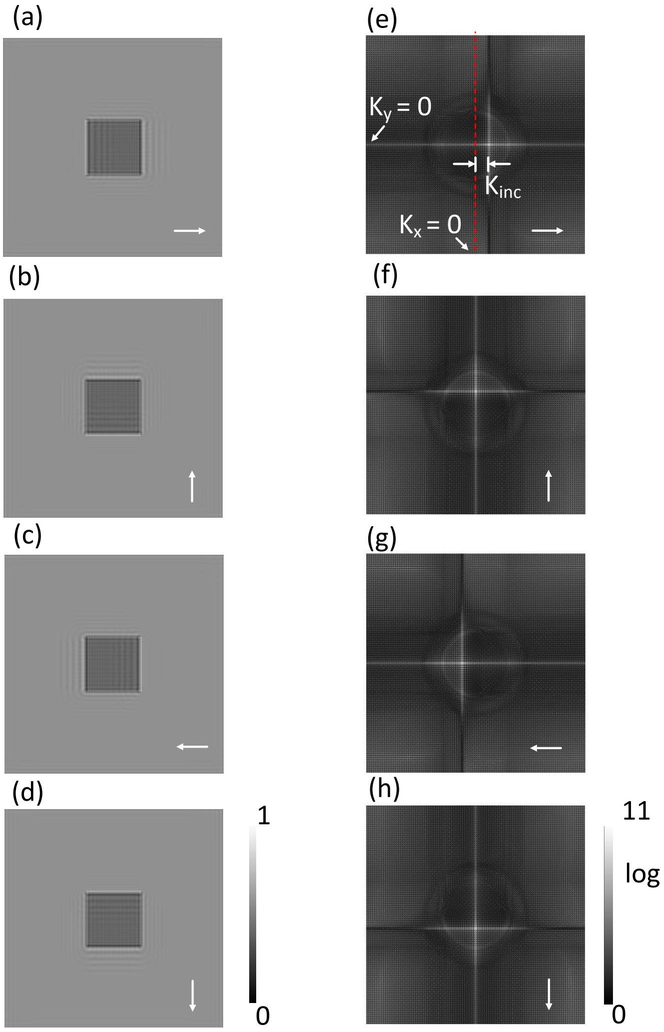

Figure 5.2: (a-d) The amplitude in linear scale and (e-h) Fourier transform in log scale of the recorded complex field with the oblique illumination orientated at 0, 90, 180 and 270 degrees, respectively. The white arrows indicate the illumination orientation of the source.

transmission field in the frequency domain

$$E_{bm}(\vec{k}) = E(\vec{k}) \cdot P(\vec{k}) \tag{5.3}$$

where $E(\vec{k})$ is the Fourier transform of the transmitted field $E(\vec{r})$ without the band limitation, see figures 5.2 (e-h). As shown in Fig. 5.3 (a-d), the high-frequency information of the transmitted field is filtered and only the low-spatial frequency information falling inside the bandwidth of the objective is collected, which is the same for each orientation of the illumination. The numerical apertures of the illuminating beam are the same as that of the microscope objective in the simulation, *i. e.* 0.45. The complex field in the real space domain with a limited bandwidth is obtained after applying an inverse Fourier transform. The squared amplitude images of the band-limited field obtained for each orientation of the illumination, shown in Fig. 5.3 (e-h), are the starting images to retrieve the phase of the field scattered by the object.

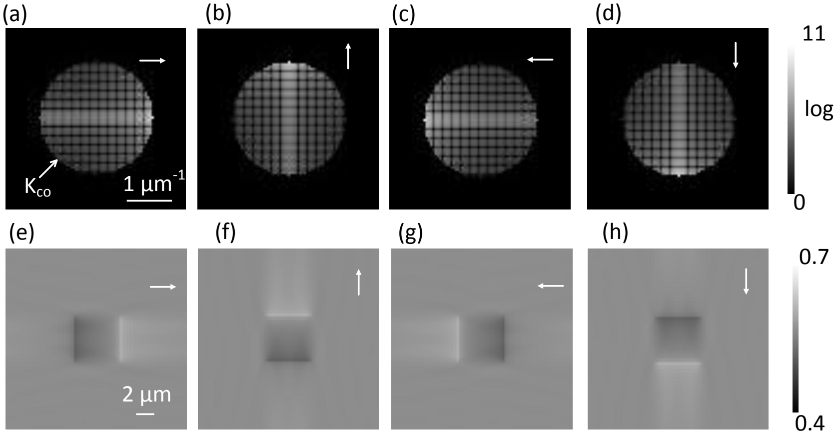

Figure 5.3: (a-d) The log-scale amplitude of Fourier transforms and (e-h) the linear-scale real space of the band-limited complex field $E_{bm}(\vec{r})$ with the oblique illumination orientated at 0, 90, 180 and 270 degrees, respectively.

5.2.2.2 Image process flow of the reconstruction algorithm

The intensity images record the amplitude information of the band-limited electric field but lose the phase information. Applying oblique illumination and working in a bright field configuration allows us to apply the KK-relations and retrieve phase information, see the discussion in section 2.3 in Chapter 2. In this part, we focus on the development of the reconstruction algorithm that is used to retrieve the phase information from the intensity of the signals. Figure 5.4 shows the flowchart of the

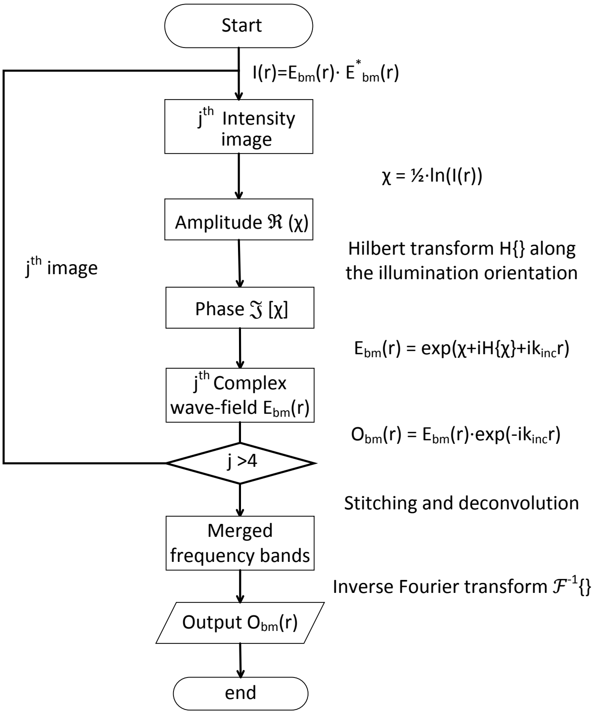

Figure 5.4: Flowchart of the reconstruction algorithm.

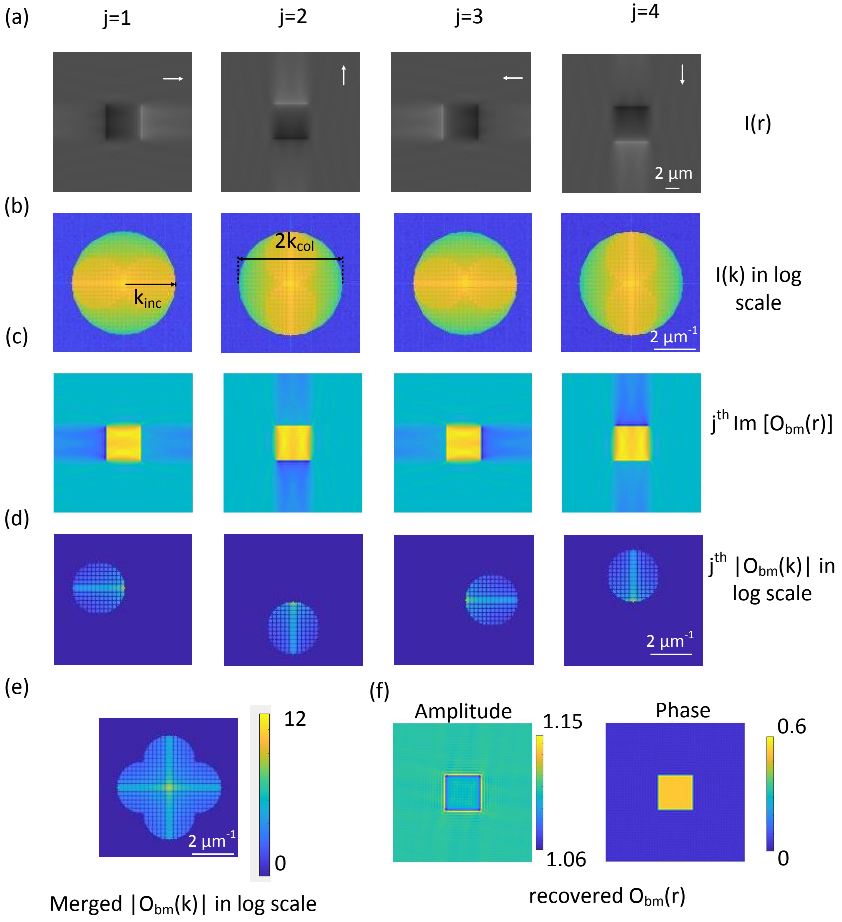

Figure 5.5: (a) Intensity images with different angled illuminations. (b) Fourier transforms of (a) in log scale. (c) Recovered phases of each intensity image. (d)Fourier transforms of (c) in log scale. (e) Retrieved complex field in Fourier domain. (f) Amplitude and phase images of the retrieved field in real space.

reconstruction algorithm. The intensity images of oblique illuminations (j= 1, 2, 3, 4) shown in Fig. 5.5(a) are imported one after the other to be processed. As the analyticity of the function of the scattered light is not guaranteed, here we define a complex function $\chi(\vec{r})$ as an intermediate function to tackle this issue. The real part of this intermediate function is given by the intensity image $\Re[\chi(\vec{r})] = \frac{1}{2}\ln I$. As shown in Fig. 5.5(b), the clear circular boundary indicates the effective bandwidth of the microscope objective. Through the Hilbert transform, the imaginary part of $\chi(\vec{r})$ is correlated with the real part by $\Im[\chi(\vec{r})] = -iH\{\Re[\chi(\vec{r})]\}$. To apply the Hilbert transform in the Matlab software, I have tested a built-in function named $'Hilbert'$ or defined a similar operator defined from a sign function. As follows:

$$H\{\vec{\chi}\} = -i \cdot \mathcal{F}^{-1}(sgn(\vec{k}) \cdot \mathcal{F}(\Re[\chi(\vec{r})])) \tag{5.4}$$

where function $sgn(\vec{k})$ is a sign function whose value depends on the illumination direction of the incident beam. With a beam illuminating along the positive k_x-axis, the sign function is defined as follows:

$$sgn(\vec{k}) = \begin{cases} -1 & k_x < 0 \\ 0 & k_x = 0 \\ 1 & k_x > 0 \end{cases}$$

Next, the complex field of each image is recovered from the intermediate function $\chi(\vec{r})$ by:

$$E_{bm}(\vec{r}) = e^{(\Re[\vec{\chi}\}] - iH\{\Re[\vec{\chi}]\} + i\vec{k}_{inc}\vec{r})} \tag{5.5}$$

This field is related to the band-limited object function O_{bm} as follows: $e^{i\vec{k}_{inc}\vec{r}}$ in view of the tilted illumination: $E_{bm}(\vec{r}) = O_{bm}(\vec{r}) \cdot e^{i\vec{k}_{inc}\vec{r}}$, where $O_{bm}(\vec{r})$ is the band-limited object function. In this work, the modulus of the wave vector of the incident light $|\vec{k}_{inc}|$ equals to that the maximum transmitted spatial frequency of the microscope objective k_{co}. The phase and log-scale amplitude spectrum of the recovered j^{th} complex object function $O_{bm}(\vec{r})$ are shown in figure 5.5(c) and (d), respectively. After stitching all the four k-space images of the complex fields $O_{bm}(\vec{r})$, the merged signal is deconvoluted to eliminate the effect of the overlap between the sub-bands, see Fig. 5.5(e). Finally, we obtain the objection function in particular its amplitude and phase after taking an inverse Fourier transform of the stitched band, see Fig. 5.5(f). With the knowledge of the refractive index of the object, we are able to retrieve the height information. In the case of oblique illumination, the refraction should be taken into account when we calculate the height from the recovered phase, which will be discussed in the next subsection. In this work, we assume that the polarization of the light is not changed after being scattered by objects. When the polarization of scattered light is modified by some materials or structures, the contrast of the image might be reduced, which leads to a lower signal-to-noise ratio.

5.2.2.3 Phase delay of oblique light induced by 3D objects

In this part, I calculate the phase delay of an oblique beam induced by a 3D object. Figure 5.6 shows the schematic of the light propagation of an oblique beam in an object. The phase of the transmitted field is determined with geometrical optics. A titled beam with an angle θ_1 incidents at the bottom of the object. The beam propagates directly from point O to point C without the presence of objects. The optical path difference between the point O and C can be written as:

$$OPD_{OC} = \frac{h}{cos(\theta_1)} \cdot n_1 \tag{5.6}$$

where n_1= 1 in the air. By contrast, the presence of the pure phase three-dimensional object induces the refraction of the light and changes the propagation path. The beam passing through the position A reaches the point C, after taking the refraction into account. As a result, the optical path difference between point A and C is given by:

$$OPD_{ABC} = h \cdot (tan(\theta_1) - tan(\theta_2))sin(\theta_1)n_1 + \frac{h}{cos(\theta_2)}n_2 \tag{5.7}$$

Considering Snell's law: $n_1 sin(\theta_1) = n_2 sin(\theta_2)$, we can obtain the phase delay introduced by the object:

$$\Delta\phi = \frac{2\pi}{\lambda_0}(OPD_{ABC} - OPD_{OC}) = \frac{2\pi}{\lambda_0}h(n_2 cos(\theta_2) - n_1 cos(\theta_1)) \tag{5.8}$$

This equation shows that the delayed phase of the transmitted light depends not only on the n value and height h of the object but also on the angle θ of the illumination. For the 50 nm square pillar structure at a NA_{ex} of 0.45, the simulated phase is 0.513 rad, see Fig. 5.5(f). This value matches well with the result of 0.512 rad obtained with the above equation. At this stage, we confirm that the developed algorithm is robust in phase reconstruction with ideal conditions, while in practice experiments are more usually carried out in some non-ideal conditions. The impact on the phase retrieval induced by non-ideal conditions will be investigated in the following subsections.

5.2.3 Impact of non-ideal conditions on the phase retrieval

5.2.3.1 Impact of laser line-width broadening

As we discussed in Chapter 2, high coherent light sources lead to speckles and decrease the spatial sensitivity in coherent imaging. The narrower linewidth of the laser leads to a stronger unexpected interference between the light scattered by the rough surface of the objects and generates speckles, resulting in artifacts

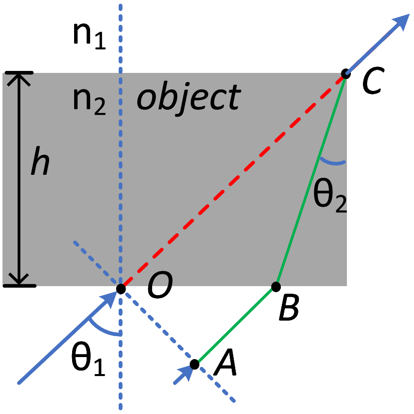

Figure 5.6: Schematic of the oblique-light propagation in mediums of different refractive index values

in the image reconstruction. In addition, the ripples produced by the interference between diffracted light can also cause artifacts. There are two typical methods to reduce the speckles and the ripples, either averaging the field over different angled illuminations or using a light source with a broad spectral linewidth. In this part, I investigate the impact of the spectral line widths of lasers on the technique of KK-relations-based phase imaging. Firstly, two kinds of light sources are investigated, one with only one frequency and another one with 5 nm broadening at a working wavelength of 360 nm. The height of the square pillar is set to 100 nm. The phase of the complex field function is recovered from the developed algorithm presented in subsection 5.2.2.2 and the phase of the complex object function is retrieved by the equation 5.8. In both cases, the proposed approach is able to retrieve the profile of the square pillar accurately, see Fig.5.7(a) and (c), respectively. The histograms are plotted in Fig. 5.7(b) and (d), respectively, to quantitatively investigate the retrieved height of the object. The height recovered by the ideal laser is 101.0 nm ± 2.3 nm, while the better matching value of 100.6 nm ± 2.0 nm is obtained using a source with a 5 nm broadening in the spectrum. As a consequence, the case with a broad light source shows slightly better accuracy in retrieving the true profile due to the fewer ripples generated by the diffraction. Next, I investigate the KK-relations-based QPI using light sources with different line-widths and square pillar objects of different heights, respectively. The studied light source includes an ideal single-frequency source and the source with broad linewidths of 50 pm, 500 pm, and 5000 pm, respectively. The heights of square pillars increase from 25 nm to 100 nm with a step of 25 nm. As shown in Fig. 5.8, the profiles are accurately recovered in all the cases. The simulated data indicated in red matches well with the dashed guiding line of the known height. The mismatch errors are lower than 1%. The error bar of the simulated data, estimated by the FWHM of the height peaks in the histogram plot, reveals the impact caused by the unexpected interference which is less than 2%. This result demonstrates that the impact of spectral broadening is negligible on phase retrieval.

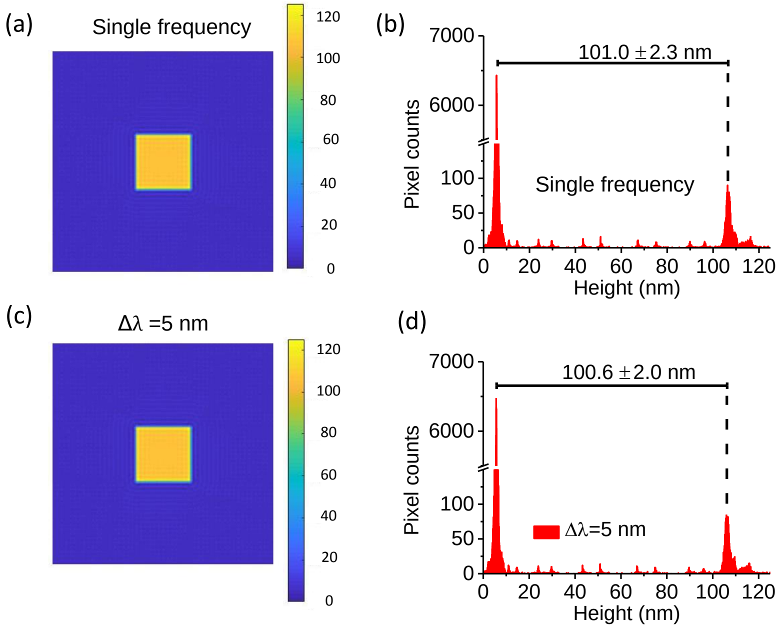

Figure 5.7: (a)Recovered height map using a source with a single frequency. (b) Histogram of (a). (c)Recovered height map using a source with a spectral linewidth (FWHM) $\Delta\lambda$=5 nm. (d) Histogram of (c).

5.2.3.2 Impact of the divergence of the illuminating beam

In the previous subsections, we assumed that the incident beam is an ideal plane wave with $E_{inc}(\vec{k}) = exp(i\vec{k}_{inc}\vec{r})$. However, there is a certain degree of divergence in the experiment due to the finite size of the beam or of the grating outcoupler. The impacts on the retrieval phase induced by this divergence will be investigated in this part. In FDTD simulation, a Gaussian beam is used for illumination and the divergence of which is varied from 0 to 0.4 degrees, see Fig. 5.9(a). Without a beam divergence, the beam is the same as the plane wave and the amplitude map of the field is homogeneous. By contrast, the amplitude profiles become Gaussian shape and the FoV becomes smaller with increasing divergence, while the phase maps are homogeneous. The FoV can be estimated by the FWHM of

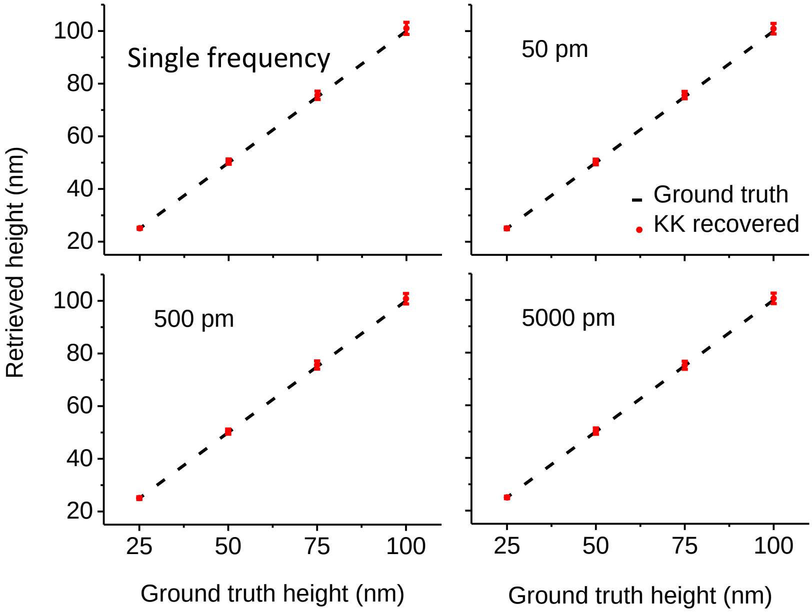

Figure 5.8: Comparison of recovered heights using light sources with a single frequency and with broadened spectral linewidths of 50 pm, 500 pm and 5000 pm, respectively.

the intensity profile of the beam. The phase images are retrieved without clear artifacts in these cases. To quantify the differences between the retrieved phase map in Fig. 5.9(a), the histograms of the height maps are analyzed and the retrieved heights are plotted in Fig. 5.9(b). The deviation between the ground truth and the retrieved height increases from 0.8% to 2.8% as the divergence increase from 0 to 0.4 degree, which concludes that an ideal plan wave without any divergence results in the best result. In our experiment, the divergence is around 0.1 degree, which implies the $1\ \%$ error of the retrieved phase is negligible.

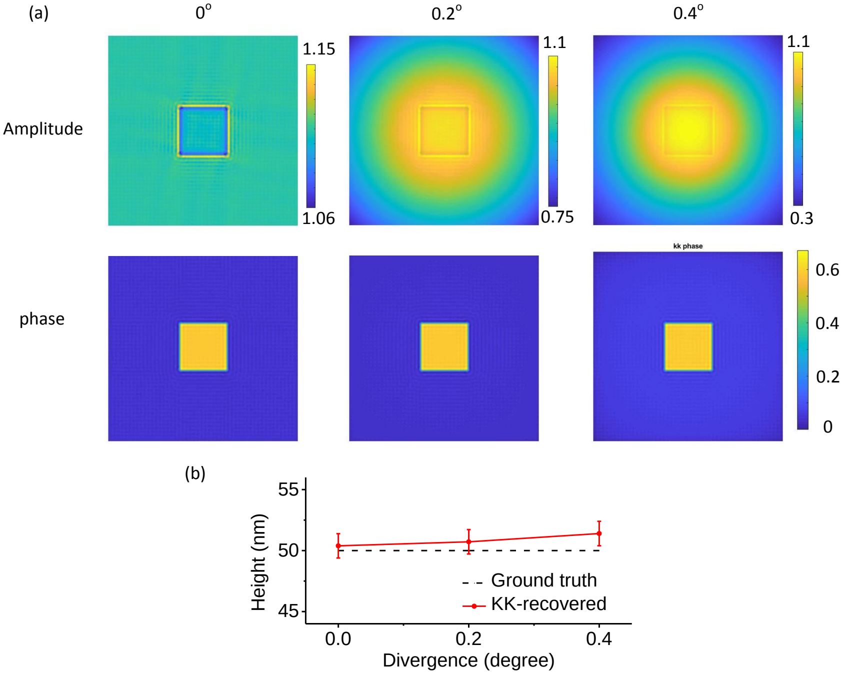

Figure 5.9: (a)Amplitudes and phases of the retrieved field at divergences of 0^o, 0.2^o *and* 0.4^o *respectively. (b) Evolution of the recovered height with the beam divergence.*

5.2.3.3 Impact of the numerical aperture mismatching

There are two conditions that need to be fulfilled to apply the space-domain Kramers-Kronig relations, as discussed in Chapter 2: the first one is working in the bright field to fulfill the analyticity and the other is vanishing one of the half-plane in the Fourier domain. These two conditions require that the angle of the illuminating beam has to match the maximum collection angle of the microscope objective, *i.e.* NA_{ex} = NA_{co}. In the case of $\mathrm{NA}_{co} < \mathrm{NA}_{ex}$, the microscope objective collects only the scattered light and misses the illumination beam, which fails to fulfill the first condition and leads to a completely incorrect phase retrieval. In the opposite case, the microscope objective collects the signals located in each half-plane of the k-space. This fails to fulfill the second condition of vanishing one of the half-planes in k-space. Due to the discrete property of digital images, it is not possible to simulate the case of the numerical aperture mismatching ΔNA smaller than the pixel unit. Here, a single pixel corresponds to a spatial frequency k of $0.05\,\mu m^{-1}$ and a ΔNA of 0.018 in the simulation. Figure 5.10(a) and (b) shows the amplitude and phase of the retrieved complex field which are obtained with one-pixel mismatching between the numerical apertures. The multiple peaks in the quantitative histogram of the phase map suggest the height deviates dramatically from the ground truth, see Fig. 5.10(c). This result confirms that there is a strict requirement for NA matching to implement KK-relations-based QPI. This means that the design of the UV-PICs should be carefully engineered to achieve perfect NA matching between the excitation and collection in the concept of the UV-PIC-based QPI.

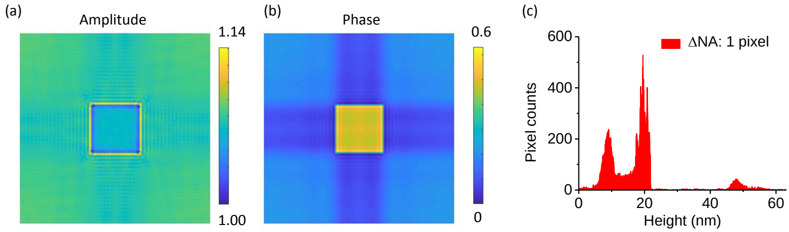

Figure 5.10: (a) Amplitudes image. (b) Recovered height map. (c) Histogram of (b). The numerical aperture mismatching is 1 pixel.

5.3 Design of UV-PICs for KK-relations-based QPI

The previous section focused on the development of the reconstruction algorithm for KK-relations-based QPI and the analysis of the impact of non-ideal conditions. Non-ideal conditions will lead to artifacts in the image reconstruction, in particular the mismatching between the excitation NA_{ex} and collection NA_{co}. To minimize the mismatch between the NA_{ex} and NA_{co}, I will design photonic integrated circuits to precisely control the angle of the illumination beam. This section introduces the design of 1x4 switches and grating out-couplers, the design and fabrication of pure phase objects, and the implementation of UV-PIC KK-relations-based QPI.

5.3.1 Design of necessary photonic components for UV-PIC-based QPI

5.3.1.1 Design of 1x4 switch on the ALD-AlO$_x$ UV-PIC platform

For a 2D high-resolution image, four oblique illuminations rotated by 90 degrees are needed to minimize the anisotropic spatial resolution. The orientation of the illumination can be controlled by the grating out-couplers. There are two ways to selectively activate one of the grating out-couplers, namely the on-chip switching approach and the off-chip switching approach. The off-chip switching approach has been implemented with the UV-PIC-based SIM technique in Chapter 3. The on-chip switching approach takes advantage of the on-chip switch to switch the input with electric injection and the key component is 1x4 switch. As shown in Fig.5.11, a typical on-chip 1x2 switch includes a 1x2 MMI, a 2x2 MMI, and two thermal phase shifters. The 1x2 MMI splits the incoming light into two paths with a split ratio of 50:50. The split two beams are combined at 2x2 MMI after one of the paths is modulated by the thermal phase shifter. Depending on the phase difference between the two optical paths, the intensity of the light at each output can be tuned from 0 to I, where I is the intensity of the input light. A 1x4 switch is constructed by cascading three 1x2 switches. As the designs of the thermal phase shifter and 1x2 MMI have been discussed in Chapter 4, here I focus on the design of 2x2 MMI.

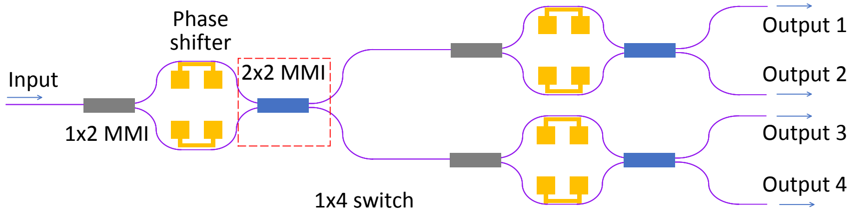

Figure 5.11: Schematic of photonic circuits of 1x4 switch.

The width of the 2x2 MMI and the thickness of AlO$_x$ layer are the same as the 1x2 MMI, namely 8 µm and 120 nm, respectively. For a 2x2 MMI coupler, the inputs and outputs are located at a distance of $\frac{W_e}{3}$ away from the boundary of MMI, see Fig. 5.12. From the analytical solution, the shortest length L of 2x2 MMI is given by $L = \frac{L_c}{2}$, where L_c is given by the equation 4.2 in Chapter 3. For an initial estimation, the effective MMI width W_e is approximated to MMI width $W_e \approx W = 8\mu m$. It follows that the estimated MMI length equals 199 µm. Then, the model is built according to the parameters estimated by the analytical solution, see Fig.5.12(a). The EME method is used to design the 2x2 MMI. The waveguide is tapered from 800 nm to 1.5 µm for a better coupling between the

MMI and the single-mode waveguide and a better tolerance in the fabrication. A fundamental TE mode is used as the source at the port 'input2' and the powers at the ports 'output1' and 'output2' are monitored. To find the optimum length of the multimode waveguide, the relationship between the normalized intensity at the outputs and the MMI length is simulated, shown in Fig. 5.12(b). The length of 180 µm is found to be the optimum length for the current configuration in view of the maximum output power. The 10% deviation of the MMI length between the analytical solution and the simulation may be explained by the approximation applied in the analytical method. The insertion loss is estimated to be 0.04 dB and the extinction ratio is as good as 44.5 dB. Ideally, the 2x2 MMI should be optimized for the two outputs to equally share the total power launched at the input, in order to minimize the insertion loss and maximize the extinction ratio of each output. The extinction ratio depends on the intensity of the light coming from each input:

$$ER = 10log(\frac{I_1 + I_2 - 2\sqrt{I_1 I_2}}{I_1 + I_2 + 2\sqrt{I_1 I_2}}) \tag{5.9}$$

where I_1 and I_2 are the intensities at the ports 'output1' and 'output2', respectively. The intensity profile of the beam propagation in the 180 µm-long multimode waveguide is shown in Fig. 5.12, which confirms that the intensities of the outputs are well balanced.

The 1x4 switch enables us to switch the route and grating out-couplers. The next critical component is the grating out-couplers, which determine the angle and orientation of the diffracted beams.

5.3.1.2 Design of Grating out-couplers with high precision control of angles

The grating out-coupler is the key structure to implement the UV-PIC for QPI. The precision of the illumination angle depends on its design. The optimization of the grating out-couplers is carried out in 2D-FDTD. As the previous grating out-coupler, the gratings are formed by etching a 120 nm-thick AlO$_x$ layer and have 1000 periods. A shallow etch depth of 20 nm is designed to maximize the coupling efficiency and at the same time achieve a large field of view. The filling factor and grating pitch are varied to target an effective numerical aperture of NA$_{ex}$ $= 0.45$ that precisely matches with that of the microscope objective NA$_{co}$. The substrate is a standard thermal oxidized silicon wafer with a 3 μm-thick layer of SiO_2. The principle of the on-chip grating design has been discussed in the section 4.2.1.3 in chapter4. The relationship between the grating pitch Λ and excitation numerical aperture NA$_{ex}$ is given by: $\Lambda = \frac{\lambda_{ex}}{NA_{ex}+n_{eff}}$, where λ_{ex}= 360 nm is the working wavelength, n_{eff} is the effective index of the Bloch mode propagating in the grating waveguide. Considering the grating is shallowly etched, the effective index n_{eff} is approximated with the value of the effective index of the fundamental TE mode of the unpatterned waveguide $n_{TE} = 1.51$. It follows that the estimated

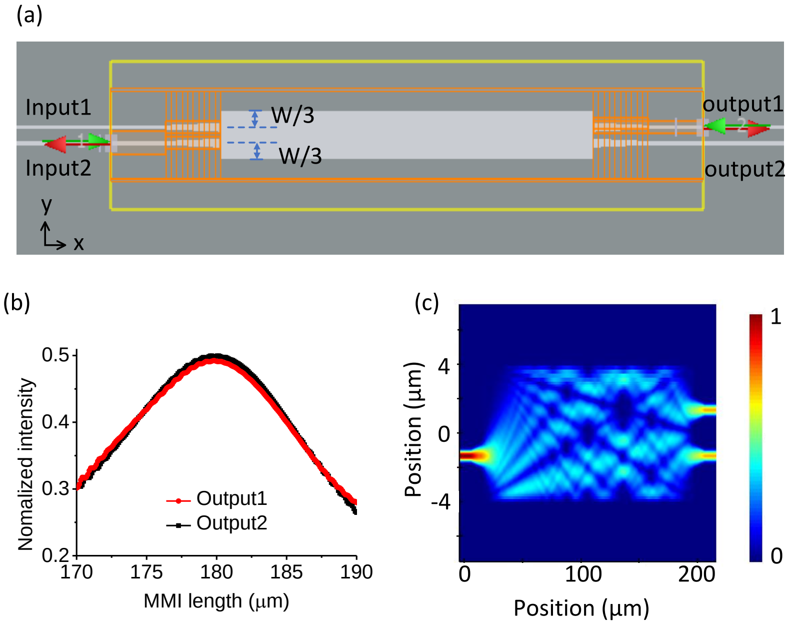

Figure 5.12: (a)Two dimensional model of the 2x2 MMI. MMI width $W = 8\mu m$. (d)Relationship between the normalized intensity at the outputs and the MMI length. (c) Intensity profile of the beam propagating in the 2x2 MMI.

grating pitch Λ equals 183.6 nm. Then, taking into account the deviation between the simulation and fabrication, several gratings are designed with different grating pitches ranging from 181 nm to 186 nm to sweep the NA$_{e}x$, in order to find the optimum. The relationship between the grating pitch Λ and the effective numerical aperture NA$_{ex}$ is shown in Fig. 5.13(a). Varying the filling factor from 0.8 (blue line) to 0.6 (red line) will shift the curve with a ΔNA of 0.005. Besides, the increment rate of NA$_{ex}$ over the grating pitch is estimated to be -0.01/nm. These results suggest that we are able to fabricate gratings of different NA$_{ex}$ values with a step as small as 0.005. In addition to the effective NA$_{ex}$, the radiant power is another crucial property of the grating out-coupler. Taking into account the back reflection at the bottom SiO$_2$/Si interface, the radiance efficiency varies with the emitted angle of the diffracted beam. The evolution of the radiant power versus the grating pitch is shown in Fig. 5.13(b). Around the desired NA$_{ex}$ $= 0.45$, the radiant power is as high as 55%.

The radiated beam has a certain broadening in spatial frequency (divergence) instead of a perfect plane wave due to the limited length of grating length. Note that working in a bright field configuration is one of the conditions to apply the KK-relations so that the slightly diverged beam should be also collected to avoid working in a partially dark field configuration. Figure 5.13(c) shows the beam profile, radiated from a grating out-coupler of ff= 0.8 and Λ=183 nm, in the spatial frequency domain. The full-width-at-half-maxima(FWHM) is estimated to be 0.03 µm^{-1} with respect to a $\Delta\theta$ of 0.11 degree. The space beam profile is plotted in Fig. 5.13(d). A large field of view of 150 µm is obtained. The intensity fluctuation inside the FoV can be normalized in the experiment by simply acquiring an image of the beam profile without any sample as a reference. Besides, as discussed in Chapter 4, the homogeneity of the diffracted beam can be improved by increasing the propagation length between the imaging area and the grating out-coupler. At this stage, all photonic components necessary for PIC-KK-relations-based QPI are designed. The next step is to connect these components on a single chip.

5.3.2 Layout design of UV-PICs for KK-relations-based QPI

This subsection introduces the layout design of the UV-PIC to implement the KK-relations-based QPI. There are two approaches to achieve the KK-relations-based QPI using PICs, namely the off-chip and on-chip switching approaches. They are named according to the way of switching the orientation of the diffracted beams. Fig. 5.14(a) shows the layout of the photonic circuits using the on-chip approach, which has a compact footprint of 0.6 cm x 1.0 cm. The grating out-couplers are spaced at a distance of 5 mm for convenient manipulation of the photonic chip. There are three different layers in the layout design. The first layer is designed for the fully-etched AlO$_x$ layer which is used for the routing waveguides, 1x2

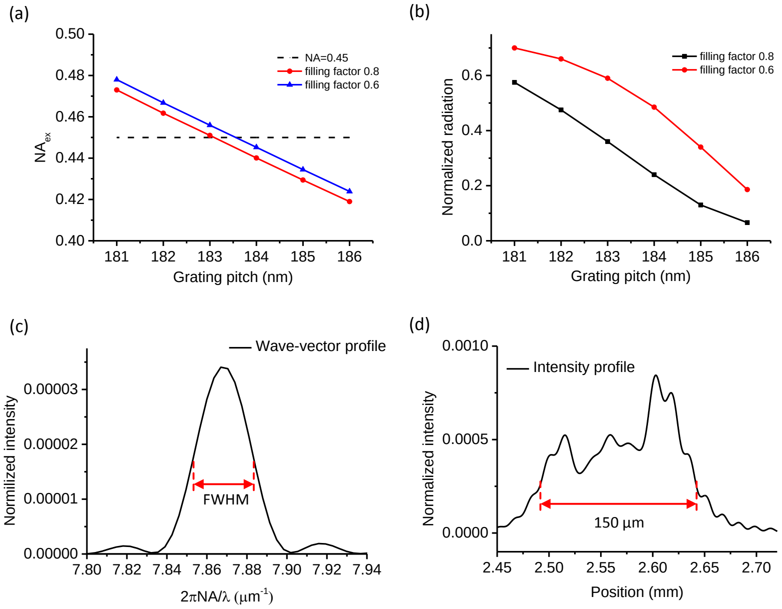

Figure 5.13: (a)Relationship between the grating pitch Λ and the effective numerical aperture NA_{ex}. (b) Relationship between the grating pitch and normalized radiant power. The data obtained with a filling factor of 0.8 and 0.6 are plotted in blue and red, respectively. (c) Beam profile in the spatial frequency domain. (d) Space beam profile captured at a horizontal distance of 2.5 mm away from grating input.

MMI, 2x2 MMI, and adiabatic tapers. The second layer is designed for patterning the grating modulation. The third layer indicated with the orange shaded box corresponds to the design of thermal heaters and square pads for the electrical injection. Each heater is designed in an arc shape surrounding the waveguides, with an edge-to-edge spacing of 1 μm, a width of 3 μm and a total length of 1 mm. In this design, there is only one input and no mechanical translation is required to implement beam switching, which is highly integrated and easy for packaging. However, the switch element introduces extra insertion losses due to the presence of multi-modal interferometers and extended waveguides. Alternatively, we can adopt an off-chip switching approach where the optical path is switched by laterally shifting the input fiber, see Fig. 5.14(b). This alternative approach simplifies the fabrication by avoiding three lithography steps and shortens the total length of circuits by removing the switch elements. In fact, we need to compromise between the low insertion loss and the high automation of beam switching. In other words, depending on the power budget or the integration level, we can choose either the off-chip switching (depicted in Fig. 5.14(b)) or on-chip switching (depicted in Fig. 5.14(a)), respectively.

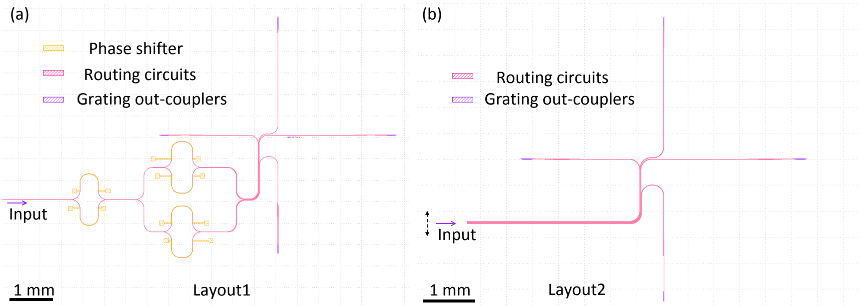

Figure 5.14: Layout designs of the (a) on-chip and (b) off-chip switching approaches.

5.4 Fabrication of UV-PICs for KK-relations-based QPI

As the techniques and the instruments involved in the fabrication of the UV-PICs are the same as the previous processes in Chapter 4, this section will skip the details of the process and directly exhibit the fabricated samples.

5.4.1 Fabrication of the routing circuit of UV-PIC

The fabricated routing circuits for the off-chip switching approach are shown in Fig. 5.15(a). Inspected by a standard optical microscope, the dimensions of the patterned structures are in line with what was designed in the layout, including the MMI and adiabatic taper. This shows the robustness of the process. The purple arrows indicate the position of broadened 20 µm waveguides, where the grating structures will be patterned in the next process to form grating out-couplers. The enlarged images of the inputs of the four different paths are shown in the dashed box, see Fig. 5.15(b). Each input is spaced at a lateral distance of 20 μm to eliminate the cross-talk between the different optical paths and allow a convenient switching.

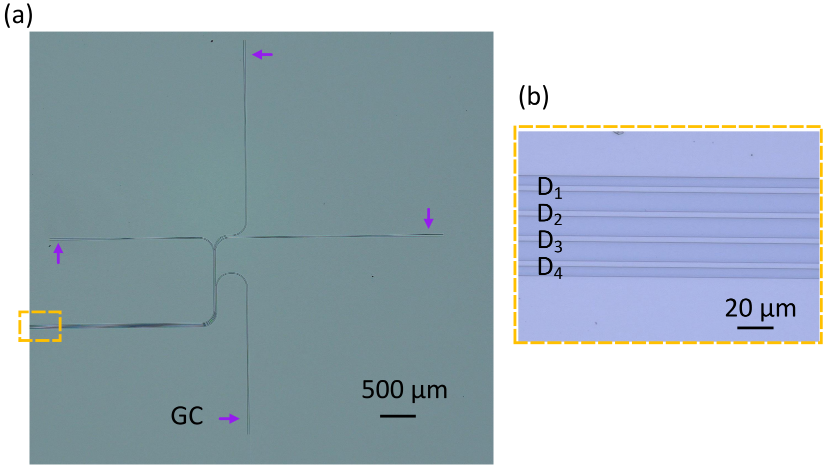

Figure 5.15: Optical images of the fabricated photonic circuits using layouts for (a)off-chip. (b) Optical images of the enlarged area indicated with the dashed yellow box in (a).

5.4.2 Fabrication of grating out-couplers with high precision control of angles

The designed gratings have a filling factor of 0.8 or 0.6 with a grating pitch of around 183 nm. The smallest structure is around 36.6 nm which is much smaller than the width of single-mode waveguides $\sim$ 800 nm. In principle, the EBL is able to pattern small features as small as $\sim$10 nm after taking into account the proximity effect. After considering the proximity effect, the optimized dose for such a grating structure is 208 $\mu C/cm^2$ which is higher than the standard dose of 160 $\mu C/cm^2$.

As the feature size of the grating is smaller than the optical resolution limit of the optical microscopy (200 nm), we are unable to inspect the individual line of grating structures with standard optical microscopy. It can be inspected by SEM if needed, as shown in Fig. 4.12 in Chapter 4. As the high energy electron beam used in SEM will damage the grating structures, the grating out-couplers have not been inspected by SEM here. Alternatively, they are characterized later by measuring the diffracted angles which can be used to deduce the grating pitch and filling factors of the gratings.

After etching the grating structure, the processes are completed by removing the residue SiN_x hard mask. At this stage, all components that are needed for the UV-PIC for the off-chip approach have been fabricated. By contrast, the UV-PIC designed for the on-chip approach needs the third step of lithography to pattern a metal layer and form thermal phase shifters for the 1x4 switch.

5.4.3 Fabrication of thermal phase shifters for 1x4 on-chip switch

Figure 5.16(a) shows the optical image of the completed UV-PIC designed for the on-chip switching approach. The UV-PIC is inspected under an optical microscope to ensure the lift-off process is completed. To see more details, the UV-PIC is inspected with a larger magnification, see Fig. 5.16(b) and (c). As the heater is designed as close as 1 µm to the waveguide structure, any gold particle residues on the waveguide will induce a high absorption loss on the waveguide and destroy the functionality of the 1x4 switch. This is currently the technology issue that needs to be solved in order to fabricate the UV-PIC designed for the on-chip switching approach. Therefore, the UV-PIC designed for the off-chip switching approach is used for the validation of the concept of the KK-relations-based QPI in this thesis.

5.5 Pure phase objects used to characterize the QPI technique

To experimentally validate the PIC-based phase imaging, we need an object with well-known features. Here, a standard 170 µm-thick cover glass made of D263M Schott glass is used as the substrate, with a refractive index of 1.547 at the working wavelength of 360 nm. This substrate is easy to access and more importantly transparent at λ=360 nm. The height information of the object is not detectable with standard optical microscopy, so the profiles of the fabricated structures will be measured by atomic force microscopy (AFM).

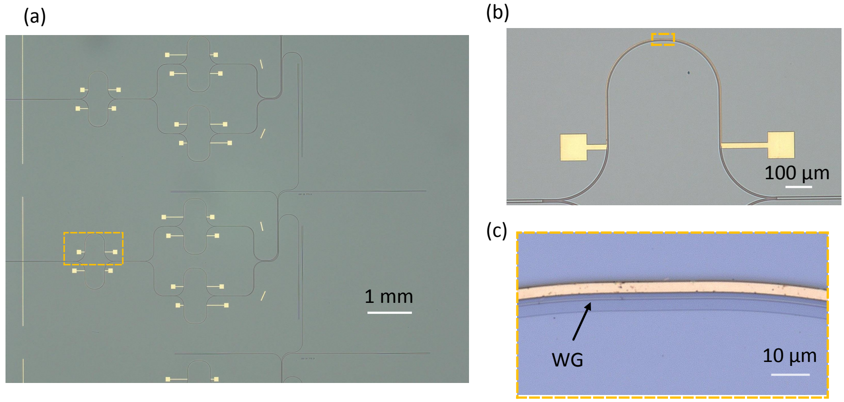

Figure 5.16: (a) Optical image of the fabricated UV-PIC. (b) Zoom-in thermal phase shifter. (c) Zoom-in image of the area in the dashed box in (b).

5.5.1 Design of pure phase objects

There are two patterns designed for the pure phase object, namely square pillar array and strip resolution target, see Fig. 5.17(a) and (b) respectively. The first design with an array of 5 μm x 5 μm squares is designed for analyzing the precision of the retrieved phase, while a strip resolution target is used to test the spatial resolution of the proposed microscopy technique. The spacing of the strips varies from 0.2 to 4 µm which is sufficient to investigate the resolution of the proposed UV-PIC-based QPI, considering the diffraction-limited resolution of the objective of NA_{co} = 0.45 is 400 nm at λ=360 nm in the case of oblique illumination.

5.5.2 Fabrication of the pure phase objects on standard cover glass

In view of the small line spacing of 200 nm, the structures of the pure phase object need also to be patterned by the EBL. The charging effect of the e-beam lithography can not be neglected when an insulating substrate such as the cover glass is used here. With the standard dose of 160 μC/ cm^2, the 200 nm-thick e-beam resist (ARP6200.09) on the cover glass will be overexposed. This leads to the disappearance of small structures like the 200 nm wide lines in the design. After optimization, the relative lower dose of 120 μC/ cm^2 is used to expose the e-beam resist and successfully pattern strips with a 200 nm-wide spacing. Then, the cover glass is etched with RIE using a gas mixture of CF_4/ H_2 with an etching rate of 47 nm/min. Followed by the O_2 plasma etching to remove the resist mask, the pure phase object is ready for use. The profile of the object acquired by the optical

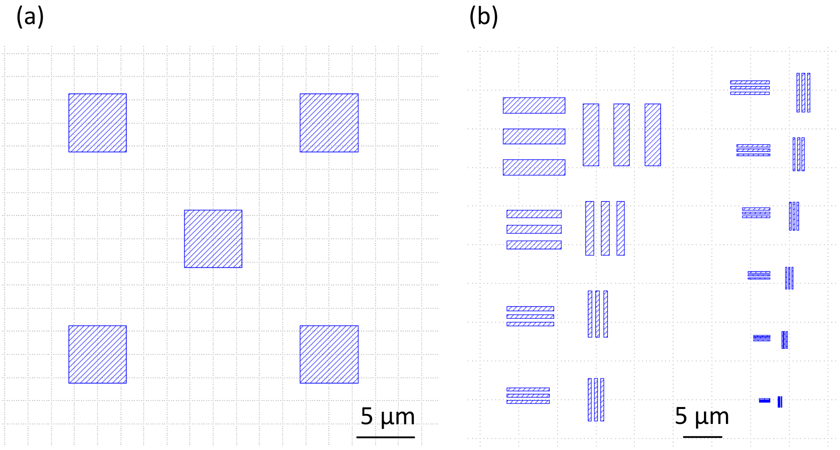

Figure 5.17: Designed layouts of the pure phase object with the pattern of the (a)square pillar array, (b) strip resolution target.

microscopy and atomic force microscopy are shown in Fig. 5.18 and Fig. 5.19, respectively. As shown in the optical images, features of the pure phase object are in line with the designed structures, but image contrast is very weak because the etched depth is below 50 nm. AFM is then employed to measure the height profile of the fabricated object, working in a non-contact mode. Analyzing the histogram of the measured image in Fig. 5.19(c), the height of the fabricated square pillar is determined to be 46.7 nm ± 5 nm. Considering the AFM offers a high vertical resolution up to 0.1 nm, we should be able to trust the measured profile in Fig. 5.19(a) and (c). It can be clearly seen that there are “spikes” present on the substrate after the dry etching of glass. The cover glass is made of many different materials including AlO_x and TiO_2. With a fluoride-based etching gas mixture, the etching rates of these two kinds of materials are much lower than the SiO_2, which forms the ’spikes’ on the surface of the cover glass. These spikes have a size of $\sim$10 nm which can not be resolved by optical phase microscopy but the height will be averaged to its near area in the retrieved height map. In order to be consistent with the case of optical microscopy, the measured profile in Fig. 5.19(a) is down-sampled and filtered, as shown in Fig. 5.19(b). The height of the square pillar in the filtered image is then determined to be 42.8 ± 5 nm by analyzing the histogram in Fig. 5.19(d). Besides, there are ’walls’ built at the edge of the square pillars. These may come from the re-deposition of the non-volatile etching products such as AlF_3 and TiF_3 during the etching.

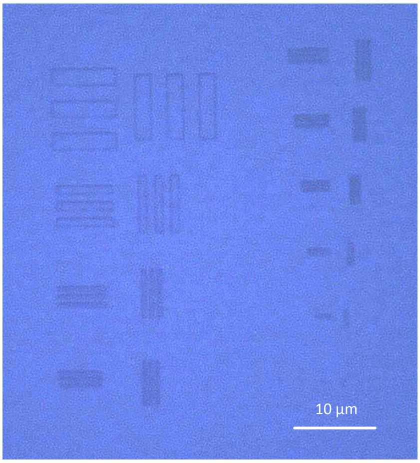

Figure 5.18: Optical image of the strip resolution target fabricated on the cover glass.

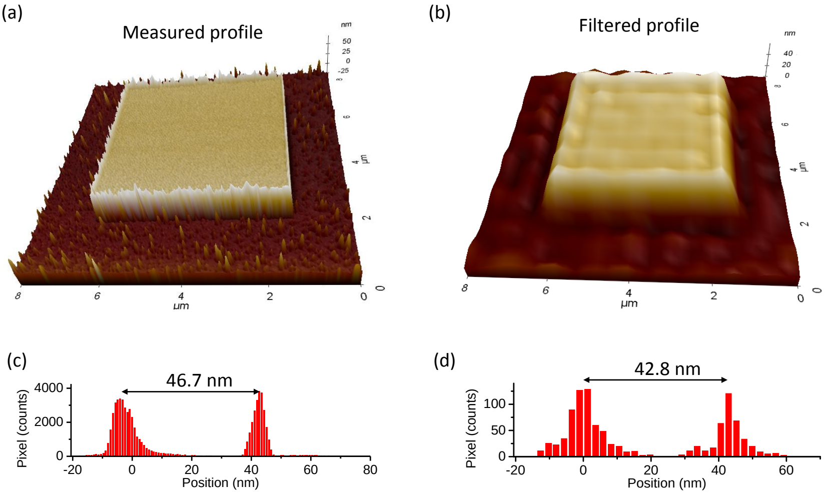

Figure 5.19: (a)Measured and (b)filtered height profile of the pure phase object acquired by the atomic force microscopy. (c-d) Histogram plots of (a) and (b), respectively. The height of the square pillar is estimated to be 46.7 nm and 42.8 nm for the measured profile and filtered profile, respectively.

5.6 Implementation of UV-PICs based QPI

In this section, we will discuss the characterization of the fabricated PIC and its use for space-domain KK-relations-based quantitative phase microscopy. From the simulation, we have realized that there is a strict requirement for the matching of numerical apertures to apply the space domain KK-relations. Even though the simulation shows that the KK-relations-based QPI is feasible, the experimental implementation can eventually lead to unexpected artifacts. Besides, it is crucial to quantify the impact of the experimental noise on the retrieved phase image.

5.6.1 Optical characterization of UV-PICs

The measurement setup of the UV-PIC-based QPI is the same as the one used for the characterization of UV-PIC-based SIM in Chapter 3. A microscope objective with a moderate NA_{co} of 0.45 is used as an example to validate the concept of PIC-KK-relations-based QPI. Other numerical apertures can also be possible but the design of grating out-couplers has to be modified. As discussed in the section 5.3.2, there are two approaches to implement the PIC-based phase imaging. Compared to the off-chip switching approach, the on-chip switching approach has an extra component, namely a 1x4 switch. To characterize the 1x4 switch, a UV laser with a working wavelength of 360 nm is coupled to the optical circuits. The light is split into two paths through a 1x2 MMI beam splitter and combined in a 2x2 MMI. Depending on the induced phase delay, the power ratio between the 2x2 MMI outputs can be adjusted by the thermal phase shifter. As shown in Fig. 5.20(a) and (b), the light can be switched from one output to another by applying a π phase shift, which corresponds to an applied voltage of 14 V for the current heater design. The relatively high V_π voltage is attributed to the low thermo-optic coefficient of the ALD-AlO$_x$. More importantly, the output is stable for a given applied voltage, namely applied phase delay. Figure 5.20(c) shows the intensity of the output over the 60s.

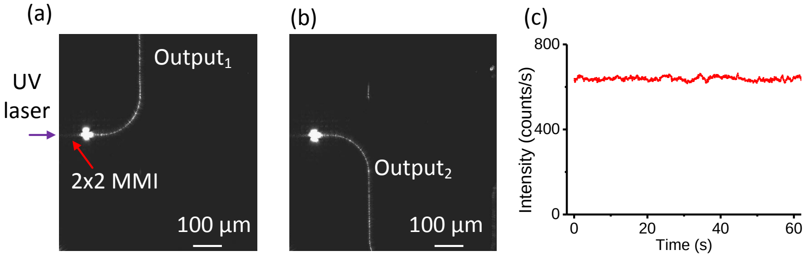

Figure 5.20: Optical image of the scattered light of the 2x2 MMI (a) with a 0 phase and (b) a π phase. (c) intensity variation at the output$_2$ in (b) over 60s time.

To image the intensity profile of the diffracted beam, the imaging plane of the objective is shifted from the chip surface to the illumination plane where four oblique beams come across. Figure 5.21(a-d) shows the measured profiles of each oblique illumination diffracted from the UV-PICs. The cross-sectional profile of the beam along the dashed red line in Fig. 5.21(c) is plotted in Fig. 5.21(d). A field-of-view of 48 µm along the illumination direction is determined by taking the FWHM of the profile. Our target is to match as accurately as possible the excitation angle with the maximum collecting angle. In other words, NA$_{ex}$ should be equal to NA$_{co}$. However, there are uncertainties in the design and fabrication. In order to mitigate the effect of these uncertainties, we have used a parameter sweep strategy. The parameters of the grating are swept and at the same time the numerical aperture NA$_{ex}$ of the diffracted beam is swept with a step of ΔNA = 0.005 around the desired value of 0.45.

The pure phase object with a square pillar array is used to investigate the illumination beam under three different cases of NA$_{ex} > NA_{co}$, NA$_{ex} = NA_{co}$ and NA$_{ex} < NA_{co}$ respectively. As shown in Fig. 5.22, it is clear that in the first case, the microscopy is working in the dark field, while it is working in bright filed imaging in the second and third cases. In this way, we are able to fine-tune the value of NA$_{ex}$ close to NA$_{co}$. From the intensity images shown in Fig. 5.22(b) and (c), it is difficult to determine whether the numerical aperture NA$_{ex}$ is matching with or is larger than the NA$_{ex}$. The reconstructed phase map or height map will give a more clear answer to this question in the following section.

5.6.2 Quantitative phase imaging with pure phase objects

In this part, we discuss the retrieved phase by using the experimental intensity images and compare the retrieved profile of the corresponding object with the profile measured with AFM.

The four intensity images illuminated by different oblique incident beams are acquired one after another, see Fig.5.23. Next, these intensity images are processed by the developed algorithm to retrieve the phase of the complex field. Then, with the knowledge of the refractive index n of 1.547, the recovered phases are converted to the height of the object function with the equation 5.8 to compare with the known height, see Fig. 5.24(a). Despite the slight non-homogeneity of the illuminating beam, the height is quite accurately retrieved as demonstrated below. Before performing the phase reconstruction, the raw intensity images are normalized with the intensity of the illuminating beams in order to remove the impact of the non-homogeneous beam profile. As shown in Fig. 5.24(b), the total amplitude of the field is in the range of 0.85 and 1.5, which suggests that the amplitude of the scattered beam E_s is smaller than the unscattered beam E_u. This confirms that the imaging is working in a bright field and the assumption of weak scattering

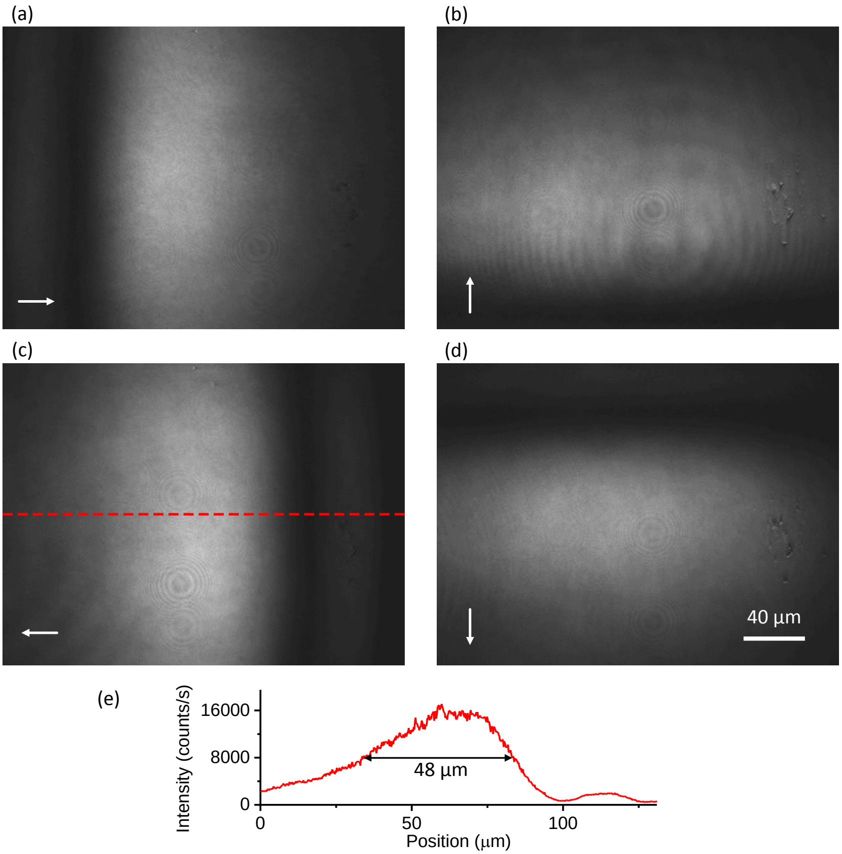

Figure 5.21: (a-d)Intensity profiles of the beam scattered from the fabricated photonic integrated circuits. (e) Intensity of the line indicated in (c). The full-width-at-half-maximum of the profile is estimated to be 48 µm.

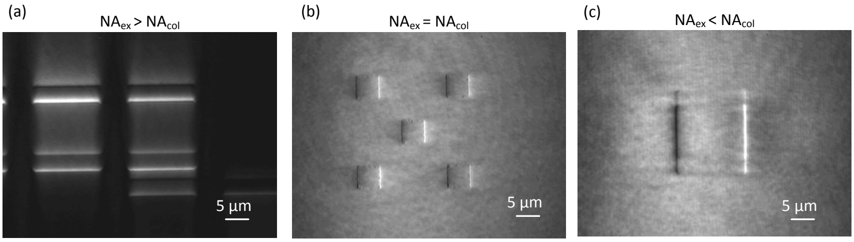

Figure 5.22: Optical images of the square pillar array illuminated by the beam with (a) $NA_{ex} > NA_{co}$, (b) $NA_{ex} = NA_{co}$ and (c) $NA_{ex} < NA_{co}$, respectively.

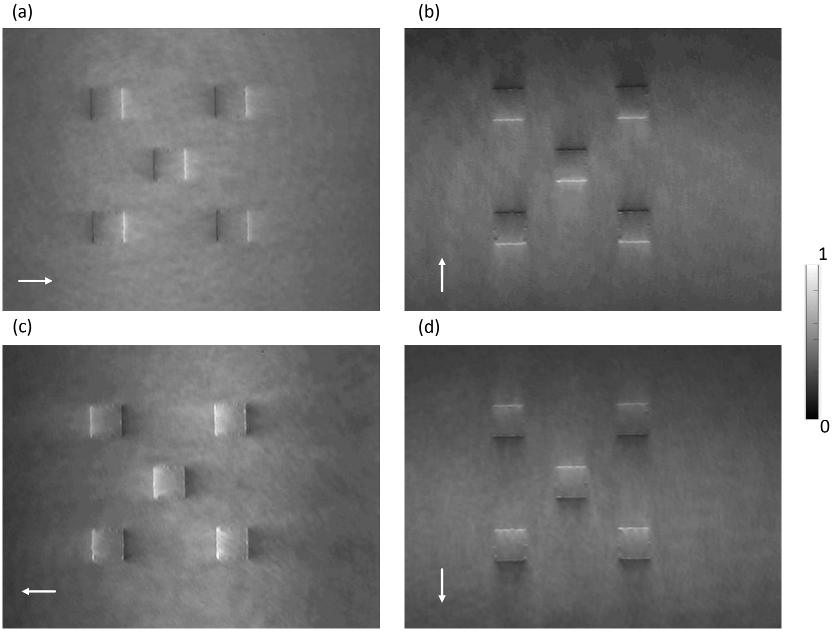

Figure 5.23: (a-d) Optical intensity images of the square pillar array obtained with different oblique illuminations rotated by a step of 90 degrees. The NA of illumination matches with the collection objective NA$_{ex}$ $= NA_{co}$.

is fulfilled. The cross-sectional profile along the red dashed line in Fig. 5.24(a) is plotted in Fig. 5.24(c). It is worth noting that the ’walls’ built at the edge of the square pillars captured by the AFM are also visible with the proposed quantitative phase microscopy. The value of height decreases a lot at the boundary of the image, which is the artifact caused by the discontinuity at the boundaries. The histogram of the height map is further analyzed to statistically evaluate the height of the square pillar array. A value of 43.1 nm ± 7.5 nm is obtained from the histogram, which agrees well with the value of 42.8 ± 5 nm measured by the filtered AFM image.

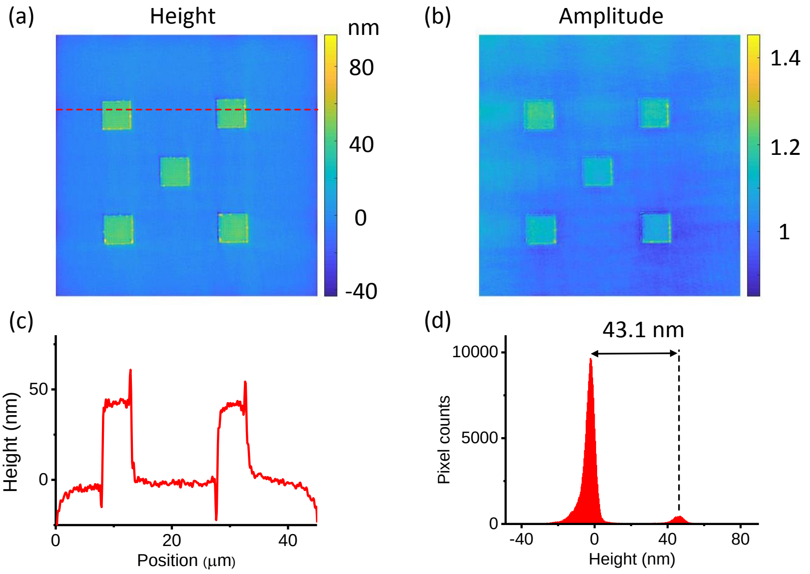

Figure 5.24: (a) Retrieved height map of the array of square pillars. (b) Amplitude of the light field transmitted through the array of square pillars. (c) Cross-sectional profile along the dashed red line indicated in (a). (d) Histogram of (a).

5.6.2.1 Estimation of the transverse optical resolution

In general cases, the features of the object are more complicated than simple periodical square pillar structures. To validate the capability of the phase imaging of complex objects, we have imaged a strip resolution target with the UV-PIC-based QPI technique. The variation of the line spacing in the resolution target allows us to estimate the optical resolution. The height map and amplitude image are shown in Fig. 5.25(a) and (b), respectively. The height map of the strips are well recovered and no strong artifact induced by speckles are present. The cross-sectional along the dashed red line in Fig. 5.25(a) is plotted in Fig. 5.25(c). From the left to right, the line spacings in four different sets of strips decrease from 700 to 400 nm with a step of 100 nm. It can be seen that the proposed method is capable of resolving features with a spacing of 400 nm, reaching the theoretical resolution limit of the configuration. It follows that the proposed method offers two times the higher resolution compared with conventional microscopy using normal illuminations.

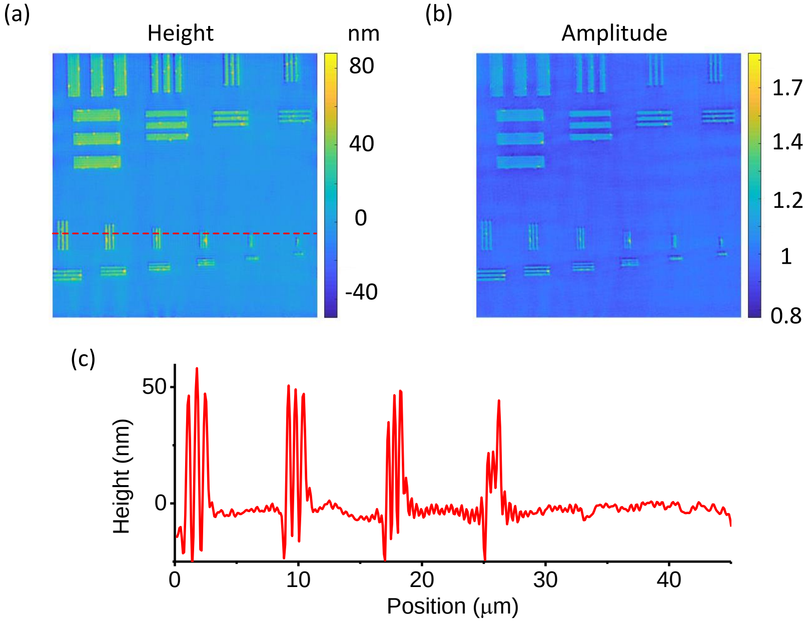

Figure 5.25: (a)Retrieved height map and (b)amplitude of the strip resolution target, respectively. (c) Cross-sectional profile along the dashed red line indicated in (a).

5.6.2.2 Estimation of the Spatial phase resolution

For quantitative phase microscopy, it is always important to characterize the minimum distinguishable phase or height in the reconstructed image. This value is mainly determined by the speckles due to the high coherency of the illumination. To measure the spatial phase resolution, we image a blank area on the cover glass where no etching is performed. Four intensity images, obtained with four different oblique illuminations respectively, are used as the background to normalize the profile of the illuminating beam. Then, the cover glass is laterally translated to another close-by blank area to acquire another set of four frames. The data are processed with the reconstruction algorithm to retrieve the phase of the field. Figure 5.26 shows the height map of the blank sample. It reveals the spatial phase noise that is characterized by a standard deviation of the phase map over the entire field σ= 1.4 mrad. It follows that a spatial height resolution of σ_h= 1.3 nm is achieved, given that the refractive index of the glass is 1.547. Considering monolayer graphene has a refractive index of 2.8 at the working wavelength of 360 nm [6], the phase resolution of 1.4 mrad corresponds to a height resolution of 0.395 nm on this material. The bilayer of graphene has a thickness of 0.345 nm. It means the proposed technique is promising to distinguish the bilayer graphene from the multiple layers. The histogram of the height map is plotted in Fig.5.26(b). The distribution of height is in a Gaussian-like shape with an average height of 77 pm. With the current off-chip switching approach, the spatial phase noise is expected to be limited by the perturbation induced by manually translating the input fiber when switching the orientation of illuminating beams. Implementing the on-chip switching approach may further decrease the spatial phase noise. Nevertheless, the current spatial phase sensitivity is comparable with the result σ_h= 1.8 nm obtained with bulky optics based on the KK-relations [3].

Here, the temporal resolution of the PIC-based QPI technique is limited by switching between different circuits. By implementing the on-chip switching approach, this technique can achieve a sub-second high temporal resolution.

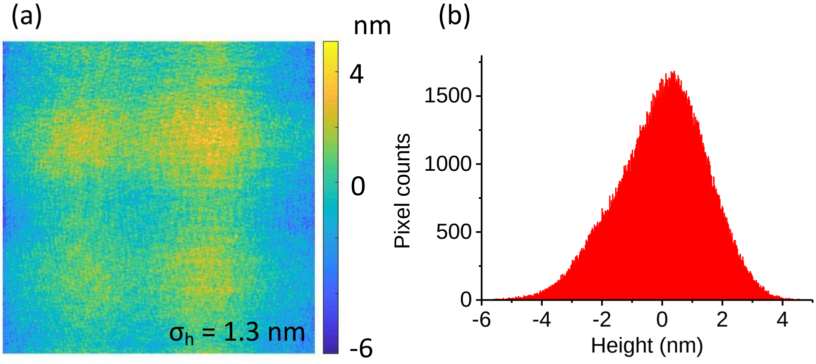

Figure 5.26: (a)Height map of a blank sample. The spatial phase noise is determined to be 1.4 mrad, corresponding to a height resolution of 1.3 nm. (b)Histogram of (a).

5.7 Conclusion

In this chapter, I have presented a quantitative phase imaging technique that makes use of the KK-relations and a UV photonic integrated circuit. It starts with the simulation of the KK-relations-based QPI technique, which validates the concept numerically and investigates the impact of non-ideal conditions. Followed by the design and fabrication, the UV-PIC is successfully applied for the KK-relations-based QPI. It achieves a high phase sensitivity with a value as low as 1.4 mrad which corresponds to a height resolution of 1.3 nm. This value is slightly better than the result obtained with bulky optics using the same KK-relations-based method. These results not only validate the feasibility of the proposed method but also demonstrate that the UV-PIC is able to upgrade a conventional microscope to a quantitative phase microscope in a low-cost and compact way. More importantly, using the on-chip switching approach is expected to further decrease the spatial phase noise and outperform the bulky optics due to its compact size. This UV-PIC-based QPI has strong potential to play a role in imaging transparent objects including biological cells, in view of its compatibility with conventional microscopes and low cost.

References

[1] YoonSeok Baek, KyeoReh Lee, Seungwoo Shin, and YongKeun Park. *Kramers–Kronig holographic imaging for high-space-bandwidth product*. Optica, 6(1), 2019.

[2] YoonSeok Baek and YongKeun Park. *Intensity-based holographic imaging via space-domain Kramers–Kronig relations*. Nature Photonics, 15(5):354–360, 2021.

[3] C. Lee, Y. Baek, H. Hugonnet, and Y. Park. *Single-shot wide-field topography measurement using spectrally multiplexed reflection intensity holography via space-domain Kramers-Kronig relations*. Opt Lett, 47(5):1025–1028, 2022.

[4] D. L. Misell and A. H. Greenaway. *An application of the Hilbert transform in electron microscopy: I. Bright-field microscopy*. Journal of Physics D: Applied Physics, 7(6):832–855, 1974.

[5] D. L. Misell and A. H. Greenaway. *An application of the Hilbert transform in electron microscopy: II. Non-iterative solution in bright-field microscopy and the dark-field problem*. Journal of Physics D: Applied Physics, 7(12):1660–1669, 1974.

[6] J. W. Weber, V. E. Calado, and M. C. M. van de Sanden. *Optical constants of graphene measured by spectroscopic ellipsometry*. Applied Physics Letters, 97(9):091904, 2010.

6

Conclusion and Perspectives

6.1 Conclusions

The main targets of this work were developing a platform of photonic integrated circuits operating at UV wavelengths and demonstrating its application for advanced microscopy techniques. There are varieties of material platforms for PIC working at visible and infrared wavelengths but limited by absorption and scattering loss they are not compatible with UV wavelengths. The development of UV-PIC can benefit a tremendous of fields including quantum information, on-chip bio-sensing, and advanced microscopy. Among them, advanced microscopy techniques including super-resolved structured illumination microscopy and quantitative phase imaging were proposed and developed decades ago, while they are not widely used due to their complicated optical system and high cost. Benefiting from the properties of compactness, low cost, and compatibility with massive production, the UV-PIC used as an add-on module to conventional microscopes is not only a solution to this issue but also able to extend the working wavelength of microscopes to the UV range.

Firstly, I have developed low-loss integrated waveguides operating in UV. The direct absorption of UV light takes place in a lot of different materials due to their limited bandgap. The ALD-HfO$_x$ and AlO$_x$ were selected to be investigated as the waveguide core layer in view of their high bandgaps of $\sim$6.2 eV and $\sim$5.5 eV, respectively. Two kinds of waveguide geometries were simulated by taking advantage of ALD techniques, namely etch-free waveguides and standard etched strip waveguides. The strip waveguide shows a lower bend loss, which allows us to integrate more circuits but suffers more scattering loss due to the etched side walls. Then, we optimized the etching process of ALD-HfO$_x$ and ALD-AlO$_x$. The fluorine-based gas mixture was demonstrated to be an improper etching medium for these materials due to the presence of non-volatile etching residues. Alternatively, the chlorine-based gas mixture of BCl_3/ Cl_2/ Ar showed a faster etching rate and smoother side walls. The ALD-HfO$_x$ waveguide showed high absorption loss, while single-mode low-loss ALD-AlO$_x$ waveguides were achieved with a value of 3 dB/cm at a working wavelength of 360 nm. Consequently, I designed and fabricated optical circuits based on the ALD-AlO$_x$ platform for the application of microscopy.

Secondly, the UV-PIC was designed and fabricated for the generation of structured illumination and used for unveiling the mechanism of spatial frequency mixing experimentally. Optical components including a 1x2 MMI beam splitter, an adiabatic taper, and a pair of grating out-couplers were designed by the EME/ FDTD methods in the Ansys Lumerical software. The MMI beam splitter was designed with a split ratio of 50:50 to maximize the visibility of the structured illumination pattern. An adiabatic taper was used for expanding the waveguide width without introducing insertion loss and keeping the single-mode propagation. A shallow etch depth of 10 nm was designed on grating out-couplers for a large FoV illumination of 150 $\mu m \times 200 \mu m$. A slightly larger etch depth of 30 nm was designed for a high irradiance with a coupling efficiency of 70%, but it resulted in a smaller FoV of $\sim$30 $\mu m \times 30 \mu m$. The UV-PIC was designed not only for generating but also for adjusting the structured illumination in the far field in terms of phase by using a thermal phase shifter. The on-chip thermal phase shifter made of a metallic stack layer of Ti/Au was designed adjacent to the waveguides at a distance as close as 1 μm, which has a V_π of 14 V. Next, the UV-PIC generated structured illumination was used to excite the homemade fluorescent gratings and unveil the mechanism of spatial frequency mixing. Furthermore, I have also demonstrated that the UV-PIC-based SIM is capable of improving the optical resolution of a conventional microscope by a factor of 1.84, which was characterized by a fluorescent Siemens star target. More importantly, the UV-PIC-based SIM achieved super-resolved label-free imaging with biological cells, taking advantage of the auto-fluorescence of intrinsic molecules NADH inside yeast cells.

Finally, I proposed a UV-PIC-based quantitative phase imaging technique. Quantitative phase imaging is a powerful tool to investigate transparent samples like biological cells and reveals the chemical compounds and geometry dimensions without the need for labeling. Generally, an interferometry setup is required to be involved for quantitative phase imaging. Here, I used the intensity-based quantitative phase imaging method based on the Kramers-Kronig relations to recover phase information from the intensity images. It allows us to retrieve the phase in a robust way but requires a high accuracy control of the angles on the oblique illumination. Benefiting from the compatibility with large-scale fabrication, I designed and fabricated the UV-PICs to deliver oblique beams with a numerical aperture NA_{ex} matching with that NA_{col} of microscope objectives with an accuracy of ΔNA_{ex}= 0.005. The UV-PIC-based QPI experimentally achieved an optical resolution of 400 nm with a NA_{col} of 0.45 and a working wavelength of 360 nm. Furthermore, the phase sensitivity was measured to be 1.4 mrad which is comparable with that measured with bulky optics.

6.2 Perspectives

6.2.1 UV-PICs for multi-modal advanced microscopy

Currently, super-resolution microscopy is mainly taking advantage of fluorescent dyes. Although it is able to achieve a high optical resolution, the photobleaching issue of the fluorescent dye hampers its application for imaging over a long exposure time. By contrast, quantitative phase imaging is able to recover the phase information of objects using coherent light illumination without the need for fluorescent dyes, which allows us to inspect objects with no acquisition time limit. However, the lateral optical resolution of QPI techniques is diffraction-limited. Therefore, there is a need to combine super-resolution microscopy with quantitative phase imaging in one instrument, namely multi-modal microscopy, to inspect either in a long acquisition time or with a high optical resolution. In this thesis, we have demonstrated that the UV-PICs are capable of label-free super-resolved structured illumination microscopy and quantitative phase imaging, respectively. The next step of integrating the designs of these two PICs in a single photonic chip will allow us to achieve multi-modal advanced microscopy in a compact, cost-effective way.

6.2.2 UV-PICs for trapped ion quantum computing

The emergence of UV-PIC can benefit not only the field of microscopy but also many others. Trapped ion quantum computing is one of the promising techniques to realize practical quantum computers, in view of its high fidelity and stability. However, the current configuration is bulky and difficult to be scaled due to the need for different lasers and electric components. The photonic integrated circuits have been recently demonstrated to be scalable platforms for trapping and controlling ions [1]. As an example, the Strontium ion Sr^+ was investigated with a surface electrode ion trapping approach. Four lasers with different working wavelengths from violet to infrared light were coupled into a single chip and shaped by grating couplers to focus and control the ion. However, the SiN PIC platform can not support beam manipulation with a low loss at UV wavelengths. For controlling more popular ions such as Ytterbium Yb^{+} ions which have hyperfine structures with an energy spacing in an order of $\sim$GHz and a long decay time [2], UV light has to be involved. The ALD-AlOx platform that has been developed in this thesis is expected to facilitate the development of scalable trapped ion quantum computers by offering the UV light manipulation in a compact and low-loss way.

6.2.3 Hybrid platform of ALD-AlO$_x$/ SiN$_x$ for UV/Vis wavelengths

In many applications like the trapped ion computing mentioned above, there is a need for manipulating simultaneously the UV and visible light. The current ALD-AlO$_x$ platform is suitable for operating at near UV and violet wavelengths but it is not interesting for visible and near-infrared (NIR) wavelengths in view of the limitation of the ALD technique. A thicker layer is required to confine the light at a longer wavelength, which results in a long deposition time of $\sim$days for the ALD technique. Besides, the dimension of AlO$_x$ waveguides and circuits is relatively large due to its low refractive index n of ~ 1.7. By contrast, the SiNx platform is more suitable to operate at visible/NIR wavelengths in view of its technological maturity, short layer deposition time ($\sim$10 minutes), and higher n value of 2. In this context, it is interesting to integrate these two materials in one single chip and enable an efficient manipulation of UV, visible and NIR light with a low propagation loss. In particular, it is easy to integrate them from the processing point of view. In this thesis, I have already demonstrated the integration of these materials by using the PECVD-SiN$_x$ layer as a hard mask and removing it at the end of processes, while it can stay on top of the ALD-AlO$_x$ layer and form a hybrid core layer of AlO$_x$/SiN$_x$ to confine and guide light at longer wavelengths. It follows that the circuits that are made of the ALD-AlO$_x$ and made of the hybrid core layer of SiN$_x$/AlO$_x$ are engineered to guide UV light and Vis/NIR light, respectively.

References

[1] R. J. Niffenegger, J. Stuart, C. Sorace-Agaskar, D. Kharas, S. Bramhavar, C. D. Bruzewicz, W. Loh, R. T. Maxson, R. McConnell, D. Reens, G. N. West, J. M. Sage, and J. Chiaverini. *Integrated multi-wavelength control of an ion qubit.* Nature, 586(7830):538–542, 2020.

[2] Colin D. Bruzewicz, John Chiaverini, Robert McConnell, and Jeremy M. Sage. *Trapped-ion quantum computing: Progress and challenges.* Applied Physics Reviews, 6(2), 2019.

A

SIM reconstruction algorithm

This appendix includes the Matlab codes used in this thesis for the image reconstruction of SIM images using nine raw frames. This algorithm includes one main file ($'Main.m'$), which reads and processes raw images before displaying the results in the end. Besides, there are Six functions involved in the process, which are modified from the OpenSIM [1]. The first function $'PsfOtf.m'$ is used to generate an ideal point spread function and optical transfer function of a given microscope objective. After importing the raw images, an edge tapering filter is applied to minimize the artifacts induced by the discontinuity of the images at the boundary. The spatial frequency of the structured illumination is estimated by determining the maxima of the sum of the cross-correlations between the raw image and its laterally shifted image in the Fourier domain, using the iterative function $'LowK\_Freq.m'$ and $'PhaseKai2opt.m'$. After successfully estimating the spatial frequency $|2\vec{k}x|$ (see Chapter 2), the phase of the structured illumination is estimated by determining the maxima of the sum of the product of the raw image and the standard sinusoidal function in the space domain, using the functions $'LowK\_phase.m'$ and $'PatternPhaseOpt.m'$. The standard sinusoidal function is defined with the estimated spatial frequency $|2\vec{k}x|$ of structured illuminations. The accurate estimation of the spatial frequency and the phase allows us to disentangle the mixed frequency bands in raw images using the function $'LowK\_disentangle.m'$. After the disentangled frequency bands are shifted and stitched in the Fourier domain, the merged image is deconvoluted by applying a Wiener filter in the main function $'Main.m'$. Finally, the reconstructed image in the space domain is obtained after performing an inverse Fourier transform.

Main.m

```
clear all;
close all;
clc;


%raw images read
ccm1=imread('dapa.tif');
ccm1=double(ccm1(:,:,1));
ccm2=imread('dapb.tif');
ccm2=double(ccm2(:,:,1));
ccm3=imread('dapc.tif');
ccm3=double(ccm3(:,:,1));
ccm4=imread('dbpa.tif');
ccm4=double(ccm4(:,:,1));
ccm5=imread('dbpb.tif');
ccm5=double(ccm5(:,:,1));
ccm6=imread('dbpc.tif');
ccm6=double(ccm6(:,:,1));
ccm7=imread('dcpa.tif');
ccm7=double(ccm7(:,:,1));
ccm8=imread('dcpb.tif');
ccm8=double(ccm8(:,:,1));
ccm9=imread('dcpc.tif');
ccm9=double(ccm9(:,:,1));

% OTF PSF generation
[w,h]=size(ccm1);
NA=0.95;%Objective NA
lambda_em=511;%emission wavelength
size_ppixel=68.6;%pixel size
[Ktof, OTFo]=PsfOtf(w,h,NA,lambda_em,size_ppixel); %
    generate ideal OTF
PSF=abs(fftshift(ifft2(OTFo)));

%%modulation factor determined from transmitted UV
    image
m1=0.88;%
m2=0.89;%
m3=0.91;
kp=362;%fringe spacing

%edge tapering to minimize ring effect
p=20;
```

```
ccm1=edgetaper(ccm1,PSF(w/2-p+1:w/2+p,w/2-p+1:w/2+p));
ccm2=edgetaper(ccm2,PSF(w/2-p+1:w/2+p,w/2-p+1:w/2+p));
ccm3=edgetaper(ccm3,PSF(w/2-p+1:w/2+p,w/2-p+1:w/2+p));
ccm4=edgetaper(ccm4,PSF(w/2-p+1:w/2+p,w/2-p+1:w/2+p));
ccm5=edgetaper(ccm5,PSF(w/2-p+1:w/2+p,w/2-p+1:w/2+p));
ccm6=edgetaper(ccm6,PSF(w/2-p+1:w/2+p,w/2-p+1:w/2+p));
ccm7=edgetaper(ccm7,PSF(w/2-p+1:w/2+p,w/2-p+1:w/2+p));
ccm8=edgetaper(ccm8,PSF(w/2-p+1:w/2+p,w/2-p+1:w/2+p));
ccm9=edgetaper(ccm9,PSF(w/2-p+1:w/2+p,w/2-p+1:w/2+p));

%Fourier transform of image
FTcm1 = fftshift(fft2(ccm1));
FTcm2 = fftshift(fft2(ccm2));
FTcm3 = fftshift(fft2(ccm3));
FTcm4 = fftshift(fft2(ccm4));
FTcm5 = fftshift(fft2(ccm5));
FTcm6 = fftshift(fft2(ccm6));
FTcm7 = fftshift(fft2(ccm7));
FTcm8 = fftshift(fft2(ccm8));
FTcm9 = fftshift(fft2(ccm9));

%normalize intensity in k-space
MaxFTcm1=(max(max(FTcm1)));
MaxFTcm2=(max(max(FTcm2)));
MaxFTcm3=(max(max(FTcm3)));
MaxFTcm4=(max(max(FTcm4)));
MaxFTcm5=(max(max(FTcm5)));
MaxFTcm6=(max(max(FTcm6)));
MaxFTcm7=(max(max(FTcm7)));
MaxFTcm8=(max(max(FTcm8)));
MaxFTcm9=(max(max(FTcm9)));

FTcm1N=FTcm1/MaxFTcm1;
FTcm2N=FTcm2/MaxFTcm2;
FTcm3N=FTcm3/MaxFTcm3;
FTcm4N=FTcm4/MaxFTcm4;
FTcm5N=FTcm5/MaxFTcm5;
FTcm6N=FTcm6/MaxFTcm6;
FTcm7N=FTcm7/MaxFTcm7;
FTcm8N=FTcm8/MaxFTcm8;
FTcm9N=FTcm9/MaxFTcm9;

MaxFTinten=(MaxFTcm1+MaxFTcm2+MaxFTcm3+MaxFTcm4+
    MaxFTcm5+MaxFTcm6+MaxFTcm7+MaxFTcm8+MaxFTcm9)/9;

```

```

%illumination spatial frequency estimation
d_ang1=150;
d_ang2=90;
d_ang3=30;

k2fa1 = [sind(d_ang1)*size_ppixel*w/kp  cosd(d_ang1)*
    size_ppixel*w/kp];%initial estimation of spatial
    frequency
k2fa2 = [sind(d_ang2)*size_ppixel*w/kp  cosd(d_ang2)*
    size_ppixel*w/kp];
k2fa3 = [sind(d_ang3)*size_ppixel*w/kp  cosd(d_ang3)*
    size_ppixel*w/kp];

kA1=LowK_Freq(k2fa1,FTcm1N,FTcm2N,FTcm3N,Ktof)%
    iterative optimation
kA2=LowK_Freq(k2fa2,FTcm4N,FTcm5N,FTcm6N,Ktof)
kA3=LowK_Freq(k2fa3,FTcm7N,FTcm8N,FTcm9N,Ktof)
%{
kA1=[  38.1372   -65.9112]
kA2=[  76.0936      0.0391]
kA3=[   37.9290     65.9656]
%}
%% phase estimation
phasea=LowK_phase(ccm1,ccm2,ccm3,kA1);
phaseb=LowK_phase(ccm4,ccm5,ccm6,kA2);
phasec=LowK_phase(ccm7,ccm8,ccm9,kA3);

%seperate frequency bands
[fcenta,fposa,fnega]=LowK_disentangle(phasea,FTcm1N,
    FTcm2N,FTcm3N,m1);
[fcentb,fposb,fnegb]=LowK_disentangle(phaseb,FTcm4N,
    FTcm5N,FTcm6N,m2);
[fcentc,fposc,fnegc]=LowK_disentangle(phasec,FTcm7N,
    FTcm8N,FTcm9N,m3);

%shift side bands and OTF to their right position
t1 = w;
t1o = t1/2;
t2 = h;
t2o = t2/2;
u = linspace(0,t1-1,t1);
v = linspace(0,t2-1,t2);
[U,V] = meshgrid(u,v);
H=h/2;
```

```

SFfaposa = fft2((ifft2(fposa)).*exp( +1i.*2*pi*(kA1(2)/(t1).*(U-t1o) + kA1(1)/(t2).*(V-t2o)) ));
SFfanega =fft2((ifft2(fnega)).*exp( -1i.*2*pi*(kA1(2)/(t1).*(U-t1o) + kA1(1)/(t2).*(V-t2o)) ));
SOTFoposa = fft2(fftshift(ifft2(OTFo)).*exp( +1i.*2*pi*(kA1(2)/(t1).*(U-t1o) + kA1(1)/(t2).*(V-t2o)) ));
SOTFonega =fft2(fftshift(ifft2(OTFo)).*exp( -1i.*2*pi*(kA1(2)/(t1).*(U-t1o) + kA1(1)/(t2).*(V-t2o)) ));

SFfaposb = (fft2((ifft2(fposb)).*exp( +1i.*2*pi*(kA2(2)/(t1).*(U-t1o) + kA2(1)/(t2).*(V-t2o)) )));
SFfanegb =(fft2((ifft2(fnegb)).*exp( -1i.*2*pi*(kA2(2)/(t1).*(U-t1o) + kA2(1)/(t2).*(V-t2o)) )));
SOTFoposb = fft2(fftshift(ifft2(OTFo)).*exp( +1i.*2*pi*(kA2(2)/(t1).*(U-t1o) + kA2(1)/(t2).*(V-t2o)) ));
SOTFonegb=fft2(fftshift(ifft2(OTFo)).*exp( -1i.*2*pi*(kA2(2)/(t1).*(U-t1o) + kA2(1)/(t2).*(V-t2o)) ));

SFfaposc = (fft2((ifft2(fposc)).*exp( +1i.*2*pi*(kA3(2)/(t1).*(U-t1o) + kA3(1)/(t2).*(V-t2o)) )));
SFfanegc =(fft2((ifft2(fnegc)).*exp( -1i.*2*pi*(kA3(2)/(t1).*(U-t1o) + kA3(1)/(t2).*(V-t2o)) )));
SOTFoposc = fft2(fftshift(ifft2(OTFo)).*exp( +1i.*2*pi*(kA3(2)/(t1).*(U-t1o) + kA3(1)/(t2).*(V-t2o)) ));
SOTFonegc =fft2(fftshift(ifft2(OTFo)).*exp( -1i.*2*pi*(kA3(2)/(t1).*(U-t1o) + kA3(1)/(t2).*(V-t2o)) ));

%Reconstruction via Wiener filter
OTF_merge=abs(SOTFoposa)+abs(SOTFonega)+3*abs(OTFo)+abs(SOTFoposb)+abs(SOTFonegb)+abs(SOTFoposc)+abs(SOTFonegc);
OTF_merge=OTF_merge/max(OTF_merge(:));
S_merge=SFfaposa+SFfanega+fcenta+SFfaposb+SFfanegb+fcentb+SFfaposc+SFfanegc+fcentc;
Wnftsum=S_merge.*conj((OTF_merge))./(abs(OTF_merge).^2+0.001);
WnftWF=(fcenta+fcentb+fcentc).*conj(abs(OTFo))./(abs(OTFo).^2+0.001);%apply Wiener filter to WF

%apodization to minimize ring artifact
MASKRo = sqrt( (U-t1o).^2 + (V-t2o).^2 );
DistApoMask1=(OTF_merge<=1e-4);%
[DistApoMask1,~] = bwdist(DistApoMask1);
maxDistApoMask1 = max(max(DistApoMask1));
```

```
Apomask1=(DistApoMask1/maxDistApoMask1);%SIM apodization mask

DistApoMask2=MASKRo>(Ktof);
[DistApoMask2,~] = bwdist(DistApoMask2);
maxDistApoMask2 = max(max(DistApoMask2));
Apomask2=(DistApoMask2/maxDistApoMask2);%WF apodization mask

Index = 0.4;%emprical index value from K. Wicker, Optics Express, 21, 2, 2013.
ApoFunc = Apomask1.^Index;
FsumA =Wnftsum.*ApoFunc.*MaxFTinten;
SIMA=abs(ifft2(FsumA));
Apo_WnftWF=WnftWF.*Apomask2.^Index*MaxFTinten;
Wiener_WF=abs(ifft2(Apo_WnftWF));
WF=abs(ifft2((fcenta+fcentb+fcentc)/3));

%image plot
figure();clf;
imshow(log(abs((fcenta+fcentb+fcentc)/3)),[]); colormap('gray');
title('Central band');

figure();clf;
imshow(log(abs(Apo_WnftWF)),[]); colormap('gray');
title('filtered Central band');

figure();clf;
imshow(log(abs(FsumA)),[]); colormap('gray');
title('FsumA');

figure;
imshow(WF,[0,max(WF(:))]);title('WF');

figure;
imshow(Wiener_WF,[0,max(Wiener_WF(:))]);title('Wiener filtered WF');

figure();
imshow((abs(SIMA)),[0,max(SIMA(:))]); colormap('gray');
axis off;
title('SIMA');
```

Function: PsfOtf.m

```
function [Kotf,OTF2dc] = PsfOtf(w,h,NA,lambda,Spixel)

% AIM: To generate PSF and OTF using Bessel function
% INPUT VARIABLES
%    w,h: image size
%    NA: NA of collecting objective
%   lambda: emission wavelength
% Spixel: pixel size
% OUTPUT VRAIBLES
%    yyo: system PSF
%    OTF2dc: system OTF

x = linspace(0,w-1,w);
y = linspace(0,h-1,h);
[X,Y] = meshgrid(x,y);
ho = h/2;
wo = w/2;
%% Generation of the PSF with Besselj.
Clambda=lambda/Spixel;
K=2*pi/Clambda;
R=sqrt((X-(w/2+1)).^2+(Y-(h/2+1)).^2);
V=K*R*NA;
yy=abs(2*besselj(1,V+eps,1)./(V+eps)).^2;
yy0 = fftshift(yy);

%Generate 2D OTF.
OTF2d=fft2(yy);
OTF2dmax = max(max(abs(OTF2d)));
OTF2d = OTF2d./OTF2dmax;
OTF2dc = abs(fftshift(OTF2d));



OTF1 = OTF2dc(ho+1,:);
OTFmax = max(max(abs(OTF2dc)));
OTFtruncate = 0.01;%k cutoff at intensity 0.01

i = 1;
while ( abs(OTF1(1,i))<OTFtruncate*OTFmax )
        Kotf = wo+1-i;
        i = i + 1;
end
```

Function: LowK_disentangle.m

```
function [fcent,fpos,fneg] = LowK_disentangle(phase,
    FTcm4N,FTcm5N,FTcm6N,m)

%disentangle frequency bands
phase1=phase(1);
phase2=phase(2);
phase3=phase(3);
%phase matrix
a1=m/2*exp(1i*(-phase1));
a2=m/2*exp(1i*(-phase2));
a3=m/2*exp(1i*(-phase3));

A= [1 a1 conj(a1);1 a2 conj(a2);1 a3 conj(a3)];
B= inv(A);

%Disentangle frequency components
fcent= B(1,1)*FTcm4N+B(1,2)*FTcm5N+B(1,3)*FTcm6N;
fpos= B(2,1)*FTcm4N+B(2,2)*FTcm5N+B(2,3)*FTcm6N;
fneg= B(3,1)*FTcm4N+B(3,2)*FTcm5N+B(3,3)*FTcm6N;
```

Function: LowK_Freq.m

```
function [kAm] = LowK_Freq(k2fa,FTcmNa,FTcmNb,FTcmNc,Ktof)


PhaseKai2opt0 = @(KA0)PhaseKai2opt(KA0,FTcmNa,Ktof);
options = optimset('LargeScale','off','Algorithm',...
          'active-set','MaxFunEvals',500,'MaxIter',500,'Display','notify');
[kA1,~] = fminsearch(PhaseKai2opt0,k2fa,options);
PhaseKai2opt0 = @(KA0)PhaseKai2opt(KA0,FTcmNb,Ktof);
options = optimset('LargeScale','off','Algorithm',...
          'active-set','MaxFunEvals',500,'MaxIter',500,'Display','notify');
[kA2,~] = fminsearch(PhaseKai2opt0,k2fa,options);
PhaseKai2opt0 = @(KA0)PhaseKai2opt(KA0,FTcmNc,Ktof);
options = optimset('LargeScale','off','Algorithm',...
          'active-set','MaxFunEvals',500,'MaxIter',500,'Display','notify');
[kA3,~] = fminsearch(PhaseKai2opt0,k2fa,options);

kAm=1/3*(kA1+kA2+kA3);
```

Function: LowK_phase.m

```
function [phase] = LowK_phase(ccm1,ccm2,ccm3,k2fa)
% AIM: illumination phase shift determination
% INPUT VARIABLES
%   ccm1: raw SIM image
%   k2fa: illumination frequency vector
% OUTPUT VARIABLE
%   phaseA1: illumination phase shift determined

PatternPhaseOpt0 = @(phaseA0)PatternPhaseOpt(phaseA0,
    ccm1,k2fa);
options = optimset('LargeScale','off','Algorithm',...
            'active-set','MaxFunEvals',500,'MaxIter',500,'
                Display','notify');
phaseA0 = 0;
[phase1,~] = fminsearch(PatternPhaseOpt0,phaseA0,
    options);
 PatternPhaseOpt0 = @(phaseA0)PatternPhaseOpt(phaseA0,
    ccm2,k2fa);
options = optimset('LargeScale','off','Algorithm',...
            'active-set','MaxFunEvals',500,'MaxIter',500,'
                Display','notify');

[phase2,~] = fminsearch(PatternPhaseOpt0,phaseA0,
    options);
 PatternPhaseOpt0 = @(phaseA0)PatternPhaseOpt(phaseA0,
    ccm3,k2fa);
options = optimset('LargeScale','off','Algorithm',...
            'active-set','MaxFunEvals',500,'MaxIter',500,'
                Display','notify');

[phase3,~] = fminsearch(PatternPhaseOpt0,phaseA0,
    options);
 phase=[phase1 phase2 phase3]
 phase.*180/pi% display phase in degree
```

Function: PatternPhaseOpt.m

```
function CCop = PatternPhaseOpt(phaseA,ccm1,k2fa)

w = size(ccm1,1);
wo = w/2;

x = linspace(0,w-1,w);
y = linspace(0,w-1,w);
[X,Y] = meshgrid(x,y);

sAo = cos( 2*pi*(k2fa(2).*(X-wo)+k2fa(1).*(Y-wo))./w +
    phaseA );%2D cos function
ccm1 = ccm1- mean2(ccm1);
CCop = -sum(sum(ccm1.*sAo));%sum of cross-correlation
    between 2D sinusoidal function and raw image
```

Function: PhaseKai2opt.m

```
function [CCop] = PhaseKai2opt(k2fa,FTcm1N,Kotf)
% Aim: Compute autocorrelation of FT of raw SIM images
%   k2fa: illumination frequency vector
%   FTcm1N: FT of raw SIM image
%   CCop: autocorrelation of FTcm1N

w = size(FTcm1N,1);
wo = w/2;


DoubleMatSize = 0;
if ( 2*Kotf > wo )
        DoubleMatSize = 1; % 1 for doubling fourier
            domain size, 0 for keeping it unchanged
end

if ( DoubleMatSize>0 )
    t = 2*w;
    fS1aT_temp = zeros(t,t);
    fS1aT_temp(wo+1:w+wo,wo+1:w+wo) = FTcm1N;
    clear fS1aT
    FTcm1N = fS1aT_temp;
    clear fS1aT_temp
else
    t = w;
end
to = t/2;
u = linspace(0,t-1,t);
v = linspace(0,t-1,t);
[U,V] = meshgrid(u,v);
SFcm1N = exp( -1i.*2*pi*( k2fa(2)/t.*(U-to)+k2fa(1)/t
    .*(V-to) ) ).*ifft2(FTcm1N);
SFFTcm1N = fft2( SFcm1N );

mA = sum(sum( FTcm1N.*conj(SFFTcm1N) ));

CCop = -abs(mA);
end
```

References

[1] Amit Lal, Chunyan Shan, and Peng Xi. *Structured Illumination Microscopy Image Reconstruction Algorithm.* IEEE Journal of Selected Topics in Quantum Electronics, 22(4):50–63, 2016.